

# Nonamphiphilic Assembly of Metal Carbonyl Complexes: Chemical Structure, Kinetics, and Hydrophobic Effect

by

Dapeng Liu

A thesis  
presented to the University of Waterloo  
in fulfillment of the  
thesis requirement for the degree of  
Doctor of Philosophy  
in  
Chemistry (Nanotechnology)

Waterloo, Ontario, Canada, 2018

©Dapeng Liu 2018

## Examining Committee Membership

The following served on the Examining Committee for this thesis. The decision of the Examining Committee is by majority vote.

|                          |                     |
|--------------------------|---------------------|
| External Examiner        | Eugenia Kumacheva   |
|                          | Professor           |
| Supervisor(s)            | Xiaosong Wang       |
|                          | Professor           |
| Internal Member          | Jean Duhamel        |
|                          | Professor           |
| Internal Member          | Juewen Liu          |
|                          | Professor           |
| Internal-external Member | Yuning Li           |
|                          | Associate Professor |

## **Author's Declaration**

I hereby declare that I am the sole author of this thesis. This is a true copy of the thesis, including any required final revisions, as accepted by my examiners.

I understand that my thesis may be made electronically available to the public.

## Statement of Contributions

The research work in Chapter 2 is submitted to *Macromolecules*. And homopolymer precipitation in THF/hexane mixed solvent was done in cooperation with Robert Kevin Arran Bennett (Undergraduate Co-op student).

The research work in Chapter 3 was published in the *Soft matter*, 2017, 13, 5130-5136. Simulation parts were performed by ZhouGuan from East China University of Science and Technology. Reproduced from Ref. [82] with permission from Royal Society of Chemistry.

The research work in Chapter 5 was published in *Chemistry- A European Journal*, 2017, 23 (41), 9736-9740. Synthesis of FpC<sub>6</sub>Pyrene and part of UV, FL characterization were done in cooperation with Shaowei Shi (Postdoctoral). Reproduced from Ref. [150] with permission from John Wiley and Sons.

The research work in Chapter 6 was published in *Chemistry-A European Journal*, 2018, 24 (26), 6737-6741. Reproduced from Ref. [83] with permission from John Wiley and Sons.



## Abstract

Self-assembly is an effective approach for the synthesis of various nanostructures. Assembly of amphiphilic molecules has been well developed, which are mostly thermodynamic controlled. Although the importance of kinetics and hydrophobic effect in self-assembly of biological molecules, such as proteins, has been well recognized, it remains to be challenging to understand these factors at molecular level. We have investigated the assembling behaviour of a few hydrophobic metal carbonyl polymers P(FpP) (FpP:  $\text{CpFe}(\text{CO})_2(\text{CH}_2)_m\text{PPh}_2$ ,  $m = 3$  or  $6$ ) and small molecules FpC<sub>6</sub>X (Fp head =  $(\text{PPh}_3)(\text{Cp})\text{Fe}(\text{CO})(\text{CO}-)$ ; C<sub>6</sub>X = hydrocarbon tail) in water. As a result, we were able to kinetically control the assemblies resulting in stable colloids in water with narrow size distribution and also gained fundamental knowledge on the hydrophobic effect at molecular level. The background of self-assembly is introduced in Chapter 1. It concludes that the assembly of non-amphiphilic molecules is less studied, but crucial for the understanding of biological supramolecular systems. Chapter 2 discusses the kinetic behaviour of hydrophobic homopolymer P(FpP) in poor solvents. We find that the kinetic pathways for the precipitation of P(FpP) is altered depending on the solution conditions. Kinetically trapped nanospheres and nanoworms with narrow PDI were produced. In Chapter 3, the assembly of P(FpP) in water is discussed. It is found that the rigidity of the backbone is a parameter determining the assembling morphology. With increasing the flexibility, the macromolecules assemble into lamellae, vesicles and irregular aggregates. As discussed in chapter 4, the vesicles formed in water do not have traditional bilayer membrane structure, which can swell upon the addition of THF. The swollen vesicles are colloidal stable and their PDI remains narrow. In addition to P(FpP), Fp acyl derivatives with pyrene or azobenzene (FpC<sub>6</sub>Azobenzene and FpC<sub>6</sub>Pyrene) were synthesis for aqueous assembly. The assembly

behaviour of FpC<sub>6</sub>Azobenzene, as influenced by the balance of aromatic interaction and hydrophobic effect of pyrene, is discussed in chapter 5. In DMSO/water or methanol/water systems, aromatic interactions are predominant and drive the assemble into lamellae, while in a THF/water system. hydrophobic effect drives the assembly into vesicles. The role of hydrophobic effect in solution behaviour of the assembled vesicles is discussed in Chapter 6. we find that the hydrophobic hydration of Fe in the MCsomes (aqueous vesicles of metal carbonyl complexes) can be detected by cyclic voltammetry and fluorescence quenching experiments. Moreover, the hydration can be adjusted by the chemical structures of tails as well as solution conditions, such as dilution and pH, which induces the hierarchical self-assembly of MCsomes. The research is summarized in Chapter 7.

## Acknowledgments

I would like to thank my supervisor, Dr. Xiaosong Wang, for the Ph.D. opportunity and guidance in the past four years. I also thank my committee members (Professor Jean Duhamel, Professor Juewen Liu, and Professor Dmitriy V Soldatov) to give me advice on the research and presentation skills. In the last four years, my presentation skills improved a lot and I also learned to how to express myself effectively. I really appreciate Professor Jean Duhamel and his student Damin Kim's help on the fluorescence experiments. I also appreciate that Professor Juewen Liu's support for me to characterize my samples by his lab's instruments. I also thank Professor Eugenia Kumacheva and Yuning Li to be external defense committee members.

I also would like to thank my friend Shaowei Shi to help me do some SEM and AFM characterization in Beijing University of Chemical Technology. I also appreciate Guan Zhou from East China University of Science and Technology for his help for his simulation to help us to better understand our molecules. Moreover, I really thank my lab mate Zhen Zhang and Robert Kevin Arran Bennett who gave me good advice and suggestion on my writing.

I really appreciate my wife (Wenya Xu) accompany in the last four years. She gives me lots of support and helps especially in the darkest time. I feel happy and warm all the time with her.

At last, I would like to thank my other lab mates who helped me a lot in organic synthesis, characterization and self-assembly experiments. They are Diya Geng, Na Zhou, Heyang Jiang, Robert Kevin Arran Bennett, Yang Yang, Huiwen He, Liao Peng, Aron Leung and Nicholas Lanigan.

## Dedication

I would like to dedicate this thesis to my lovely family...

## Table of Contents

|   |       |
|---|-------|
| Examining Committee Membership .....  | ii    |
| Author's Declaration.....   | iii   |
| Statement of Contributions .....  | iv    |
| Abstract .....  | v     |
| Acknowledgments.....  | vii   |
| Dedication.....   | viii  |
| Table of Contents .....   | ix    |
| List of Figures.....  | xvi   |
| List of Tables .....  | xxxi  |
| List of Abbreviations.....  | xxxii |
| Chapter 1 Introduction.....   | 1     |
| 1.1 Self-assembly .....   | 1     |
| 1.1.1 Introduction to self-assembly .....                                     | 1     |
| 1.2 Living cell self-assembly .....   | 1     |
| 1.2.1 Cell membranes self-assembled from amphiphilic phospholipids .....      | 1     |
| 1.2.1 Self-assembly based on nonamphiphilic proteins and DNA. ....            | 2     |
| 1.2.3 The hydrophobic hydration on the protein folding and self-assembly..... | 6     |

|  |    |
|--|----|
| 1.2.4 Kinetic study on the living cell self-assembly .....   | 7  |
| 1.3 Chemical self-assembly based on amphiphiles in aqueous solution.....   | 9  |
| 1.3.1 Chemical self-assembly of small amphiphilic molecules or surfactants .....                                       | 11 |
| 1.3.2 Chemical self-assembly based on amphiphilic block copolymers .....   | 12 |
| 1.3.3 Vesicles self-assembled from amphiphiles .....   | 15 |
| 1.4 Chemical self-assembly based on nonamphiphilic in aqueous solution .....   | 16 |
| 1.4.1 Self-assembly of hydrophilic-hydrophilic block copolymers .....  | 16 |
| 1.4.2 Self-assembly based on homopolymers .....  | 18 |
| 1.5 Self-assembly of metal carbonyl Fp complexes .....   | 22 |
| 1.5.1 Self-assembly of P(FpP).....   | 22 |
| 1.5.2 Self-assembly of Fp-based small molecules .....  | 23 |
| 1.6 Thesis outline.....  | 25 |
| Chapter 2 Kinetic Control of Homopolymer Precipitation in Solution for the Synthesis of Nanospheres and Nanowires..... | 27 |
| 2.1 Introduction .....   | 28 |
| 2.2 Experimental section.....  | 30 |
| 2.2.1 Materials and instrumentation .....  | 30 |
| 2.2.2 Synthesis of P(FpP).....   | 31 |

|   |    |
|---|----|
| 2.2.3 Preparation of colloidal solution of P(FpP) in THF/hexane .....                                   | 32 |
| 2.2.4 Preparation of colloidal solution of P(FpP) in DMSO .....   | 32 |
| 2.2.5 Segregation and stabilization of P(FpP) nanoparticles in DMSO.....                                | 33 |
| 2.3 Results and discussion .....  | 33 |
| 2.3.1 Kinetic assembly of P(FpP) in THF/hexane .....  | 33 |
| 2.3.2 Kinetic assembly of P(FpP) by cooling DMSO solutions. ....  | 37 |
| 2.3.3 Kinetic arrest and assembly of P(FpP) particles formed by cooling DMSO solutions. ....            | 40 |
| 2.4 Conclusions .....   | 44 |
| Chapter 3 Aqueous Self-Assembly of Hydrophobic Macromolecules with Adjustable Backbone<br>Rigidity..... | 46 |
| 3.1 Introduction.....   | 47 |
| 3.2 Experimental section .....  | 49 |
| 3.2.1 Materials and instrumentation. ....   | 49 |
| 3.2.2 Synthesis of P(FpP).....  | 50 |
| 3.2.3 Self-assembly of P(FpP).....  | 50 |
| 3.2.4 All-atom simulation. ....   | 51 |
| 3.2.5 DPD simulation system. ....   | 51 |
| 3.3 Results and discussion .....  | 52 |

|  |    |
|--|----|
| 3.3.1 Temperature-dependent chain conformation of P(FpP). .....  | 52 |
| 3.3.2 Temperature-dependent self-assembly of P(FpP). .....   | 53 |
| 3.3.3 Self-assembled morphologies reproduced by simulation. ....   | 56 |
| 3.4 Conclusions .....  | 65 |
| Chapter 4 Breathing Behavior of Vesicles Assembled from Hydrophobic Metal Carbonyl<br>Homopolymers P(FpP)..... | 67 |
| 4.1 Introduction .....   | 68 |
| 4.2 Materials and methods .....  | 70 |
| 4.2.1 Synthesis of P(FpP).....   | 71 |
| 4.2.2 Preparation of P(FpP) vesicles in water .....  | 71 |
| 4.2.3 Preparation of P(FpP) vesicles in water/THF mixture .....  | 72 |
| 4.3 Results and discussion .....   | 72 |
| 4.3.1 Characterization of the membrane structure of P(FpP) vesicles .....                                      | 72 |
| 4.3.2 Swelling behavior of P(FpP) vesicles .....   | 76 |
| 4.3.3 Membrane structure behavior in response to THF content.....  | 79 |
| 4.3.4 Swelling behavior of FpC <sub>6</sub> Pyrene bilayer vesicles .....                                      | 81 |
| 4.4 Conclusions .....  | 82 |



|   |     |
|---|-----|
| Chapter 5 The Effect of Solution Condition on the Driving Force for Self-Assembly of a Pyrene Molecule..... | 84  |
| 5.1 Introduction.....   | 85  |
| 5.2 Experimental Section.....   | 87  |
| 5.2.1 Materials.....  | 87  |
| 5.2.2 Measurements and Characterization. ....   | 87  |
| 5.2.3 Synthesis of FpC <sub>6</sub> Pyrene. ....  | 88  |
| 5.2.4 Preparation of FpC <sub>6</sub> Pyrene solution in DMSO/water or THF/water.....                       | 89  |
| 5.2.5 Preparation of FpC <sub>6</sub> Pyrene solution in methanol or ethanol. ....                          | 89  |
| 5.3 Results and discussion .....  | 89  |
| 5.3.1 Self-assembly of FpC <sub>6</sub> Pyrene in DMSO/water .....  | 89  |
| 5.3.2 The self-assembly behavior of FpC <sub>6</sub> Pyrene in THF/water .....                              | 97  |
| 5.3.3 The effect of $\sigma$ on the aromatic interactions .....   | 98  |
| 5.4 Conclusion .....  | 100 |
| Chapter 6 Hydrophobic Effect for Hierarchical Self-Assembly .....   | 102 |
| 6.1 Introduction.....   | 103 |
| 6.2 Experimental section .....  | 105 |
| 6.2.1 Materials and Methods.....  | 105 |

|   |     |
|---|-----|
| 6.2.2 Synthesis of FpC <sub>6</sub> Azobenzene <sup>trans</sup> .....                         | 107 |
| 6.2.3 Preparation of FpC <sub>6</sub> X MCsomes in water .....                                | 108 |
| 6.3 Results and Discussion.....   | 108 |
| 6.3.1 Dilution-induced assembly of FpC <sub>6</sub> Azobenzene <sup>trans</sup> MCsomes. .... | 108 |
| 6.3.2 The conditional effect of HH. ....  | 110 |
| 6.3.3 Hierarchical self-assembling behavior. ....   | 112 |
| 6.3.4 The effect of tail-tail interactions. ....  | 115 |
| 6.4 Conclusions .....   | 118 |
| Chapter 7 General Conclusions.....  | 120 |
| 7.1 Conclusions .....   | 120 |
| Bibliography .....  | 124 |
| Chapter 8 Appendices.....   | 150 |
| 8.1 Supporting information for Chapter 2.....   | 150 |
| 8.2 Supporting information for Chapter 3.....   | 153 |
| 8.2.1 Dissipative Particle Dynamic (DPD) simulation method .....                              | 157 |
| 8.2.2 $\pi$ - $\pi$ stack conjugate potential.....  | 158 |
| 8.2.3 Parameter setting.....  | 158 |
| 8.3 Supporting information for Chapter 4.....   | 162 |

|   |     |
|---|-----|
| 8.4 Supporting information for Chapter 5 .....                                    | 162 |
| 8.5 Supporting information for Chapter 6 .....                                    | 173 |
| 8.6 Synthesis and solution behavior of Fp-dendrimer complex .....                 | 187 |
| 8.6.1 Materials and instruments .....   | 187 |
| 8.6.2 Synthesis of Fp-dendrimer complex 6 .....                                   | 187 |
| 8.6.3 Solution behavior of complex 6 in organic solvents .....                    | 195 |
| 8.7 Fabrication of gold nanoparticle arrays using P(FpP) film as a template ..... | 196 |
| 8.7.1 Proposal.....   | 196 |
| 8.7.2 Preparation method .....  | 196 |
| 8.7.3 TEM characterization and preliminary results.....                           | 196 |
| 8.8 To coordinate Gd <sup>3+</sup> on the P(FpP) MCsomes .....                    | 197 |
| 8.8.1 Proposal.....   | 197 |
| 8.8.2 Preparation of P(FpP) aqueous colloid .....                                 | 198 |
| 8.8.3 Adding GdCl <sub>3</sub> aqueous solution into P(FpP) colloid .....         | 198 |

## List of Figures

|   |   |
|---|---|
| Figure 1.1. Chemical structure of a single phospholipid composed of two moieties, one hydrophilic head and two hydrophobic chains and schematic representation of its self-assembly into a membrane. ....   | 2 |
| Figure 1.2. The schematic representation and TEM image of the tobacco mosaic virus. The virus was composed of a single RNA and 2130 protein subunits which self-assembled around the RNA. Reproduced with permission from ref 14. ....  | 3 |
| Figure 1.3. a) Schematic representation of DNA icosahedra self-assembled from sticky-ended five-point-star motifs (tiles). b) Three views of the DNA icosahedron structure reconstructed from cryo-EM images. c) Schematic representation of self-assembly of DNA nanogrids using 4×4 DNA tile strand structure followed by scaffold assembly of streptavidin and the bottom images are the corresponding AFM images. Reproduced with permission from ref 8. .... | 5 |
| Figure 1.4. a) The schematic representation of protein surfaces where the hydrophobic and hydrophilic moieties are shown on the surface. b) Various assemblies were fabricated by proteins or peptides. Reproduced with permission from ref 9-10. ....  | 7 |
| Figure 1.5. a) The schematic presentation of self-assembly process with different kinetic barriers. b) Schematic biological assembly of lamins and the corresponding TEM images. Reproduced with permission from ref 24. ....   | 8 |
| Figure 1.6. Schematic presentation for the kinetic self-assembly process of amyloid fibril growth. Reproduced with permission from ref 25. ....   | 9 |

|   |    |
|---|----|
| Figure 1.7. Schematic representation of the block copolymers and their possible self-assembled nanostructures. Reproduced with permission from ref 30. ....   | 10 |
| Figure 1.8. The definition of CPP and its relationship with the formed morphology self-assembled from amphiphilic surfactants. Reproduced with permission from ref 40. ....   | 12 |
| Figure 1.9. The multiple nanostructures self-assembled by the amphiphilic block copolymers. The formed nanostructures are determined by the dimensionless packing parameter $p$ . Reproduced with permission from ref 41. ....  | 13 |
| Figure 1.10 a) Triblock copolymer, PAA-b-PMA-b-PS. b) growth mechanism of the hierarchical self-assembly of spherical micelles by addition of THF and c) its corresponding TEM images. Reproduced with permission from ref 44. ....   | 15 |
| Figure 1.11. Schematic presentation of the external stimuli drug-releasing behavior of vesicles. Reproduced with permission from ref 51. ....   | 16 |
| Figure 1.12 a) Chemical structure of the hydrophilic blockpolymer Dex-PEO. b) Cryogenic scanning electron microscopy images of vesicle-like aggregates of DEX-PEO at different concentrations. Reproduced with permission from ref 58. ....   | 18 |
| Figure 1.13 a) Model for homopolymer PVPPy self-assembly into homopolymer vesicles b) DLS profile and c) SEM micrograph images of PVPPy vesicles in THF/water (6/4 v/v). d) DLS profile and e) SEM micrograph images of PVPPy vesicles in THF/water (1/9 v/v). Reproduced with permission from ref 69. .... | 19 |

|  |    |
|--|----|
| Figure 1.14. Model for the formation of homopolymer vesicles by self-assembly of PHNA and the synergistic mechanism of the excellent catalytic efficiency of AuNPs@vesicles for the reduction of 4-nitrophenol (4-NP). Reproduced with permission from ref 71. ....  | 21 |
| Figure 1.15. Chemical structures of the metal carbonyl Fp compounds.....   | 22 |
| Figure 1.16 a) Self-assembly of hydrophobic P(FpP) and b) IR spectrums of P(FpP) solution by addition of water. Reproduced with permission from ref 79. ....   | 23 |
| Figure 1.17. a) The schematic presentation of Fp-based nanovesicles and b) self-assembly of MpC <sub>6</sub> in the aqueous solution. c) Synthesis and chemical structure for FpC <sub>n</sub> and Photographs illustrating the aqueous behavior of FpC <sub>1</sub> and FpC <sub>18</sub> . Reproduced with permission from ref 73,74 and 81. ....                      | 24 |
| Figure 2.1 a) The size change and b) PDI of P(FpP) colloids prepared in THF/hexane mixed solutions with varied THF contents. c) Size change and d) PDI of P(FpP) colloids prepared in THF/hexane with 4 vol%, 16 vol% and 40 vol% THF contents with time aging. ....   | 35 |
| Figure 2.2 TEM images for P(FpP) colloids formed in the THF/hexane solutions containing a) 4 vol%, b) 16 vol%, and c) 40 vol% THF. The inset images in the Figures 2.2a and 2.2b are the large magnification image of the corresponding P(Fp)P aggregates. The images were recorded after the solutions were prepared by shock precipitation and aged for one hour. .... | 36 |
| Figure 2.3. a) The transmittance curves of the three DMSO solutions of P(FpP) with varying concentrations as a function of temperature. b) The time-dependent transmittance of DMSO solution of P(FpP) (0.125 wt%) at 25 °C. The experiment started right after the solution was cooled from 65 °C to 25 °C. ....  | 38 |

Figure 2.4. a) DLS count rates as a function of temperature, and b) TEM image for P(FpP) particles resulted from DMSO solutions with P(FpP) concentrations of *ca.*0.125 wt% c) DLS profiles of P(FpP) colloid based on intensity before and after a membrane filtration. The inset image is the DLS profiles based on number. d) TEM image for the particles prepared from DMSO solution of P(FpP) (0.125 %wt) after a membrane filtration (*ca.*220 nm for the pore sizes). e) Schematic presentation of solution behavior of P(FpP) polymers during the cooling process..... 39

Figure 2.5. a) The  $D_h$  size change of P(FpP) colloid (0.125 wt%) upon addition of ethanol, methanol and H<sub>2</sub>O (8% mol%). b)  $D_h$  as a function of aging time for P(FpP)/DMSO colloids the upon addition of ethanol, methanol and H<sub>2</sub>O (8% mol%) TEM images for the aggregates prepared from DMSO solution of P(FpP) (0.125 wt%) after addition of c) ethanol and d) H<sub>2</sub>O, the insert image is the large magnification of the worm-like structures. e) Methanol, the insert image is the large magnification of the one-dimensional structures and f) linear aggregates by addition of H<sub>2</sub>O. g) The schematic presentation of the behavior of P(FpP) nanoparticles by addition of water, methanol and ethanol. .... 43

Figure 3.1. Morphologies of P(FpP) chain in response to temperatures. The green groups represent the neighboring phenyl rings and the red numbers indicate the distances between the groups..... 52

Figure 3.2. a) AFM phase mode image, b) height mode image, c) height profile along the line in b (the full scale of Y-axis is 19 nm) and d) TEM image for P(FpP) nano-sheets assembled at 25 °C in DMSO/H<sub>2</sub>O (10/90 by volume) solution (0.1 mg/mL). Scale bar for TEM: 500 nm. .... 53

Figure 3.3. a, b, c, d) TEM images of P(FpP) nano-vesicles assembled at 40 °C in DMSO/H<sub>2</sub>O (10/90 by volume) solution (0.1 mg/mL). scale bar: 100 nm. .... 55

Figure 3.4. a) The DLS profile and b, c, d) TEM images of P(FpP) nano-vesicles assembled at 70 °C in DMSO/H<sub>2</sub>O (10/90 by volume) solution (0.1 mg/mL). scale bar: 100 nm. ....56

Figure 3.5. Schematic illustration for the coarse-grained model of P(FpP) used for DPD simulation. a) Coarse-grained groups for P(FpP) (green, orange and red beads represent benzyl/Cp, COFeCO, and (CH<sub>2</sub>)<sub>3</sub>P groups, respectively). b) Coarse-grained P(FpP) chain. ....57

Figure 3.6. Persistence length as a function of  $k_c$  in DPD simulation (the black curve) and temperature in all-atom simulation (the red curve). The chain conformations at 25 and 70 °C, corresponding to  $k_c$  of 5 and 0  $k_B T$ , are shown in the figure. ....58

Figure 3.7. a) Morphologies of the simulated lamellae structure at 25 °C ( $k_c = 5k_B T$  and  $a_{RO} = a_{RP} = 60$ ,  $a_{RS} = 75$ ). The dashed lines indicate where the structure is sliced and enlarged for further analysis; b) The densities of O, P and R groups along the cross section (x1 direction). c) The order parameter of the backbones along the membrane plane (x2 direction). ....60

Figure 3.8. a) Morphologies of the simulated vesicular structure at 40 °C ( $k_c = 2k_B T$  and  $a_{RO} = a_{RP} = 50$ ,  $a_{RS} = 60$ ). The dashed lines indicate where the structure is sliced and enlarged for further analysis; b) The cross section of the vesicle, c) The densities of O, P and R groups along the cross section (x direction in the Figure 8b). ....61

Figure 3.9. Volumetric map images of a) curved lamellae simulated with  $k_c$  of 4  $k_B T$ , b) vesicles simulated with  $k_c$  of 2  $k_B T$ , and c) ruptured vesicles simulated with  $k_c$  of 1  $k_B T$ . ....62



Figure 3.10. (a) Morphologies of irregular aggregates simulated with  $k_c = 0$  k<sub>B</sub>T and  $a_{RO} = a_{RP} = 40$ ,  $a_{RS} = 50$ , b) Morphologies of wormlike nanoparticles simulated with  $k_c = 0$  k<sub>B</sub>T and  $a_{RO} = a_{RP} = 35$ ,  $a_{RS} = 35$ , c) Densities of O, P and R groups along the x direction of one wormlike nanoparticle. .... 63

Figure 3.11. The effect of stiffness on the morphologies self-assembled from macromolecules without water-soluble groups in aqueous media..... 65

Figure 4.1 a) DLS profile of P(FpP) colloids with various polymer concentrations. TEM images of the P(FpP) colloids with various polymer concentrations b) 0.10 mg/mL c) 0.05 mg/mL d) 0.03 mg/mL. .... 74

Figure 4.2 a)  $D_h$  of P(FpP) colloids prepared in THF/water mixed solvent with various THF contents. B) TEM image of the P(FpP) aggregates in THF/water mixed solvent with 30 vol% THF contents (Label red in the Figure 4.2a), the insert image is the large magnification of P(FpP) aggregates. .... 75

Figure 4.3 (a) The  $D_h$  change of P(FpP) colloids in aqueous solution (14  $\mu$ M) by addition of different amounts of THF. The inset image is the DLS profiles with different THF contents. (b) the size change as time aging for different P(FpP) colloid with varied THF amounts. .... 77

Figure.4.4 (a) The DLS profiles of P(FpP) vesicles in response to THF contents. TEM image of the P(FpP) vesicles obtained from the P(FpP) colloids with (b) 0 vol% THF and (c) 50 vol% THF. (d) and (e) TEM image of the P(FpP) aggregates with large magnification from the P(FpP) colloid (50 vol% THF content)..... 78

Figure 4.5 CV results of P(FpP) colloids (0.1 mg/mL) by addition of varied amounts of THF added into the dispersion: (a) 0 vol% and (b) 50 vol%. c) Zeta potential of P(FpP) colloid as a function of varied

amounts of THF. d) Solubility of P(FpP) in THF and acetonitrile with same concentration (1 mg/mL). e) DLS profiles with different acetonitrile contents: 10 vol%, 20 vol% and 30 vol%. f) The photograph image of P(FpP) colloids with high content of acetonitrile: 40 vol% and 50 vol%. ..... 80

Figure 4.6 a)  $D_h$  change of FpC<sub>6</sub>Pyrene colloids with low THF contents (0~30 vol%). The inset image is the solution behavior of FpC<sub>6</sub>Pyrene colloids with higher THF contents (30 vol%~ 50 vol%) b) DLS profiles of FpC<sub>6</sub>Pyrene colloid below 30 vol% THF/water mixed solvents. c) Schematic presentation of FpC<sub>6</sub>Pyrene nanovesicles by addition of different amounts of THF. .... 82

Figure 5.1. a) UV/Vis absorption and b) fluorescent spectra, and c) hydrodynamic diameter ( $D_h$ ) for the solution of FpC<sub>6</sub>Pyrene in DMSO/water ( $1.4 \times 10^{-4}$  M) with various water contents. .... 92

Figure 5.2. a) TEM image for the aggregates assembled from FpC<sub>6</sub>Pyrene in DMSO/water solutions (40 vol% water), b) photograph for the solutions of FpC<sub>6</sub>Pyrene in DMSO/water, c) TEM images for the cotton-like assemblies separated from the solution of DMSO/water (40 vol% water), d) TEM images for the nanoparticles formed in the solution containing 90 vol% water. (The solution concentration is  $1.4 \times 10^{-4}$  M) ..... 95

Figure 5.3 a) UV/Vis, b) fluorescent spectra, and c) the hydrodynamic diameters ( $D_h$ ) for the solution of FpC<sub>6</sub>Pyrene in THF/water ( $1.4 \times 10^{-4}$  M) with various water contents, d) cryo-TEM image for the FpC<sub>6</sub>Pyrene assemblies in THF/water (90 vol% water). .... 97

Figure 5.4 TEM images for a) the aggregates formed in FpC<sub>6</sub>Pyrene solution in ethanol with a lower  $\sigma$  ( $1 \times 10^{-4}$  M), b) in methanol/DMSO (10 vol% DMSO), c) TEM image and (d) AFM image for the aggregates assembled from the solution of FpC<sub>6</sub>Pyrene in methanol with a higher  $\sigma$  ( $5.5 \times 10^{-4}$  M). All the solutions were prepared via a cycle of heating and cooling. .... 99

Figure 6.1. Schematic illustration for MCsomes assembled from FpC<sub>6</sub>X molecules in water. .... 105

Figure 6.2. (a) TEM image of the MCsome assembled from FpC<sub>6</sub>Azobenzene<sup>trans</sup> in water (140 μM).

(b) The time-dependent  $D_h$  of FpC<sub>6</sub>Azobenzene<sup>trans</sup> MCsomes in water for the solutions with

concentrations of 140 μM and 14 μM. (c) TEM image of the helix assembled from FpC<sub>6</sub>Azobenzene<sup>trans</sup>

MCsomes that were diluted to 14 μM and aged for 30 days. (d) Electron energy loss spectrum (EELS)

of carbon elements distributing along and normal to the helical axis. Scale bar: 500 nm. .... 109

Figure 6.3. (a) Schematic illustration for the hydrophobic hydration (HH) of the Fp head in response to

dilution and lowering pH. The zeta potential of the FpC<sub>6</sub>Azobenzene MCsomes in dependence of the

dilution from 140 μM to 14 μM and pH lowering from 7.3 to 3.0 is indicated in the scheme. (b) Zeta

potential of FpC<sub>6</sub>Azobenzene<sup>trans</sup> MCsome in water upon dilution (from 140 μM to 14 μM). (c) The

cyclic voltammogram (CV) for FpC<sub>6</sub>Azobenzene<sup>trans</sup> MCsome in water with the concentration of 140

μM, 70 μM, 35 μM and 14 μM. (d) The Stern-Volmer plot for the fluorescence quenching of calcein

(0.17 μM) in water by FpC<sub>6</sub>Azobenzene<sup>trans</sup> MCsomes with different concentrations. The inset displays

the corresponding emission spectra.  $F_0$  and  $F$  refer to the emission intensity of calcein in the absence

and presence of MCsomes. (e) pH-dependent zeta potential of FpC<sub>6</sub>Azobenzene<sup>trans</sup> MCsome in water

(140 μM)..... 111

Figure 6.4. (a-h) TEM images for the diluted FpC<sub>6</sub>Azobenzene<sup>trans</sup> MCsome (14 μM) in water at

different aging times. (a) Initially prepared MCsomes, (b) Fused MCsomes after aging for 10 days, (c)

Fusion intermediates. The red circles represent hemifusion where the thickness of the contact zone is

close to the membrane thickness and the blue circles represent full fusion where two vesicles are fused

without membrane separation, (d) One-dimensional arrays of vesicles after aging for 14 day, (e)

Intermediates for the coalescence of the vesicles into nanotubes, (f) Hollow tube structures after aging for 20 day, (g) Helical structures after aging for 30 day, (h) The intermediates for tube-to-helix transition. (i-k) pH-induced solution behavior of FpC<sub>6</sub>Azobenzene<sup>trans</sup> MCsomes (140 μM) without dilution, including (i) Time-dependent D<sub>h</sub> measured by DLS at pH 3, (j) Optical microscopy and (k) TEM images of the assembly after aging for 3 days at pH 3. Scale bar = 500 nm unless otherwise indicated in figures. .... 114

Figure 6.5. (a) TEM image for the diluted FpC<sub>6</sub>Pyrene colloid (14 μM) after aging for 60 days. (b) TEM image of one-dimensional arrays of FpC<sub>6</sub>Pyrene MCsomes (14 μM) recorded before the formation of nanotubes. (c) Fluorescence spectra of calcein solutions (0.17 μM) in the presence of three different MCsomes (140 μM). The inset is the cyclic voltammogram of FpC<sub>6</sub> MCsomes in water (140 μM). (d) Fluorescence spectra of calcein (0.17 μM) in the presence of FpC<sub>6</sub>Azobenzene<sup>trans</sup> MCsomes (140 μM) before and after UV light irradiation (365 nm). The inset is the cyclic voltammograms for the FpC<sub>6</sub>Azobenzene<sup>trans</sup> MCsomes in water (140 μM) before and after UV light irradiation (365 nm). Scale bar: 1 μm. .... 117

Figure 8.1. Concentration-dependent thermoresponsive behaviors for the solution of P(FpP) in DMSO. .... 151

Figure 8.2. UV-Vis absorption spectrum for the solution of P(FpP) in DMSO at 65 °C. .... 152

Figure 8.3. TEM images for the precipitates of P(FpP) suspension in DMSO at room temperature. 152

Figure 8.4. TEM images of the particles prepared from DMSO solution of P(FpP) a) 0.5 wt% and b) 1 wt%) after cooling to room temperature. .... 153

|  |     |
|--|-----|
| Figure 8.5 a) The DLS profile of the prepared P(FpP) aggregates at 25 °C. b) nanosheets observed in the TEM images for the prepared P(FpP) aggregates at 25 °C. ....   | 154 |
| Figure 8.6 DLS profile of P(FpP) nanovesicles at 40 °C cooling to 25 °C and 25 °C for 2 days TEM images of P(FpP) nanovesicles formed at 40 °C. b) The aggregation of nanovesicles. c) and d) Independent nanovesicles found in the same TEM grid. Scale bar: 100 nm ..... | 155 |
| Figure 8.7 DLS profile of the formed P(FpP) irregular aggregates at 60 °C, cooling to 25 °C and 2 days later at 25 °C. ....  | 156 |
| Figure 8.8 TEM images of the irregular P(FpP) aggregates breaking up with time aging under electron beam of TEM. Scale bar: 100 nm .....   | 156 |
| Figure 8.9. Values of $\chi_{ij}$ for the pairs of different species as a function of temperature. ....  | 159 |
| Figure 8.10. Persistence length as a function of $k_c$ in DPD simulation and temperature in the all-atom simulation. The all-atom morphologies under different temperatures are shown in the figure. ....  | 161 |
| Figure 8.11. $^1\text{H-NMR}$ and $^{31}\text{P-NMR}$ spectra of FpC <sub>6</sub> Pyrene in CDCl <sub>3</sub> .....  | 163 |
| Figure 8.12. The intensity of fluorescent emission as a function of water content in DMSO/water system (1.4 x 10 <sup>-4</sup> M). ....  | 163 |
| Figure 8.13. Hydrodynamic diameters ( $D_h$ ) of the colloids assembled from FpC <sub>6</sub> Pyrene in DMSO/water (40-90 vol% water content, concentration: 1.4 x 10 <sup>-4</sup> M). The experiments were performed right after the preparation of the solution. ....   | 165 |

Figure 8.14. TEM images of FpC<sub>6</sub>Pyrene assemblies formed in DMSO/water solutions (50-80 vol% water content, concentration:  $1.4 \times 10^{-4}$  M). The experiments were performed right after the preparation of the solutions. .... 166

Figure 8.15. Representative TEM images of the cotton-like suspension formed in DMSO/water solution of FpC<sub>6</sub>Pyrene (40-80 vol% water content, concentration:  $1.4 \times 10^{-4}$  M). .... 167

Figure 8.16 UV spectra of FpC<sub>6</sub>Pyrene (50 vol% and 60 vol% water content) aqueous solution at the different time. .... 168

Figure 8.17. SEM image of FpC<sub>6</sub>Pyrene aggregates dried from the solution of THF/water (90 vol% water). .... 169

Figure 8.18. TEM image of FpC<sub>6</sub>Pyrene precipitates formed in methanol ( $2.5 \times 10^{-4}$  M). The sample was prepared after aging the solution for a few days. The solution was prepared via a cycle of heating at 60 °C and cooling to 23 °C ..... 170

Figure 8.19. TEM images of FpC<sub>6</sub>Pyrene aggregates formed in ethanol solution with a various degree of supersaturation. The solution was prepared via a cycle of heating at 60 °C and cooling to 23 °C. (a) The solution with a lower degree of supersaturation ( $2.5 \times 10^{-4}$  M) is aged for a week, (b) the solution with a higher degree of supersaturation ( $1.1 \times 10^{-3}$  M) results in a cotton-like suspension in a few hours. .... 171

Figure 8.20. UV-Vis spectra of the ethanol solution of FpC<sub>6</sub>Pyrene with a lower degree of supersaturation ( $2.5 \times 10^{-5}$  M). (a) the freshly prepared solution (b) the colloid formed after aging for a week. .... 172

Figure 8.21 TEM image with a relatively large magnification for the aggregates assembled from FpC<sub>6</sub>Pyrene in methanol with a higher  $\sigma$  ( $5.5 \times 10^{-4}$  M)..... 173

Figure 8.22. a, FpC<sub>6</sub>Azobenzene<sup>trans</sup> directly mixed with water. b, Concentration-dependent surface tension of FpC<sub>6</sub>Azobenzene<sup>trans</sup> MCsomes in water. Figure 8.22 indicate that FpC<sub>6</sub>Azobenzene<sup>trans</sup> is hydrophobic and non-surface active..... 174

Figure 8.23. a, DLS count rates of FpC<sub>6</sub>Azobenzene<sup>trans</sup> in THF/water solutions with varied water contents. b, IR absorption of the terminal and acyl CO groups for the solutions of FpC<sub>6</sub>Azobenzene<sup>trans</sup> in THF/D<sub>2</sub>O with varied D<sub>2</sub>O contents. As shown in Figure 8.23a, FpC<sub>6</sub>Azobenzene<sup>trans</sup> starts to aggregate when the water content is larger than 50 vol%. After the aggregation (80 vol%), the IR signals for the acyl CO and terminal CO groups shift to lower wavenumbers (Figure 8.23b), suggesting the presence of water carbonyl interactions (WCIs). ..... 174

Figure 8.24 a, DLS curve and b Berry plot for FpC<sub>6</sub>Azobenzene<sup>trans</sup> MCsome in water (1.4  $\mu$ M). Figures 8.24a and 8.24b reveal that the hydrophobic radius ( $R_h$ ) and gyration radius ( $R_g$ ) are *ca.* 84 nm and 83 nm, respectively. The  $R_g/R_h$  of *ca.* 1.0 indicates that FpC<sub>6</sub>-azobenzene<sup>trans</sup> assembles into nanovesicles. c, AFM height mode image with height profiles for FpC<sub>6</sub>Azobenzene<sup>trans</sup> nanovesicles. The AFM analysis of the aggregates shows that the ratio of diameter-to-height is *ca.* 5.0 due to the deformation of hollow structure upon dry. d, SEM image for FpC<sub>6</sub>Azobenzene<sup>trans</sup> nanovesicles. The inset image is the large magnification of a bowl-shaped vesicle due to the deformation of hollow structure. Scale bar = 500 nm, unless otherwise indicated..... 175

Figure 8.25. a, UV/Vis absorption spectra for FpC<sub>6</sub>Azobenzene<sup>trans</sup> molecules in THF (50  $\mu$ M) and FpC<sub>6</sub>Azobenzene<sup>trans</sup> MCsomes (60  $\mu$ M) in water. The shift of the absorption peak to a larger

wavelength suggests that the azobenzene groups in the MCsomes are intermolecular  $\pi$ - $\pi$  interacted. b, Concentration-dependent DLS profiles for FpC<sub>6</sub>Azobenzene<sup>trans</sup> MCsomes in water. The solutions were diluted from a prepared MCsome (140  $\mu$ M) and measured right after the dilution. It indicates that the dilution process does not change the size of the MCsomes. .... 176

Figure 8.26. Dark-field TEM images of the helix assembled from FpC<sub>6</sub>Azobenzene<sup>trans</sup> MCsomes and its EDX analysis profile. Scale bar: 500 nm. .... 177

Figure 8.27. (a and b) EDX line scanning for the elements of C, O, P and Fe (a) along the helix and (b) normal to the helix. Scale bar: 500 nm. The same element distributions for all the elements confirm that the helix is assembled from FpC<sub>6</sub>Azobenzene<sup>trans</sup>. .... 178

Figure 8.28. TEM images recorded after aging the diluted FpC<sub>6</sub>Azobenzene<sup>trans</sup> MCsomes in water (14  $\mu$ M) for 30 days. The long helixes have a low concentration, so each image only captures one helix. Scale bar: 500 nm. .... 179

Figure 8.29 a, Concentration-dependent UV absorption at 360 nm for FpC<sub>6</sub>Azobenzene<sup>trans</sup> MCsomes in water. No shift in the wavelength of the absorption peak suggests that the dilution does not alter the  $\pi$ - $\pi$  interactions. b, Concentration-dependent IR absorption for the acyl and terminal CO groups. No shifts in the wavenumbers for the absorption peaks suggest that the dilution results in no detectable variation in WCIs. .... 180

Figure 8.30. a, pH-dependent zeta potential of the diluted FpC<sub>6</sub>Azobenzene<sup>trans</sup> MCsomes (14  $\mu$ M). b, Time-dependent D<sub>h</sub> of diluted FpC<sub>6</sub>Azobenzene<sup>trans</sup> MCsomes (14  $\mu$ M) at pH 3. .... 181



|  |     |
|--|-----|
| Figure 8.31. Concentration-dependent zeta potential recorded in a process of dilution of a, FpC <sub>6</sub> MCsomes and b, FpC <sub>6</sub> Pyrene MCsomes.....   | 181 |
| Figure 8.32. pH-dependent zeta potential of a FpC <sub>6</sub> MCsomes and b FpC <sub>6</sub> Pyrene MCsomes. The concentrations for both MCsomes are 140 μM.....  | 182 |
| Figure 8.33. TEM images recorded for the diluted FpC <sub>6</sub> Azobenzene <sup>trans</sup> MCsomes (14 μM) after aging for 14 and 17 days. a, one-dimensional arrays of vesicles and b, the arrays with partial coalescence of vesicles. Scale bar: 500 nm.....   | 182 |
| Figure 8.34. TEM images of the precipitates resulting from FpC <sub>6</sub> Azobenzene <sup>trans</sup> MCsomes (140 μM) at pH = 3 after aging for <i>ca.</i> 2 weeks. Scale Bar: 500 nm.....  | 183 |
| Figure 8.35. Time-dependent DLS profiles for FpC <sub>6</sub> Pyrene MCsomes in water (140 μM).....  | 183 |
| Figure 8.36. a, DLS profiles for the diluted FpC <sub>6</sub> Pyrene MCsomes (14 μM) in water before and after aging. b, The cyclic voltammogram (CV) for FpC <sub>6</sub> Pyrene MCsome in water (140 μM). .....  | 184 |
| Figure 8.37. Zeta potential of the three different MCsomes in water at 140 μM.....   | 184 |
| Figure 8.38. a, UV/Vis spectra of FpC <sub>6</sub> Azobenzene <sup>trans</sup> MCsomes (70 μM) in water after UV light (wavenumber = 365 nm) irradiation for different times. b, <sup>31</sup> P NMR spectra of FpC <sub>6</sub> Azobenzene <sup>trans</sup> molecules in CDCl <sub>3</sub> . These molecules were recovered from their aqueous solutions via freeze-drying before and after UV irradiation (365 nm). There is no change in the spectra after the irradiation suggesting no degradation of the molecules. c, DLS profile of FpC <sub>6</sub> Azobenzene <sup>trans</sup> MCsomes (140 μM) before and after UV irradiation. d, TEM image of the FpC <sub>6</sub> Azobenzene <sup>trans</sup> MCsomes after UV |     |

|   |     |
|---|-----|
| irradiation for 2 min (Scale bar: 500 nm). Figures 8.38c and 8.38d indicate that the irradiation does not change the vesicular morphology. ....   | 185 |
| Figure 8.39 $^1\text{H}$ NMR spectrum of 3,4,5-tris(dodecyloxy)benzoate in chloroform- $\text{d}_1$ at 298 K.....   | 189 |
| Figure 8.40 $^1\text{H}$ NMR spectrum of 3,4,5-tris(dodecyloxy)benzoic acid in chloroform- $\text{d}_1$ at 298 K ...  | 189 |
| Figure 8.41 $^1\text{H}$ NMR spectrum of N-(3-bromopropyl)-3,4,5-tris(dodecyloxy)benzamide in chloroform- $\text{d}_1$ at 298 K .....   | 191 |
| Figure 8.42 $^1\text{H}$ NMR spectrum of complex 5 in chloroform- $\text{d}_1$ at 298 K.....  | 193 |
| Figure 8.43 $^1\text{H}$ NMR spectrum of target complex 6 in chloroform- $\text{d}_1$ at 298 K.....   | 194 |
| Figure 8.44 $^{31}\text{P}$ NMR spectrum of target complex 6 in chloroform- $\text{d}_1$ at 298 K.....  | 194 |
| Figure 8.45 TEM images of the film formed on the surface of the solution a) low magnification, b) large magnification. ....   | 197 |
| Figure 8.46 The size change ( $D_h$ ) of P(FpP) aggregates by addition of various amounts of $\text{GdCl}_3$ solution. And TEM images of P(FpP) colloids with various amounts of $\text{GdCl}_3$ aqueous solution (25 $\mu\text{M}$ ), b) 1 mL, c) 2 mL $\text{GdCl}_3$ aqueous solution..... | 199 |

## List of Tables

|   |     |
|---|-----|
| Table 5.1. The self-assembling behavior of FpC <sub>6</sub> Pyrene in response to solution conditions. ....                             | 90  |
| Table 8.1. The viscosity and refractive index for DMSO at different temperatures.....   | 150 |
| Table 8.2 The repulsive parameter ( $a_{ij}$ ) and the chain stiffness potential ( $k_c$ ) of P(FpP) as a function of temperature. .... | 153 |
| Table 8.3 The viscosity and refractive index for THF/water mixed solvents with varied THF contents. ....                                | 162 |
| Table 8.4. The viscosity of DMSO/water* .....   | 164 |
| Table 8.5. The viscosity of THF/water* .....  | 164 |
| Table 8.6 The solubility of complex 6 in different organic solvents .....   | 195 |

## List of Abbreviations

|          |                                      |
|----------|--------------------------------------|
| AFM      | Atomic force microscope              |
| ACQ      | Aggregation-caused quenching         |
| CAC      | Critical aggregation concentration   |
| CO group | Carbonyl group                       |
| Cp       | Cyclopentadienyl group               |
| CV       | Cyclic voltammetry                   |
| CWC      | Critical water content               |
| $D_h$    | Hydrodynamic diameter                |
| DLS      | Dynamic light scattering             |
| DMF      | Dimethylformamide                    |
| DMSO     | Dimethyl sulfoxide                   |
| DPD      | Dissipative particle dynamics        |
| DP       | Degree of polymerization             |
| EDX      | Energy-dispersive X-ray spectroscopy |
| EELS     | Electron energy loss spectra         |

|                  |  |
|------------------|--|
| ESI-MS           | Electrospray ionization-mass spectrometry                    |
| FL               | Fluorescence   |
| Fp               | $(\text{PPh}_3)(\text{Cp})\text{Fe}(\text{CO})(\text{CO}^-)$ |
| FpK              | Cyclopentadienyl dicarbonyl potassium                        |
| GPC              | Gel permeation chromatography                                |
| HE               | Hydrophobic effect   |
| HH               | Hydrophobic hydration  |
| HI               | Hydrophobic interaction                                      |
| MIP              | Migration insertion polymerization                           |
| MCsomes          | Aqueous vesicles of metal carbonyl complexes                 |
| MCH              | Methylcyclohexane  |
| NMR              | Nuclear magnetic resonance                                   |
| NP               | Nanoparticles  |
| PDI              | Polydispersity index   |
| Ph               | Phenyl ring  |
| PPh <sub>3</sub> | triphenylphosphine   |

|                  |  |
|------------------|--|
| $R_g$            | Radius of gyration   |
| $R_h$            | Hydrodynamic radius  |
| SEM              | Scanning electron microscope   |
| SLS              | Static light scattering  |
| TEM              | Transmission electron microscopy                                       |
| THF              | Tetrahydrofuran  |
| WCIs             | Water carbonyl interactions  |
| $\gamma$         | Surface tension  |
| $\zeta$          | Zeta Potential   |
| $\Delta E_{1/2}$ | Redox coupling (Separation between two oxidation peaks in a CV curve.) |

## Chapter 1 Introduction

### 1.1 Self-assembly

#### 1.1.1 Introduction to self-assembly

Self-assembly has become a rapidly growing research field,<sup>1-2</sup> because it is an effective approach for the synthesis of complex ordered structures and also a strategy for a better understanding of biological structures and functions. Cell functions rely highly on the assembling behaviour, which is referred as living cells self-assembly. Chemists have tried to mimic this assembly for functional materials.<sup>1,3</sup> A typical example is the bilayer membranes assembled from amphiphilic molecules or block copolymers. Living cells assembly also includes assembling behaviour based on non-amphiphilic building blocks, such as proteins, which is far from understood and requires substantial research effort.<sup>4</sup>

#### 1.2 Living cell self-assembly

The living cells self-assembly creates a range of complex ordered structures, such as cell membranes, DNA, and protein assemblies. The cell membrane inspired amphiphilic assembly is the result of amphiphilic assembly;<sup>5</sup> DNA assemblies are mainly based on hydrogen bonding and structure rigidities.<sup>6-8</sup> Protein assemblies are strongly influenced by hydrophobic effect and kinetic pathways, which are complicated and difficult to study.<sup>9-10</sup>

##### 1.2.1 Cell membranes self-assembled from amphiphilic phospholipids

The bilayer structure of cell membranes self-assembled from phospholipids is well known.<sup>11</sup> Phospholipids are amphiphilic molecules that consist of two hydrophobic chains and one hydrophilic head (Figure 1.1). The bilayer is formed via the association of the hydrophobic chains, which exposes the hydrophilic heads to water, thus stabilizing the cell membrane.<sup>5</sup> The formed cell membrane not only protects the cell but also serves as a barrier for the selective permeation of certain molecules.<sup>12-13</sup> Cell

membrane is the most understandable structure in living cell self-assembly, based on the phase segregation of hydrophobic and hydrophilic segments which has been developed as a basic principle for the synthesis of aqueous colloids.

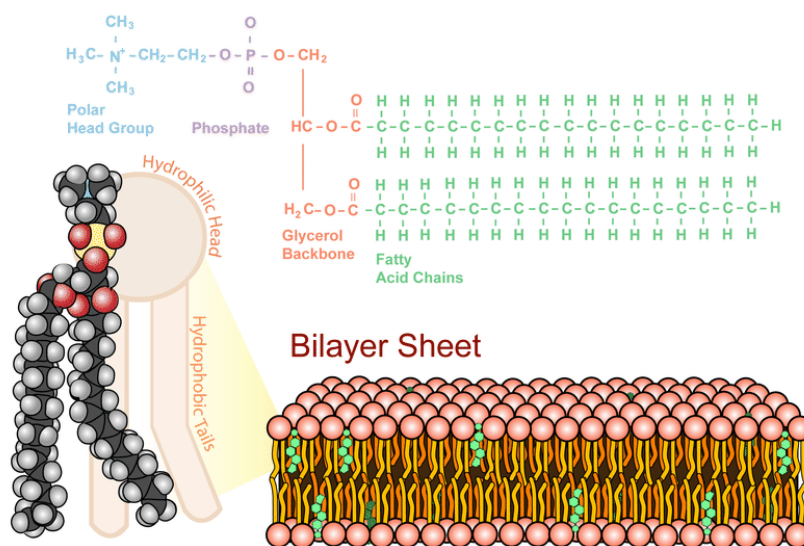


**Figure 1.1. Chemical structure of a single phospholipid composed of two moieties, one hydrophilic head and two hydrophobic chains and schematic representation of its self-assembly into a membrane.**

### 1.2.1 Self-assembly based on nonamphiphilic proteins and DNA.

Examples of self-assembly that occur in living cells include the assemblies of DNA and proteins that are far more complex than the formation of the cell membrane. For example, large amounts of protein subunits surround a single RNA forming a tobacco mosaic virus that has a length of 300 nm and width of 18 nm (Figure 1.2).<sup>14</sup> This assembly cannot be explained based on the theory of amphiphilicity, because proteins and RNA exhibit no obvious separation between their hydrophobic and hydrophilic



moieties as lipids do. To better understand the complexity in the living cell self-assembly, it is required to explore the effect of factors other than amphiphilicity on self-assembly. Among these factors, the effect of structural rigidity is crucial for DNA self-assembly, and the hydrophobic effect is essential for protein folding that usually is influenced by its kinetic pathways.

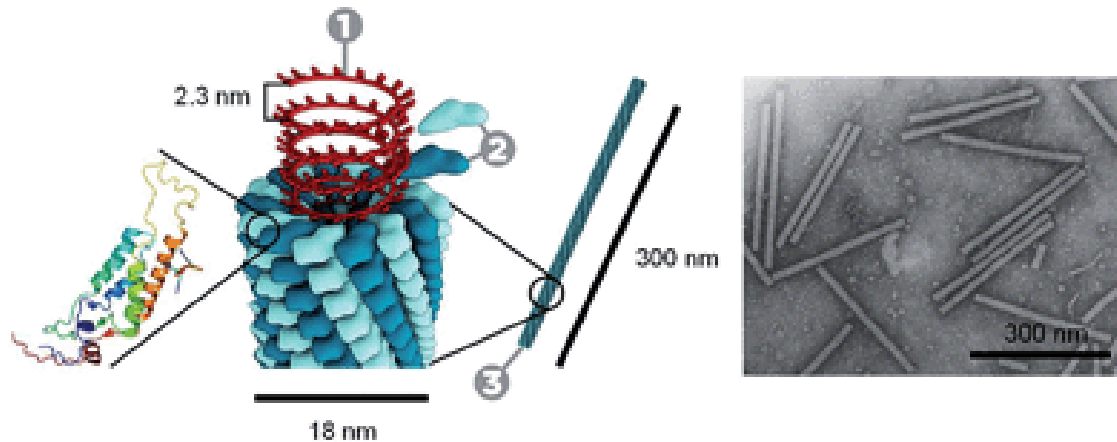


**Figure 1.2. The schematic representation and TEM image of the tobacco mosaic virus.**

**The virus was composed of a single RNA and 2130 protein subunits which self-assembled around the RNA. Reproduced with permission from ref 14.**

### **1.2.2 The influence of DNA structural rigidity on their self-assembly**

DNA and RNA have no hydrophobic and hydrophilic segments, but they can assemble through specific hydrogen bonding between the base pairs.<sup>6-7</sup> It is found that the conformational flexibility of these biological macromolecules is important for the construction of well-defined nanostructures.<sup>15</sup> For example, Mao's group demonstrated that the five-point-star DNA icosahedra tiles could self-assemble into various 3D nanostructures, including tetrahedra, dodecahedra, and buckyballs, depending on the conformational flexibility of the building blocks (Figure 1.3).<sup>8</sup> The Mao group also reported that the

three-point-star DNA tiles could self-assemble into 2D nanocrystals on a solid surface. To realize this self-assembly process, the reducing flexibility of the DNA tiles was reduced by weak interactions between the DNA tiles and the solid surface which played a critical role.<sup>16</sup> The rigidity of the DNA could make the self-assembled DNA nanostructures exhibit unusual motifs or lattices.<sup>17</sup> These motifs could be employed in the construction of certain periodic patterns where structures have great potential applications in scaffold assembly of other molecules like proteins or inorganic nanoparticles. For example, as shown in Figure 1.3c, DNA self-assembled into a 4×4 DNA tile with immobile DNA branched junctions.<sup>18</sup> These DNA tiles could self-assemble into nanogrids (Figure 1.3c). The nanogrids could further induce self-assembly of protein streptavidin shown to fabricate periodic streptavidin arrays.

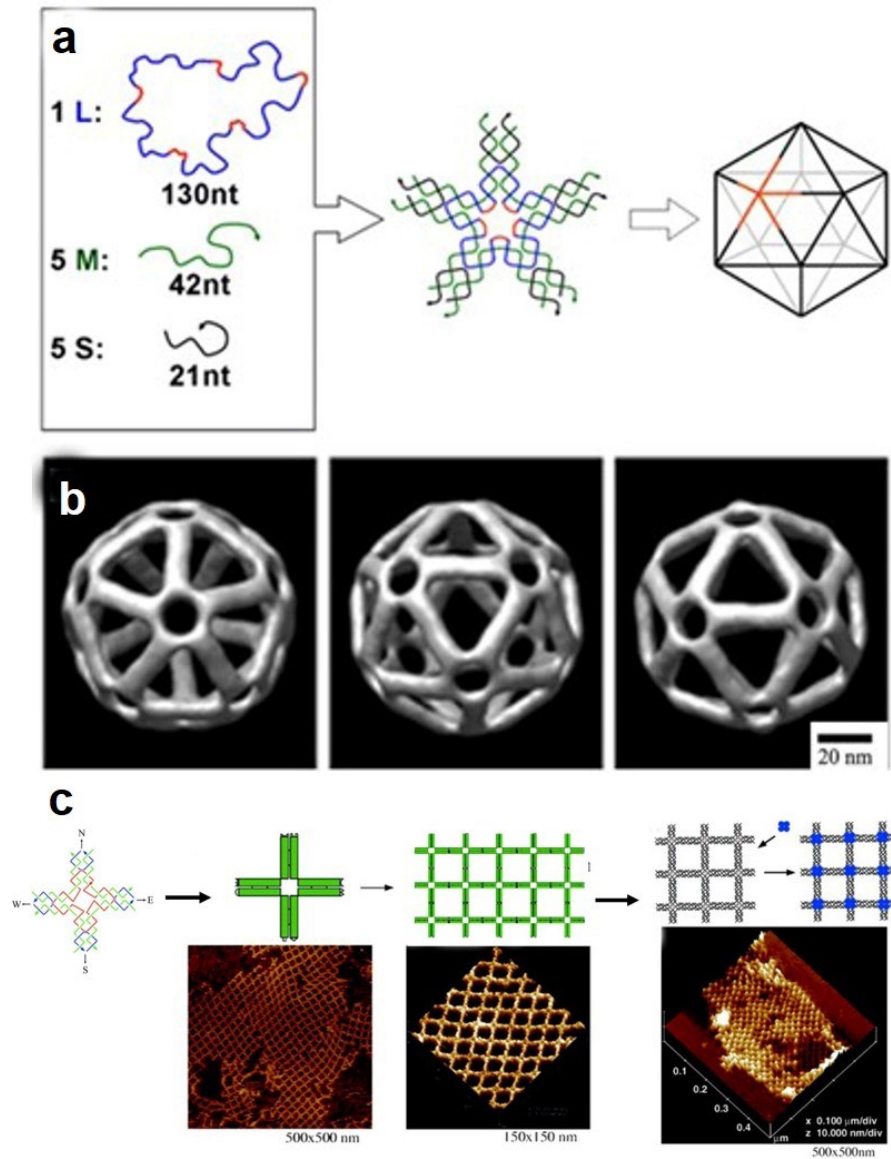


**Figure 1.3. a) Schematic representation of DNA icosahedra self-assembled from sticky-ended five-point-star motifs (tiles). b) Three views of the DNA icosahedron structure reconstructed from cryo-EM images. c) Schematic representation of self-assembly of DNA nanogrids using 4×4 DNA tile strand structure followed by scaffold assembly of**

**streptavidin and the bottom images are the corresponding AFM images. Reproduced with permission from ref 8.**

### **1.2.3 The hydrophobic hydration on the protein folding and self-assembly**

Hydrophobic hydration plays an important role in proteins self-assembly.<sup>19</sup> It is well known that the surface of proteins is not completely hydrophilic.<sup>9</sup> Hydration of the hydrophobic surface determines the solubility and stability of proteins in water (Figure 1.4a). With the assistance of computer simulations and the structure characterization of hydrated water using advanced techniques, including NMR, Raman and dielectric relaxation (DR) measurements, it is revealed that hydrophobic hydration is sensitive to the solution conditions,<sup>20</sup> e.g. concentration, pH and salts, as well as the surface topography.<sup>21</sup> The hydrophobic hydration of proteins can, then, be adjusted, which influences the structure of the assemblies and their biological functions. For example, enzyme activities can be influenced by the conformation of proteins which is easily affected by temperature and pH. A detailed understanding of the role of hydrophobic hydration in protein conformation has yet to be achieved.<sup>10</sup> Protein self-assembly also depends on the degree of hydration.<sup>10</sup> For example, globular proteins can self-assemble into various aggregates depending on the solution conditions (Figure 1.4b). Although the effect of the hydrophobic hydration has been observed, its role is far from understood.

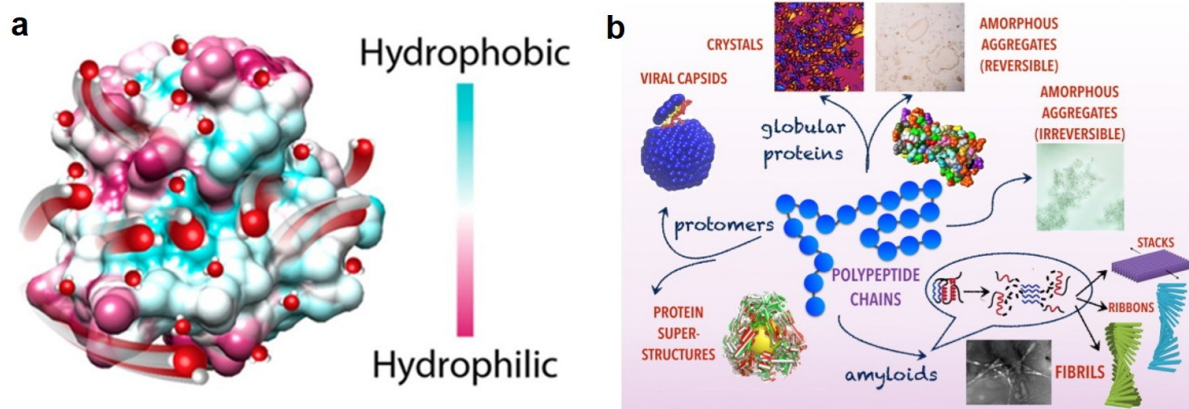


**Figure 1.4. a) The schematic representation of protein surfaces where the hydrophobic and hydrophilic moieties are shown on the surface. b) Various assemblies were fabricated by proteins or peptides. Reproduced with permission from ref 9-10.**

#### 1.2.4 Kinetic study on the living cell self-assembly

In the last decades, much progress has been made to study the thermodynamics of large-scale structures.<sup>22</sup> However, the self-assembly process from monomers to large-scale structures is not a continuous downhill process but results in intermediate structures that are trapped by various kinetic barriers and form certain intermediate structures (Figure 1.5a).<sup>23</sup> For examples, the self-assembly of lamins begins with the association of two dimers into tetramers followed by the growth in the axial direction (I). The radial growth (II and III) subsequently occurs as shown in Figure 1.5b.<sup>24</sup> Investigating these different intermediates is possible by taking advantage of advanced imaging techniques and is essential to understand the living cells self-assembly process.

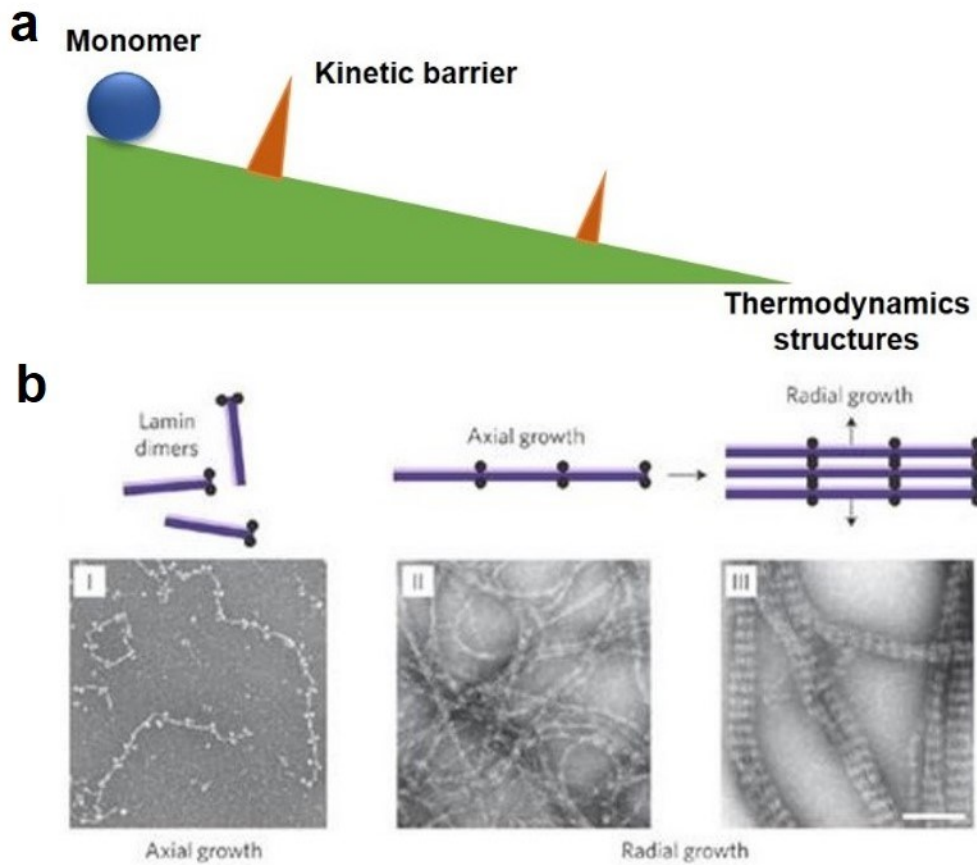


**Figure 1.5. a) The schematic presentation of self-assembly process with different kinetic barriers. b) Schematic biological assembly of lamins and the corresponding TEM images. Reproduced with permission from ref 24.**

In addition to the study focusing on the intermediates or kinetically trapped structures, the kinetics of the self-assembly processes have been investigated. For instance, the formation of amyloid  $\beta$  ( $A\beta$ ) fibrils proceeds through a complicated kinetic self-assembly process (Figure 1.6). Nucleation-growth sigmoidal model alone is not sufficient to describe the process. Additional processes have been

considered, including a secondary growth process as well as an elongation process (Figure 1.6) for the formation of the fibrils. However, these kinetic studies are mainly dependent on simulations. The experimental research is still at its infancy stage due to the lack of techniques to follow the complex self-assembly processes.<sup>25</sup>

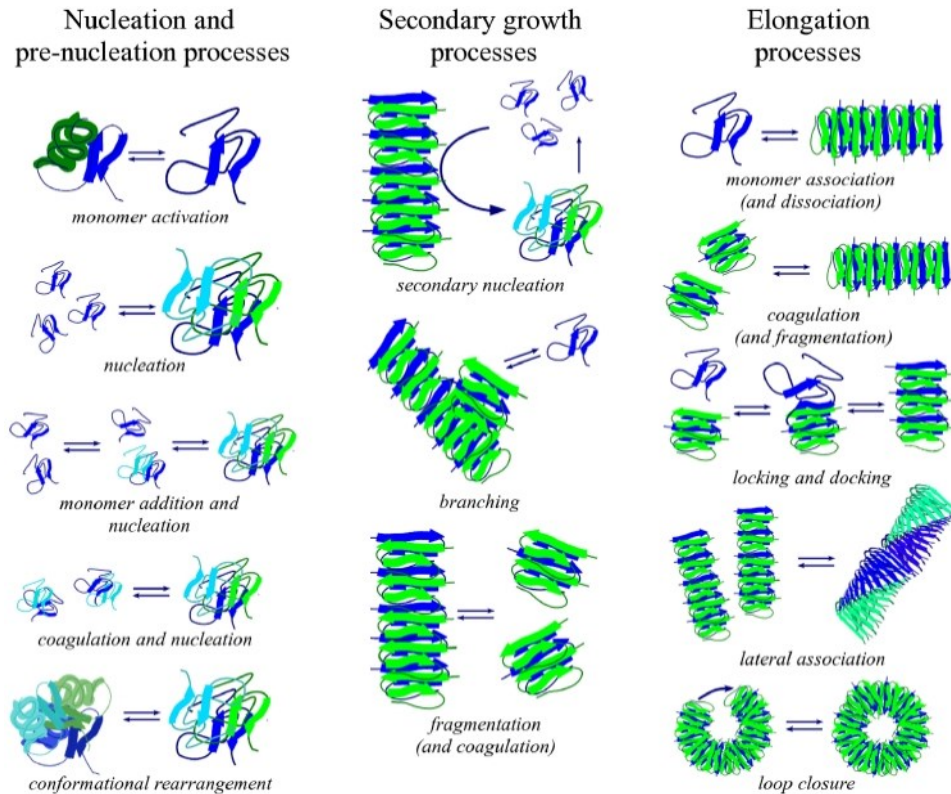


**Figure 1.6. Schematic presentation for the kinetic self-assembly process of amyloid fibril growth. Reproduced with permission from ref 25.**

### 1.3 Chemical self-assembly based on amphiphiles in aqueous solution

To mimic the self-assembly observed in nature, chemists have made great efforts to fabricate different model systems. Amphiphilic molecules or block copolymers have been the most studied. They form

various nanostructures by taking advantage of their amphiphilicity. As shown in Figure 1.7, amphiphilic block copolymers can self-assemble into various nanostructures either in bulk or solution.<sup>26</sup> Among these nanostructures, vesicles and micelles have been intensively studied for potential biological applications such as drug delivery and in vivo imaging.<sup>27-29</sup> Moreover, theories and mechanisms have been well developed to control and predict the self-assembling behavior when these amphiphiles are used as building blocks.<sup>30</sup>

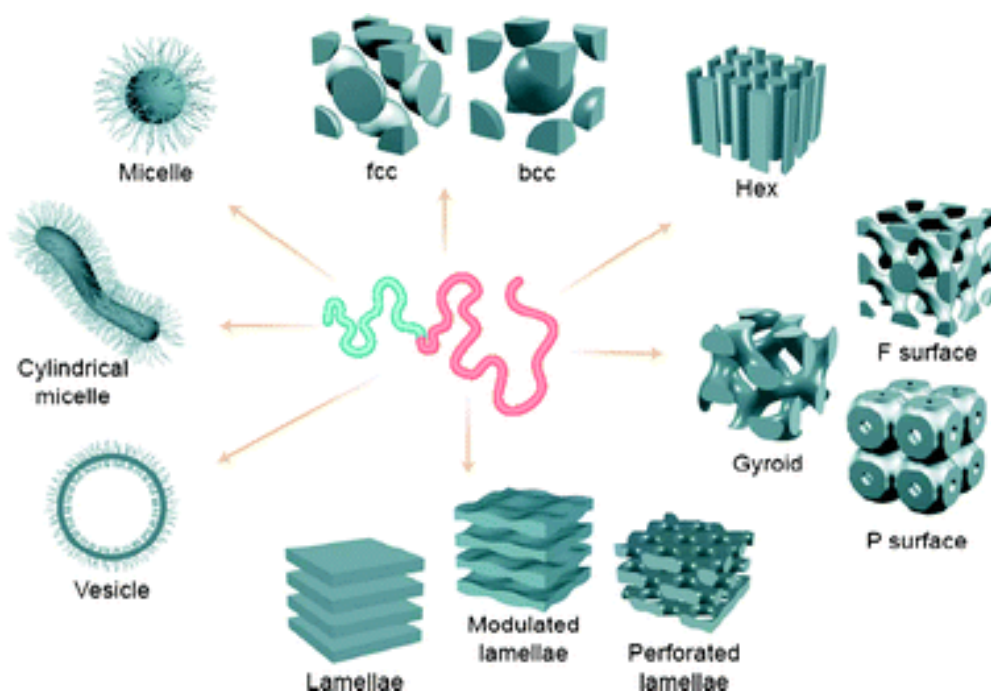


**Figure 1.7. Schematic representation of the block copolymers and their possible self-assembled nanostructures. Reproduced with permission from ref 30.**

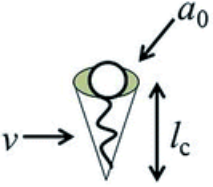
To introduce the chemical self-assembly of amphiphiles, we will first discuss the assembly of small amphiphilic molecules or surfactants, analogous to phospholipid molecules, which have been employed



for various applications.<sup>31</sup> Subsequently, the self-assembly of amphiphilic block copolymers will be briefly introduced.<sup>32-34</sup> As the vesicles assembled from block copolymers are particularly interesting and potentially useful, the progress in the synthesis and applications of nanovesicles will be discussed.<sup>35-38</sup>

### **1.3.1 Chemical self-assembly of small amphiphilic molecules or surfactants**

The self-assembly of small amphiphilic molecules is commonly used in our life and has been studied for many years.<sup>3,39</sup> The theory describing this assembling behaviour has been well developed. The critical packing parameter (CPP) can be calculated based on the structure of amphiphilic molecules and used to predict the structure of assembled morphologies. The CPP is defined as  $p = v/a_0l_c$ , where  $v$  represents the volume of hydrophobic segments,  $a_0$  is the interfacial area of the hydrophilic head, and  $l_c$  is the length of hydrophobic segments. As shown in Figure 1.8, when  $p < 1/3$ , spherical micelles are formed; while  $1/3 < p < 1/2$  results in cylindrical micelles and bilayer membranes are formed when  $1/2 < p < 1$ . The planar bilayers formed when the  $p = 1$ . The condition  $p > 1$  leads to the formation of the inverted micelles.<sup>40</sup>



$CPP = v/a_0 l_c$

| Critical Packing Parameter<br>( $v/a_0 l_c$ ) | Critical Packing Shape           | Structures Formed           |
|---|----------------------------------|-----------------------------|
| $< 1/3$                                       | Cone                             | Spherical micelles          |
| $1/3 - 1/2$                                   | Truncated cone                   | Cylindrical micelles        |
| $1/2 - 1$                                     | Truncated cone                   | Flexible bilayers, vesicles |
| $\sim 1$                                      | Cylinder                         | Planar bilayers             |
| $> 1$   | Inverted truncated cone or wedge | Inverted micelles           |

**Figure 1.8. The definition of CPP and its relationship with the formed morphology self-assembled from amphiphilic surfactants. Reproduced with permission from ref 40.**

### 1.3.2 Chemical self-assembly based on amphiphilic block copolymers

Amphiphilic block copolymers consist of two or more immiscible blocks that are linked together by covalent bonds (Figure 1.9). These molecules have a similar assembling behavior as amphiphilic surfactants do. The amphiphilicity, which causes a phase segregation in aqueous solution, is a major reason for the assembly. The morphologies of the resultant assemblies depend on the relative volume

of the two different immiscible blocks. Under thermodynamic conditions, the structure of the assemblies is determined by the dimensionless packing parameter ( $p$ )<sup>41</sup> As shown in Figure 1.9,  $p$  is defined as the ratio between the volume ( $v$ ) of the insoluble chains and that occupied by the product of the interfacial area  $a_0$  and the length of the insoluble chains  $l_c$  (Figure 1.9).  $p$  is similar to the CPP mentioned in the self-assembly of amphiphilic surfactants, which is the basic parameter governing the amphiphilic block copolymer self-assembly.<sup>30</sup> The conditions  $p < 1/3$ ,  $1/3 < p < 1/2$ , and  $1/2 < p < 1$  result in the formation of spherical micelles, cylindrical micelles and polymersomes.<sup>41</sup> The self-assembled aggregates from amphiphilic block copolymers usually possess higher stability and durability than the ones self-assembled from small surfactants. This makes the aggregates self-assembled from amphiphilic block copolymers have greater potential biological applications than those obtained from small surfactants.<sup>30</sup>

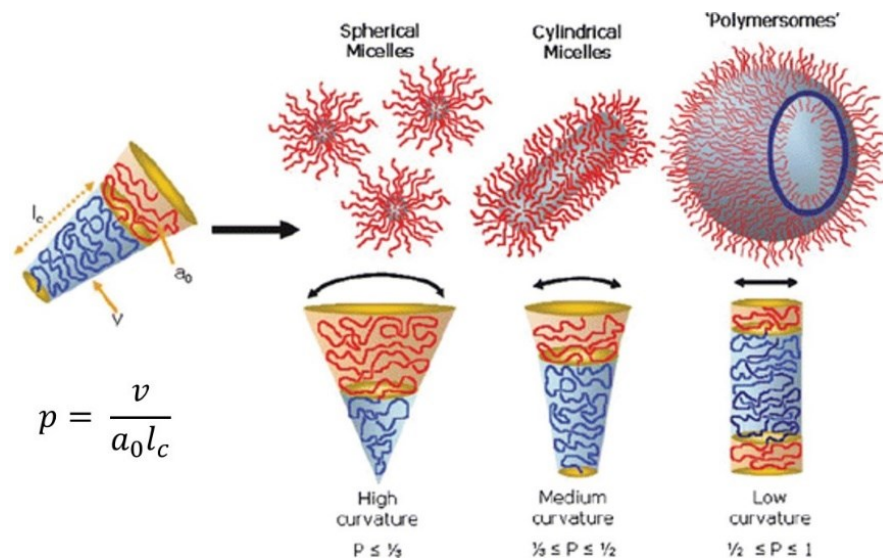


**Figure 1.9. The multiple nanostructures self-assembled by the amphiphilic block copolymers. The formed nanostructures are determined by the dimensionless packing parameter  $p$ . Reproduced with permission from ref 41.**

Due to the unique mechanical and physical properties of block copolymers, the self-assembly of amphiphilic block copolymers is a slow dynamic process which could lead to kinetically trapped structures.<sup>42</sup> Kinetically trapped structures are non-equilibrium structures that sometimes possess exotic morphologies such as stripped cylinders,<sup>43</sup> patchy spheres<sup>44</sup> and toroids<sup>45</sup> and which enrich the variety of self-assembled nanostructures. These exotic morphologies of kinetically trapped structures cannot be predicted by the dimensionless packing parameters ( $p$ ) because they are the results of kinetic pathways.<sup>46</sup> Considering that kinetically trapped structures are non-equilibrium structures, the kinetically trapped structures could self-assemble in a hierarchical manner into more complex structures by manipulating the solution conditions. For example, with the cosolvent mixing method, the PAA<sub>94</sub>-b-PMA<sub>103</sub>-b-PS<sub>44</sub> could self-assemble into spherical micelles in THF/water mixtures. By introducing more THF, the spherical micelles could further transform into disk-like micelles. Moreover, the formed disk-like micelles could self-assemble into one-dimensional supra-assemblies by anisotropic growth as shown in Figure 1.10.

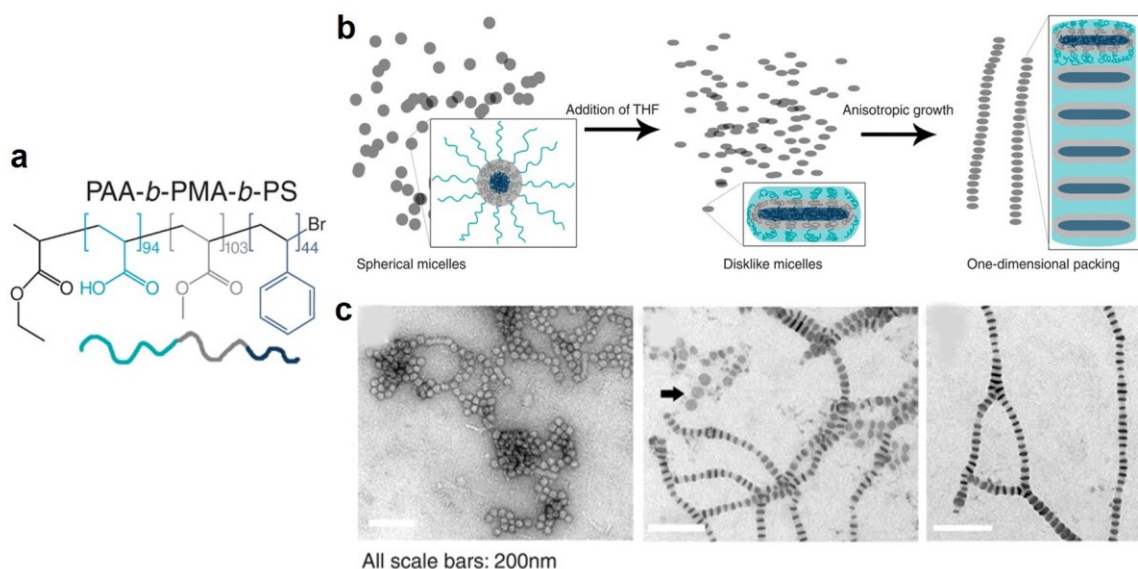


**Figure 1.10 a) Triblock copolymer, PAA-*b*-PMA-*b*-PS. b) growth mechanism of the hierarchical self-assembly of spherical micelles by addition of THF and c) its corresponding TEM images. Reproduced with permission from ref 44.**

### 1.3.3 Vesicles self-assembled from amphiphiles

Among the multiple morphologies, vesicles assembled from block copolymers (polymersomes) have been the most studied.<sup>47-48</sup> Different types of cargos, such as drug molecules, dyes and inorganic nanoparticles, have been encapsulated within the hollow interior of polymersomes for various applications including drug delivery, controlled catalysis, and cell imaging.<sup>47-50</sup> For example, by introducing certain functional groups to amphiphiles, the corresponding vesicles can respond to external stimuli, such as pH, temperature, light and redox potential, for a controlled release of cargos (Figure 1.11).<sup>51</sup> However, most vesicles assembled from amphiphiles suffer from a number of

drawbacks, including broad size distribution and low reproducibility, which is still a big issue for potential clinical applications.<sup>48</sup>

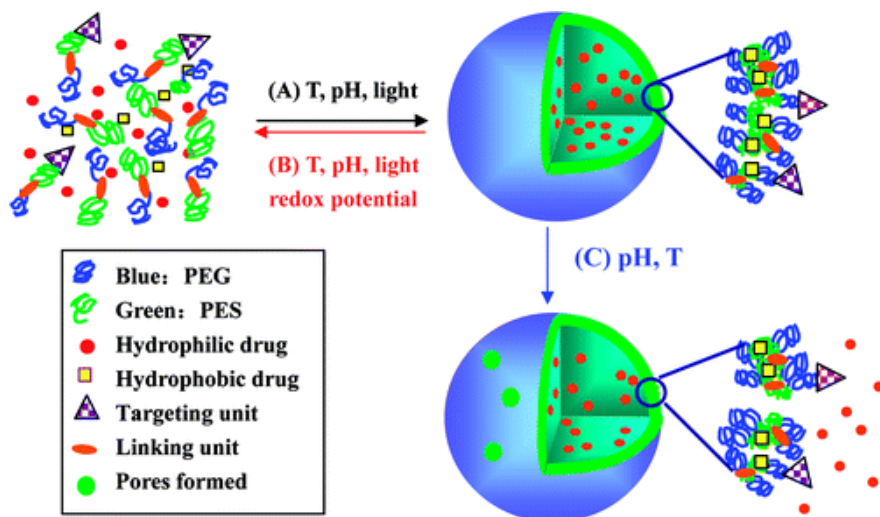


**Figure 1.11. Schematic presentation of the external stimuli drug-releasing behavior of vesicles. Reproduced with permission from ref 51.**

## 1.4 Chemical self-assembly based on nonamphiphilies in aqueous solution

In addition to amphiphilic molecules, a number of non-amphiphiles have been reported to assemble in water. Though the assembly of non-amphiphiles is commonly observed for biological molecules, the supramolecular theory on this aspect is not developed and remains to be explored.

### 1.4.1 Self-assembly of hydrophilic-hydrophilic block copolymers

The mixing of two water-soluble macromolecules has been shown to result in an immiscible mixture in aqueous solution.<sup>52</sup> As shown in Figure 1.12a, two-phase separation occurs when the aqueous solution of poly(ethylene oxide) is mixed with the solutions of water-soluble homopolymers dextran

and pullulan, respectively. The water solutions of dextran and poly(sarcosine) also causes phase separation. Block copolymers containing these types of hydrophilic blocks were able to assemble in water into defined aggregates with various morphologies including micelle-like structures, lamellae, and cylinders.<sup>53-56</sup> The hydrophilic phase separation in water was attributed to the difference in the water absorption capabilities of the two hydrophilic blocks. This difference produced an osmotic pressure at the interface of the two hydrophilic blocks, which induced the microphase separation.<sup>57</sup> Recently, Brosnan and co-workers created first nano- and microsized vesicle-like aggregates using this hydrophilic phase separation mechanism.<sup>58</sup> As shown in Figure 1.11a and b, the hydrophilic block copolymers of dextran-*block*-poly(ethylene oxide) (Dex-PEO) self-assembles into nanovesicles at a low polymer concentration (0.1-0.5 wt%) and microsized vesicles at a high polymer concentration (15-25 wt%). In contrast to the polymersomes formed by traditional amphiphilic block copolymers,<sup>29</sup> the vesicle-like structures formed by hydrophilic block copolymers may have a highly permeable membrane.

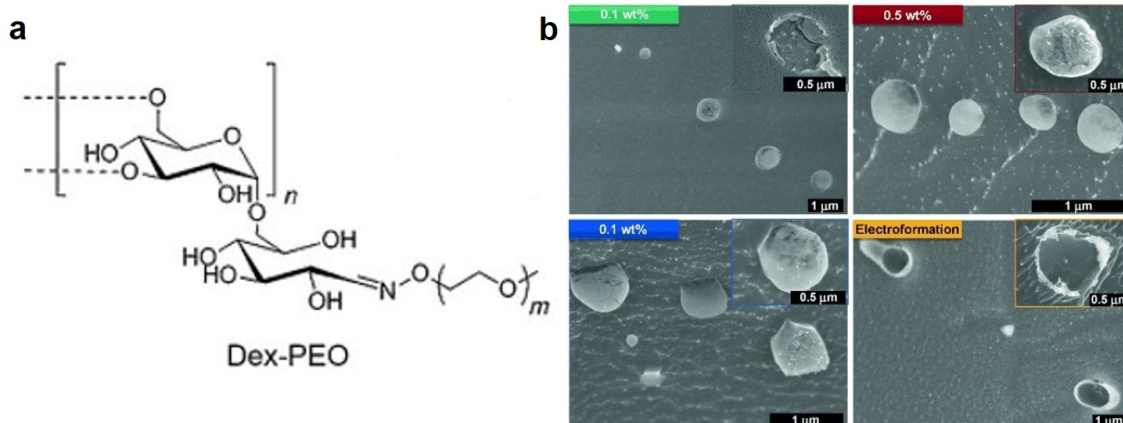


**Figure 1.12 a) Chemical structure of the hydrophilic blockpolymer Dex-PEO. b) Cryogenic scanning electron microscopy images of vesicle-like aggregates of DEX-PEO at different concentrations. Reproduced with permission from ref 58.**

#### 1.4.2 Self-assembly based on homopolymers

Homopolymers could also self-assemble into various defined aggregates.<sup>59-63</sup> The aggregates self-assembled from homopolymers usually exhibit unique properties compared to the ones self-assembled from amphiphilic block copolymers.<sup>63-65</sup> Unlike the distinct amphiphilic nature of block copolymers, no obvious boundary exists between the hydrophobic and hydrophilic segments in homopolymers. And this “fuzzy” boundary makes the homopolymer vesicles possess nonbilayer membrane structures which exhibit interesting and unique properties. However, the homopolymer vesicles are unusual and rarely reported, which remains a main challenge in this field.<sup>60,66-69</sup>

##### 1.4.1.1 Homopolymer vesicles with flexible membrane structures

Changez and co-workers synthesized a homopolymer poly(2-(4-vinylphenyl)pyridine) (PVPPy) with hydrophilic moieties attached to each repeating unit of the flexible hydrophobic chain.<sup>69</sup> As shown in



Figure 1.12a, the homopolymer PVPPy can self-assemble into well-defined vesicles in the THF/H<sub>2</sub>O mixed solvent. The PVPPy vesicles have a membrane bilayer, which is formed by the hydrophobic interaction of the vinyl backbone. The rigid 2-phenyl pyridine pendent groups in each monomer unit is at the exterior of the membrane (Figure 1.12a). The thickness of the PVPPy vesicles measured by inverse fast Fourier transform (IFFT) images supports the proposed bilayer structure.<sup>69</sup>

Due to the unique membrane structure compared to lipid-membrane bilayers, the homopolymer PVPPy vesicles show distinct sizes increase depending on the solvent composition. The size changed from 795 nm to 90 nm by increasing the water content from 40 % to 90 %. Based on our knowledge, this large size variation obtained by manipulating the solvent composition has rarely been reported for block copolymer vesicles.<sup>32</sup> The authors attributed it to the flexible backbone nature of the PVPPy homopolymer.

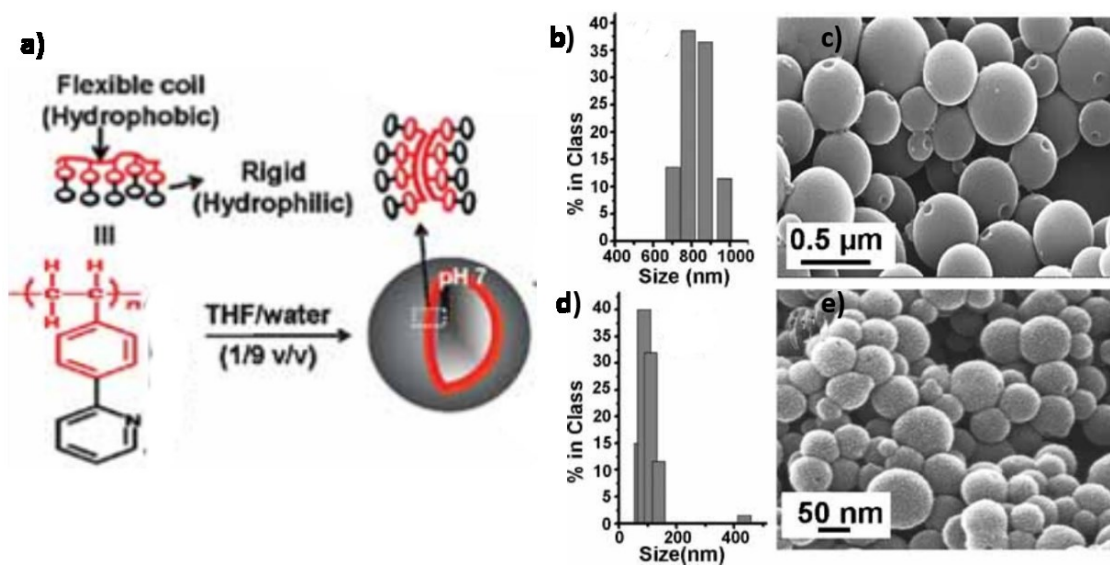


**Figure 1.13 a) Model for homopolymer PVPPy self-assembly into homopolymer vesicles**  
**b) DLS profile and c) SEM micrograph images of PVPPy vesicles in THF/water**

**(6/4 v/v). d) DLS profile and e) SEM micrograph images of PVPPy vesicles in THF/water (1/9 v/v). Reproduced with permission from ref 69.**

#### 1.4.1.2 Homopolymer vesicles with the membrane structures containing inner polar groups

Recently the Du group fabricated new homopolymer vesicles self-assembled from poly[2-hydroxy-3-(naphthalene-1-acylamino)propyl methacrylate] (PHNA). The membrane contained both hydrophobic and hydrophilic moieties as shown in Figure 1.14. This unique homopolymer caused the hydrophilic moieties to be embedded in the membrane (Figure 1.14). This hybrid membrane composition could lead to PHNA homopolymer vesicles with unusual functionalities.<sup>70</sup> The authors found that the homopolymer PHNA vesicle membrane could immobilize Au nanoparticles thanks to the secondary amines -NH-. This hybrid particles could be useful for water remediation by removing trace carcinogenic organic pollutants.<sup>71</sup> Moreover, due to the compatibility of the hydrophobic and hydrophilic moieties in the membrane structure, the membrane shows some swelling that enhances the permeability of the membrane. The traditional amphiphilic block copolymer vesicles do not have this unique property.<sup>32</sup>

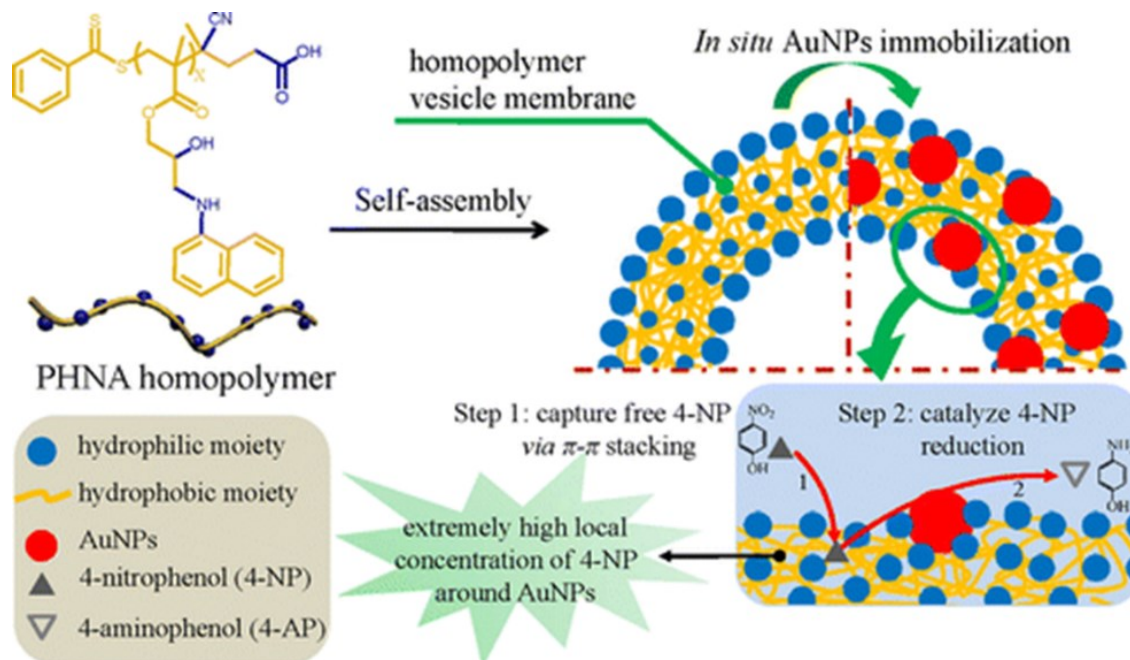


**Figure 1.14. Model for the formation of homopolymer vesicles by self-assembly of PHNA and the synergistic mechanism of the excellent catalytic efficiency of AuNPs@vesicles for the reduction of 4-nitrophenol (4-NP). Reproduced with permission from ref 71.**

Self-assembly of nonamphiphiles (the nonamphiphilic assembly) is still not common and the theory describing the nonamphiphilic assembly behavior is in its early stage. The effects of the properties of nonamphiphiles such as structural rigidity and hydrophobic effects on the self-assembly behaviors are rarely studied. Moreover, the lack of appropriate molecular models is another reason for the limited number of studies on nonamphiphilic assembly. Few examples of nonamphiphilic assemblies including small molecules and homopolymers could self-assemble into well-defined nanostructures.<sup>64</sup> So finding a suitable model system in chemical self-assembly to elucidate nonamphiphilic assembly is needed.

## 1.5 Self-assembly of metal carbonyl Fp complexes

Our group has synthesized a series of metal carbonyl Fp((Cp)Fe(CO)(CO-)) compounds using migration insertion polymerization and reaction.<sup>72-78</sup> These compounds include macromolecules, P(FpP), and small molecules (Figure 1.14) which are hydrophobic but can self-assemble in water into colloids with defined nanostructures such as vesicles.<sup>73,79</sup>

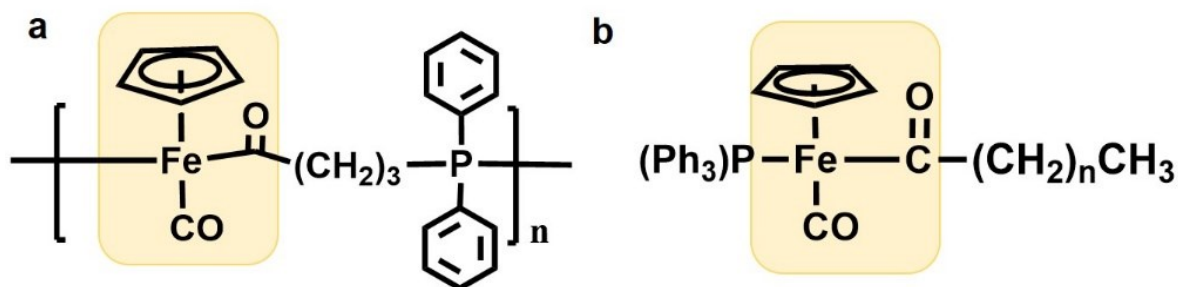
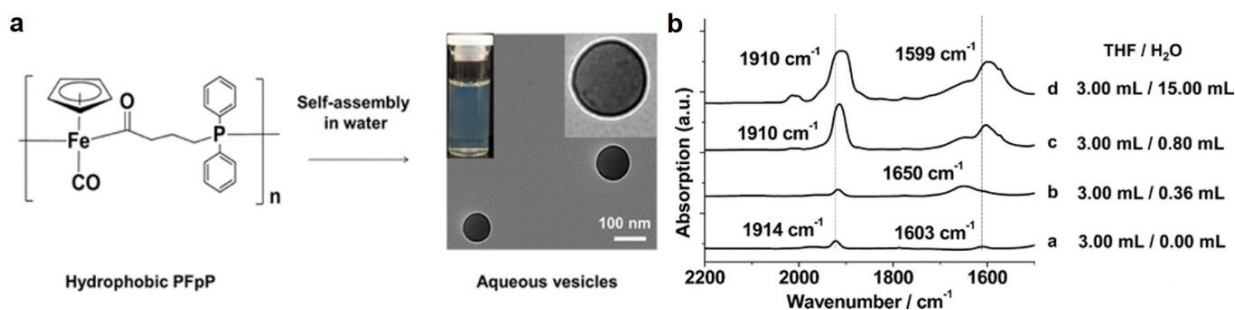


Figure 1.15. Chemical structures of the metal carbonyl Fp compounds.

### 1.5.1 Self-assembly of P(FpP)

The homopolymer P(FpP) (Figure 1.15) is hydrophobic but could self-assemble into vesicles in water as shown in Figure 1.16a. The hydrophobic P(FpP) was first dissolved in THF followed by quick addition of a large excess of deionized water. The formed P(FpP) nanovesicles were quite stable for several months. IR (Infrared spectroscopy) was used to investigate the reason for the stability of the P(FpP) nanovesicles. The IR absorption peaks of the acyl and terminal CO groups are shown in Figure 1.16b. When a large amount of water was added, the absorption peaks of the acyl (*ca.*  $1603\text{ cm}^{-1}$ ) and terminal CO groups (*ca.*  $1914\text{ cm}^{-1}$ ) shifted to lower wavenumbers. These shifts demonstrated that water carbonyl groups interact with water to form the water carbonyl interactions (WCIs) which stabilized the colloids. Moreover, the formed P(FpP) nanovesicles had a high loading efficiency of water-soluble

molecules which has a great application potential for drug delivery.<sup>79</sup> The solubility of homopolymer P(FpP) in DMSO is different at various temperatures. At room temperature, the homopolymer P(FpP) with a high molecular weight (8.9 kg/mol<sup>-1</sup>) is insoluble. However, as the temperature increases to a certain point, P(FpP) becomes soluble. This phenomenon demonstrates that the homopolymer P(FpP) has an upper critical solution temperature (UCST) behavior in DMSO.<sup>80</sup>



**Figure 1.16 a) Self-assembly of hydrophobic P(FpP) and b) IR spectrums of P(FpP) solution by addition of water. Reproduced with permission from ref 79.**

### 1.5.2 Self-assembly of Fp-based small molecules

We not only explored the self-assembly behavior of the hydrophobic homopolymers P(FpP) but also that of small hydrophobic Fp acyl derivatives. Fp acyl derivatives which contain the Fp head group and an alkyl tail also assemble in water into vesicles as shown in Figure 1.17. During the assembling process, the CO moiety in the Fp head group interacts with water via WCIs and the alkyl chains come together resulting in the formation of bilayer vesicles (Figure 1.17a).

The stability of the formed nanovesicles was investigated in details. The WCIs and the hydrophobic interactions between the alkyl chains played an essential role in the stability of the assembled

nanovesicles. To prove this idea, CpMo-based molecules (MpC<sub>6</sub>) were synthesized as shown in Figure 1.17b. They contain three CO groups in the head group. IR measurements demonstrated that the WCIs were enhanced in water.<sup>74</sup> Moreover, the formed nanovesicles were quite stable.<sup>74</sup> Additional molecules were prepared with alkyl chains of different lengths as shown in Figure 1.17c. By comparing the stability of these Fp molecules as a function of different alkyl chain length (Figure 1.17c), we demonstrated that longer alkyl chain lengths enhanced the hydrophobic interactions of tail-tail groups which further increased the stability of the self-assembled aggregates.<sup>81</sup>

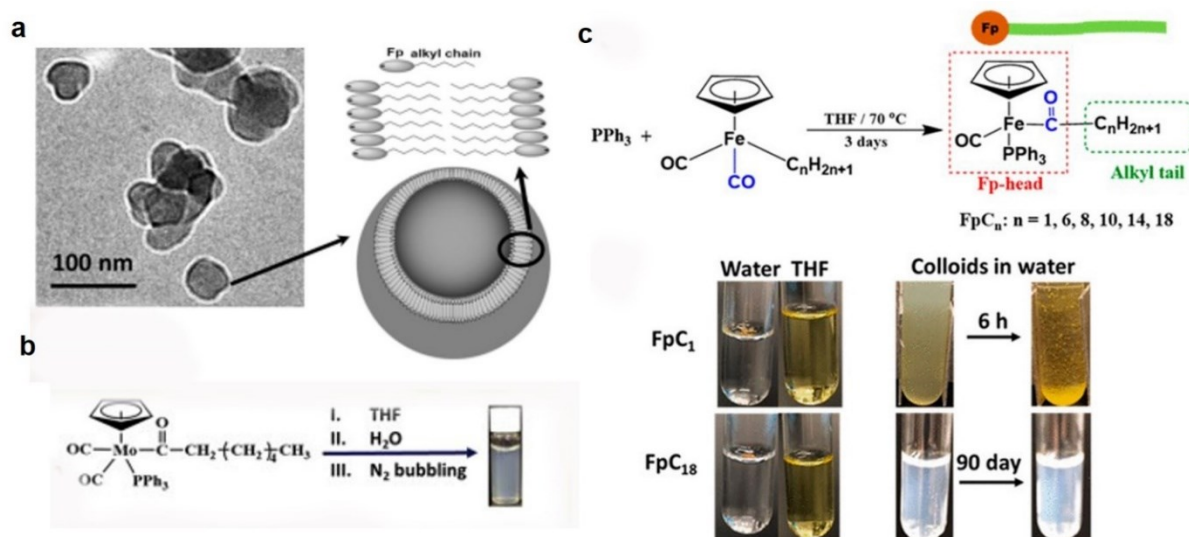


**Figure 1.17. a) The schematic presentation of Fp-based nanovesicles and b) self-assembly of MpC<sub>6</sub> in the aqueous solution. c) Synthesis and chemical structure for FpC<sub>n</sub> and Photographs illustrating the aqueous behavior of FpC<sub>1</sub> and FpC<sub>18</sub>.**

Reproduced with permission from ref 73,74 and 81.

Consequently, the Fp-based molecules provide an opportunity to study the role of nonamphiphilic nature on self-assembly. As mentioned in this chapter, the nonamphiphilic nature is critical in the living cells self-assembly observed in numerous systems, including in living cells but is much less studied.<sup>74,81</sup> The hydrophobic Fp-based compounds including P(FpP) and small Fp-based molecules have been shown to self-assemble into stable nanovesicles that are stabilized by WCIs. The effect of hydrophobic interactions between tail-tail groups on the stability of the nanovesicles has also been studied. However, the research on the self-assembly of Fp-based materials is still in its infancy. This inspired us to explore more on the self-assembly of Fp-based compounds. In this thesis, the nonamphiphilic assembly of metal carbonyl Fp complexes was studied based on kinetic trapping, structural rigidity and hydrophobic effect.<sup>82-83,149</sup>

## 1.6 Thesis outline

This thesis includes seven chapters. The first chapter introduced the nonamphiphilic assembly observed in nature and chemistry. It was stated that the study of the nonamphiphilic assembly is at an early stage and that it is urgent to widen the variety of molecular model systems to study. Herein we employ Fp-based complexes as a model to study how its kinetic assembly, structural rigidity, and hydrophobic effect on its self-assembly behavior.

In the second chapter, we first investigate the kinetics of homopolymer P(FpP) precipitation in different solution conditions. We find that the P(FpP) could self-assemble into spherical nanoparticles by decreasing the temperature or addition of a nonsolvent. The P(FpP) nanoparticles were instable and easily aggregated into precipitates. However, addition of protic solvents or changing the nonsolvent content enabled the kinetic trapping of the P(FpP) nanoparticles which suggests that the self-assembly

of P(FpP) was kinetically and not thermodynamically controlled. In the third chapter, we explored the self-assembly behavior of P(FpP) in DMSO/water mixtures solution as a function of temperature. A wide range of nanostructures including nanosheets, nanovesicles and worm-like micelles could be generated by changing the temperature. With the assistance of (dissipative particle dynamics) DPD simulation, the self-assembled structures were shown to be mainly dependent on the structural flexibility of the homopolymer P(FpP). The fourth chapter reports on the nonbilayer vesicles self-assembled from P(FpP) and their swelling properties in response to THF contents.

In the fifth chapter, we employed the metal carbonyl molecule FpC<sub>6</sub>Pyrene as a model to investigate the role of  $\pi$ - $\pi$  interactions in the self-assembly behavior. From the self-assembled results, we know that the  $\pi$ - $\pi$  interactions in response to solution conditions can be adjusted as a driving force or not where various nanostructures are assembled from the same aromatic molecule. In the sixth chapter, we investigate the hydrophobic effect on the hierarchical self-assembly of the formed nanovesicles. Moreover, we further explore the relationship between the hydrophobic interaction of tail-tail groups and hydrophobic hydration of Fe in the Fp head groups. In the last chapter (Chapter seven) a general summary is provided.



## Chapter 2 Kinetic Control of Homopolymer Precipitation in Solution for the Synthesis of Nanospheres and Nanowires

The kinetics of homopolymer precipitation in solution was explored for the synthesis of nanoparticles. The metal carbonyl homopolymer P(FpP) (FpP:  $\text{CpFe}(\text{CO})_2(\text{CH}_2)_3$  or  $6\text{PPh}_2$ ) is soluble in THF, insoluble in hexane and exhibits an upper critical solution temperature (UCST) behavior in DMSO. This polymer precipitates by adding hexane to THF solutions or cooling DMSO solutions below the UCST temperature. By varying kinetic pathways for the precipitation, kinetically-trapped nanostructures with narrow size distributions, including spherical and worm-like nanoparticles, were produced. A number of parameters, including concentration, additive and the solvation quality, e.g. THF/hexane ratio, were adjustable for the kinetic control. Kinetic assembly of readily available homopolymers in solutions is, therefore, worthwhile to be explored as a reliable technique for nanosynthesis.

## 2.1 Introduction

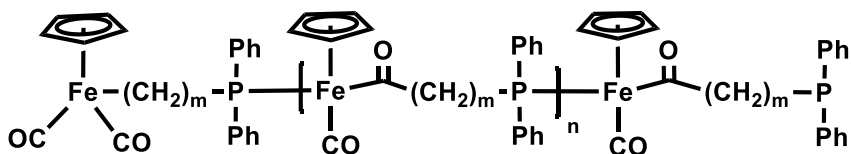
The kinetics of self-assembly, relative to thermodynamics, is less studied, but crucial for developing supramolecular theory as well as fabricating non-equilibrium and exotic nanostructures.<sup>23,46,84</sup> One challenge in this research is to produce well-defined and reproducible kinetically-trapped assemblies.<sup>85</sup> Precipitation of homopolymers in poor solvents is a commonly used purification technique to remove contaminated small molecules. Intermolecular cohesive interactions, relative to solute-solvent interactions, are stronger for macromolecules,<sup>86</sup> which drive a phase separation of polymers from the media, resulting in precipitation. Kinetic control of this precipitation process by adjusting the balance between polymer-polymer and polymer-solvent interactions has not been systematically studied,<sup>87-88</sup> but is attractive as a reliable approach for the synthesis of nanostructures using readily available homopolymers.

By contrast, block selective precipitation of block copolymers in solution has been explored and flourished as a major technique for nanosynthesis.<sup>30,89-91</sup> Although the assembling behavior of block copolymers governed by thermodynamic equilibrium is well explained,<sup>30,92</sup> the assembly has a propensity to be kinetically trapped in nonequilibrium states depending on the processing route taken.<sup>46</sup> It has attracted significant attention to the kinetic pathways, resulting in a remarkable progress in the synthesis of nanostructures.<sup>85,91,93-94</sup> This kinetic assembly allows the structure-related functions of nanoobjects assembled from the same materials to be investigated.

Unlike block copolymers, only a few experiments illustrate that homopolymers with or without solvent-soluble groups assemble in a poor solvent into non-equilibrium nanostructures.<sup>60,64,87,95</sup> These empirical discoveries motivate the investigation into the kinetics of homopolymer precipitation. The

research may eventually lead to the recognition of kinetic barriers and pathways in dependence of the chemical structure of homopolymers and solution conditions. This knowledge will be fundamentally important for polymer supramolecular chemistry and nanosynthesis.<sup>1</sup>

We have created a new class of metal carbonyl polymers, P(FpP) (Scheme 2.1) *via* migration insertion polymerization (MIP) of CpFe(CO)<sub>2</sub>(CH<sub>2</sub>)<sub>3</sub> or <sub>6</sub>PPh<sub>2</sub> (FpP).<sup>96-98</sup> P(FpP) is hydrophobic, but able to assemble in water into kinetically stable vesicles.<sup>79</sup> Water-carbonyl interactions are responsible for the colloidal stability in water.<sup>79</sup> Like many other homopolymers, P(FpP) in THF, a good solvent, undergoes a precipitation upon the addition of hexane, a poor solvent for P(FpP).<sup>72</sup> The DMSO solution of P(FpP) exhibits a molecular weight-dependent upper critical solution temperature (UCST) behavior.<sup>80</sup> Phase separation is observed when a solution of P(FpP) with DP of 64 is cooled from 65 °C to 25 °C in DMSO.<sup>80</sup>



**Scheme 2.1 Chemical structure of P(FpP) ( $m = 3$  or  $6$ , the degree of polymerization (DP)  $n = 4\sim 63$ )**

Herein, we report the kinetic behavior for the precipitation of a P(FpP) solution either in THF upon addition of hexane or DMSO upon decreasing the temperature. By adjusting the balance between the polymer-polymer and polymer-solvent interactions, the kinetic pathways for the precipitation can be altered into a one-dimensional growth of nanostructures. Several parameters, including concentration,

additive, temperature and the ratio of THF/hexane, have been used to adjust this balance, resulting in the synthesis of kinetically-trapped nanospheres and nanoworms with narrow size distribution.

## **2.2 Experimental section**

### **2.2.1 Materials and instrumentation**

Sodium (Na), potassium (K), 1-bromo-3-chloropropane, 1, 6-dichlorohexane, cyclopentadienyl iron dicarbonyl dimer ( $\text{Fp}_2$ ) were purchased from Sigma-Aldrich. Chlorodiphenylphosphine was purchased from Tokyo Chemical Industry (TCI). Benzophenone was purchased from Fisher Scientific. DMSO and all other solvents were commercially available and were used without further purification.

$^1\text{H}$ ,  $^{31}\text{P}$ , and  $^{13}\text{C}$  NMR were carried out on a Bruker-300 (300 MHz) spectrometer at ambient temperature using either  $\text{CDCl}_3$  or  $\text{DMSO-d}_6$  as a solvent. NMR samples were prepared under a dry nitrogen atmosphere. Gel permeation chromatography (GPC) was employed to characterize the molecular weights of polymers. THF was used as an eluent at a flow rate of 1.00 mL/min. The Viscotek GPC max unit was equipped with a VE 2001 GPC, three PolyAnalytik organic mixed bed columns, PAS-103-L, PAS-104-L and PAS-105-L, with dimensions of 8 mm (ID)  $\times$  300 mm (L), and a Viscotek triple detector array, including refractive index, viscosity, and dual-angle light scattering detectors. Polystyrene standards were used as references. Dynamic light scattering (DLS) measurements were carried out on a Malvern Zetasizer (Nano S90) with a laser operating at 633 nm. The auto measure mode was selected and the evaluation method was based on a standard Gaussian method. The measurements were made at a scattering angle of  $90^\circ$ . The viscosity and refractive index of DMSO at different temperatures used in the DLS measurements are listed in the Table 8.1. Transmission electron microscopy (TEM) images were obtained on a LVEM5 Benchtop (DeLong) with a low voltage (5 kV)

and Philips CM10 with the acceleration voltage of 60 kV. TEM samples were prepared by casting a drop of P(FpP) solution on a copper grid covered by carbon film followed by drying at room temperature. Statistical analyses of the size of nanoparticles in the TEM images were performed by the Gatan Digital Microscopy software. UV-Vis spectroscopy was performed on the Varian Cary 100 Bio UV-Visible Spectrophotometer. The turbidity experiments were performed by measuring the transmittance of the light with a wavelength at 600 nm as a function of temperature under a thermodynamic model. The heating and cooling rates were set at 1 °C/min. The spectra of transmittance (600 nm) as a function of time at 25 °C was obtained when the instrument was operated in the kinetic model.

### 2.2.2 Synthesis of P(FpP)

P(FpP) (n=6, DP=4) was synthesized based on the previous report.<sup>98-99</sup> Polymerization of CpFe(CO)<sub>2</sub>(CH<sub>2</sub>)<sub>6</sub>PPh<sub>2</sub> (FpP) was performed in bulk at 70 °C for 14 h. Afterward, the crude products were dissolved in THF and precipitated in hexane. The obtained precipitates were collected by filtration and dried at room temperature. <sup>1</sup>H NMR (CDCl<sub>3</sub>): 7.24–7.44 ppm (10H, C<sub>6</sub>H<sub>5</sub>), 4.32–4.62 ppm (5H, C<sub>3</sub>H<sub>5</sub>), 2.75 ppm, 2.30 ppm (4H, COCH<sub>2</sub>, PCH<sub>2</sub>), 1.00–1.30 ppm (8H, CH<sub>2</sub>CH<sub>2</sub>CH<sub>2</sub>CH<sub>2</sub>). <sup>13</sup>C NMR (CDCl<sub>3</sub>): 23 ppm and 24 ppm (CH<sub>2</sub>CH<sub>2</sub>CH<sub>2</sub>CH<sub>2</sub>), 28 ppm, 29 ppm, 30 ppm (CH<sub>2</sub>P(Ph)<sub>2</sub>), 65 ppm and 68 ppm (COCH<sub>2</sub>CH<sub>2</sub>CH<sub>2</sub>CH<sub>2</sub>), 84 ppm (C<sub>3</sub>H<sub>5</sub>), 128 ppm, 131 ppm, 132 ppm, 135 ppm, 136 ppm, 137 ppm (Ph), 218 ppm (FeC≡O), 278 ppm (FeCOCH<sub>2</sub>). <sup>31</sup>P NMR (CDCl<sub>3</sub>): 73.4 ppm (backbone PFe), -13.7 ppm (end group PPh<sub>2</sub>), and 34.8 ppm (oxidized end group PPh<sub>2</sub>O). FTIR: 1909 cm<sup>-1</sup> (terminal CO stretch) and 1604 cm<sup>-1</sup> (migrated CO groups stretching). GPC: M<sub>n</sub> = 2000; PDI = 1.67.

P(FpP) ( $n=3$ ,  $DP=64$ ) was synthesized using the reported procedure.<sup>96-98</sup> A typical synthesis is described as follows: Polymerization of  $CpFe(CO)_2(CH_2)_3PPh_2$  (FpP) was carried out in the presence of DMSO (ca 5% by weight) at 105 °C for 20 h. After the polymerization, the solution was cooled to room temperature. The crude product was first dissolved in a minimum amount of THF and then precipitated in a large amount of hexane. The precipitates were collected via filtration and dried under vacuum overnight at room temperature yielding yellow powders. The resultant bright yellow powders were characterized using NMR, IR, and GPC. P(FpP) ( $M_n = 25700 \text{ g mol}^{-1}$ ):  $^1H$  NMR ( $DMSO-d_6$ ): 7.8–7.1 ppm (10H,  $C_6H_5$ ), 4.4–4.2 ppm (5H,  $C_3H_5$ ), 2.78–2.60 ppm (1H,  $COCH_2$ ), 2.47–2.17 ppm (1H,  $COCH_2$ ), 2.13–1.89 ppm (2H,  $CH_2PFe$ ), and 1.32–0.74 ppm (2H,  $CH_2CH_2CH_2$ ).  $^{31}P$  NMR ( $CDCl_3$ ): 73.4 ppm (coordinated phosphorus in the main chain), 73.2 ppm (Coordinated phosphorus in the terminal repeating unit) and -13.6 ppm (uncoordinated phosphorus in the end group). IR: 1910  $cm^{-1}$  (terminal carbonyl groups), 1600  $cm^{-1}$  (migrated carbonyl groups). GPC:  $M_n = 25700 \text{ g/mol}$ ; PDI = 1.73.

### 2.2.3 Preparation of colloidal solution of P(FpP) in THF/hexane

P(FpP) ( $n=6$ ,  $DP=4$ ) was first dissolved in THF to obtain P(FpP)/THF solution (1.0 mg/mL). Afterward, 30  $\mu\text{L}$  of the prepared P(FpP) in THF solutions was injected separately into THF/hexane solvents (0.72 mL) with varying amounts of THF. After addition of the P(FpP)/THF solution, a clear, blue-tinted solution was observed.

### 2.2.4 Preparation of colloidal solution of P(FpP) in DMSO

111.60 mg, 55.30 mg and 13.80 mg of P(FpP) ( $n = 3$ ,  $DP = 64$ ) were added to DMSO (10 mL) in three vials separately at room temperature. Upon heating at 65 °C, P(FpP) ( $n = 3$ ,  $DP = 64$ ) dissolved in

DMSO resulted in solutions with respective concentrations of 1.00, 0.50 and 0.125 wt%. The solutions were filtered at 65 °C via a syringe filter with pore size of 220 nm to remove dust before cooling to 25 °C.

### **2.2.5 Segregation and stabilization of P(FpP) nanoparticles in DMSO**

After three solutions (4 mL) of P(FpP) ( $n = 3$ ,  $DP = 64$ ) in DMSO (0.125 wt%) were cooled from 65 °C to 23 °C, the protic solvents H<sub>2</sub>O, MeOH and EtOH (480 mmol) were separately added to these solutions and the vials were gently shaken. DLS was subsequently employed to track the hydrodynamic diameter ( $D_h$ ) as a function of aging time.

## **2.3 Results and discussion**

### **2.3.1 Kinetic assembly of P(FpP) in THF/hexane**

When hexane was added dropwise to a P(FpP) solution in THF, the solution was initially cloudy, and a precipitate was observed shortly thereafter. However, when a THF solution of P(FpP) was added quickly to hexane (shock precipitation), a clear, blue-tinted colloidal solution was obtained. This suggested that the shock precipitation was able to arrest the kinetics of the assembled nanostructures. The effect of the THF/hexane ratio on the shock precipitation was examined. Solutions with varied ratios of THF/hexane were prepared by injecting a THF solution (30  $\mu$ L with P(FpP) concentration varying from 1.0 mg/mL to 0.72 mL) into THF/hexane mixed solvents with various amounts of THF. After aging for one hour, these solutions were analyzed using dynamic light scattering (DLS). The hydrodynamic radii ( $D_h$ ) and polydispersities (PDI) for the colloids as a function of the THF/hexane ratio were plotted in Figure 2.1. As shown in Figure 2.1a and b, at THF contents below 10 and above

30 vol%, the colloids had large  $D_h$  values and broad size distributions. For THF contents between 10 and 30 vol%, the  $D_h$  value for the assembled particles was *ca.* 200 nm and the PDI was *ca.* 0.10 or less. The short-term kinetic behavior of P(FpP) colloids in THF/hexane mixtures containing 4 vol%, 16 vol%, and 40 vol% THF was subsequently investigated. As shown in Figure 2.1c and d, the  $D_h$  value for the samples containing 16 vol% THF remained unchanged and the PDI was below 0.1, suggesting that the colloids were kinetically trapped. However, the colloids in the solutions containing 4 vol% and 40 vol% THF grew noticeably over the course of the first hour (Figure 2.1c), increasing in  $D_h$  by 110 % and 88 %, respectively. The PDI for the colloids in the latter solution increased rapidly, suggesting that the particles were aggregating irregularly. In contrast, although the colloids in the solution with a smaller amount of THF (4 vol%) grew continuously (Figure 2.1c), the PDI remained less than 0.20 (Figure 2.1d), suggesting that the growth followed a structure-controlled pathway.



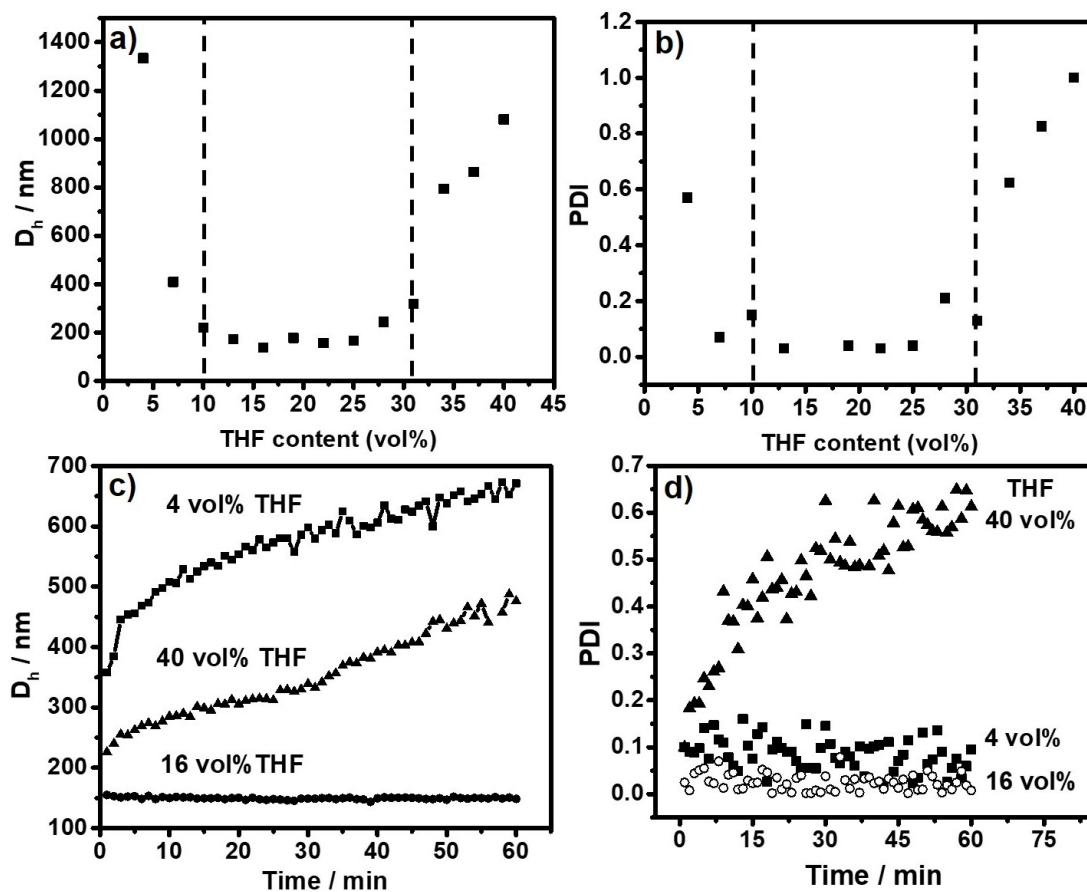


**Figure 2.1 a) The size change and b) PDI of P(FpP) colloids prepared in THF/hexane mixed solutions with varied THF contents. c) Size change and d) PDI of P(FpP) colloids prepared in THF/hexane with 4 vol%, 16 vol% and 40 vol% THF contents with time aging.**

The P(FpP) aggregates after aging for one hour in THF/hexane mixed solvents were characterized by TEM. The results are shown in Figure 2.2. One-dimensional branched fibres were formed in the system

containing 4 vol% THF (Figure 2.2a), while spherical particles with varied sizes were observed in the solutions with a larger amount of THF (40 vol%) (Figure 2.2c). This comparison suggests that, by lowering the THF content, the kinetic pathway for aggregate formation by precipitation varies from isotropic to one-dimensional growth, resulting in precipitates in a few days. At a THF content of 16 v%, the assemblies were kinetically-trapped (Figure 2.2b) into worm-like particles. These experimental results demonstrate that the shock precipitation can be adjusted into a one-dimensional growth pathway depending on the solvation quality. The system with a medium THF contents (10-30 vol %) creates an energy barrier arresting the worm-like assemblies that are stable for a few months. This experiment illustrates that the precipitation kinetics can be controlled for nanosynthesis by varying the solvation quality.

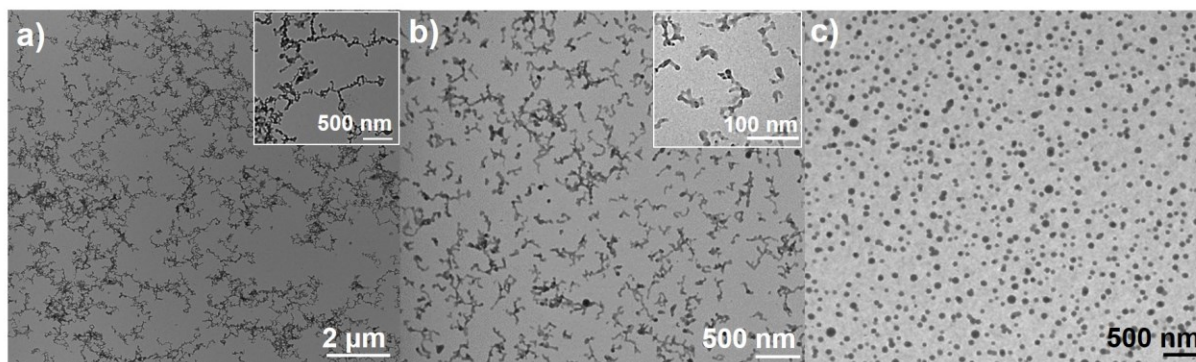


**Figure 2.2 TEM images for P(FpP) colloids formed in the THF/hexane solutions containing a) 4 vol%, b) 16 vol%, and c) 40 vol% THF. The inset images in the Figures 2.2a and 2.2b are the large magnification image of the corresponding P(Fp)P aggregates. The images were recorded after the solutions were prepared by shock precipitation and aged for one hour.**

### 2.3.2 Kinetic assembly of P(FpP) by cooling DMSO solutions.

We have reported that P(FpP) with DP of 64 in DMSO has a UCST behaviour.<sup>80</sup> The polymer precipitated by cooling from 65 °C to 25 °C (Figure 8.1). The effect of concentration on this precipitation was first investigated. Three solutions of P(FpP) in DMSO with concentrations of 1.00, 0.50 and 0.125 wt% were separately heated. The light transmittance at 600 nm for these solutions at 65 °C was greater than 80 % (Figure 2.3), suggesting a good solubility. The more concentrated solution exhibited a relatively lower transmittance, which was attributed to the light absorption by P(FpP) (Figure 8.2). While cooling, the transmittance dropped abruptly at 43.9 °C, 40.5 °C and 33 °C, respectively, for the solutions with decreased concentrations. After cooling to 25 °C, the transmittance for the more concentrated solutions (0.50 and 1.00 wt%) approached 0 % due to the phase separation, which is commonly observed for polymers with UCST behaviour.<sup>100-101</sup> However, the more diluted solution (0.125 wt%) had slower kinetics for the phase transition and could still transmit 53 % of the incident light at the end of the cooling process. Poly(N-acryloyl amino acid) (PNAA) solutions (< 1.0 wt%) at pH 2.0 have a similar behavior.<sup>102</sup> The phase separation continued from 25 °C to 26 °C as the heating cycle started immediately upon cooling to 25 °C (Figure 2.3a). If the solution was retained at 25 °C after the cooling process, the transmittance decreased continuously from 53% to 39% over 1.5 h (Figure 2.3b) and a precipitate was produced in a few hours (Figure 8.3).

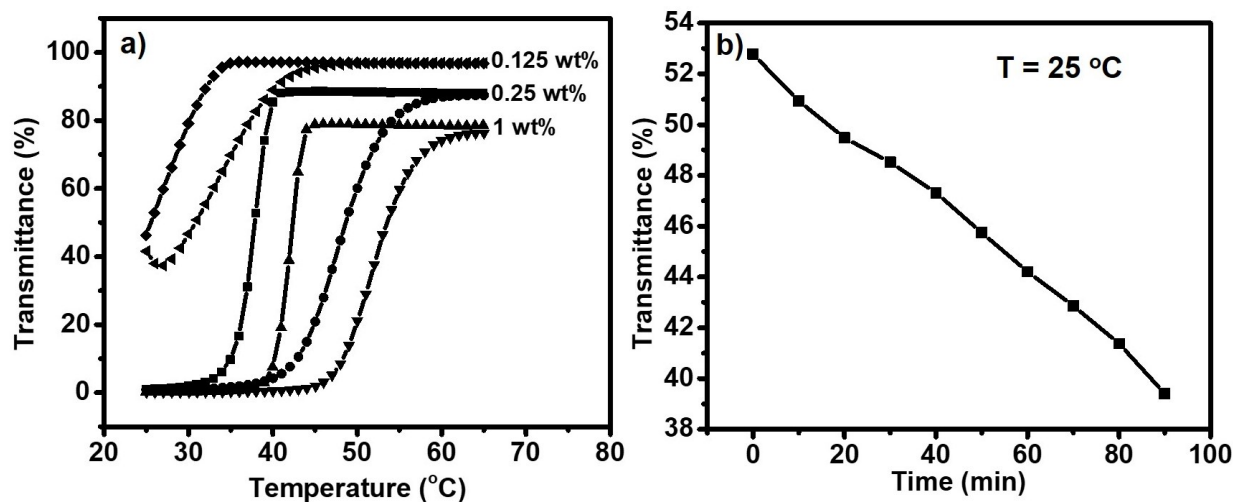


**Figure 2.3. a) The transmittance curves of the three DMSO solutions of P(FpP) with varying concentrations as a function of temperature. b) The time-dependent transmittance of DMSO solution of P(FpP) (0.125 wt%) at 25 °C. The experiment started right after the solution was cooled from 65 °C to 25 °C.**

The phase separation process for the (0.125 wt%) solution was also examined using the DLS technique. As shown in Figure 2.4a, the count rate abruptly increased as the solution cooled to 35 °C, indicative of the occurrence of phase separation. This temperature was higher than that obtained from the turbidity experiment (33 °C) (Figure 2.3a), because light scattering, compared to light transmittance, is more sensitive to the onset of aggregation. To further examine the phase separation, the solutions after cooling to 25 °C, were examined using TEM. As shown in Figure 2.4b, the cooling process induced the P(FpP) in 0.125 wt% solution in DMSO to assemble into spherical particles with a fairly uniform diameter of *ca.* 150 nm (Figure 2.4b). The spherical particles were also formed for the more concentrated solutions (1.00 wt% and 0.50 wt%), which agglomerated relatively faster resulting in precipitates (Figure 8.4). The formation of nanoparticles was reasonable, as the phase separation of

polymers in solution usually starts from the contraction of individual polymer chains, followed by the aggregation of the folded polymers into a globule structure.<sup>103-104</sup>

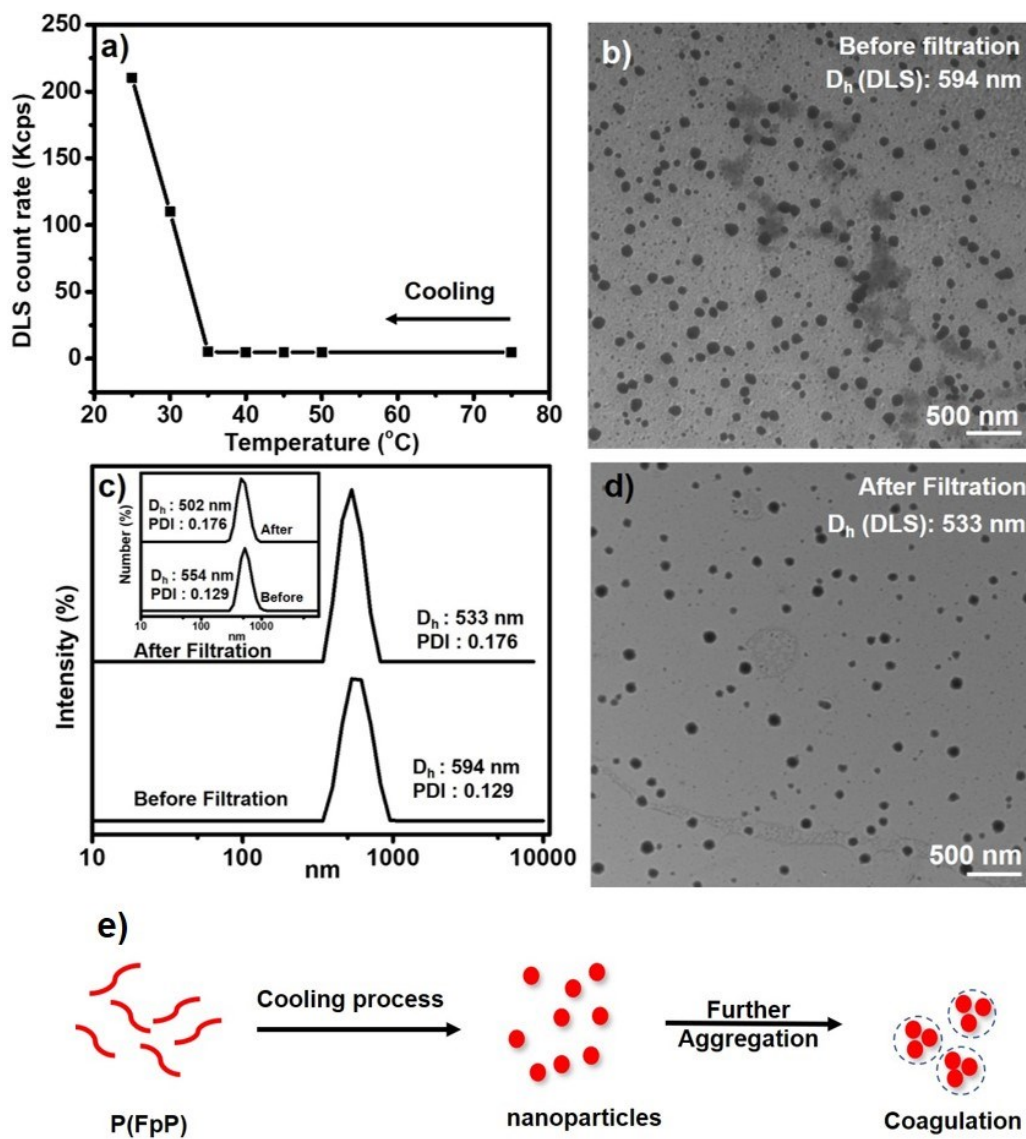


Figure 2.4. a) DLS count rates as a function of temperature, and b) TEM image for P(FpP) particles resulted from DMSO solutions with P(FpP) concentrations of *ca.*0.125

**wt% c) DLS profiles of P(FpP) colloid based on intensity before and after a membrane filtration. The inset image is the DLS profiles based on number. d) TEM image for the particles prepared from DMSO solution of P(FpP) (0.125 %wt) after a membrane filtration (ca. 220 nm for the pore sizes). e) Schematic presentation of solution behavior of P(FpP) polymers during the cooling process.**

### **2.3.3 Kinetic arrest and assembly of P(FpP) particles formed by cooling DMSO solutions.**

It caught our attention that the diameter estimated from the TEM image of the P(FpP) aggregates (ca. 150 nm) is much smaller than their  $D_h$  (ca. 594 nm). The larger  $D_h$  could be caused by the presence of large-sized contaminants that dominated the light scattering intensity. As a result the solution was filtered through a membrane with pore sizes of ca. 220 nm. The  $D_h$  of the filtered solution, measured based on the intensity of scattered light (ca. 533 nm) as well as the number of particles (ca. 502 nm), was similar to that obtained with the solutions before the filtration (ca. 594 nm based on the intensity and ca. 554 nm based on the number) (Figure 2.4c). Furthermore, the average diameter (ca. 140 nm) for the filtered sample as shown in the TEM image (Figure 2.4d) was also smaller than the  $D_h$  (ca. 533 nm). The larger  $D_h$  relative to the diameter estimated from TEM is, therefore, not caused by the presence of contaminants. To rationalize this phenomenon, we propose that the particles are loosely associated in the solution (Figure 2.4e). The interactions between the particles are weak and readily disrupted by the mechanical forces generated during the filtration, which dissociates the agglomerates and allows the particles (ca. 150 nm) to pass through the pores (220 nm). After the filtration, the agglomeration occurs

again. No agglomerates were observed in the TEM images, because the interactions between the particles were too weak to hold the agglomerates when the solution dried on the TEM grid.

The surfaces of the P(FpP) particles possess polarized CO groups that can interact with protic solvents *via* dynamic hydrogen bonds.<sup>79</sup> Therefore, the addition of protic solvents may be able to kinetically arrest the assembled particles, like ligands for metallic particles. On the other hand, protic solvents, such as H<sub>2</sub>O and alcohol solvents, are poor solvents for P(FpP), which can be an unfavored factor for colloidal stability. The outcome of these two opposite effects was investigated by adding H<sub>2</sub>O, methanol and ethanol (8 mol% relative to DMSO) separately into three DMSO solutions of P(FpP) (0.125 wt%) that were prepared by cooling from 65 to 25 °C.

As shown in Figure 2.5a, the addition of these protic solvents decreases the  $D_h$ . The  $D_h$  for the solution with ethanol reduced to 336 nm, but is still larger than the single particle shown in Figure 2.4b. This suggests that the interparticle interactions are partially disrupted by ethanol. Time-dependent DLS indicates that the addition of ethanol kinetically stabilizes the colloids and maintain the  $D_h$  at *ca.* 350 nm over a few days (Figure 2.5b). The TEM image indicates that the trapped particles are spherical and the diameter is *ca.* 200 nm (Figure 2.5c). The addition of H<sub>2</sub>O or methanol is able to segregate the agglomerates more completely because these two solvents are stronger donors for hydrogen bonding as compared with ethanol. Right after the addition of these two protic solvents, the  $D_h$  drops from *ca.* 594 nm to *ca.* 200 nm which is close to the diameter estimated from the TEM image (Figure 2.5b). However, the particles subsequently assembled into suspensions within one hour. These suspensions were characterized by TEM. As shown in Figure 2.5d, 2.5e and 2.5f, entangled worm-like structures are observed and the unentangled nanoworms parallelly align on the substrate into a nematic ordered

pattern due to the rigidity of the nanoobject.<sup>105</sup> The addition of water or methanol, therefore, separates the agglomerates first, the separated particles are, however, not kinetically trapped and undergo a one-dimensional growth. The width of the worm is *ca.* 190 nm and *ca.* 250 nm for the systems with H<sub>2</sub>O (Figure 2.5d) and methanol (Figure 2.5e), respectively. The worm-like structures also have a smooth surface, suggesting that the particles, upon one-dimensional aggregation, coalesced and fused together. The fusion is caused by the flow of polymer chains within solvophobic domains, which is commonly observed and responsible for a local structure adjustment of block copolymer micelles.<sup>106-109</sup>

Chain growth of nanoparticles has been reported and several assembling mechanisms were proposed depending on the type of nanoparticles.<sup>23,110-113</sup> For example, the stability and assembly of metal nanoparticles stabilized by ligands are influenced by the dynamic exchange rate of ligands adsorbed and detached from the nanoparticles. This “on”/“off” ratio of ligand is proposed as a reason governing the anisotropic assembly of nanoparticles.<sup>113</sup> In our case, the protic solvents used for the kinetic investigation may function as ligands. The affinity of ethanol to the P(FpP) particles is weaker resulting in a smaller “on”/“off” ratio, resulting in an isotropic growth. In contrast, the “on”/“off” ratio of water and methanol is higher due to the stronger affiliation to the particles, which cause a directional assembly directing the kinetic pathway into a one-dimensional growth as observed.

The above experiments indicate that the protic solvents function as ligands and poor solvents, which segregate the coagulated particles and subsequently induce a one-dimensional growth depending on the capability of proton donation (Figure 2.5g). H<sub>2</sub>O can completely segregate the particles and induce an assemble into branched fibres. Methanol induces the same solution behavior, but results in relatively thick fibres, probably because the P(FpP) particles are not completely segregated by methanol. Ethanol,



a weak proton donor, only partially segregate the coagulated particles, but do not substantially decrease the solvation power, resulting in kinetically trapped spherical particles.

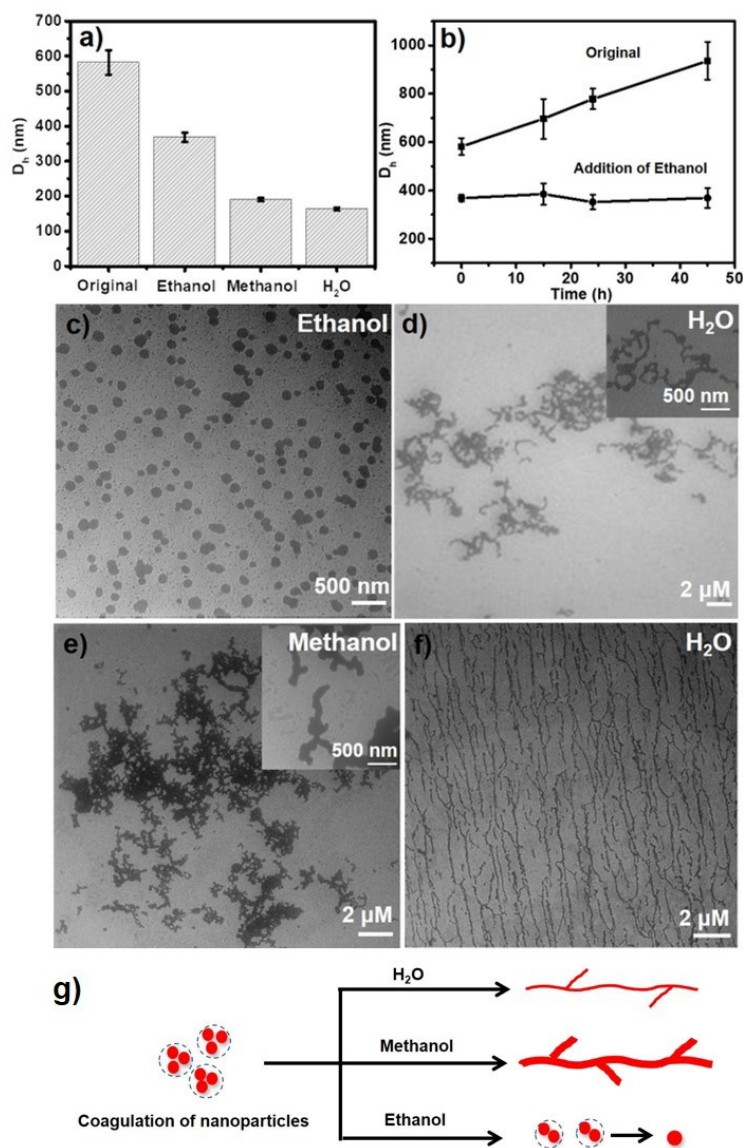


**Figure 2.5.** a) The  $D_h$  size change of P(FpP) colloid (0.125 wt%) upon addition of ethanol, methanol and H<sub>2</sub>O (8% mol%). b)  $D_h$  as a function of aging time for

**P(FpP)/DMSO colloids the upon addition of ethanol, methanol and H<sub>2</sub>O (8% mol%) TEM images for the aggregates prepared from DMSO solution of P(FpP) (0.125 wt%) after addition of c) ethanol and d) H<sub>2</sub>O, the insert image is the large magnification of the worm-like structures. e) Methanol, the insert image is the large magnification of the one-dimensional structures and f) linear aggregates by addition of H<sub>2</sub>O. g) The schematic presentation of the behavior of P(FpP) nanoparticles by addition of water, methanol and ethanol.**

## **2.4 Conclusions**

In conclusion, by varying the conditions for the precipitation of P(FpP), we experimentally illustrated that the kinetic pathways of P(FpP) aggregates could be selectively adjusted to yield a one-dimensional assembly. Kinetically trapped worm-like and spherical particles were produced. By quick addition of P(FpP) solution in THF into THF/hexane mixtures, the precipitation started from the aggregation of the polymer into spheres in the system with a higher content of THF (40 vol%). By lowering the THF content from 40 vol% to 4 vol%, the polymer assembled into branched fibers before precipitation. At a medium THF content (16 vol%), worm-like aggregates were kinetically stable for a few months. P(FpP) with DP of 64 in DMSO has a UCST behavior, and also assembled into spheres when the solution was cooled from 65 °C to 25 °C. The spheres further agglomerated into larger aggregates than the more diluted solution (0.125 wt%). It had slow aggregation kinetics which could be controlled by addition of a trace amount of protic solvents, e.g. ethanol, methanol or water. The addition of ethanol trapped the spheres in a kinetic stable state, while water and methanol with stronger dynamic hydrogen bonds with the P(FpP) spheres enabled the assembling of particles into nanoworms. Kinetic control of

homopolymer precipitation is, therefore, a promising technique for nanosynthesis and worth a systematic investigation, given the fact that homopolymers with various functional groups are readily available.

### Chapter 3 Aqueous Self-Assembly of Hydrophobic Macromolecules with Adjustable Backbone Rigidity

P(FpP) (Fp: CpFe(CO)<sub>2</sub>; P: propyl diphenyl phosphine) has a helical backbone, resulting from the piano stool metal coordination geometry, which is rigid with the intramolecular aromatic interaction of the phenyl groups. The macromolecule is hydrophobic, but the polarized CO groups can interact with water for aqueous self-assembly. The stiffness of P(FpP), which can be adjusted by changing the temperature, determines the nature of the assembled morphologies. P(FpP) self-assembles in DMSO/water (10/90 by volume) mixtures into lamellae at 25 °C, vesicles at 40 °C and irregular aggregates at higher temperatures (60 and 70 °C). Dissipative particle dynamic (DPD) simulations revealed that the same temperature-dependent self-assembled morphologies were obtained with an interior of hydrophobic aromatic groups covered by the metal coordination units. The rigid backbone at 25 °C resulted in a layered morphology, while the more flexible P(FpP) at 40 °C curved up the lamellae into vesicles. At a higher temperature (60 or 70 °C), P(FpP) behaved as a random coil without obvious amphiphilic segregation, thus resulting in irregular aggregates. The stiffness is, therefore, a crucial factor for the aqueous assembly of macromolecules without obvious amphiphilic segregation, which is reminiscent of the solution behavior observed for many biological macromolecules that display hydrophobic microdomains such as proteins.

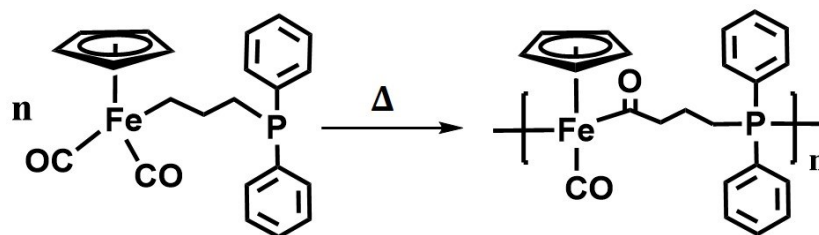
### 3.1 Introduction

The development of supramolecular chemistry relied substantially on the inspiration from nature.<sup>114-117</sup> Amphiphilic lipids have led to the development of the synthesis and self-assembly of surfactants and block copolymers.<sup>30,32,118-119</sup> Many biological macromolecules like DNA, RNA, and proteins, contain hydrophobic segments without obvious amphiphilic features, which also assemble into various defined structures laced with a few groups interacting with water at the surface.<sup>3,18,120-124</sup> This assembly is strongly influenced by factors other than amphiphilic segregation, such as the conformational flexibility.<sup>8,125</sup>

Many synthetic polymers are rigid, such as helical polypeptides, aromatic polyesters, and conjugated polymers.<sup>126-128</sup> It is well known that rigid-coil block copolymers display an assembling behavior that is substantially different from coil-coil amphiphilic block copolymers in terms of the assembled nanostructures.<sup>129-132</sup> However, it is not easy to elucidate the effect of chain stiffness on the assembling process, because the segregation of the amphiphilic blocks is usually the overwhelming factor. Macromolecular building blocks with variable rigidity and no obvious amphiphilic segments, reminiscent of some biological species, are ideal systems to investigate the effect of stiffness on self-assembly, but this type of macromolecules are rarely available.

P(FpP) (Fp: CpFe(CO)<sub>2</sub>; P: propyl diphenyl phosphine) is a macromolecule synthesized by migration insertion polymerization (MIP) of FpC<sub>3</sub>P (Scheme 1). As illustrated in Scheme 3.1, the backbone of P(FpP) is constructed from the connection of phosphine coordinated Fp acyl repeating units that have a piano stool coordination geometry.<sup>72,80,99</sup> The polymer adopts a helical conformation in good solvents,<sup>80</sup> and the phenyl groups from the neighboring repeating units interact closely with each other.

<sup>80</sup>The strength of this aromatic interaction can be adjusted by varying the solvent quality,<sup>99</sup> which may be a variable that can be used to modify the stiffness of P(FpP).



### Scheme 3.1 Synthesis of P(FpP) by migration insertion polymerization

P(FpP), regardless of its degree of polymerization (DP), is soluble in THF.<sup>79</sup> When water is added into a THF solution, P(FpP) assembles into vesicles with the metal coordination units exposed to water via water carbonyl interactions (WCIs).<sup>79</sup> DMSO, however, is a marginal solvent. P(FpP) with DP of 64 is only soluble in DMSO at an elevated temperature.<sup>80</sup> This temperature-dependent solvation may be a factor affecting the self-assembly behaviour of P(FpP). To perform this study, P(FpP) with DP of 7 was used as a building block, as the solvation can be adjusted in a range of temperature from 25 °C to 70 °C.<sup>80</sup> A theoretical simulation was performed to assist the investigation,<sup>133-134</sup> because the theory underlying the aqueous self-assembly of homopolymers without water-soluble groups is less developed.<sup>63,66,71,135</sup> The temperature-dependent chain conformation was quantitatively correlated to the stiffness of the backbone using both all-atom and dissipative particle dynamics (DPD) simulation.<sup>136-</sup>

139

Herein, we report that the stiffness of P(FpP) can be varied from a rigid backbone at 25 °C to a less rigid chain at 50 °C and a random coil at 70 °C. The effect of this temperature-dependent rigidity on the assembly of P(FpP) in a DMSO/water (10/90 by volume) mixture was described for the first time. Both

experiment and simulation reveal that P(FpP) lamellae, vesicles, and irregular aggregates are formed at 25 °C, 40 °C and higher temperatures (60 and 70 °C), respectively. Regardless of the temperature, the molecules associated into a sandwich structure with an interior made of the aromatic groups covered by the metal coordination groups. The rigidity of the backbone at 25 °C directs the sandwich structure into lamellae. By increasing the temperature to 40 °C, the lower rigidity of the chains allowed the membranes to curve up and form vesicles. At a higher temperature (60 and 70 °C), P(FpP) became a random coil without obvious amphiphilic segregation and the sandwich aggregates became irregular particles.

## **3.2 Experimental section**

### **3.2.1 Materials and instrumentation.**

Sodium (Na), potassium (K), 1-bromo-3-chloropropane and cyclopentadienyl iron dicarbonyl dimer (Fp<sub>2</sub>) were purchased from Sigma-Aldrich. Benzophenone was purchased from Fisher Scientific. DMSO was commercially available from Sigma-Aldrich and used without further purification.

<sup>1</sup>H, <sup>31</sup>P, and <sup>13</sup>C NMR experiments were carried out on a Bruker-300 (300 MHz) spectrometer at ambient temperature using either CDCl<sub>3</sub> or DMSO as a solvent. NMR samples were prepared under a dry nitrogen atmosphere. Dynamic light scattering (DLS) measurements were carried out on a Malvern Zetasizer (Nano S90) with a laser wavelength of 633 nm. The Auto measure mode was selected and the evaluation method was based on a standard Gaussian method. Transmission electron microscopy (TEM) experiments were performed using a transmission electron microscope (Philips CM10) with an acceleration voltage of 60 KV. TEM samples were prepared by dipping a carbon-coated TEM copper grid into the solution of P(FpP) colloids, followed by drying in air. Atom force microscopy (AFM)

experiments were performed using a Nanoscope MultiMode™ AFM microscope. The measurements were carried out in tapping mode using a Conical AFM tip with a spring constant of 40 N/m, a resonance frequency of 300 kHz, and tip radius of 8 nm. A freshly prepared colloidal dispersion was dropped on a freshly cleaved mica substrate for spin-coating. The substrates were then dried at room temperature before the measurements.

### 3.2.2 Synthesis of P(FpP).

P(FpP) was synthesized using the reported technique.<sup>72,80,99</sup> The polymerization of FpC<sub>3</sub>P (*ca.* 1 g) was carried out in the bulk at 70 °C for 20 h. The system was then cooled to room temperature. The crude product was first dissolved in a minimum amount of THF (*ca.* 5 mL) and then precipitated in a large amount of hexane (100 mL). The precipitates were collected via filtration and dried under vacuum overnight at room temperature yielding yellow powders. The resultant bright yellow powders were further characterized using NMR, IR and GPC. <sup>1</sup>H NMR (DMSO-d<sub>6</sub>): 7.6–7.1 ppm (b, 10H, C<sub>6</sub>H<sub>5</sub>), 4.4–4.0 ppm (b, 5H, C<sub>5</sub>H<sub>5</sub>), 2.8–2.60 ppm (b, 1H, COCH<sub>2</sub>), 2.4–2.1 ppm (b, 1H, COCH<sub>2</sub>), 2.1–1.8 ppm (b, 2H, CH<sub>2</sub>P), and 1.4–0.8 ppm (b, 2H, CH<sub>2</sub>CH<sub>2</sub>CH<sub>2</sub>). <sup>31</sup>P NMR (DMSO-d<sub>6</sub>): 73.2 ppm, 35.5 ppm. IR: 1910 cm<sup>-1</sup> (terminal carbonyl groups), 1600 cm<sup>-1</sup> (migrated carbonyl groups). GPC: M<sub>n</sub> = 3320 g/mol; M<sub>w</sub> = 3920 g/mol, PDI = 1.18.

### 3.2.3 Self-assembly of P(FpP).

Self-assembly of P(FpP) was performed using DMSO as a co-solvent. A DMSO solution of P(FpP) (1 mg/mL) was prepared first. Then distilled water was added to the solution rapidly resulting in a colloidal dispersion. The final concentration of P(FpP) was 0.1 mg/mL. To investigate the effect of temperature



on the assembly, the DMSO solution of P(FpP) and distilled water were first heated at a certain temperature for 24 h before they were used for the preparation of the colloids.

### **3.2.4 All-atom simulation.**

The all-atom simulations were performed using Materials Studio, v8.0.<sup>24</sup> One macromolecule was mixed with water molecules in a periodic simulation box using the Amorphous Cell modulus. The Discover modulus was adopted to run the simulation. The Nose thermostat was used to control the system temperature during the simulations. The compass force field was acted in the whole system, and the atom based summation method was applied to both van der Waals and Coulomb forces. First, the system was optimized to minimize the free energy using the steepest descent method. Then molecular dynamics simulations were performed under an NVT ensemble for temperatures ranging from 25 to 75 °C. The time step was set to 1.0 fs and all the simulations were run for 10  $\mu$ s. The Blend modulus in Materials Studio was used to calculate the Flory-Huggins Parameter ( $\chi_{ij}$ ) between the different species.

### **3.2.5 DPD simulation system.**

A detailed description of the DPD simulation method can be found in Supporting Information. The DPD simulations were performed using LAMMPS packages. The simulations were run in a periodic simulation box with a size of  $50 r_c^3$  where  $r_c$  is the length unit. The bead density was set to  $3 r_c^{-3}$ . All the simulations were performed for  $10^4 \tau$  ( $\tau$  is the time unit), providing enough time for the system to reach equilibrium.

### 3.3 Results and discussion

#### 3.3.1 Temperature-dependent chain conformation of P(FpP).

To reveal the chain conformation of P(FpP) in response to temperature, all-atom simulations were performed using Materials Studio.<sup>99</sup> Figure 3.1 exhibited the conformations of P(FpP) in water at equilibrium. As shown in Figure 3.1a, an alpha-helical structure is observed at 25 °C and the average distance for the neighboring aromatic groups is *ca.* 4.7 Å, indicating strong  $\pi$ - $\pi$  interactions. Upon increasing the temperature to 50 °C, the aromatic pendent groups do not interact in the same fashion and the distance between them increased to 5.9 Å (Figure 3.1b), suggesting the helical nature of the chain is weakened. The chain appeared to be a random coil without obvious alpha-helix at 70 °C (Figure 3.1c) and the distance between the aromatic groups equalled 7.3 Å. This simulation revealed that both the aromatic interaction and chain conformation of P(FpP) was temperature-dependent.

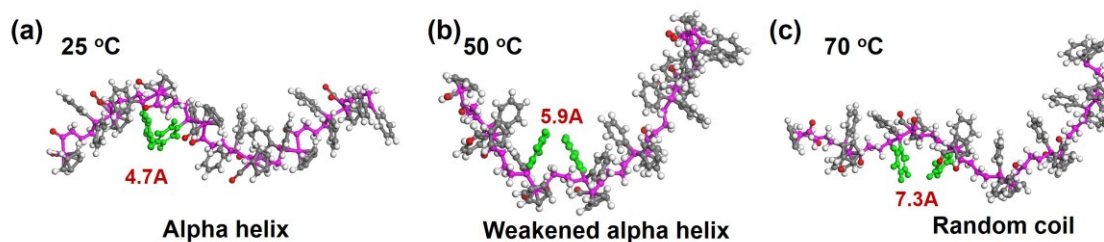


**Figure 3.1. Morphologies of P(FpP) chain in response to temperatures. The green groups represent the neighboring phenyl rings and the red numbers indicate the distances between the groups.**

### 3.3.2 Temperature-dependent self-assembly of P(FpP).

To evaluate the effect of temperature-dependent chain conformation on the self-assembly, solutions of P(FpP) (1 mg/mL) were prepared in DMSO/water (1/9 by volume) mixture at various temperatures. The resultant assemblies were characterized by TEM, AFM, and DLS. P(FpP) assembled at 25 °C into aggregates with hydrodynamic diameters ( $D_h$ ) of *ca.* 87 nm and PDI of 0.21 (Figure 8.5a). The AFM image shown in Figure 3.2a indicated that the size of P(FpP) assemblies was *ca.* 70 nm. The height profile (Figure 3.2b and 3.2c) revealed that the thickness of the aggregates was *ca.* 3.5 nm. The size-to-thickness ratio was high confirming that nano-sheets were obtained. The TEM images, shown in Figures 3.2d and 8.5b, also displayed a layered structure, but the size was over a few micrometers (Figure 3.2d). The larger size observed in TEM images is attributed to the drying effect resulting from the fusion of the nano-sheets (Figure 8.5b). The AFM samples were prepared by spin coating, which minimized the drying effect and resulted in a measured size that was comparable to the  $D_h$  (Figure 8.5a).

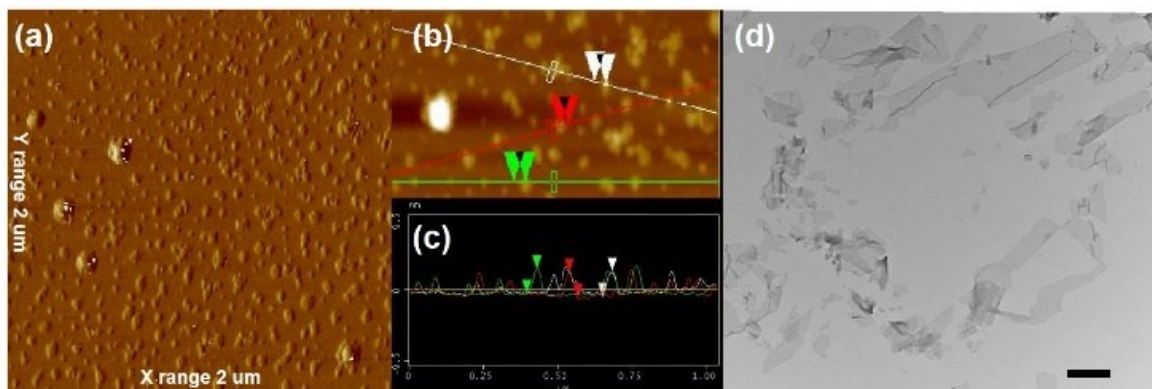


**Figure 3.2.** a) AFM phase mode image, b) height mode image, c) height profile along the line in b (the full scale of Y-axis is 19 nm) and d) TEM image for P(FpP) nano-sheets

**assembled at 25 °C in DMSO/H<sub>2</sub>O (10/90 by volume) solution (0.1 mg/mL). Scale bar for TEM: 500 nm.**

P(FpP) assemblies prepared at 40 °C had a  $D_h$  of 98 nm with PDI of 0.361 as indicated by DLS analysis (Figure 8.6a). Cooling the solution brought no change in  $D_h$  suggesting that the aggregates were kinetically stable (Figure 8.6b). The TEM images for the assemblies were displayed in Figures 3.3, 8.6c and 8.6e. As shown in Figures 3.3a and 3.3b, some spherical aggregates showed a contrast between the periphery and center, suggesting that nano-vesicles were formed. The thickness of the wall was *ca.* 3.2 nm that is similar to the height of the nano-sheet obtained at 25 °C. Interestingly, many collapsed nano-vesicles with a severe indentation and distortion also appeared in the TEM images (Figures 3a and 8.6). Figures 3.3c and 3.3d showed that the vesicle had a bowl-shape. The side view indicates that the periphery is relatively dark (Figure 3.3c), suggesting that the wall of the vesicles was not broken. PAA-*b*-PS (PAA: polyacrylic acid; PS: polystyrene) block copolymer has been reported to form bowl-shaped vesicles. This result was attributed to the preparation method for the TEM specimens.<sup>140</sup> When the sample was dried under high vacuum, a pressure gradient between the two sides of vesicles was generated which caused the deformation of the vesicles. The mechanism for the formation of bowl-shaped vesicles was later studied in details.<sup>141-143</sup> It was found that the PEG-*b*-PS (PEG: poly(ethylene glycol)) bowl-shaped vesicles can be formed in solution due to the deflation of spherical vesicles induced by the osmotic pressure. For example, the addition of water to the solution of vesicles in a dioxane/H<sub>2</sub>O mixture led to the diffusion of dioxane through the PS wall resulting in a negative pressure within the vesicles, which promoted the indentation. The evaporation of DMSO/water at ambient condition is slow and might not be able to generate sufficient osmotic pressure to deform the vesicles.

The bowl-shaped vesicles are, therefore, formed during the addition of water to the DMSO solution. In addition to the deformed vesicles, some vesicles with a ruptured wall were captured in the TEM images (Figures 3.3e and 8.6c).

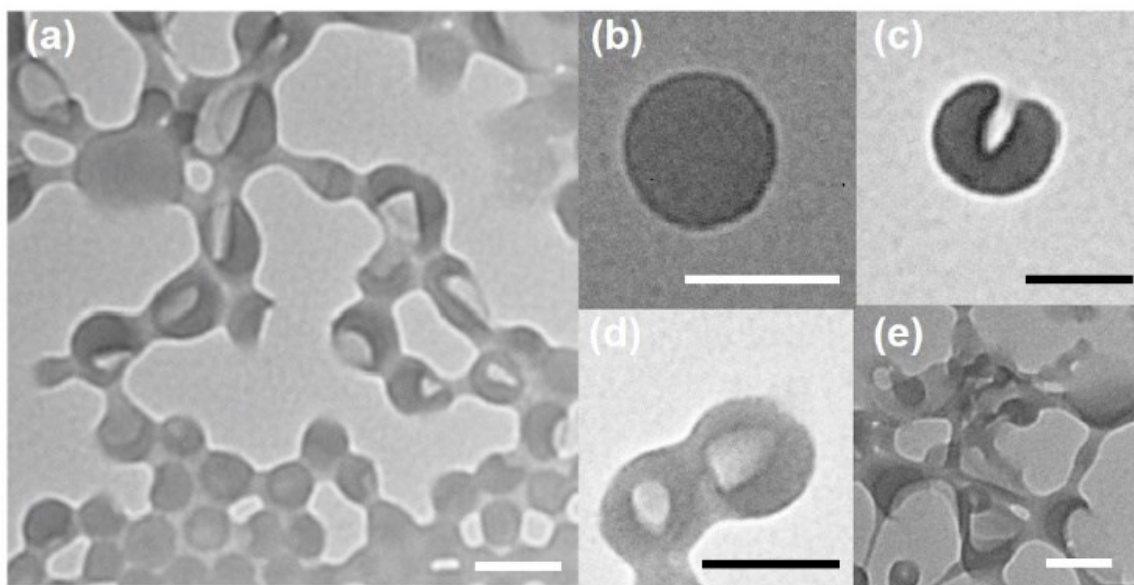


**Figure 3.3. a, b, c, d) TEM images of P(FpP) nano-vesicles assembled at 40 °C in DMSO/H<sub>2</sub>O (10/90 by volume) solution (0.1 mg/mL). scale bar: 100 nm.**

P(FpP) assemblies prepared at 60 °C have a  $D_h$  of *ca.* 71 nm with PDI of 0.236 (Figure 8.7). TEM images indicated that irregular aggregates were formed (Figure 8.8a). We also noticed that the irregular aggregates, unlike the aggregates formed at other temperatures, were not stable and easily broken when exposed to the electron beam (Figures 8.8b-8.8d). Further increasing the temperature to 70 °C led to the assembly of the macromolecules into aggregates with three size populations from 50 nm to 4500 nm as indicated in the DLS profile (Figure 3.4a). As shown in a TEM image (Figure 3.4b), the aggregates appeared to have a worm-like structures (Figure 3.4c). Many of them were entangled

together (Figure 3.4d), and might exist in the solution as large aggregates, as detected by DLS analysis (Figure 3.4a).

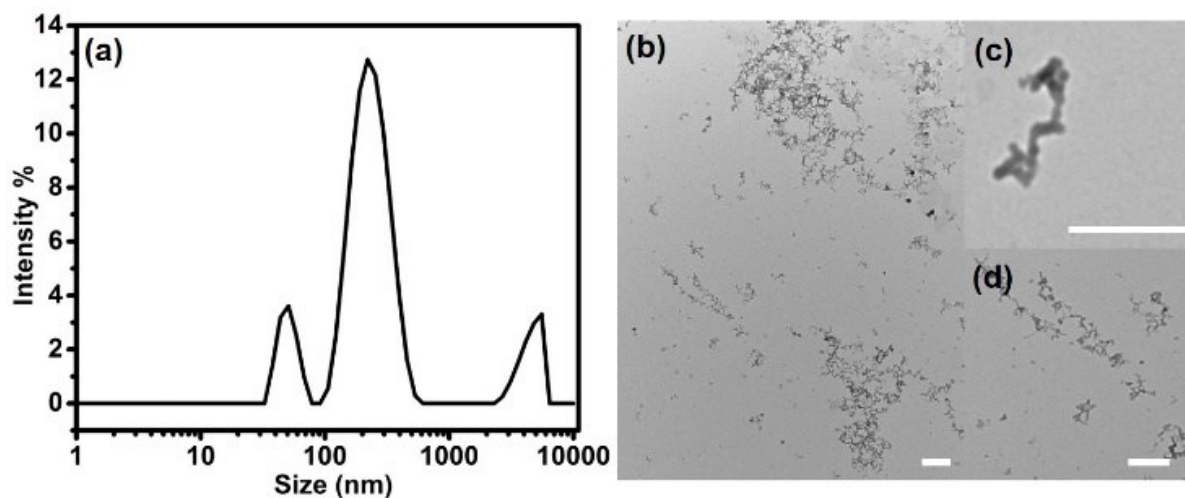


**Figure 3.4. a) The DLS profile and b, c, d) TEM images of P(FpP) nano-vesicles assembled at 70 °C in DMSO/H<sub>2</sub>O (10/90 by volume) solution (0.1 mg/mL). scale bar: 100 nm.**

### **3.3.3 Self-assembled morphologies reproduced by simulation.**

To simulate the self-assembling behavior, DPD simulations were performed using a coarse-grained molecular model of P(FpP). As shown in Figure 3.5a, COFeCO and (CH<sub>2</sub>)<sub>3</sub>P were grouped as polar beads of O (yellow) and P (red), respectively, while the phenyl and Cp groups were denoted as hydrophobic beads R (green). Figure 3.5b displays the coarse-grained chain. As shown in the chain, the macromolecule possesses a polar metal coordination backbone with hydrophobic beads as side groups. The repulsive parameters ( $a_{ij}$ ) of the hydrophobic beads (R groups) with the backbone (O and P groups) and solvents were denoted as  $a_{RO}$ ,  $a_{RP}$ , and  $a_{RS}$ , respectively, which is calculated from Flory-Huggins

Parameter ( $\chi_{ij}$ ) and listed in Table 8.2 (SI).<sup>144</sup> The value for  $\chi_{ij}$  as a function of temperature was calculated using Materials Studio v8.0.<sup>99</sup>

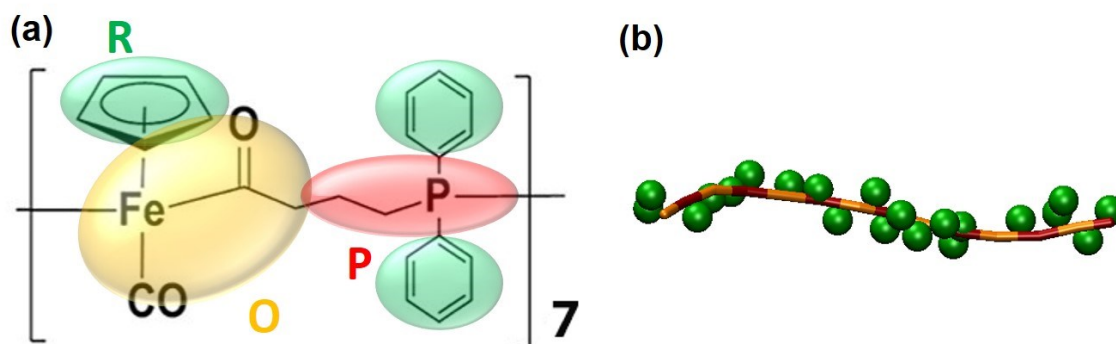


**Figure 3.5. Schematic illustration for the coarse-grained model of P(FpP) used for DPD simulation. a) Coarse-grained groups for P(FpP) (green, orange and red beads represent benzyl/Cp, COFeCO, and  $(\text{CH}_2)_3\text{P}$  groups, respectively). b) Coarse-grained P(FpP) chain.**

The all-atom simulations have suggested that the backbone is helical and rigid. In the DPD simulation, we adjusted this rigidity by the strength of a three-body angle potential (denoted by  $k_c$ ) that was applied to the backbone (formed by O and P groups). The larger the  $k_c$  value and the stronger the chain stiffness. To confirm that the variation of  $k_c$  from 0 to 5  $k_B\text{T}$  can effectively capture the evolutionary rigidity of the chain in a DPD simulation, the persistence length ( $l_p$ ) of a single chain which is proportional to chain stiffness,<sup>37</sup> was calculated using both all-atom and DPD simulations. The  $l_p$  in response to a temperature varying from 25 to 70 °C (calculated from the all-atom simulation) and the profile of  $l_p$  as a function of  $k_c$  (calculated from the DPD simulations) are compared in Figure 3.6. As shown in Figure 3.6, the profiles ( $l_p$  vs  $k_c$  and  $l_p$  vs temperature) calculated from the two simulations are similar. The  $l_p$

is larger at 25 °C, corresponding to a  $k_c$  value of  $5k_B T$ , and gradually decreased with increase in temperature (all atom simulation) or a decrease in  $k_c$  (DPD simulation). At 60 °C, corresponding to a  $k_c$  value of 0,  $l_p$  decreased to its minimum value and plateaued off. The chain conformations in response to  $k_c$  simulated from the DPD simulations of a single chain were also similar to those simulated from the all-atom simulation (Figure 3.6). The similarity of these two calculations elaborates that the temperature-dependent change in chain conformation was caused by the variations in backbone rigidity, which is a parameter crucial for the assembly of P(FpP).

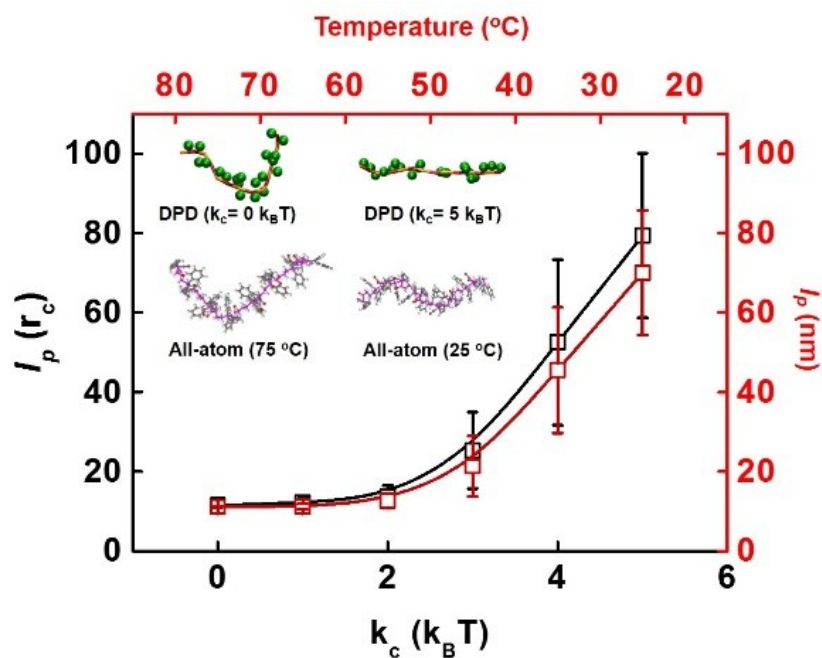


**Figure 3.6. Persistence length as a function of  $k_c$  in DPD simulation (the black curve) and temperature in all-atom simulation (the red curve). The chain conformations at 25 and 70 °C, corresponding to  $k_c$  of 5 and 0  $k_B T$ , are shown in the figure.**



DPD simulations of the assembling process in response to changes in temperature were performed. Figure 3.7a shows a lamella at the end of the simulation conducted at 25 °C. The backbones of P(FpP) were aligned almost parallel to each other. As shown in the cross section of a lamella (Figure 3.7b), the hydrophobic R groups (green) aggregated into a layer with the surfaces decorated by the polar O (orange) and P groups (red). By examining the densities of these three groups along the normal direction (denoted by  $x_1$  in Figure 3.7b), the R groups yielded a wider peak between the peaks for O and P groups, supporting a sandwich layered structure. As the thickness of the assembled nano-sheet was 3.2 nm as measured by AFM, the sandwich membrane was likely a face-to-face assembly of two P(FpP) molecules. The density profile (Figure 3.7b) indicated that the thickness of the sandwich was *ca.*  $7 r_c$  ( $r_c$  is the cut-off distance in the simulation) with  $5 r_c$  representing the middle layer of the aggregated R groups. Figure 3.7c described the calculated order parameter ( $S$ ) for P(FpP) backbones packing along lamellae (denoted by  $x_2$ ). As shown in Figure 3.7c, a relatively larger value of  $S$  ( $0.8, 0 \leq S \leq 1$ ) was observed, suggesting that the P(FpP) backbones were highly ordered. A small value of  $S$  (*ca.* 0.5) indicating a less ordered alignment, was obtained near the edges of the lamella (Figure 3.7c). This reduced alignment was caused by the coverage of the polar groups (O, P) on the high-energy edges to minimize the contacts between the hydrophobic R groups and water. The formation of lamellar assemblies at 25 °C was, therefore, caused by the chain stiffness (Table 8.2).

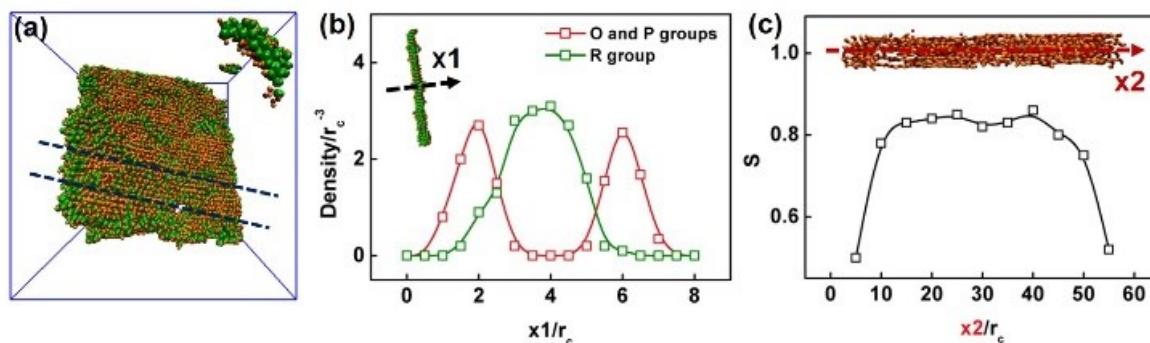


**Figure 3.7. a) Morphologies of the simulated lamellae structure at 25 °C ( $k_c = 5k_B T$  and  $a_{RO} = a_{RP} = 60$ ,  $a_{RS} = 75$ ). The dashed lines indicate where the structure is sliced and enlarged for further analysis; b) The densities of O, P and R groups along the cross section ( $x1$  direction). c) The order parameter of the backbones along the membrane plane ( $x2$  direction).**

Figures 3.8a and 3.8b displayed the morphology of P(FpP) assembled at 40 °C and the cross-section image. The density profiles for the polar O, P and hydrophobic R groups along the radial direction is displayed in Figure 3.8c. As shown in the figures, the vesicular wall also showed a sandwich structure similar to that for the lamellae formed at 25 °C, where a hydrophobic domain of R groups (denoted by green) was covered by the polar O (orange) and P groups (red). The thickness of the vesicular wall shown in Figure 8c was also similar with that of the lamella. The chain stiffness potential at 40 °C ( $k_c = 2k_B T$ ) was lower than that at 25 °C ( $k_c = 5k_B T$ ) (Table 8.2), which allowed the membrane to curve up and form vesicles to reduce the total free energy.

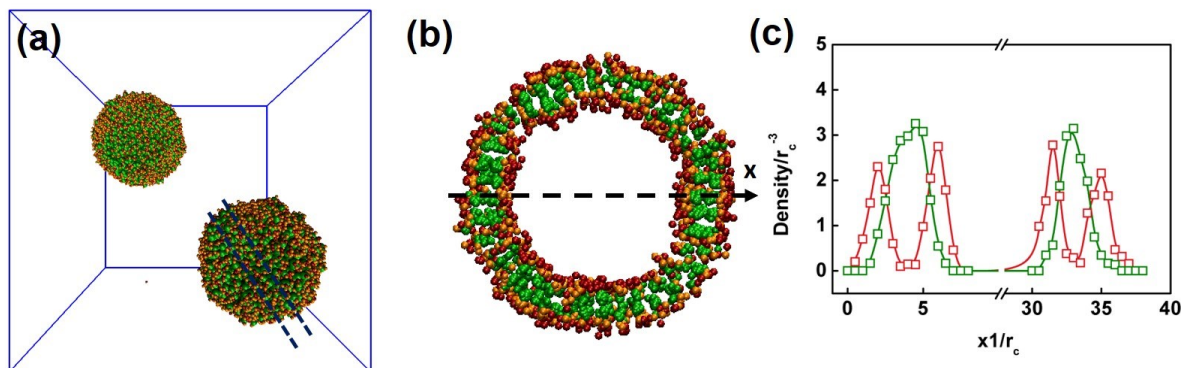


**Figure 3.8. a) Morphologies of the simulated vesicular structure at 40 °C ( $k_c = 2k_B T$  and  $a_{RO} = a_{RP} = 50$ ,  $a_{RS} = 60$ ). The dashed lines indicate where the structure is sliced and enlarged for further analysis; b) The cross section of the vesicle, c) The densities of O, P and R groups along the cross section (x direction in the Figure 8b).**

The response of the assembling behavior to the stiffness of P(FpP) was further investigated. We performed a simulation by adjusting the stiffness ( $k_c$ ) of P(FpP) to 4  $k_B T$ , a value between that at 25 °C (5  $k_B T$ ) and 40 °C (2  $k_B T$ ). As shown in Figure 3.9a, the volumetric map image of the simulated assemblies indicated a curved lamella, which confirmed that the vesicles (Figure 3.9b) result from the curve up of the lamellae due to a reduced stiffness. When the stiffness was adjusted to 1  $k_B T$ , lower than that at 40 °C (2  $k_B T$ ), the rigidity of the molecules was not sufficient to integrate the vesicular membrane and resulted in ruptured vesicles (Figure 3.9c).

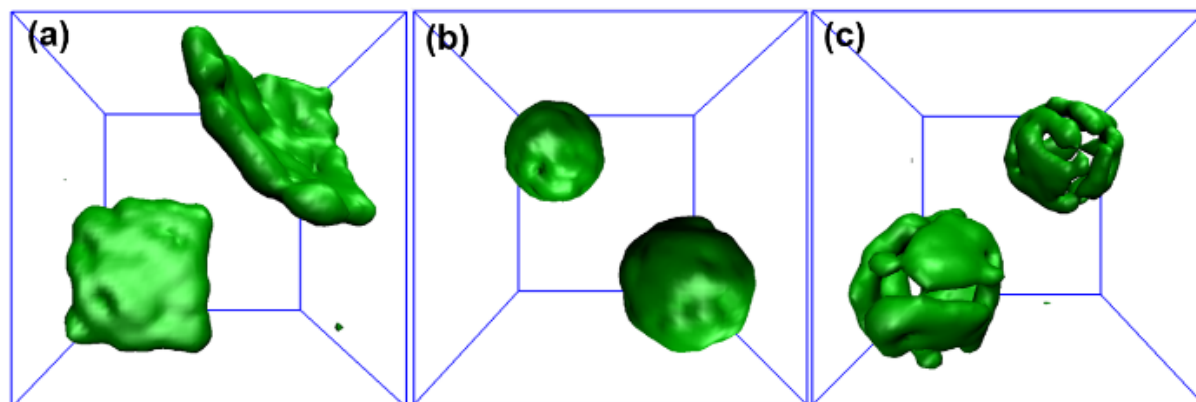


**Figure 3.9. Volumetric map images of a) curved lamellae simulated with  $k_c$  of 4  $k_B T$  , b) vesicles simulated with  $k_c$  of 2  $k_B T$ , and c) ruptured vesicles simulated with  $k_c$  of 1  $k_B T$ .**

A higher temperature at either 60 or 70 °C further reduced the bending energy of the macromolecular chain. P(FpP) lost its rigidity at these temperatures (Table 8.2) and took a coil conformation (Figure 3.1c). Consequently, the rigidity plays no role in the self-assembly of P(FpP) at these two temperatures. The degree of solvation of the R group ( $a_{RS}$ ) and the segregation between the polar O and P with R groups ( $a_{RO}$ ,  $a_{RP}$ ) regulated the assembling process. As shown in Figures 3.10a and 3.10b, the P(FpP) aggregated into irregular particles when it adopted a random coil. Both experiments and simulations indicated that the aggregates formed at 70 °C (Figures 3.4b and 3.10b) were larger than those formed at 60 °C (Figures 8.8a and 3.10a), which was attributed to a lower de-solvation of the R groups and lower repulsive forces between the R groups, O and P groups at 70 °C (Table 8.2). The cross-section of the aggregates (Figure 3.10c) also revealed a sandwich structure with the hydrophobic association of the R group. The packing density (Figure 3.10c) was relatively lower as compared with that for the lamellae (Figure 3.7b) due to the lower segregation between the R groups and the solvent, and the O and P groups. The sandwich structure resulting from the assembly of both rigid chain and flexible coil

suggests that the assembling is initiated by the hydrophobic association of the R groups. However, unlike amphiphilic molecules, the coil at a higher temperature lacks sufficient segregation force to drive the assembly into defined nanostructures.

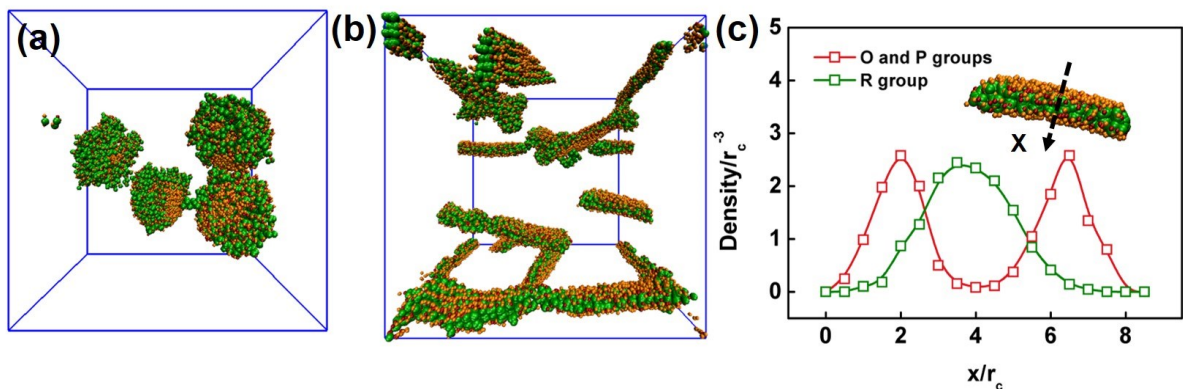


**Figure 3.10. (a) Morphologies of irregular aggregates simulated with  $k_c = 0$  k<sub>B</sub>T and  $a_{RO} = a_{RP} = 40$ ,  $a_{RS} = 50$ , b) Morphologies of wormlike nanoparticles simulated with  $k_c = 0$  k<sub>B</sub>T and  $a_{RO} = a_{RP} = 35$ ,  $a_{RS} = 35$ , c) Densities of O, P and R groups along the x direction of one wormlike nanoparticle.**

The DPD simulation has reproduced the self-assembled nanostructures observed experimentally at various temperatures, which helped us elucidate the effect of the rigidity of PFpC<sub>3</sub>P on the assembling process. PFpC<sub>3</sub>P assembled in the aqueous media into aggregates through the association of hydrophobic aromatic groups, exposing its metal coordination polar backbone to water. The stiffness of the chain at 25 °C directed the assembly into a layered structure. By lowering the rigidity of the macromolecules at 40 °C, the layered structures started to curve and subsequently closed up forming vesicles. As the chain became flexible, the membrane of the vesicles was ruptured. Under the conditions

at higher temperatures (60 and 70 °C), P(FpP) lost its rigidity and became a random coil without obvious amphiphilic segregation, the self-assembly was only regulated by the hydrophobic interaction of the R groups resulting in less ordered aggregates as shown in Figure 3.11.

This temperature-induced variation in morphology of P(FpP) aggregates could be further explained in a thermodynamics view. Figure 8.9 indicated that, as temperature increased, the values of  $\chi_{ij}$  for R-O, R-P and R-S pairs decreased linearly. This result suggested that increasing temperature could weaken the interactions of these different pairs. So, the enthalpy was unfavored ( $\Delta H > 0$ ) with increase in the temperature. Meanwhile, the chain conformations of P(FpP) became flexible with increase in the temperature, which demonstrated that the entropy was favored and  $\Delta S > 0$ .

This analysis indicated that increasing temperature would make the self-assembly process of P(FpP) from enthalpy-dominant process to entropy-dominant one. When the temperature was at 25 °C, the self-assembly process was enthalpy-dominant and ordered lamellae structures were preferred to form. However, as temperature increased, the self-assembly process became entropy-dominant and less ordered structures comparing to lamellae were fabricated such as nanovesicles, irregular nanoparticles and worm-like structures shown in Figure 3.11.

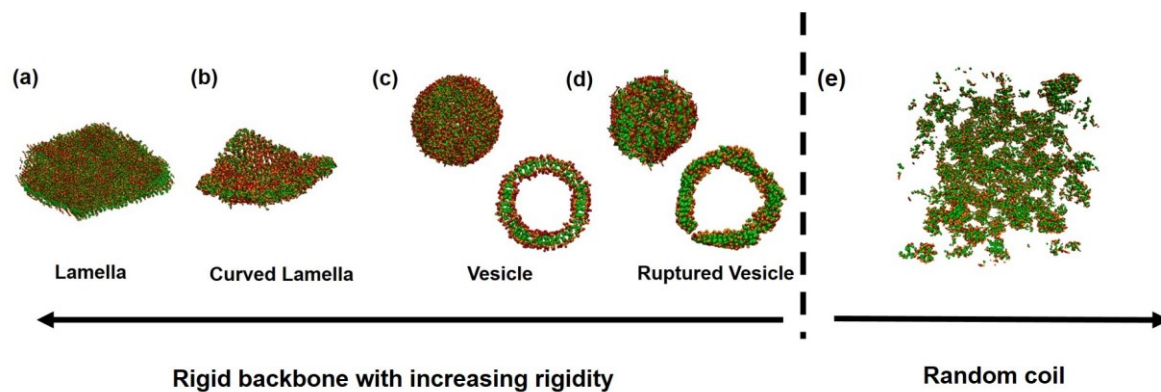


**Figure 3.11. The effect of stiffness on the morphologies self-assembled from macromolecules without water-soluble groups in aqueous media.**

### 3.4 Conclusions

In summary, P(FpP) assembled in DMSO/water mixtures into nano-sheets, vesicles, and irregular aggregates at 25 °C, 40 °C and higher temperatures (60 and 70 °C), respectively. DPD simulations reproduced this temperature-dependent assembling behavior and indicated that the macromolecules packed into a sandwich structure with an interior constituted of R groups covered by metal coordination polar groups. The rigidity of P(FpP) at 25 °C was a crucial parameter that directed the assembly into a layered structure. The formation of the vesicles at 40 °C was due to the decrease in the rigidity. P(FpP) eventually lost its rigidity at higher temperatures (60 and 70 °C). Consequently, the membrane was ruptured and irregular aggregates were formed. This combination of experiments and simulation combined investigation established the effect of rigidity of P(FpP) on the self-assembly of macromolecules that do not bear water-soluble groups. This work will guide further research into the biomimetic supramolecular synthesis using hydrophobic macromolecules as building blocks.





## **Chapter 4 Breathing Behavior of Vesicles Assembled from Hydrophobic Metal Carbonyl Homopolymers P(FpP)**

P(FpP) is hydrophobic, but can self-assemble into nanovesicles in water. Unlike traditional nanovesicles with bilayer membrane, the membrane of P(FpP) vesicles is the result of the stacking of polymer chains. Due to this difference in membrane structure, P(FpP) vesicles in water/THF mixtures exhibited unique “breathing” behavior in response to the THF content. This behavior is discussed in this chapter.

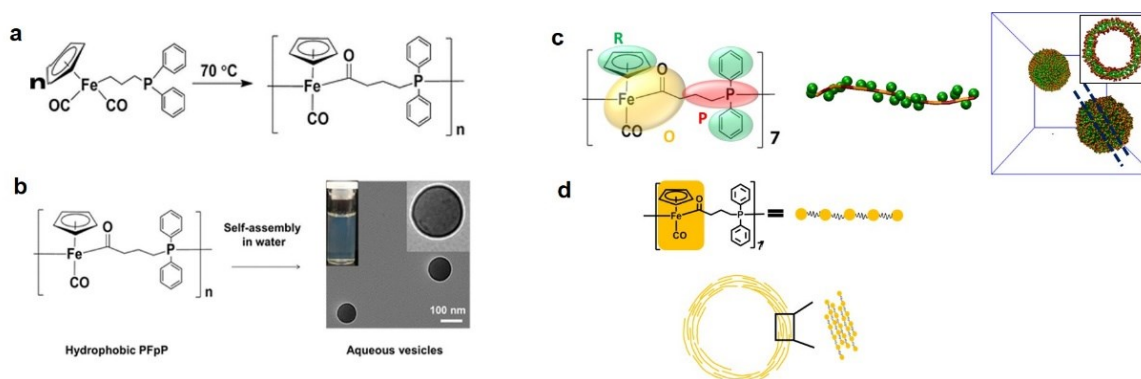
## 4.1 Introduction

Proteins without obvious amphiphilic character can self-assemble into hollow nanostructures like virus capsids.<sup>14,145</sup> The surface of the virus capsids is hydrophobic and is laced with a few polar groups interacting with water.<sup>9,146</sup> This structure is different from that of bilayer vesicles assembled from amphiphilic molecules or block copolymers.<sup>147</sup>

Self-assembly of vesicle-like structures from nonamphiphilic block copolymers<sup>58</sup> and homopolymers<sup>64,71</sup> have been explored. Recently the Du group has prepared a nonbilayer vesicle self-assembled from the homopolymer poly[2-hydroxy-3-(naphthalen-1-acylamino)propyl methacrylate] (PHNA). The homopolymer vesicles possess nonbilayer membrane structures where there is no obvious boundary between the hydrophilic and hydrophobic segments. Though the exact membrane structure of this homopolymer vesicle is not clear, the hydrophilic moieties like the amide or hydroxyl groups were confirmed to be embedded inside the membrane of homopolymer vesicles membranes. Due to the presence of the amide or hydroxyl groups, the PHNA homopolymer vesicles could immobilize Au nanoparticles.<sup>71</sup> The exploration of the membrane structure of this kind of vesicles and the discovery of new properties is still at an early stage and still need more investigation.

Recently our group has synthesized a new metal carbonyl homopolymer P(FpP) using Migration Insertion Polymerization (MIP) as shown in Scheme 4.1a, P(FpP) is hydrophobic, but can self-assemble into vesicles in water (Scheme 4.1b).<sup>79</sup> The formed nanovesicles are quite stable and their stability has been attributed to the water carbonyl interactions.<sup>79</sup> The dissipative particle dynamic (DPD) simulation results for P(FpP) vesicles are shown in Scheme 4.1c. The simulation results indicate that the polar COFeCO (labeled yellow in Scheme 4.1c) and nonpolar moieties including Cp rings and C<sub>3</sub>P(Ph)<sub>2</sub> both

exist on the surface of the P(FpP) vesicles which is similar to the membrane structure of the virus capsids.<sup>9</sup> The simulation results suggested that the membrane of P(FpP) vesicles are formed by the stacking of homopolymer chains as shown in Scheme 4.1d.<sup>82</sup>



**Scheme 4.1. a) Migration Insertion Polymerization (MIP) of monomer FpP, b) Self-assembly of P(FpP) into nanovesicles in water, c) Schematic illustration for the coarse-grained model of P(FpP) used for DPD simulation and the simulated morphology of the vesicular structure by the DPD simulation. d) The schematic presentation of the P(FpP) vesicles and its possible membrane structures.**

In this chapter, we investigate the breathing behavior of homopolymer P(FpP) vesicles in THF/water mixtures in response to the changes in THF content. Moreover, we also investigate the swelling mechanism of the P(FpP) vesicles by addition of THF. During the swelling process, the solvation of the homopolymer plays an essential role in the swelling and shrinking of the vesicle membranes.

## 4.2 Materials and methods

Sodium (Na), potassium (K), 1-bromo-3-chloropropane, 1, 6-dichlorohexane and cyclopentadienyl iron dicarbonyl dimer ( $\text{Fe}_2$ ) were purchased from Sigma-Aldrich. Chlorodiphenylphosphine was purchased from Tokyo Chemical Industry (TCI). Benzophenone was purchased from Fisher Scientific. DMSO and all other solvents were commercially available and were used without further purification.

$^1\text{H}$ ,  $^{31}\text{P}$ , and  $^{13}\text{C}$  NMR were carried out on a Bruker-300 (300 MHz) spectrometer at ambient temperature using either  $\text{CDCl}_3$  or DMSO as a solvent. NMR samples were prepared under a dry nitrogen atmosphere. Gel permeation chromatography (GPC) was employed to characterize the molecular weight of the polymers. THF was used as an eluent at a flow rate of 1.00 mL/min. The Viscotek GPC max unit was equipped with a VE 2001 GPC, three PolyAnalytik organic mixed bed columns, PAS-103-L, PAS-104-L and PAS-105-L, with dimensions of 8 mm (ID)  $\times$  300 mm (L), and a Viscotek triple detector array, including refractive index, viscosity, and dual-angle light scattering detectors. The polystyrene standards were utilized as references. Dynamic light scattering (DLS) measurements were carried out on a Malvern Zetasizer (Nano S90) with a laser operating at 633 nm. The auto measure mode was selected and the evaluation method was based on a standard Gaussian method. The measurements were made at a scattering angle of 90°. The viscosity and refractive index of the THF/water mixtures used in DLS measurements are listed in Table 8.3. Transmission electron microscopy (TEM) images were obtained on a Philips CM10 microscope with an acceleration voltage of 60 kV. Cyclic voltammetry (CV) experiments were carried out at 25 °C using a DY2000 Multi-Channel Potentiostat (Digi-Ivy Inc.) workstation with a scan rate of 50 mV s<sup>-1</sup> and Ag as a reference electrode. Before measurements, a KCl solution in water was added into the colloids and the

final KCl concentration in the dispersion equalled 0.1 mol/L. The UV-vis spectra were obtained from a UV-vis spectrometer (Agilent 8453A).

#### 4.2.1 Synthesis of P(FpP)

P(FpP) was synthesized using a reported procedure.<sup>72,80,99</sup> A typical synthesis is described as follows: The polymerization of FpP (*ca.* 1 g) was performed in bulk without solvents at 70 °C for 20 h. The system was cooled to room temperature. The crude product was first dissolved in a minimal amount of THF (*ca.* 5 mL) followed by precipitation in a large amount of hexane (100 mL). The precipitates were then collected via a filtration method and dried under vacuum overnight at room temperature yielding yellow powders. The resultant bright yellow powders were further characterized using NMR, IR and GPC. <sup>1</sup>H NMR (DMSO-*d*<sub>6</sub>): 7.6–7.1 ppm (b, 10H, C<sub>6</sub>H<sub>5</sub>), 4.4–4.0 ppm (b, 5H, C<sub>5</sub>H<sub>5</sub>), 2.8–2.60 ppm (b, 1H, COCH<sub>2</sub>), 2.4–2.1 ppm (b, 1H, COCH<sub>2</sub>), 2.1–1.8 ppm (b, 2H, CH<sub>2</sub>P), and 1.4–0.8 ppm (b, 2H, CH<sub>2</sub>CH<sub>2</sub>CH<sub>2</sub>). <sup>31</sup>P NMR (DMSO-*d*<sub>6</sub>): 73.2 ppm, 35.5 ppm. IR: 1910 cm<sup>-1</sup> (terminal carbonyl groups), 1600 cm<sup>-1</sup> (migrated carbonyl groups). GPC: M<sub>n</sub> = 3320 g/mol; M<sub>w</sub> = 3920 g/mol, PDI = 1.18.

#### 4.2.2 Preparation of P(FpP) vesicles in water

The P(FpP) vesicles were prepared by adding large amounts of deionized water into the P(FpP)/THF solution (1 mg/mL) in THF. The volume ratio of deionized water to THF was 10:1 (v/v). The obtained P(FpP) colloid in water/THF mixture was dialyzed against water for 24 hours to remove the THF. At last, an aqueous dispersion of the P(FpP) was obtained.

### **4.2.3 Preparation of P(FpP) vesicles in water/THF mixture**

Different amounts of THF was added into the prepared P(FpP) colloid in deionized water to obtain the P(FpP) colloid in a water/THF mixture. The THF amounts in the final P(FpP) colloid in the water/THF mixture were 10, 20, 30, 40 and 50 vol%.

## **4.3 Results and discussion**

### **4.3.1 Characterization of the membrane structure of P(FpP) vesicles**

Previous experiments and simulation results<sup>79,82</sup> suggest that the membrane structures of the P(FpP) vesicles are formed by the packing of polymer chains shown in Scheme 4.1. The P(FpP) vesicles were prepared by the addition of large amounts of water into the P(FpP)/THF solutions followed by dialysis against water to remove the organic solvent. This nanoprecipitation method suggested that the P(FpP) vesicles were kinetically trapped structures.<sup>46</sup> So it is possible to obtain P(FpP) vesicles with different membrane thickness by controlling the solution conditions. P(FpP) vesicles with different membrane thicknesses were obtained by changing the initial polymer concentrations and THF contents during the preparation.

#### **4.3.1.1 The effect of polymer concentrations on the self-assembly of P(FpP) in water**

We first changed the initial polymer concentration and checked its effect on the self-assembled P(FpP) nanovesicles. P(FpP) solutions in THF were prepared with different polymer concentrations (1.0 mg/mL, 0.5 mg/mL and 0.3 mg/mL). To this solution, a large amount of water was added to prepare the P(FpP) colloids. The P(FpP) colloids in THF/water mixtures were dialyzed for 24 h to remove the THF. DLS was first employed to characterize the size of the formed P(FpP) aggregates in water. The

results were shown in Figure 4.2a. The DLS results indicated that P(FpP) vesicles formed at these three different concentrations had similar size and low polydispersity index (PDI), suggesting that the formed P(FpP) vesicles were well dispersed. Moreover, TEM was used to characterize the morphology of the formed P(FpP) aggregates. From the TEM images shown in Figure 4.2b, c and d, the P(FpP) aggregates formed at different polymer concentrations were found to exhibit features that were similar to the ones reported before.<sup>79</sup> No clear contrast between the periphery and interior of the P(FpP) aggregates were observed in the low concentration samples (0.05 and 0.03 mg/mL). This suggested that the membrane thickness of the P(FpP) vesicles did not change with polymer concentration. This conclusion was reasonable considering that the vesicles were prepared by a fast nanoprecipitation process which may be less related to the initial polymer concentration.<sup>46</sup> This conclusion led to the hypothesis that changing the THF content during the preparation process could alter or change the membrane thickness of the P(FpP) vesicles.

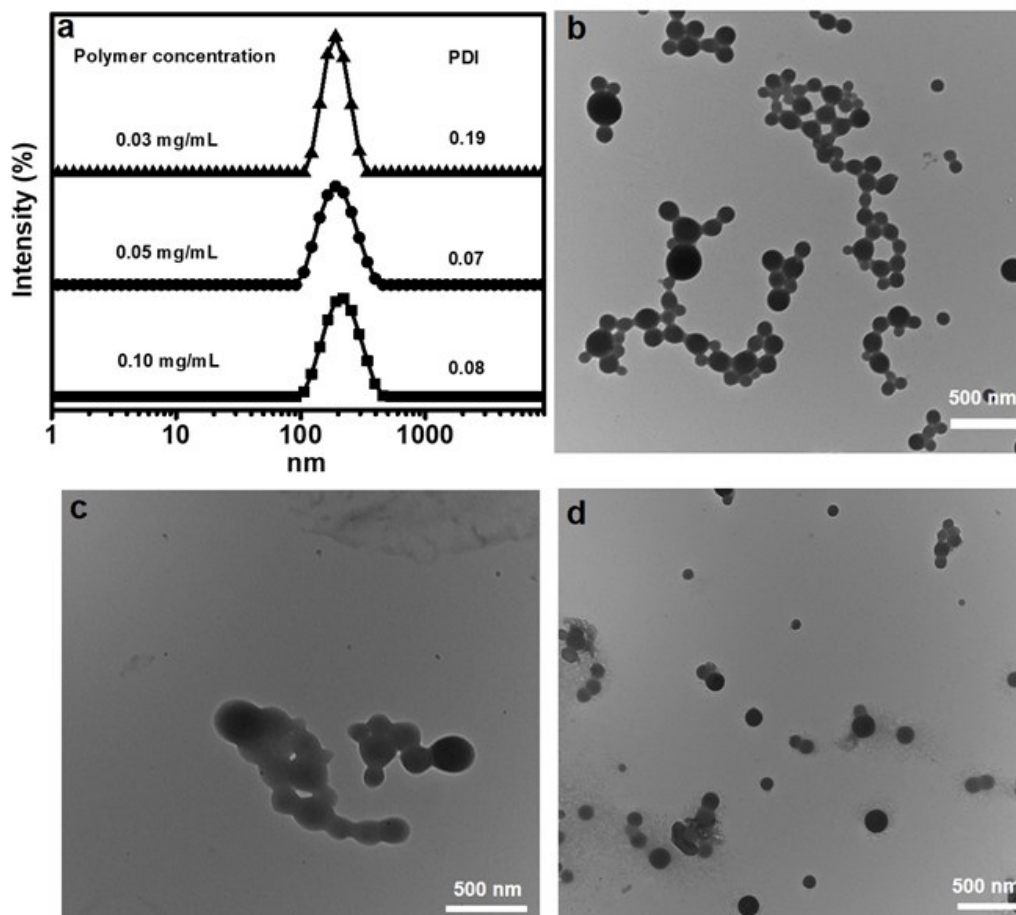


**Figure 4.1 a) DLS profile of P(FpP) colloids with various polymer concentrations. TEM images of the P(FpP) colloids with various polymer concentrations b) 0.10 mg/mL c) 0.05 mg/mL d) 0.03 mg/mL.**

#### 4.3.1.2 The effect of THF content on the self-assembly of P(FpP)

The effect of THF content on the self-assembly of P(FpP) was also investigated. The experiments were done as follows. P(FpP) was first dissolved in THF to obtain a P(FpP)/THF solution (1 mg/mL). Then  $\chi$  mL of THF was added to 1 mL of P(FpP)/THF solutions, followed by quick addition of (10 –



$\chi$ ) mL of water. Then P(FpP) colloids with various THF contents in the THF/water mixture were prepared. The formed colloids were characterized by DLS. Figure 4.2a showed that the size of the P(FpP) aggregates increased with THF content. Moreover, the PDI of the P(FpP) also became larger with higher THF content, which demonstrated that the formed P(FpP) aggregates were unstable and not uniform. TEM was employed to characterize the P(FpP) aggregates in the 30 vol% THF. Interestingly, large lamellae structures were clearly observed under TEM as shown in Figure 4.2b. From the previous report, we know that the P(FpP) aggregates in 10 vol% THF were nanovesicles.<sup>79</sup> By comparing the TEM results of the P(FpP) colloids in 10 vol% THF and 30 vol% THF, we know that the morphologies of the P(FpP) nanostructures could be altered by THF content adjusted between 10 and 30 vol%. Further experiments are still under way to obtain P(FpP) vesicles with various membrane thicknesses.

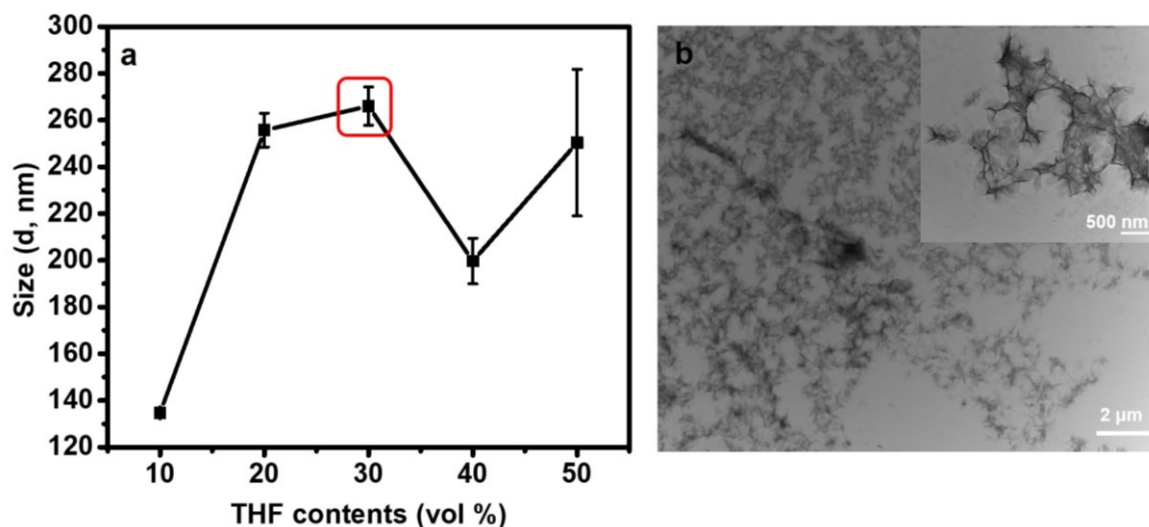


**Figure 4.2 a) D<sub>h</sub> of P(FpP) colloids prepared in THF/water mixed solvent with various THF contents. B) TEM image of the P(FpP) aggregates in THF/water mixed solvent**

**with 30 vol% THF contents (Label red in the Figure 4.2a), the insert image is the large magnification of P(FpP) aggregates.**

#### **4.3.2 Swelling behavior of P(FpP) vesicles**

Though the detailed membrane structure of P(FpP) vesicles was not experimentally verified, simulation and experimental results have shown that the P(FpP) vesicles do not have a traditional bilayer membrane. It is already well known that the membrane structure determines the broad range of the membrane curvature and size.<sup>148</sup> So here we explore the size changing of the P(FpP) vesicles upon addition of THF. As shown in Figure 4.3a, the addition of THF into the P(FpP) colloids in water could increase the size of the P(FpP) vesicles. The size of the P(FpP) vesicles increased from *ca.*200 nm to 430 nm upon increasing THF content to 30 vol%. No significant size difference was observed after the THF content was further increased to 50 vol%. Though the size of the P(FpP) vesicles increased, the PDI of the various P(FpP) vesicles caused by the addition of THF remained small (less than 0.1) (Figure 4.3a), which indicated that the formed P(FpP) vesicles were uniform. Moreover, the vesicles by addition of THF were quite stable. Figure 4.3b shows the size of P(FpP) colloids in THF/water mixtures over 2 weeks. The sizes remained stable and no precipitates were observed over two weeks. This indicated that various P(FpP) nanovesicles with a narrow size distribution could be formed in response to different THF contents.

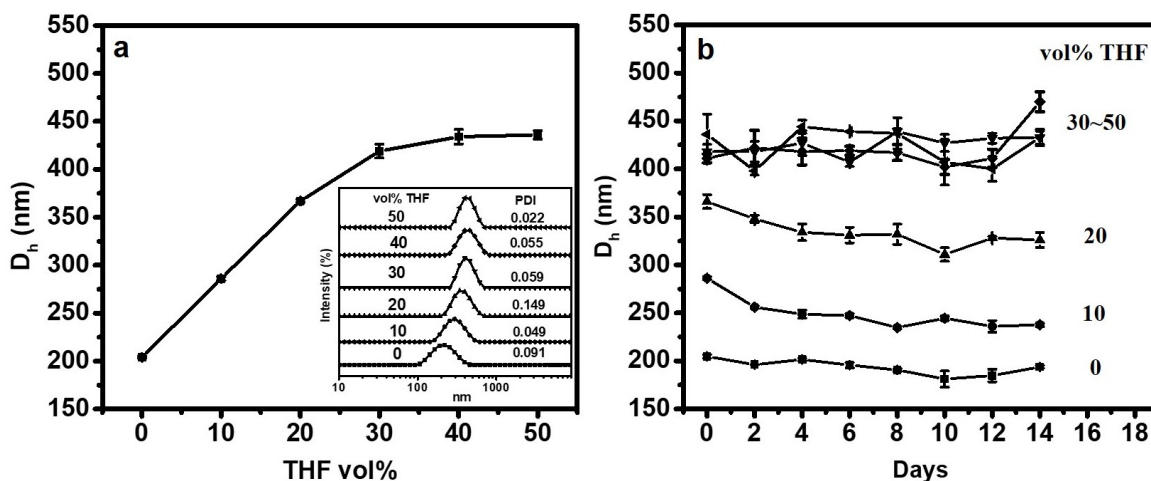


**Figure 4.3 (a) The  $D_h$  change of P(FpP) colloids in aqueous solution ( $14 \mu\text{M}$ ) by addition of different amounts of THF. The inset image is the DLS profiles with different THF contents. (b) the size change as time aging for different P(FpP) colloid with varied THF amounts.**

The P(FpP) vesicles exhibited not only swelling but also shrinking behavior in response to THF content. As shown in Figure 4.4a, the size of the P(FpP) vesicles in 10 vol% THF/water mixture increased immediately from 250 nm to 440 nm by addition of THF to 50 vol%. The size of the vesicles could reversibly decrease to the original size (*ca.*250 nm) by addition of water. The reversible size change of the P(FpP) vesicles in response to THF content indicated that the P(FpP) vesicles exhibited a breathing behavior. In addition, the change in vesicle size changing was an immediate process with no intermediates being observed by DLS. We also employed TEM to characterize the P(FpP) aggregates in a 50 vol% THF/water mixture. As shown in Figure 4.4c, the size of the aggregates was about 400 nm which was consistent with the measured  $D_h$  from DLS. The inset image in the Figures 4.4d and

4.4e shows a broken P(FpP) aggregate. There was a clear contrast between the periphery and interior of the aggregates, compared to the P(FpP) vesicles prepared without addition of THF, which suggested that the formed P(FpP) aggregates had vesicle-type morphology. Moreover, we could also see that the thickness of the membranes was about 30 nm. Here we hypothesised that the stability of the P(FpP) vesicles by addition of a large amount of THF could be attributed to the large thickness of the vesicle membranes.

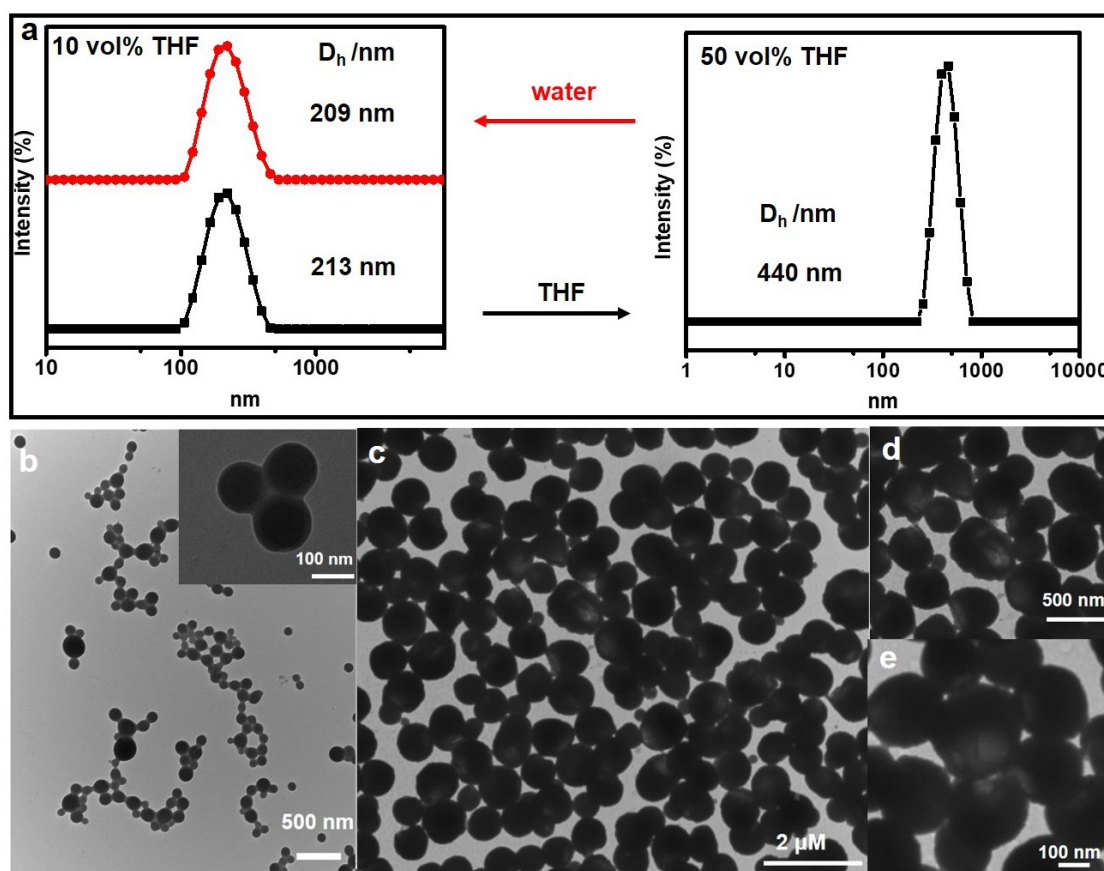


**Figure.4.4 (a) The DLS profiles of P(FpP) vesicles in response to THF contents. TEM image of the P(FpP) vesicles obtained from the P(FpP) colloids with (b) 0 vol% THF**

and (c) 50 vol% THF. (d) and (e) TEM image of the P(FpP) aggregates with large magnification from the P(FpP) colloid (50 vol% THF content).

#### 4.3.3 Membrane structure behavior in response to THF content

We also explored how the membrane structure changed upon addition of THF. Addition of THF could change the polarity of the solvent around the P(FpP) nanovesicles from a polar media to an apolar media. In response to the change in the local polarity experienced by the membrane, the membrane structure of P(FpP) nanovesicles must be changed correspondingly. To verify the change in the membrane structure upon addition of THF, cyclic voltammetry (CV) experiments were conducted to check the Fe oxidation signal arising from the membranes of the P(FpP) vesicles. A previous report established that only the hydration of Fe could be detected by the CV experiments.<sup>149</sup> As shown in Figure 4.5a, without THF, no Fe oxidation signal was detected in the CV profile. Upon addition of THF, the oxidation signal appeared and the  $d_{\text{Fe-Fe}}$  became larger which indicated that the Fe element was hydrated on the surface of the membranes and became detectable by CV. By increasing the THF content to the 50 vol%, the Fe oxidation signal was still observed in the CV profile shown in Figure 4.5b. The behavior of Fe in the membranes induced by addition of THF could be further probed from the zeta potential profiles. As shown in Figure 4.5c, addition of THF to the 50 vol% into the P(FpP) colloid dispersion decreased the zeta potential. This could be attributed to the hydrated  $\text{Fe}[\delta^+]$  which appeared on the membrane due to the increased solvation of the polymer chains and neutralized the negative surface charge of the P(FpP) nanovesicles which is consistent with the obtained CV results. Interestingly, for the samples with high THF contents (30, 40 and 50 vol%), the P(FpP) colloid is still stable even though the zeta potential is much lower than -30 mV. We hypothesized that the stability of the P(FpP)

nanovesicles with high THF content was due to the solubility of the hydrophobic moieties on the surface of the nanovesicles. To prove this hypothesis, we added acetonitrile instead of THF into the prepared P(FpP) nanovesicles because P(FpP) is soluble in THF but insoluble in acetonitrile (Figure 4.5d). After addition of acetonitrile into the prepared dispersion of P(FpP) nanovesicles, the P(FpP) nanovesicles became unstable in the 20 vol% acetonitrile sample with Figure 4.5e showing multiple peaks in its DLS profile and precipitates were immediately formed in the high acetonitrile contents dispersions (40 vol% and 50 vol% acetonitrile) as shown in Figure 4.5f. The above experiments indicated that the addition of THF could enhance the hydration of Fe, and in the higher THF contents (40 vol% - 50 vol%), the solubility of the hydrophobic moieties plays an important role in the stability of the P(FpP) vesicles.

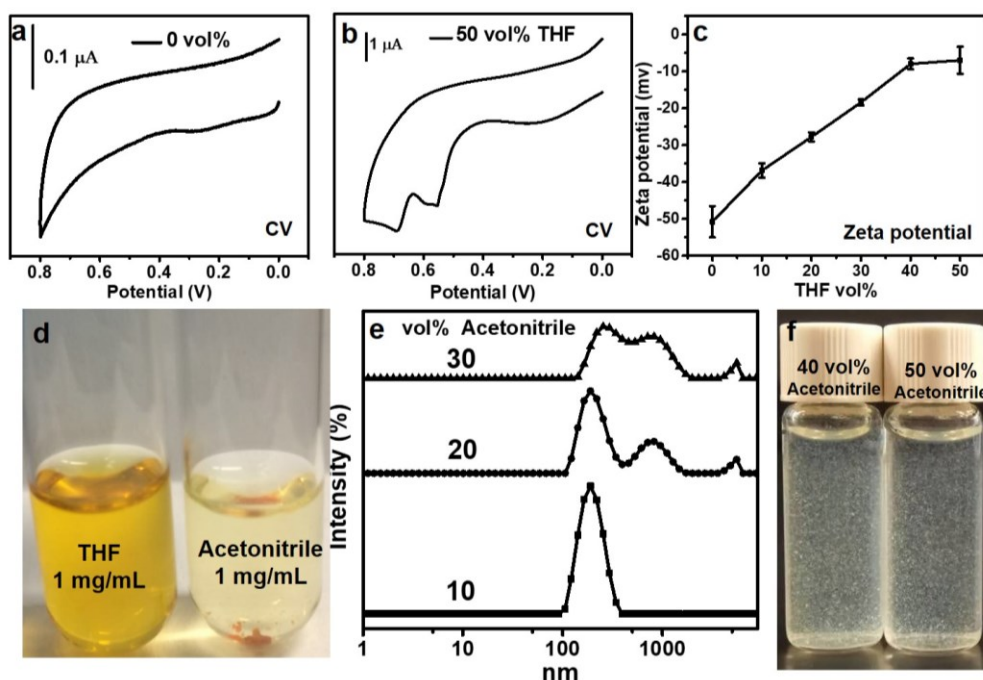


**Figure 4.5 CV results of P(FpP) colloids (0.1 mg/mL) by addition of varied amounts of THF added into the dispersion: (a) 0 vol% and (b) 50 vol%. c) Zeta potential of P(FpP)**

**colloid as a function of varied amounts of THF. d) Solubility of P(FpP) in THF and acetonitrile with same concentration (1 mg/mL). e) DLS profiles with different acetonitrile contents: 10 vol%, 20 vol% and 30 vol%. f) The photograph image of P(FpP) colloids with high content of acetonitrile: 40 vol% and 50 vol%.**

#### **4.3.4 Swelling behavior of FpC<sub>6</sub>Pyrene bilayer vesicles**

Previous reports have shown that the metal carbonyl molecule FpC<sub>6</sub>Pyrene could self-assemble into nanovesicles in water as shown in Figure 4.6a.<sup>148,150</sup> The nanovesicles have a bilayer membrane structure.<sup>150</sup> Here we compare the swelling behaviors between P(FpP) vesicles and FpC<sub>6</sub>Pyrene bilayer vesicles. By addition of THF, FpC<sub>6</sub>Pyrene nanovesicles with a bilayer membrane structure exhibited different swelling behaviors compared to the P(FpP) nanovesicles. As shown in Figure 4.6a, the size of the FpC<sub>6</sub>Pyrene nanovesicles increased to *ca.* 350 nm upon addition of THF to 10 vol%. Further addition of THF to 20 vol% resulted in no significant size change. Meanwhile, FpC<sub>6</sub>Pyrene nanovesicles showed a large size distribution as confirmed by the large PDI value (0.23) shown in Figure 4.6b. When the THF content increased to 30 vol%, the FpC<sub>6</sub>Pyrene colloid became unstable and large aggregates were formed. Moreover, precipitates could be observed in the dispersion (Figure 4.6a). Interestingly, when the THF content increased to 40 vol% and 50 vol%, the FpC<sub>6</sub>Pyrene dispersion became transparent unlike the original FpC<sub>6</sub>Pyrene colloid as shown in Figure 4.6a. This phenomenon indicated that the formed nanovesicles may be soluble in the 40 vol% THF and 50 vol% THF samples where there was no signal in DLS profiles and precipitates appeared in the 30 vol% THF colloid illustrated in the Figure 4.6c. Comparing the FpC<sub>6</sub>Pyrene nanovesicles with the P(FpP) nanovesicles,

we could see that the uncommon swelling behavior of P(FpP) nanovesicles could be mainly attributed to the nonbilayer membrane structure of the P(FpP) nanovesicles.

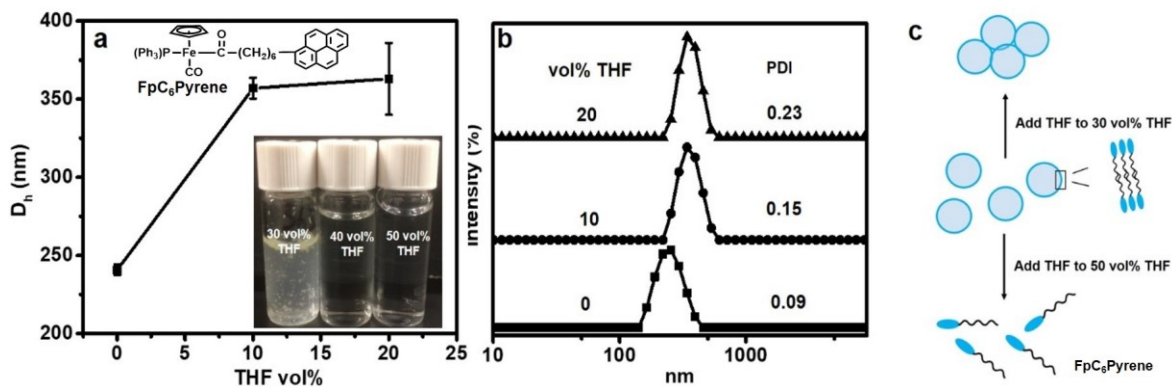


**Figure 4.6 a)  $D_h$  change of FpC<sub>6</sub>Pyrene colloids with low THF contents (0~30 vol%).**

**The inset image is the solution behavior of FpC<sub>6</sub>Pyrene colloids with higher THF**

**contents (30 vol%~ 50 vol%) b) DLS profiles of FpC<sub>6</sub>Pyrene colloid below 30 vol%**

**THF/water mixed solvents. c) Schematic presentation of FpC<sub>6</sub>Pyrene nanovesicles by**

**addition of different amounts of THF.**

#### 4.4 Conclusions

Hydrophobic homopolymer P(FpP) could self-assemble into nanovesicles in aqueous solutions. The formed nanovesicles had different membranes whose structure was different from that of the traditional membrane bilayers. The membrane of P(FpP) nanovesicles was formed by the stacking of the homopolymer chains based on simulation results. This unique membrane structure determined the properties of P(FpP) nanovesicles with a particular swelling behavior in response to THF content. The formed nanovesicles were stable and uniform for a variety of THF contents. This is different from



traditional vesicles self-assembled from amphiphilic molecules or block copolymers.<sup>148</sup> This could provide an opportunity to mimic the hollow structures self-assembled from proteins in cytometric chemistry and investigate the unique properties that amphiphilic bilayer vesicles do not have.

## Chapter 5 The Effect of Solution Condition on the Driving Force for Self-Assembly of a Pyrene Molecule

FpC<sub>6</sub>Pyrene is soluble in DMSO and THF, but insoluble in water, methanol and ethanol. The hydrophobic force drives the molecules to assemble into vesicles in THF/water mixtures. The  $\pi$ - $\pi$  interactions between the pyrene groups subsequently occurred within the vesicular membrane. The assembly, however, is driven by the  $\pi$ - $\pi$  interactions in DMSO/water (water content: 40-80 vol%) into membranes, which is attributed to the relatively higher degree of de-solvation ( $\delta$ ) of pyrene in DMSO. Further increase in  $\delta$  (90 vol% water/DMSO) suppresses the  $\pi$ - $\pi$  interactions and spherical particles are formed. On the other hand, the supersaturated solutions were prepared via a cycle of heating and cooling of FpC<sub>6</sub>Pyrene in methanol or ethanol. FpC<sub>6</sub>Pyrene aggregates into particles without the  $\pi$ - $\pi$  interactions in the solutions with a lower supersaturation  $\sigma$ . In contrast, a higher  $\sigma$  induces  $\pi$ - $\pi$  interactions, which drives the assembly into nanotapes. The  $\pi$ - $\pi$  interactions in response to solution conditions can be adjusted as a driving force to produce various nanostructures assembled from a same aromatic molecule.

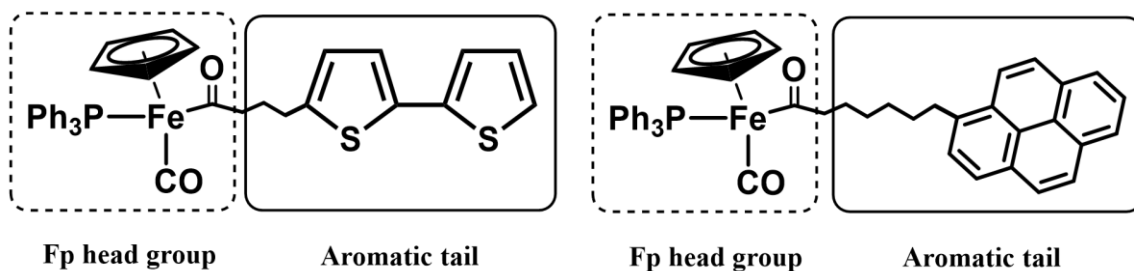
## 5.1 Introduction

Intermolecular interactions between  $\pi$ -conjugated molecules, widely used for functional or structure-defined assemblies,<sup>151-160</sup> are far from understood.<sup>161-165</sup> As aromatic interactions are usually induced by the de-solvation of planar molecules, it is debated whether  $\pi$ - $\pi$  interactions<sup>166-168</sup> result in or are a consequence from assembled nanostructure.<sup>161-162,165,169</sup> This question can be better discussed if the occurrence of  $\pi$ - $\pi$  interactions and the structures of the assemblies can be adjusted by the de-solvation conditions. Such research is rarely reported because  $\pi$ - $\pi$  interactions in many systems are complicated by other forces and not sensitive enough to solution conditions for the study.<sup>170</sup>

We have discovered that  $\text{Fe}(\text{CO})_2$  (Fp) hydrophobic derivatives are able to self-assemble in water into aqueous colloids.<sup>79,171-173</sup> For example,  $[\text{Fe}(\text{CO})(\text{Cp})(\text{PPh}_3)]$  ( $\text{FpC}_6$ ) assembled in water into a metal carbonyl vesicle (MCsome) with the alkyl groups hydrophobically associated into a bilayer wall and the carbonyl groups interacting with water. The water-carbonyl interaction (WCI) is a weak force,<sup>174-176</sup> so it is expected that the assembling behavior may be sensitive to the association of the hydrophobic tails. Aromatic groups tethered to Fp derivatives will, therefore, constitute ideal model systems for the investigation on the role of  $\pi$ - $\pi$  interactions in the assembly of hydrophobic Fp aromatic derivatives.

A bithiophene tethered Fp derivative (Fp-bithiophene) (Scheme 5.1) self-assembled in water into a metal carbonyl vesicle (MCsome) with the aromatic group confined within the vesicular wall without  $\pi$ - $\pi$  interactions. The resultant MCsome exhibited the aggregation-induced emission (AIE).<sup>177</sup> As the degree of de-solvation ( $\delta$ ) of aromatic groups was considered as a factor influencing the  $\pi$ - $\pi$  interactions,<sup>178-179</sup> we examined the assembly of Fp-bithiophene in various solvent mixtures, including THF/water and DMSO/water. The MCsome without  $\pi$ - $\pi$  interactions was exclusively formed,<sup>177</sup> which

is in line with the inherently weak  $\pi$ - $\pi$  interactions of bithiophene groups. Pyrene is a large polycyclic aromatic hydrocarbon (PAH), which generates a relatively stronger aromatic interaction. The  $\pi$ - $\pi$  interactions of the pyrene groups have been reported in the assembling of a pyrene trimer in aqueous media.<sup>180-181</sup> It is therefore expected that the self-assembly of a pyrene tethered Fp derivative (FpC<sub>6</sub>Pyrene) (Scheme 5.1) may involve  $\pi$ - $\pi$  interactions and be influenced by solution conditions. The solution conditions can be varied using different solvent systems. FpC<sub>6</sub>Pyrene is soluble in DMSO and THF but insoluble in water. The solubility of the molecules decreases in the mixed solvents of DMSO/water and THF/water with increased water content. The  $\delta$  for pyrene group is larger in DMSO/water than in THF/water mixture with a same water content, because the experimental mole fraction solubility,  $X_s^{\text{sat}}$ , for pyrene in DMSO and THF equals 0.01694 and 0.1402, respectively.<sup>182</sup> On the other hand, FpC<sub>6</sub>Pyrene is insoluble in methanol or ethanol at 23 °C, but soluble at 60 °C, Thus the supersaturated solutions with various degrees of supersaturation ( $\sigma$ ) can be prepared via a cycle of heating and cooling of FpC<sub>6</sub>Pyrene in these two solvents. The effect of  $\delta$  and  $\sigma$  on the  $\pi$ - $\pi$  interactions can, therefore, be revealed by studying the assembling behavior in response to the solution conditions.



**Scheme 5.1. The chemical structure for Fp-bithiophene (left) and FpC<sub>6</sub>Pyrene (right).**

Herein, we report the effect of solution conditions on the  $\pi$ - $\pi$  interactions between the pyrene groups and the role of this aromatic interaction in the self-assembly of FpC<sub>6</sub>Pyrene. UV-Vis and fluorescence

spectroscopies were used to probe the  $\pi$ - $\pi$  interactions while dynamic light scattering (DLS) and imaging techniques, including TEM, SEM, and AFM, were used to investigate the assembly behavior under various solution conditions as listed in Table 5.1. The experimental results support that the  $\pi$ - $\pi$  interactions is required for the assembling depending on  $\delta$  or  $\sigma$ . When the  $\delta$  or  $\sigma$  parameter favor for the  $\pi$ - $\pi$  interactions, it is a driving force directing the assembly into layered structures. On the other hand, if  $\delta$  or  $\sigma$  is not in favor of the  $\pi$ - $\pi$  interactions, vesicles or particles are formed driven by the hydrophobic interactions. The  $\pi$ - $\pi$  interactions occur within the vesicular wall via the confined packing of the pyrene groups, whereas the particles result from the absence of the  $\pi$ - $\pi$  interactions.

## 5.2 Experimental Section

### 5.2.1 Materials

1-(6-Bromohexyl) pyrene was synthesized according to the procedures reported in the literature.<sup>183</sup> Dichloromethane (DCM) was distilled with CaH<sub>2</sub>. Tetrahydrofuran (THF) and diethyl ether were distilled from Na/benzophenone prior to use. All reactions were carried out under an inert atmosphere of N<sub>2</sub>. The other chemicals are commercially available and used directly.

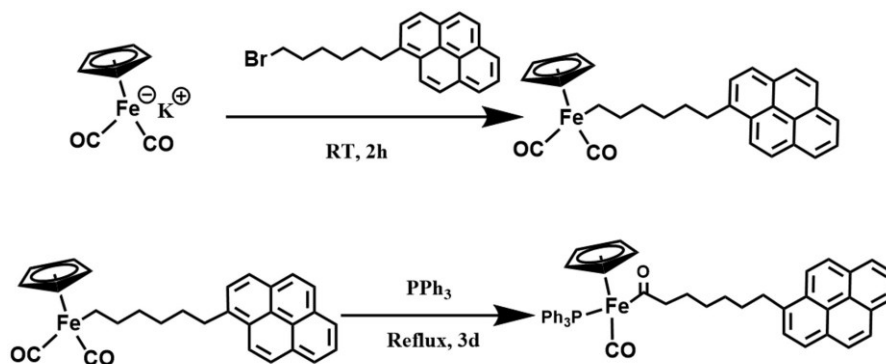
### 5.2.2 Measurements and Characterization.

Dynamic light scattering (DLS) analysis was performed at 25 °C using a Zetasizer Nano Series (Nano-S90, Malvern Instruments) with a laser wavelength of  $\lambda = 633$  nm at a fixed angle of 90°. <sup>1</sup>H and <sup>31</sup>P NMR spectra were recorded at room temperature using a Bruker-300 (300 MHz) spectrometer. Transmission electron microscopy (TEM) experiments were performed using an electron microscopy (Philips CM10) with an acceleration voltage of 60 KV. Cryo-TEM measurements were carried out on

a Cryo Tecnai G2 F20 microscope with the acceleration voltage of 200 KV. SEM measurements were carried on a JSM-7800F scanning electron microscope. Atomic force microscopy (AFM) experiments were conducted using a Nanoscope MultiMode<sup>TM</sup>. A conical AFM tip with a spring constant of 40 N m<sup>-1</sup>, a resonance frequency of 300 KHz and a tip radius of 8 nm were used. The sample was prepared by transferring one drop of the FpC<sub>6</sub>Pyrene suspension onto a freshly cleaved mica substrate and then left to dry overnight before scanning. The UV–Vis spectra were acquired using a UV–Vis spectrometer (Agilent 8453A). Fluorescence emission was monitored using a Varian Eclipse fluorometer and the solutions were excited at 330 nm.

### 5.2.3 Synthesis of FpC<sub>6</sub>Pyrene.

The synthesis of FpC<sub>6</sub>Pyrene was based on the protocol shown in Scheme 5.2. A solution of 1-(6-bromohexyl) pyrene (3.8 g, 10.4 mmol) in THF (20 mL) was added dropwise to a solution of FpK (2.4 g, 11.1 mmol) in THF (80 mL) at 0 °C. The mixture was stirred at 0 °C for 30 min and then at room temperature for 2 h. Triphenylphosphine (2.9 g, 11.1 mmol) was added in one pot and then the reaction mixture was refluxed for 72 h. After cooling to room temperature, excess FpK and KBr were removed by filtration on a short silica column using THF eluent. The filtrate was concentrated in vacuo yielding a crude product that was washed with hexane and diethyl ether. The resultant product appeared as a yellow powder (5.6 g, 79%). <sup>1</sup>H NMR (300 MHz, CDCl<sub>3</sub>): δ (ppm) 8.34-7.75 (m, 9H), 7.56-7.08 (m, 15H), 4.38 (s, 5H), 3.26 (t, 2H), 2.93-2.44 (m, 2H), 1.75 (t, 2H), 1.48-0.94 (m, 6H). <sup>31</sup>P NMR (300 MHz, CDCl<sub>3</sub>): δ (ppm) 77.97.



**Scheme 5.2 Synthetic scheme for FpC<sub>6</sub>Pyrene**

#### 5.2.4 Preparation of FpC<sub>6</sub>Pyrene solution in DMSO/water or THF/water.

FpC<sub>6</sub>Pyrene was dissolved in DMSO or THF (X mL, X ranges from 1 to 9). Various amounts of water (10 - X mL) was then added to prepare the solution with the same concentration of FpC<sub>6</sub>Pyrene in the mixed solvents.

#### 5.2.5 Preparation of FpC<sub>6</sub>Pyrene solution in methanol or ethanol.

FpC<sub>6</sub>Pyrene was mixed with methanol or ethanol and then heated to 60 °C for a few minutes. The solutions were then cooled to 23 °C.

### 5.3 Results and discussion

#### 5.3.1 Self-assembly of FpC<sub>6</sub>Pyrene in DMSO/water

FpC<sub>6</sub>Pyrene was prepared by reacting 1-(6-bromohexyl) pyrene with potassium cyclopentadienyldicarbonyliron (FpK), followed by a migration insertion reaction (MIR) in the presence of triphenylphosphine (Scheme 5.2, Figure 8.11).<sup>72,171,177</sup> The self-assembly was first

performed by injecting water into the DMSO solution of FpC<sub>6</sub>Pyrene, which resulted in the same concentrated solutions with various volume ratios of the two solvents.

**Table 5.1. The self-assembling behavior of FpC<sub>6</sub>Pyrene in response to solution conditions.**

| <b>Solution systems</b>                | <b>Aromatic interaction /Driving force</b> | <b>Morphology</b> |
|--|--|-------------------|
| DMSO/water (40-80 vol%)                | On/yes                                     | Membranes         |
| DMSO/water (90 vol%)                   | Off/no                                     | Particles         |
| THF/water (70-90 vol%)                 | On/no                                      | Vesicles          |
| Methanol, ethanol (lower $\sigma^*$ )  | Off/no                                     | Particles         |
| Methanol, ethanol (higher $\sigma^*$ ) | On/yes                                     | Nano-tapes        |

\*  $\sigma$  represents the degree of supersaturation of the solution  
The contents in the table show the contents of organic solvents such as DMSO and THF.

The UV-Vis spectrum for the DMSO solution of FpC<sub>6</sub>Pyrene shows two absorptions at the wavelengths of 330 nm and 346 nm due to the second electronic transitions of the pyrene group (Figure 5.1a).<sup>184</sup> These two absorptions appear at the same wavelengths for the systems with lower water contents (10-30 vol%), whereas a redshift, due to the J-aggregation of pyrene units,<sup>180-181</sup> occurs when the water content ranges from 40 to 80 vol% (Figure 5.1a). It suggests that a certain level of  $\delta$  resulting from higher water contents is required to induce aromatic interactions. However, there is no redshift of the peaks for the system with 90 vol% water (Figure 5.1a), suggesting that the  $\pi$ - $\pi$  interactions is suppressed when the  $\delta$  is too strong. By reducing the water content from 90 vol% to 80 vol%, the redshift appeared. Apparently, the level of  $\delta$  should be high enough (> 30 vol% water) to induce the  $\pi$ -



$\pi$  interactions, but lower than a maximum value (< 90 vol% water) to ensure the mobility of molecules for parallel packing.<sup>165</sup>

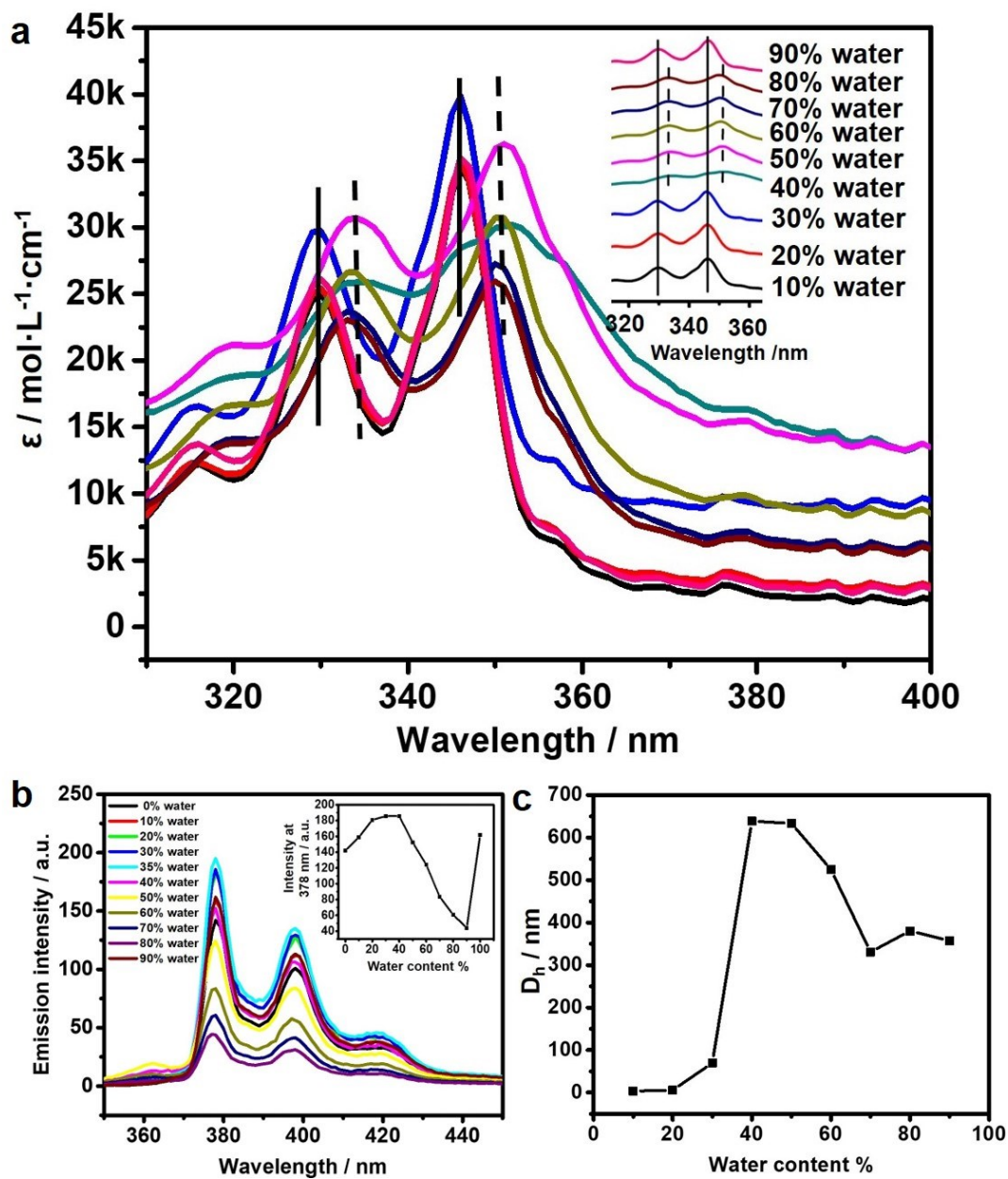
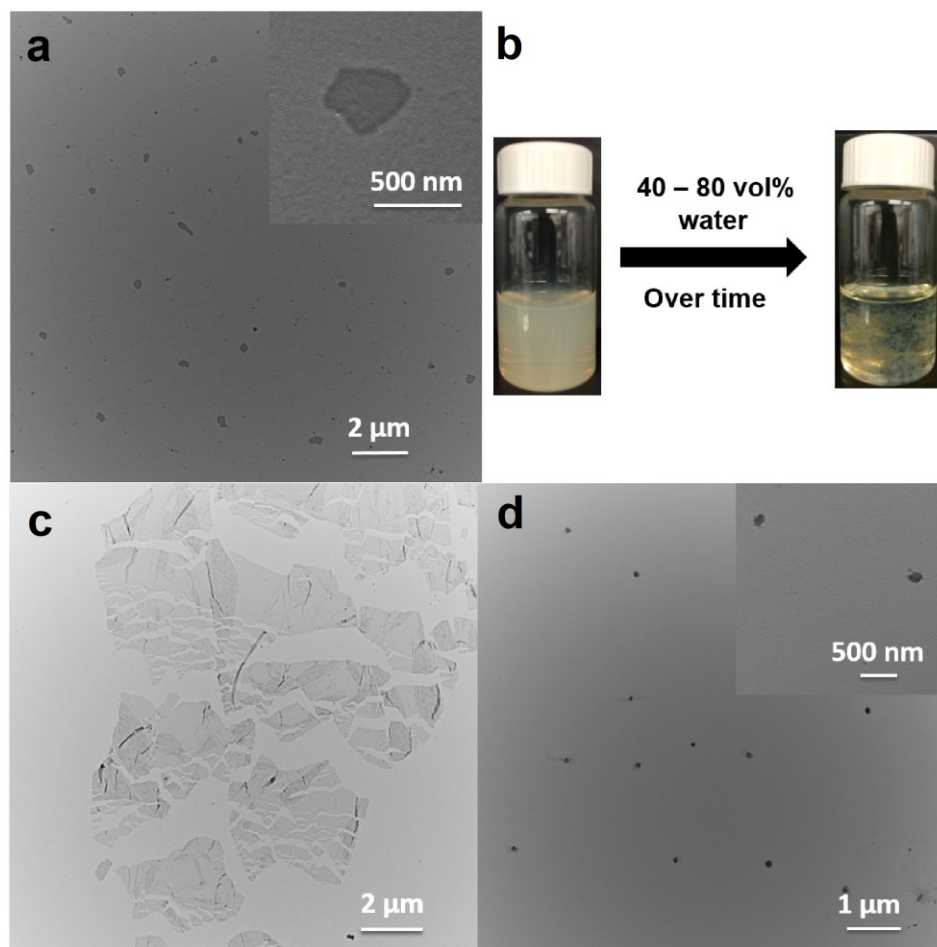


Figure 5.1. a) UV/Vis absorption and b) fluorescent spectra, and c) hydrodynamic diameter ( $D_h$ ) for the solution of FpC<sub>6</sub>Pyrene in DMSO/water ( $1.4 \times 10^{-4}$  M) with various water contents.

Figure 5.1b showed the fluorescence spectra for the FpC<sub>6</sub>Pyrene solutions with various water content. The main observation was that no excimer fluorescence was observed despite the strong aggregation of the pyrene labels probed by absorption measurements. Contrary to most dyes, pyrene aggregation results in excimer formation.<sup>185</sup> This implied that pyrene aggregation provides a photophysical pathway for emission, similar to the AIE phenomenon.<sup>186</sup> The lack of excimer emission was due to quenching by electron transfer between an excited pyrene and the iron in the head group of FpC<sub>6</sub>Pyrene. The residual fluorescence observed in Figure 5.1b was probably due to a small fraction of cleaved pyrene label that was free in solution. Since water has a much lower solubility for oxygen, a known quencher of pyrene fluorescence, addition of water to the DMSO solution reduced the oxygen concentration which increased the quantum yield of free pyrene in the solution. At a water content of 30 vol%, the formation of FpC<sub>6</sub>Pyrene aggregates generated hydrophobic microdomains that drove the association of the free pyrenes which were then quenched by electron transfer with the Fe present in the head groups. The formation of FpC<sub>6</sub>Pyrene aggregates resulted in the incorporation of the free pyrenes into the FpC<sub>6</sub>Pyrene aggregates and the quenching of their fluorescence which became more prominent as more water was added to the mixtures. The absence of pyrene aggregation observed in water based on the absorption spectra shown in Figure 5.1a agreed with the increase in fluorescence observed in Figure 5.1b, although its cause is not fully understood at the present time.

As shown in Figure 5.1c, the DLS analysis indicated that FpC<sub>6</sub>Pyrene molecules did not aggregate until the water content was larger than 30 vol%. The aggregates with hydrodynamic diameters ( $D_h$ ) of a few hundreds of nanometers were formed in the solution with water contents in the range between 40-80 vol% (Figure 8.13). These aggregates are nano-plates as displayed in the TEM images (Figures 5.2a and 8.14). These plates grew over time and eventually evolved into cotton-like assemblies floating

in the solution (Figures 5.2b and 8.15). The cotton-like solids, as examined using TEM (Figures 5.2c and 8.15), were micro-sized thin membranes. The  $\pi$ - $\pi$  interactions (Figure 5.1a, b) were responsible for the formation of the layered structure. When the water content increased to 90 vol%, the  $\pi$ - $\pi$  interactions were suppressed (Figures 5.1a, b). And particles ( $D_h \approx ca. 100$  nm) were obtained (Figure 5.2d). When the water content was adjusted from 90 vol% to 40-80 vol% to decrease  $\delta$ , the  $\pi$ - $\pi$  interactions was turned on and the particles were converted to membranes. The  $\pi$ - $\pi$  interactions is therefore induced by  $\delta$  in the systems (40-80 vol% water), which drives the assembly into the layered structure.



**Figure 5.2. a) TEM image for the aggregates assembled from FpC<sub>6</sub>Pyrene in DMSO/water solutions (40 vol% water), b) photograph for the solutions of FpC<sub>6</sub>Pyrene in DMSO/water, c) TEM images for the cotton-like assemblies separated from the solution of DMSO/water (40 vol% water), d) TEM images for the nanoparticles formed in the solution containing 90 vol% water. (The solution concentration is  $1.4 \times 10^{-4}$  M)**

FpC<sub>6</sub>Pyrene molecules in THF/water did not show  $\pi$ - $\pi$  interaction up to a water content of 60 vol% as indicated by the absence of the shifts in the UV-Vis absorption (Figure 5.3a) spectra. DLS analysis,

however, suggested that the molecules started to aggregate at this water content (Figure 5.3c). The hydrophobic interaction is, therefore, responsible for the assembly. The solutions with water contents of 50 and 60% did not show any  $\pi$ - $\pi$  interactions even after aging for 5 days (Figure 8.16). Only when the water content was larger than 60 vol%, the red-shift in the UV-Vis spectra (Figure 5.3a) and the quenching (Figure 5.3b) of the emission observed, suggesting that the occurrence of the  $\pi$ - $\pi$  interactions is a consequence of the aggregation driven by hydrophobic interaction. The increase in the intensity of emission as shown in Figure 5.3b before the assembling at 60 vol% water is attributed to a decrease in the solubility of oxygen, a known quencher of the fluorescence of pyrene in water.

### 5.3.2 The self-assembly behavior of FpC<sub>6</sub>Pyrene in THF/water

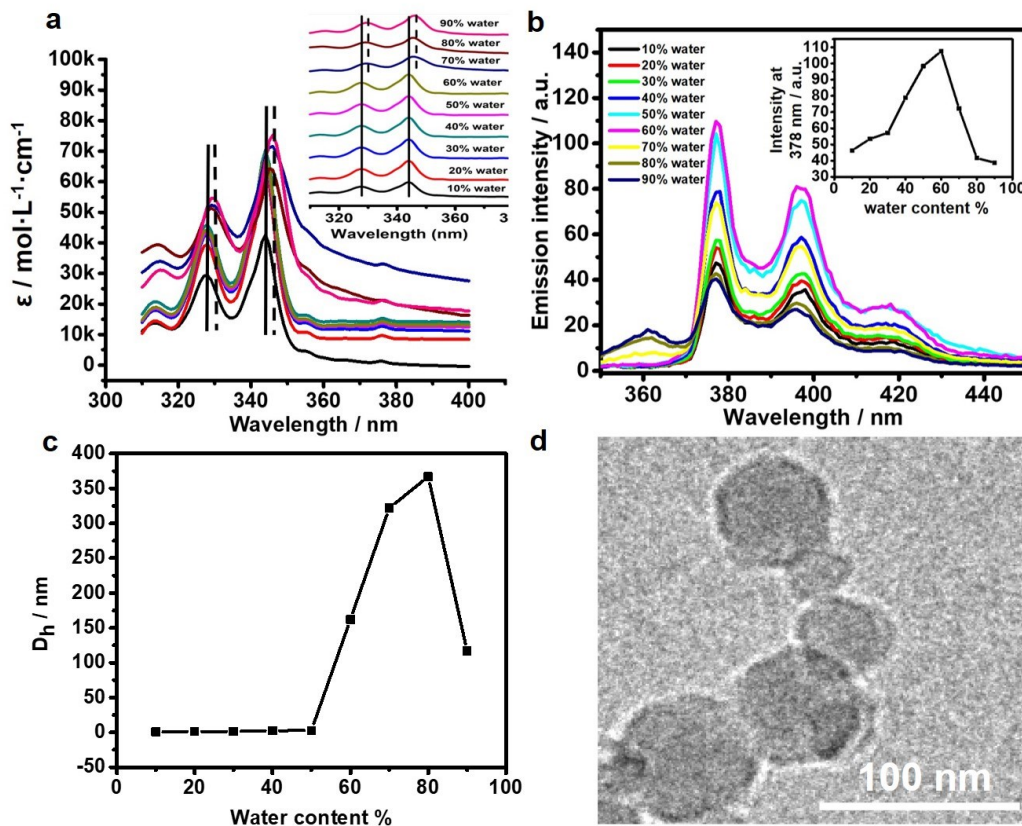


**Figure 5.3 a) UV/Vis, b) fluorescent spectra, and c) the hydrodynamic diameters ( $D_h$ ) for the solution of FpC<sub>6</sub>Pyrene in THF/water ( $1.4 \times 10^{-4}$  M) with various water contents, d) cryo-TEM image for the FpC<sub>6</sub>Pyrene assemblies in THF/water (90 vol% water).**

The assemblies observed in in THF/water (90 vol% water) mixture as indicated by the SEM image was larger than *ca.* 500 nm (Figure 8.17), but the DLS analysis suggested that the  $D_h$  equaled 105 nm with PDI of 0.162. This difference in size was attributed to the drying effect, consequently, the cryo-TEM experiments were performed. As shown in the cryo-TEM image (Figure 5.3d), the particles have

a diameter of *ca.* 80 nm and a relatively dark periphery, suggesting that vesicles are formed. This morphology is similar to the MCsomes assembled from Fp-bithiophene.<sup>177</sup> The difference is that the FpC<sub>6</sub>Pyrene vesicles are subjected to the  $\pi$ - $\pi$  interactions within the vesicular wall (Figure 5.3b, c). The strength of this aromatic interaction apparently is relatively weak and exerts no impact on the assembling nanostructure. As the  $\pi$ - $\pi$  interactions occur after the aggregation was initiated. It was not the driving force for the assembly of FpC<sub>6</sub>Pyrene in THF/water mixture.

### 5.3.3 The effect of $\sigma$ on the aromatic interactions

$\sigma$  is another factor influencing aromatic interactions.<sup>187</sup> FpC<sub>6</sub>Pyrene is not soluble in methanol and ethanol at 23 °C, but soluble at an elevated temperature. So, after a cycle of heating at 60 °C and cooling to 23 °C, supersaturated solutions were prepared with various  $\sigma$ . The freshly prepared solutions of FpC<sub>6</sub>Pyrene ( $2.5 \times 10^{-4}$  M) in either methanol or ethanol barely scattered light as indicated by DLS analysis, suggesting no aggregation occurred right after the preparation. The methanol solution generated precipitates after a few days, whereas colloids were formed after aging the ethanol solution for a week. TEM images indicate that both the precipitates and colloids were spherical particles with diameters of *ca.* 150 nm (Figures 5.4a, 8.18 and 8.19a). UV-vis analysis of the freshly prepared ethanol solutions and corresponding aged colloids indicates that the colloids showed no  $\pi$ - $\pi$  interactions (Figure 8.20). This behavior can be explained by the strong  $\delta$  in the supersaturated solutions. To test this hypothesis, we prepared a solution in methanol/DMSO (10 vol% DMSO) mixture via a cycle of heating and cooling ( $2.5 \times 10^{-4}$  M). The lower  $\delta$  due to the presence of DMSO allowed the  $\pi$ - $\pi$  interactions to drive the assembly into nano-tapes (Figure 5.4b).



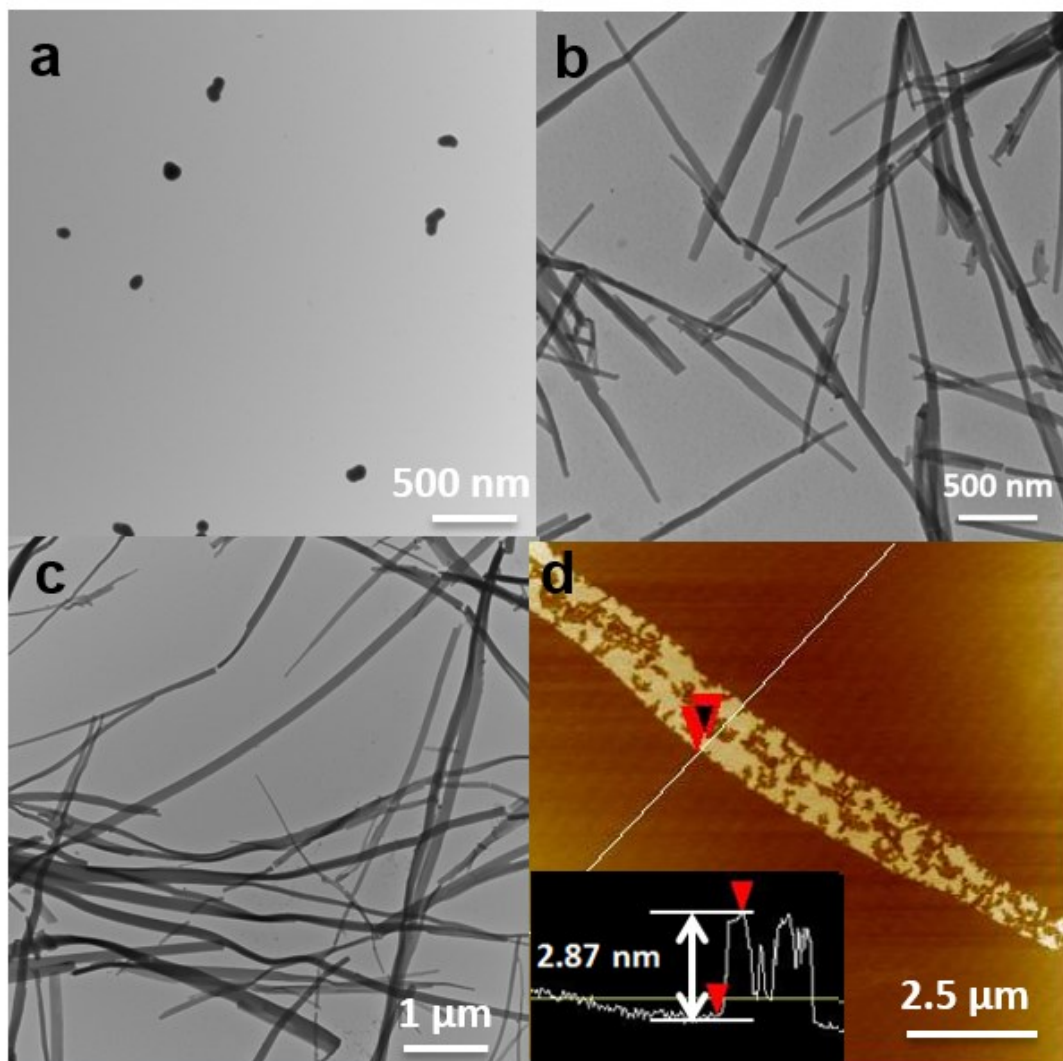


**Figure 5.4** TEM images for a) the aggregates formed in FpC<sub>6</sub>Pyrene solution in ethanol with a lower  $\sigma$  ( $1 \times 10^{-4}$  M), b) in methanol/DMSO (10 vol% DMSO), c) TEM image and (d) AFM image for the aggregates assembled from the solution of FpC<sub>6</sub>Pyrene in methanol with a higher  $\sigma$  ( $5.5 \times 10^{-4}$  M). All the solutions were prepared via a cycle of heating and cooling.

Although the large  $\delta$  in the supersaturated solutions does not favor  $\pi$ - $\pi$  interactions as discussed above, a higher  $\sigma$  might force a compact packing of FpC<sub>6</sub>Pyrene via a parallel arrangement of the pyrene groups, which subsequently induced the  $\pi$ - $\pi$  interactions. We, therefore, prepared the solution in methanol ( $5.5 \times 10^{-4}$  M) and ethanol ( $1.1 \times 10^{-3}$ ) with a relatively higher  $\sigma$ . The solutions were clear right after cooling, but gradually turned cloudy and eventually, cotton-like aggregates appeared after a few hours at 23 °C. The TEM image of the aggregates, as illustrated in Figures 5.4c and 8.19b, showed a tape-like morphology with widths of *ca.* 200~500 nm. The height of the nano-tape as indicated in the AFM image was approximately 2.9 nm (Figure 5.4d) that was close to twice the length of FpC<sub>6</sub>Pyrene. It suggested that the nano-tape, like the wall for MCsomes,<sup>177</sup> had a double-layered structure. The height profile indicated that there were holes in the tapes (Figure 5.4d), whereas the TEM image with a larger magnification (Figure 8.21) indicated a smooth surface. The holes may, therefore, be generated during the preparation or measurement of the AFM samples. It also suggests that the intermolecular interactions, which led to the formation of the thin tape, were weak.

## 5.4 Conclusions

In summary, the solution condition for the de-solvation of aromatic groups is a parameter determining whether  $\pi$ - $\pi$  interactions can act as a driving force or not. When the condition in  $\delta$  and  $\sigma$  favors the  $\pi$ - $\pi$  interactions, this interaction drives the assembly of FpC<sub>6</sub>Pyrene into layered structures with the parallel packing of the pyrene groups. On the other hand, hydrophobic interaction resulting from the de-solvation drives the assembly.  $\pi$ - $\pi$  interactions may subsequently occur depending on the assembled structure. This  $\pi$ - $\pi$  interaction responds to solution conditions and results in various assemblies from the same molecule. Like the effect of solvents on organic synthesis,<sup>21</sup> the de-solvation condition is a

parameter adjusting the role of  $\pi$ - $\pi$  interactions in self-assembly. This knowledge is fundamentally important in the context of precise and sophisticated supramolecular synthesis.<sup>158,22</sup>

## Chapter 6 Hydrophobic Effect for Hierarchical Self-Assembly

The hydrophobic Effect (HE), including Hydrophobic Hydration and Interaction (HH and HI), is crucial in protein chemistry. Its role in the organization of molecules in water, however, remains elusive and difficult to investigate without appropriate model systems. Metal Carbonyl vesicles (MCsomes), assembled from hydrophobic  $FpC_6X$  ( $Fp$  head =  $(PPh_3)(Cp)Fe(CO)(CO^-)$ ;  $C_6X$  = hydrocarbon tail), are dispersible in water via HH of the  $Fp$  heads. By taking advantage of the redox activity and the fluorescence quenching ability of hydrated Fe elements, we examined the dependence of the HH on solution conditions as well as on the HI of  $C_6X$  tails within the vesicular wall. A subtle variation in the HH and HI substantially varied the solution behavior of the MCsomes for hierarchical structural evolutions. This scrutiny resolved a long-standing challenge to explain the role of HE in self-assembly at the molecular level, an imperative step to understand biological systems.

## 6.1 Introduction

The hydrophobic Effect (HE) rationalizes the solution behavior of many biological assemblies<sup>19,188-191</sup> including dilution-induced refolding of denatured proteins,<sup>192-193</sup> stabilization of proteins by hydrophobic interaction (HI)<sup>194</sup> and protein-protein interactions depending on the hydrophobic hydration (HH) of metal center in metalloproteins.<sup>195-196</sup> The role of the HE in this observed behavior, however, cannot be explained at the molecular level. Although the HE, being sensitive to subtle changes in solution conditions and chemical structures,<sup>20,197-198</sup> is being studied via simulation and characterization of hydrated water,<sup>20,190,199-201</sup> the solution behavior of solutes in response to the HE (including HH and HI) is difficult to study without appropriate model systems.<sup>19,188,197,202</sup> Amphiphiles are commonly used for aqueous assemblies,<sup>200,203</sup> in which the role of the HE is concealed by a strong affinity of water with water-soluble heads. Systems with colloidal behavior sensitive to the HE, therefore, are desirable to enable this investigation.

We have reported the aqueous self-assembly of hydrophobic molecules,  $\text{FpC}_6\text{X}$  (Fp head =  $(\text{PPh}_3)(\text{Cp})\text{Fe}(\text{CO})(\text{CO}-)$ ;  $\text{C}_6\text{X}$  = hydrocarbon tail) (Figure 6.1).<sup>73,150</sup>  $\text{FpC}_6\text{X}$  molecules are neither surface active nor amphiphilic,<sup>81</sup> but can assemble in water into Metal Carbonyl bi-layer vesicles (MCsome) (Figure 6.1) driven by HI of the tails.<sup>73,75</sup> HH of the hydrophobic Fp heads<sup>81</sup> is responsible for the dispersion of the MCsomes in water.<sup>73,75</sup> The zeta potential ( $\zeta$ ) of MCsomes is negative due to the presence of water carbonyl interactions (WCIs).<sup>73,75,173</sup> It suggests that the carbonyl oxygen is partially negatively charged ( $\text{O}[\delta^-]$ ) with its HH level relatively higher than the partially positively charged Fe ( $\text{Fe}[\delta^+]$ ).  $\text{Fe}[\delta^+]$  results from the back  $\pi$  bonding from Fe to CO groups<sup>204</sup> (Figure 6.1). The

solution behavior of MCsomes is expected to be sensitive to the HH of Fp heads and HI of the tails, which offers an ideal opportunity for the exploration of the HE on hierarchical self-assembly.

HH is higher for a same solute at a lower concentration, which is explained by the entropy term.<sup>19,205-206</sup> It is, therefore, possible to enhance the HH of Fe[ $\delta^+$ ] by dilution. The hydrated Fe[ $\delta^+$ ] can be probed using electrochemical<sup>149</sup> and fluorescence (FL) quenching experiments.<sup>207</sup> The HH of O[ $\delta^-$ ] by WCIs via hydrogen bonds<sup>199,208</sup> may be less dependent on concentrations but can be dehydrated by protonation. The  $\zeta$  of MCsomes reflects the relative HH level of Fe[ $\delta^+$ ] and O[ $\delta^-$ ], which is measurable. These features associated with the Fp head enable an investigation on the HH effect resulting from different solution conditions. Three MCsomes with the same Fp head, but various tails, were investigated to study the influence of the tail-tail interaction on the HH of the head (Figure 6.1). The consequent solution behavior of MCsomes was examined to explore the role of the HE in hierarchical self-assembly. In addition, this assembly, unlike many reported assemblies of solid nanoparticles,<sup>209-211</sup> is a platform to understand the structural evolution via vesicular fusion.<sup>32,212</sup>

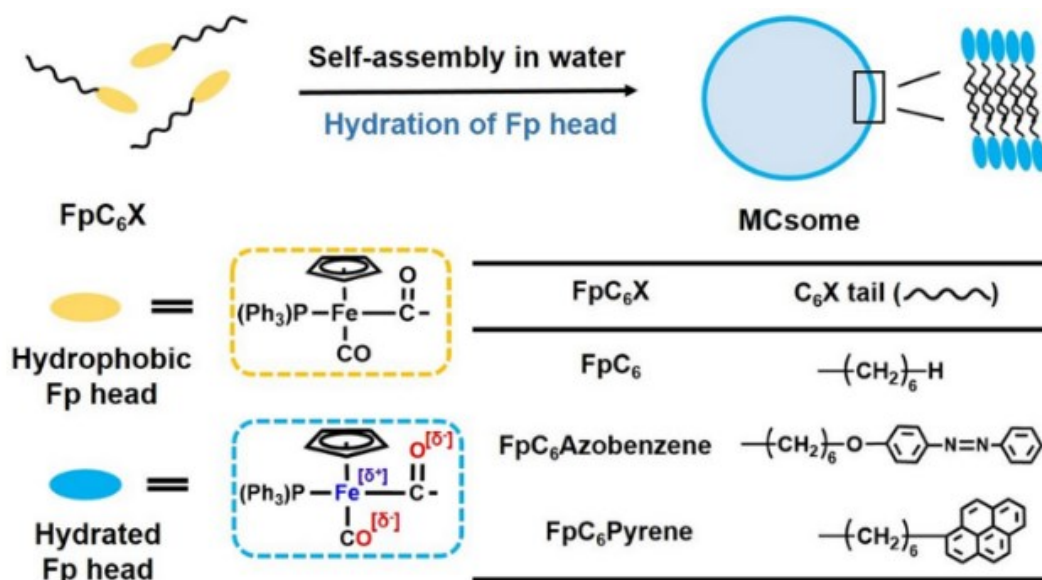


**Figure 6.1. Schematic illustration for MCsomes assembled from  $\text{FpC}_6\text{X}$  molecules in water.**

## 6.2 Experimental section

### 6.2.1 Materials and Methods

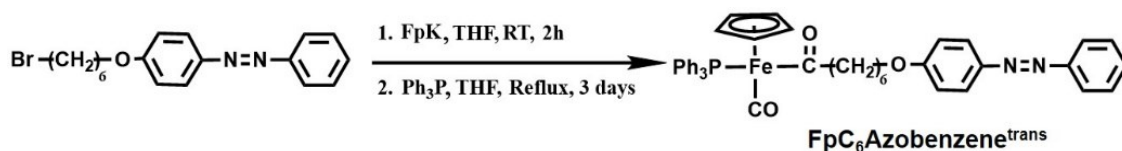
4-Phenylazophenol and 1,6-dibromohexane were obtained from Sigma-Aldrich. Potassium carbonate and triphenylphosphane were obtained from TCI Chemicals. Tetrahydrofuran (THF) was distilled from Na/benzophenone under  $\text{N}_2$  atmosphere prior to use. Other solvents or chemicals were commercially available and used directly.  $\text{FpC}_6$  and  $\text{FpC}_6\text{Pyrene}$  were synthesized based on the previous reports.<sup>73,150</sup>

$^1\text{H}$  and  $^{31}\text{P}$  NMR spectra were recorded at room temperature on a Bruker-300 (300 MHz) spectrometer. Mass spectrometry was performed using Thermo Scientific Q-Exactive Orbitrap. Acetonitrile was used as the carrier solvent. DLS analysis was performed on a Zetasizer Nano Series instrument (Nano-S90,

Malvern Instruments). Multi-angle SLS measurements were carried out on a Brookhaven Laser Light Scattering System equipped with a BI-200 SM goniometer. TEM (transition electron microscope) experiments were performed on an electron microscope (Philips CM10) with the acceleration voltage of 60 KV. EDX (Energy Dispersive X-Ray Spectroscopy) and EELS (Electron energy loss spectroscopy) analyses were performed on Jeol 2010F at Canadian Center for Electron Microscopy. SEM (scanning electron microscope) measurements were carried out on a JSM-7800F scanning electron microscope. Atomic force microscopy (AFM) experiments were carried out using a Nanoscope MultiMode™. The surface tension of pure water and the aqueous colloid dispersions with different concentrations were measured at 24 °C using a tensiometer Data Physics DCAT 21 system. The ATR-FTIR spectra were obtained with a Bruker Tensor 27 spectrophotometer with a germanium crystal Pike MIRacle™ ATR Attachment using Pike Technologies. Cyclic voltammetry (CV) experiments were carried out at 25 °C using a DY2000 Multi-Channel Potentiostat (Digi-Ivy Inc.) workstation with a scan rate of 50 mV s<sup>-1</sup> and Ag as a reference electrode. Before measurements, a KCl solution in water was added into the colloid dispersions and the final KCl concentration in the colloid was 0.1 mol/L. The UV-Vis spectra were obtained from a UV-Vis spectrometer (Agilent 8453A). Fluorescence emission spectra (FL) were carried out on a Varian Eclipse fluorometer. For the FL quenching experiments, the MCsomes were used as quenchers. A calcein solution (1.7 μM) in water (100 μL) was added into MCsomes solutions (1 mL) with concentrations varied from 14 to 140 μM. The solutions were excited at 490 nm and emitted fluorescence at 514 nm. F<sub>0</sub> and F refer to the emission intensity of calcein in the absence and presence of MCsomes. A Stern-Volmer plot was made by plotting F<sub>0</sub>/F against the concentration of MCsomes.



## 6.2.2 Synthesis of FpC<sub>6</sub>Azobenzene<sup>trans</sup>



### Scheme 6.1 Synthetic scheme for FpC<sub>6</sub>Azobenzene<sup>trans</sup>

6-Bromohexane-4-azobenzene and cyclopentadienyl dicarbonyliron potassium (FpK) were synthesized based on previous reports.<sup>97,213</sup> As shown in Scheme 6.1, 6-bromohexane-4-azobenzene (3.46 g, 0.01 mol) in dry THF was added dropwise under N<sub>2</sub> to a solution of freshly prepared FpK (4.32 g, 0.02 mmol) in dry THF (30 mL) cooled by an ice bath. After the addition, the solution was warmed to room temperature and stirred for 2 h. Then triphenylphosphine (5.24 g, 0.02 mmol) was added directly to the solution. The mixture was refluxed for 3 days under N<sub>2</sub> atmosphere and then cooled to room temperature. After removing salts by a short plug of silica gel, the solvent was removed under reduced pressure. The crude product was purified by chromatography (CH<sub>2</sub>Cl<sub>2</sub> as eluent) using a silica gel column and the orange phase was collected. After removing the solvents by using rotary evaporation, an orange solid was obtained in 55 % yield. <sup>1</sup>H NMR (CDCl<sub>3</sub>): δ 0.90-1.00 ppm (m, 2H, -CH<sub>2</sub>CH<sub>2</sub>CH<sub>2</sub>CH<sub>2</sub>O-), 1.20-1.35 ppm (m, 2H, -CH<sub>2</sub>CH<sub>2</sub>CH<sub>2</sub>CH<sub>2</sub>O-), 1.62-1.75 ppm (m, 2H, -CH<sub>2</sub>CH<sub>2</sub>CH<sub>2</sub>CH<sub>2</sub>O-), 2.60 ppm (s, 1H, COCH<sub>2</sub>), 2.80 ppm (s, 1H, COCH<sub>2</sub>), 3.93-4.04 ppm (t, 2H, CH<sub>2</sub>O), 4.35-4.43 ppm (s, 5H, C<sub>5</sub>H<sub>5</sub>), 6.93-7.01 ppm (d, 2H, aromatic), 7.19-7.28 ppm (m, 2H, aromatic), 7.27-7.39 ppm (m, 8H, aromatic), 7.42-7.54 ppm (m, 8H, aromatic), 7.81-7.93 ppm (m, 4H, aromatic). <sup>31</sup>P NMR (CDCl<sub>3</sub>): 77.9 ppm. ESI-MS [M+H<sup>+</sup>]: calcd for C<sub>43</sub>H<sub>42</sub>FeN<sub>2</sub>O<sub>3</sub>P 721.2274; found 721.2277.

### 6.2.3 Preparation of FpC<sub>6</sub>X MCsomes in water

FpC<sub>6</sub>X was first dissolved in THF to obtain a yellow solution. Then deionized water was quickly added into the solution (water/THF: 10:1 v/v). The resultant FpC<sub>6</sub>X colloid was dialyzed against water for 24 hours to remove THF.

## 6.3 Results and Discussion

### 6.3.1 Dilution-induced assembly of FpC<sub>6</sub>Azobenzene<sup>trans</sup> MCsomes.

FpC<sub>6</sub>Azobenzene<sup>trans</sup> (trans: trans configuration) is hydrophobic and non-surface active (Figure 8.22) and can self-assemble in water using THF as a common solvent (Figure 8.23a).<sup>73,214</sup> Like FpC<sub>6</sub> and FpC<sub>6</sub>Pyrene,<sup>73,150</sup> FpC<sub>6</sub>Azobenzene<sup>trans</sup> assembles in water into MCsomes (140 μM) (Figures 6.2a and 8.24) with detectable WCIs (Figure 8.23b). The zeta potential (ζ) of the colloids is *ca.* -51 ± 0.8 mV, suggesting that the HH of O[δ<sup>-</sup>], relative to Fe[δ<sup>+</sup>], is stronger due to the presence of WCIs.<sup>73,173,214</sup> The hydrodynamic diameter (D<sub>h</sub>) was *ca.* 168 nm (Figures 8.24a and 6.2a) and remained unchanged after aging for 25 days (Figure 6.2b). This colloidal stability was attributed to a considerable HI of the tails<sup>81</sup> assisted by the π-π interactions of trans-azobenzene groups as indicated by the UV-Vis spectrum (Figure 8.25a). When the solution was diluted from 140 μM to 14 μM, there was no change in D<sub>h</sub> (*ca.* 170 nm) right after the dilution (Figure 8.25b). However, time-resolved DLS experiment indicated that the diluted MCsomes (14 μM), unlike those at 140 μM, enlarged to micrometers over 25 days (Figure 6.2b). The TEM image of the aged sample showed a helical morphology (Figure 6.2c) that is supported by the Energy Dispersive X-ray (EDX) line analyses of C, Fe, P, O elements (Figures 8.26 and 8.27). As shown in Figure 6.2d, the distribution of C elements is wave-shaped along the helix and is higher in the middle when the cross section is analyzed. The helical pitch is *ca.* 500 nm, the width is *ca.* 500 nm

(Figure 6.2c) and the length varied from *ca.* 7  $\mu\text{m}$  to 30  $\mu\text{m}$  (Figure 8.28). It is worth noting that dilution-induced self-assembly of a guest-host complex in water has been reported with experimental phenomena implying the crucial role of dilution-enhanced hydration.<sup>215</sup>

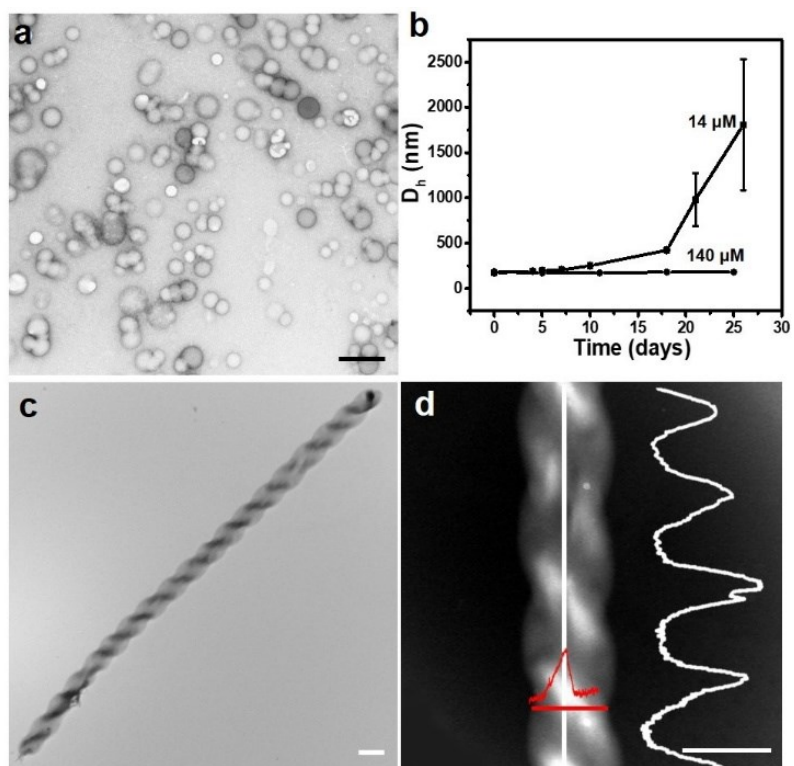


**Figure 6.2.** (a) TEM image of the MCsomes assembled from FpC<sub>6</sub>Azobenzene<sup>trans</sup> in water (140  $\mu\text{M}$ ). (b) The time-dependent  $D_h$  of FpC<sub>6</sub>Azobenzene<sup>trans</sup> MCsomes in water for the solutions with concentrations of 140  $\mu\text{M}$  and 14  $\mu\text{M}$ . (c) TEM image of the helix assembled from FpC<sub>6</sub>Azobenzene<sup>trans</sup> MCsomes that were diluted to 14  $\mu\text{M}$  and aged for 30 days. (d) Electron energy loss spectrum (EELS) of carbon elements distributing along and normal to the helical axis. Scale bar: 500 nm.

### 6.3.2 The conditional effect of HH.

HH is a conditional effect depending on the solution conditions.<sup>19-20</sup> This elusive concept was examined using MCsomes as a model system (Figure 6.3a). As shown in Figure 6.3b, the dilution reduces the net surface charge, but does not obviously affect the hydration of  $O[\delta^-]$  as indicated by IR analysis (Figure 8.29). It suggests that the HH of  $Fe[\delta^+]$  is enhanced upon the dilution. This enhancement was confirmed by cyclic voltammetry (CV) experiments. As shown in Figure 6.3c, the oxidation signals due to the hydrated  $Fe[\delta^+]$  at 140  $\mu\text{M}$  were barely detectable, but appeared even after 10 times dilution to 14  $\mu\text{M}$ . In addition, the oxidation coupling ( $\Delta E_{1/2}$ ) of the two-oxidation peaks is smaller for the solution with a lower concentration, suggesting that the distance between the Fp heads ( $d_{\text{Fp-Fp}}$ ) in close proximity was increased,<sup>73,214,216</sup> resulting from the dilution-enhanced HH<sup>19,205-206</sup>. This concentration-dependent hydration of  $Fe[\delta^+]$  was further verified by fluorescence (FL) quenching experiments. Figure 6.3d shows that the Stern-Volmer plot for the solution of calcein presented a downward curve as the MCsomes is diluted, because the dilution-enhanced HH of  $Fe[\delta^+]$  facilitated its interaction with the water-soluble dye and enhanced the quenching effect. To show that the  $\zeta$  results from the charge balance between the hydrated  $Fe[\delta^+]$  and  $O[\delta^-]$ , the pH-dependent  $\zeta$  was measured. As shown in Figure 6.3e,  $\zeta$  of MCsomes at 140  $\mu\text{M}$  reduced to *ca.* -26 mV by lowering the pH to 3.0 due to the protonation of  $O[\delta^-]$ . For the diluted solution (14  $\mu\text{M}$ ), the  $\zeta$  at pH 3 is even lower (*ca.* -8.2 mV) due to the combined effect of protonation of  $O[\delta^-]$  and dilution-enhanced HH of  $Fe[\delta^+]$  (Figure 8.30a). The three MCsomes listed in Figure 6.1 showed the same concentration- and pH-dependent  $\zeta$  (Figures 8.31 and 8.32), confirming that the HH of the Fp head is a conditional effect depending on the concentration and pH (Figure 6.3a). The HH effect was also dependent on the chemical structure of the

tails and was discussed separately in the section where the effect of tail-tail interactions on self-assembly was examined.

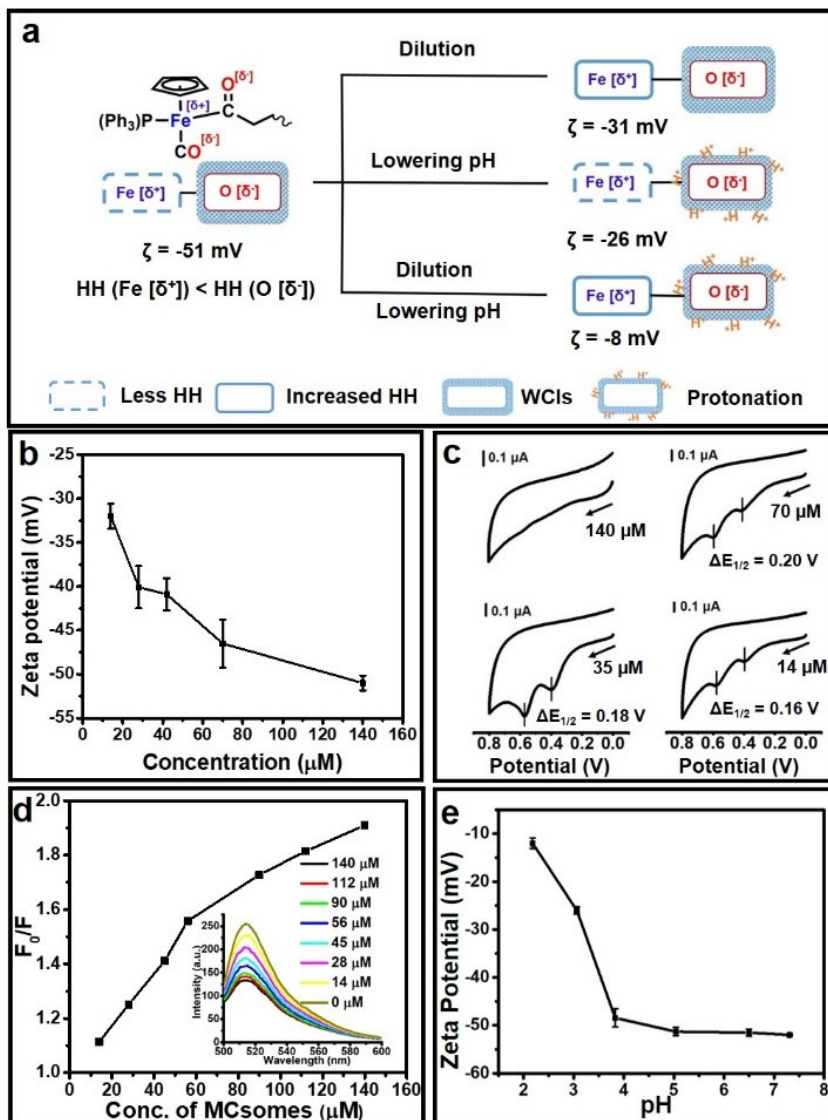


Figure 6.3. (a) Schematic illustration for the hydrophobic hydration (HH) of the Fp head in response to dilution and lowering pH. The zeta potential of the FpC<sub>6</sub>Azobenene

**MCsomes in dependence of the dilution from 140  $\mu\text{M}$  to 14  $\mu\text{M}$  and pH lowering from 7.3 to 3.0 is indicated in the scheme. (b) Zeta potential of FpC<sub>6</sub>Azobenzene<sup>trans</sup> MCsome in water upon dilution (from 140  $\mu\text{M}$  to 14  $\mu\text{M}$ ). (c) The cyclic voltammogram (CV) for FpC<sub>6</sub>Azobenzene<sup>trans</sup> MCsome in water with the concentration of 140  $\mu\text{M}$ , 70  $\mu\text{M}$ , 35  $\mu\text{M}$  and 14  $\mu\text{M}$ . (d) The Stern-Volmer plot for the fluorescence quenching of calcein (0.17  $\mu\text{M}$ ) in water by FpC<sub>6</sub>Azobenzene<sup>trans</sup> MCsomes with different concentrations. The inset displays the corresponding emission spectra.  $F_0$  and  $F$  refer to the emission intensity of calcein in the absence and presence of MCsomes. (e) pH-dependent zeta potential of FpC<sub>6</sub>Azobenzene<sup>trans</sup> MCsome in water (140  $\mu\text{M}$ ).**

### **6.3.3 Hierarchical self-assembling behavior.**

The dilution triggered a hierarchical self-assembly (Figure 6.2) caused by the suppression of coulombic repulsions due to the dilution-enhanced HH of Fe[ $\delta^+$ ] (Figure 6.3). The effect of HH on assembly might explain the dilution-induced refolding of denatured proteins.<sup>192-193</sup> The TEM images were recorded at different stages of the assembly. As shown in Figures 6.4a and 6.4b, the diluted MCsomes (14  $\mu\text{M}$ ) fused and enlarged from *ca.* 170 nm to *ca.* 500 nm in diameter after aging for *ca.* 10 days to lower the membrane tension and the interfacial energy.<sup>212</sup> Several intermediates at different fusion stages, including hemifusion and full fusion,<sup>212</sup> are shown in Figure 6.4c. On the day 14 of the assembly process, one-dimensional arrays of vesicles were observed (Figures 6.4d and 8.33a). This behavior was attributed to the dipole-dipole interactions<sup>217</sup> of the dielectric MCsomes that possess a local electric field.<sup>73,214</sup> The majority of the vesicles in the arrays were of larger size (*ca.* 500 nm in

diameter) (Figure 6.4d), indicating that the fusion occurred prior to the one-dimensional assembly. Upon aggregation, the vesicular membrane started to coalesce (Figures 6.4e and 8.33b) and the arrays evolved into nanotubes (Figure 6.4f) as indicated by the TEM images taken at day 20. The parallel packing of aromatic groups might result in the formation of nanotubes with lower curvature.<sup>218-219</sup> These nanotubes eventually evolved into helices, which was attributed to the packing behavior of asymmetric trans-azobenzene groups (Figure 6.4g).<sup>159,220</sup> This nanotube-to-helix transition was supported by the intermediate as shown in Figure 6.4h, where the assembly generated partially twisted tubes. The tube-to-helix transition has been reported before for lipid bilayer membranes.<sup>221</sup>

The assembly could also be triggered by protonation of  $O[\delta^-]$  without dilution.  $\zeta$  of the  $FpC_6Azobenzene^{trans}$  MCsome (140  $\mu$ M) was reduced to -26 mV by adjusting the pH to 3 (Figure 6.3e). Consequently,  $D_h$  of the colloids increased to micrometers in 3 days (Figure 6.4i), resulting in one-dimensional arrays of vesicles as indicated by the optical microscope and TEM images (Figures 6.4j and 4k). The vesicles in these arrays had smaller diameters (*ca.* 200 nm) (Figure 6.4k), which is attributed to the relatively slower kinetics of vesicular fusion<sup>32</sup> as compared to the formation of the arrays at 140  $\mu$ M. The coalescence of the vesicular membrane within the arrays was also observed (see arrows in Figure 6.4k), but this process generated precipitates before the transition to the nanotubes (Figure 8.34). At the lower concentration (14  $\mu$ M) and pH = 3,  $D_h$  of the colloids increased fairly quickly (Figure 8.20b) and precipitates formed in only a few days, because  $\zeta$  for the solution (*ca.* -8 mV) was too low to suspend the colloids for structural evolution.

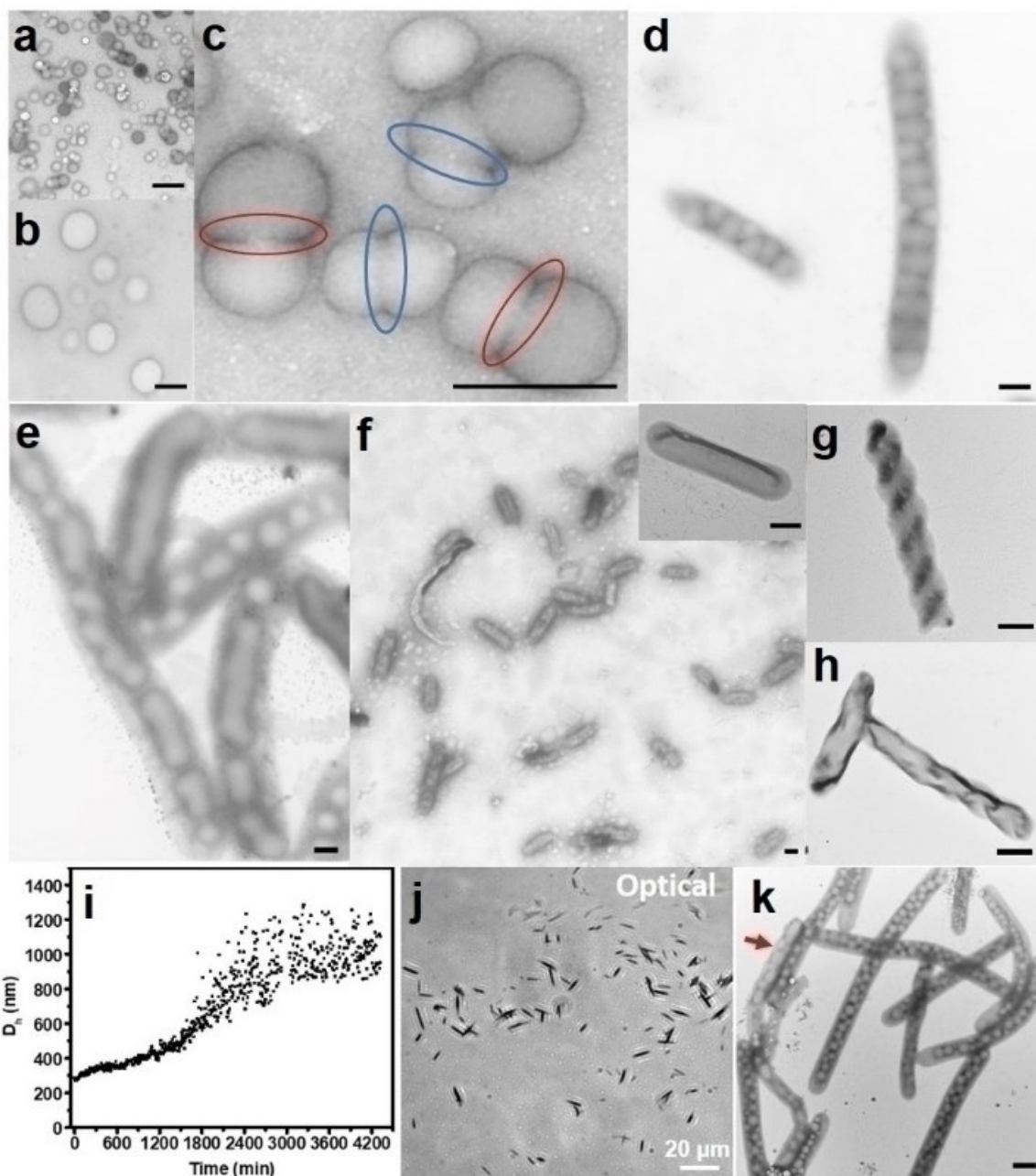


Figure 6.4. (a-h) TEM images for the diluted FpC<sub>6</sub>Azobenzene<sup>trans</sup> MCsome (14 μM) in water at different aging times. (a) Initially prepared MCsomes, (b) Fused MCsomes



after aging for 10 days, (c) Fusion intermediates. The red circles represent hemifusion where the thickness of the contact zone is close to the membrane thickness and the blue circles represent full fusion where two vesicles are fused without membrane separation, (d) One-dimensional arrays of vesicles after aging for 14 day, (e) Intermediates for the coalescence of the vesicles into nanotubes, (f) Hollow tube structures after aging for 20 day, (g) Helical structures after aging for 30 day, (h) The intermediates for tube-to-helix transition. (i-k) pH-induced solution behavior of FpC<sub>6</sub>Azobenzene<sup>trans</sup> MCsomes (140 μM) without dilution, including (i) Time-dependent  $D_h$  measured by DLS at pH 3, (j) Optical microscopy and (k) TEM images of the assembly after aging for 3 days at pH 3. Scale bar = 500 nm unless otherwise indicated in figures.

#### 6.3.4 The effect of tail-tail interactions.

The effect of tail-tail interaction on the solution behavior of MCsomes was evaluated.  $D_h$  for the FpC<sub>6</sub> MCsomes, even at a higher concentration (140 μM), enlarged over time and precipitates were eventually observed.<sup>173</sup> This lower colloidal stability and the absence of structural evolution were attributed to the weaker HI of the hexyl tails.<sup>81</sup> FpC<sub>6</sub>Azobenzene<sup>trans</sup> and FpC<sub>6</sub>Pyrene MCsomes involve  $\pi$ - $\pi$  interactions that strengthen tail-tail interactions and stabilize the MCsomes at the concentration of 140 μM (Figures 6.2b and 8.35). During the dilution-triggered assemblies, the strength of  $\pi$ - $\pi$  interactions, like those in biomolecules,<sup>222</sup> is a factor influencing the structural evolution. The relatively weaker  $\pi$ - $\pi$  interactions of trans-azobenzene<sup>223</sup> endows the hierarchical evolution as discussed above. In contrast, the stronger  $\pi$ - $\pi$  interactions of pyrene suppresses the assembly of FpC<sub>6</sub>Pyrene MCsomes. As shown in

Figures 6.5a and 8.36a, after diluting from 140  $\mu\text{M}$  to 14  $\mu\text{M}$  and subsequently aging for 60 days, only a small amount of FpC<sub>6</sub>Pyrene MCsomes assembled and evolved to nanotubes. One-dimensional arrays of the MCsomes were captured as intermediates by TEM experiments (Figure 6.5b), suggesting that the evolution resulted from the membrane fusion as well.

The observed effect of tail-tail interaction was a reminder that HI contributes to the stability of proteins.<sup>194</sup> The possible reason underlying this effect would be further investigated by taking advantage of the model system. The oxidation signals due to the hydrated Fe[ $\delta^+$ ] are obvious for FpC<sub>6</sub> MCsome (Figure 6.5c), while being barely observed for the two aromatic MCsomes (Figures 6.3c and 8.36b) at the same concentration (140  $\mu\text{M}$ ). This comparison suggested that the weaker HI results in a stronger HH of Fe[ $\delta^+$ ]. The FL quenching experiments also indicate that the HH level of Fe[ $\delta^+$ ] in FpC<sub>6</sub> MCsome is higher as compared with the aromatic MCsomes (Figure 6.5c). We also noticed that the FpC<sub>6</sub>Pyrene MCsome (140  $\mu\text{M}$ ) with a stronger tail-tail interaction had a relatively larger  $\zeta$  (-65 mV) (Figure 8.37), and its colloidal stability was higher (Figure 8.35). It was, therefore, reasonable to think that the stability resulting from the large net surface charge was caused by a lower HH of Fe[ $\delta^+$ ] due to the stronger tail-tail interactions. To elaborate this effect of tail-tail interactions on the HH of Fe[ $\delta^+$ ], we irradiated FpC<sub>6</sub>Azobenzene<sup>trans</sup> MCsomes (140  $\mu\text{M}$ ) using UV light (wavelength = 365 nm), which partially converted the configuration of azobenzene from trans to cis (Figure 8.38a). The presence of nonplanar cis-azobenzene is expected to disrupt the tail-tail interaction due to steric hindrance against the adjacent planar trans-azobenzene.<sup>224</sup> Although the morphology remained unchanged (Figures 8.38b, c and d), the appearance of the oxidation signal after UV irradiation (Figure 6.5d) suggests that the HH of Fe[ $\delta^+$ ] was improved without dilution. As a result, the FL quenching ability of the UV-irradiated MCsomes

was higher (Figure 6.5d). The HI of the tail was, therefore, also a factor influencing the HH degree of the  $\text{Fe}[\delta^+]$  head, which affected the subsequent solution behaviour of MCsomes.

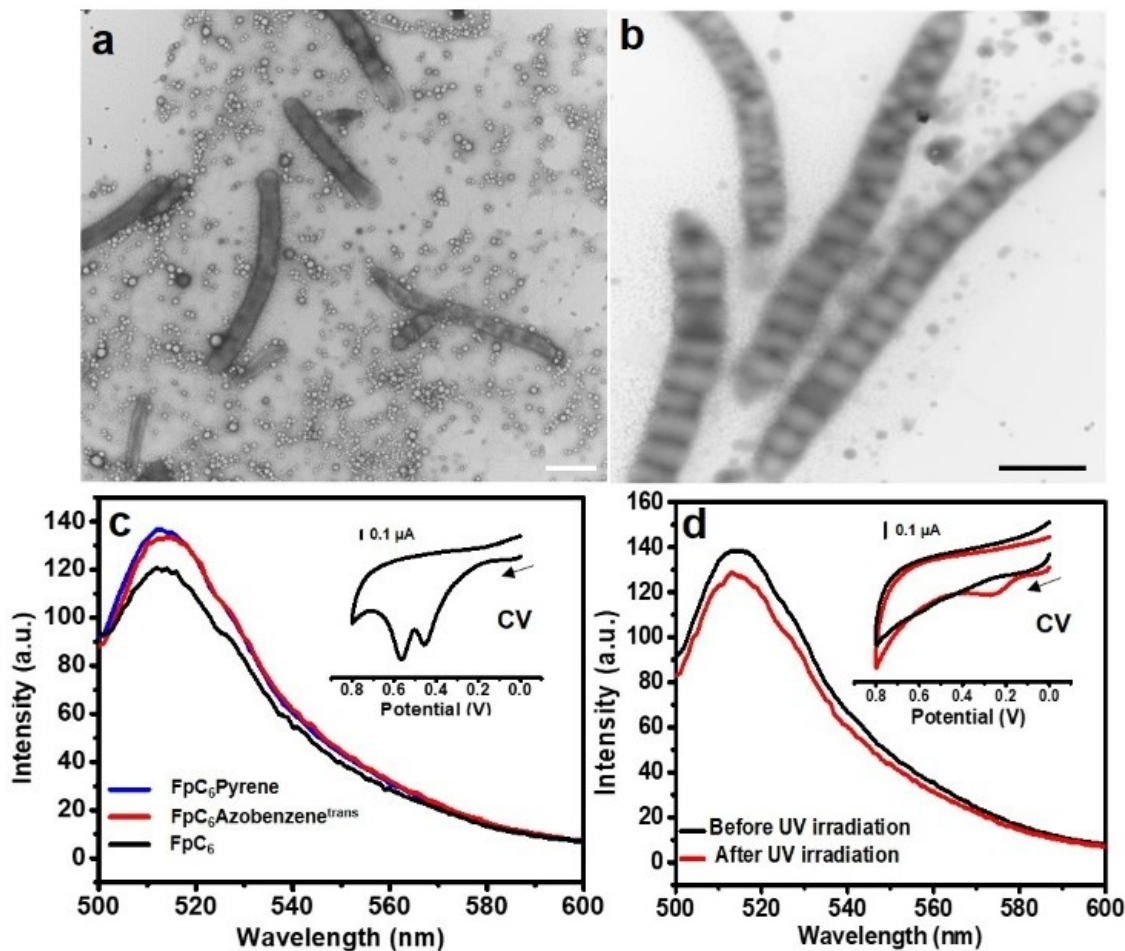


**Figure 6.5.** (a) TEM image for the diluted FpC<sub>6</sub>Pyrene colloid (14 μM) after aging for 60 days. (b) TEM image of one-dimensional arrays of FpC<sub>6</sub>Pyrene MCsomes (14 μM) recorded before the formation of nanotubes. (c) Fluorescence spectra of calcein solutions (0.17 μM) in the presence of three different MCsomes (140 μM). The inset is

**the cyclic voltammogram of FpC<sub>6</sub> MCsomes in water (140 μM). (d) Fluorescence spectra of calcein (0.17 μM) in the presence of FpC<sub>6</sub>Azobenzene<sup>trans</sup> MCsomes (140 μM) before and after UV light irradiation (365 nm). The inset is the cyclic voltammograms for the FpC<sub>6</sub>Azobenzene<sup>trans</sup> MCsomes in water (140 μM) before and after UV light irradiation (365 nm). Scale bar: 1 μm.**

## **6.4 Conclusions**

HE is fundamentally crucial in life science, but remains yet to be fully understood at the molecular level. MCsomes, assembled from hydrophobic FpC<sub>6</sub>X, were used to enable this study. The highly polarized Fp head (with Fe-CO groups) contained hydrated O[δ<sup>-</sup>] via WCIs and less hydrated Fe[δ<sup>+</sup>]. Interestingly, the high HH level of neutral peptide bonds (NH-CO) in proteins was also attributed to the higher tendency of water at interacting with the carbonyl O, rather than the N-H moiety in the amide group.<sup>225</sup> This similarity in HH behavior made MCsomes a suitable model system to gain insight into the solution behavior of proteins. For example, the dilution-induced refolding of denatured proteins<sup>192-193</sup> may be related to the enhanced HH of N-H. Particularly, the HE sensitivity of MCsomes, the detectable hydration of Fe[δ<sup>+</sup>] resolved a long-standing difficulty in the evaluation of the HH role in self-assemblies. By taking advantage of these properties, we have elucidated the HH effect resulting from the changes in the concentration and pH of the solutions as well as the chemical structure of the tails, and have explained how this effect triggers an assembly of MCsomes.

The subsequent assembling behavior was affected by the tail-tail interactions of C<sub>6</sub>X. The weaker HI of hexyl tails in FpC<sub>6</sub> MCsomes caused a higher HH degree for Fe[δ<sup>+</sup>] that weakened colloidal stability, preventing the MCsomes to evolve into more complex structures. The presence of π-π interactions, like

in many biological systems, improved the colloidal stability, which allowed the aromatic MCsomes to undergo hierarchical self-assemblies generating high-level structures. This evolution was explained based on the understanding of electrostatic, dipole-dipole,<sup>217</sup> and  $\pi$ - $\pi$  interactions,<sup>218-219</sup> etc. The effect of tail-tail interactions sheds some light on how hydrophobicity contributes to the stability of proteins and how the structure of proteins influences the HH level and redox behavior of the metal center in metalloproteins.<sup>195</sup>

This study using the molecular model system, complementary to the research focusing on hydrated water,<sup>190,200-201</sup> is essential to evaluate and create the theory of HE<sup>197,202</sup> for an improved understanding of biological events and rational design of waterborne materials.<sup>19,188</sup>

## Chapter 7 General Conclusions

### 7.1 Conclusions

In this thesis, the nonamphiphilic assembly of metal carbonyl complexes was studied based on kinetic trapping, structural rigidity, and hydrophobic effect.

Self-assembly is crucial for life and nature because self-assembly could provide an effective approach to synthesize various nanostructures from small molecules or monomers. To mimic the self-assembly in nature, chemists have made a great progress in the past decades. For examples, small amphiphilic lipid molecules are employed to self-assemble into liposomes which mimic the cellular bilayer membrane structures. The formed liposomes have a great potential application in drug delivery, nanoreactors, and other biological applications. Moreover, to enhance the stability of liposomes, amphiphilic block copolymers are used to form polymersomes. However, the synthetic self-assembly still focuses on the molecules or macromolecules which possess an amphiphilic character. And the self-assembled nanostructures were mostly thermodynamically controlled. As well known, the self-assembly in life is more complex. First, the self-assembly of proteins or DNA which realizes the advanced biological functions was not based on the amphiphilic nature but on more complex factors such as hydrophobic effect and structural conformation. Second, the advanced biological function is determined by the kinetics of the self-assembly process. In this context, we studied the self-assembly behavior of pure hydrophobic metal carbonyl complexes. By investigating the self-assembly of pure hydrophobic metal carbonyl complexes, the role of nonamphiphilic nature like kinetic trapping, structural rigidity and hydrophobic effect on the self-assembly was addressed which would develop the theory to better understand the self-assembly process in life.

The first chapter described the background of the self-assembly in nature and synthetic chemistry. We first briefly introduced the self-assembly in nature. Then we highlighted the achievements of synthetic self-assembly based on amphiphilic molecules or macromolecules as well as the related theories and applications in biology. Some challenging areas in synthetic self-assembly are described, especially the nonamphiphilic assembly. In this thesis, we utilized the hydrophobic metal carbonyl Fp-complexes as model systems to investigate the role of nonamphiphilic nature on self-assembly.

In the second chapter, the kinetic precipitation process of the hydrophobic homopolymer P(FpP) in a nonsolvent was investigated. The metal carbonyl homopolymer P(FpP) was soluble in THF, insoluble in hexane and exhibits a UCST behavior in DMSO. UV, DLS and TEM characterization demonstrated the precipitation process of P(FpP) in THF/hexane or DMSO upon cooling, which was a slow kinetic process. The slow kinetic process for the precipitation could be adjusted by various solution conditions. By varying kinetic pathways for the precipitation, kinetically-trapped nanostructures with narrow size distributions, including spherical and worm-like nanoparticles, were produced. A number of parameters, including concentration, additive and the solvation quality, e.g. THF/hexane ratio, were adjustable for the kinetic control. Kinetic assembly of readily available homopolymers in solutions is, therefore, worthwhile to be explored as a reliable technique for nanosynthesis.

In the third chapter, the role of backbone rigidity on the self-assembly behaviors of hydrophobic homopolymer P(FpP) with the assistance of simulation was studied. Simulation results demonstrated that increasing temperature would cause the backbone of P(FpP) in DMSO flexible. And the change of the backbone rigidity could affect the self-assembly behavior. Preparing the self-assembled samples at different temperatures various nanostructures were formed such as lamellae, vesicles and irregular

aggregates. And further increasing the flexibility of the homopolymer chains by increasing temperature would make the self-assembled structures disordered and irregular. This work could guide further research into the biomimetic supramolecular self-assembly using hydrophobic macromolecules as building blocks.

In the fourth chapter, the unique membrane structure of nonbilayer P(FpP) vesicles and the corresponding unique swelling behavior in response to THF were investigated. It was found that the formed homopolymer P(FpP) vesicles could be formed by the packing of the homopolymer chains. Considering the formed P(FpP) vesicles were kinetic trapped structures, various kinetic conditions were employed to fabricate P(FpP) vesicles with various thickness. Moreover, the breathing properties of P(FpP) vesicles in response to THF were studied. By addition of THF, we discovered that the P(FpP) vesicles could swell into large vesicles which are stable and possess a narrow size distribution. This was different from traditional bilayer vesicles. Moreover, the mechanism of the swelling behavior of P(FpP) vesicles in response to THF was also discussed. And the role of solvation of polymer chains seemed to play a critical role in the swelling behavior of P(FpP) vesicles in response to THF.

The effect of hydrophobic interaction and  $\pi$ - $\pi$  interactions on the self-assembly behavior of proteins or other biological molecules is a long debate. In the fifth chapter, we exploited the metal carbonyl molecule FpC<sub>6</sub>Pyrene as a model system to investigate the self-assembly behaviors under various solutions conditions. DLS, TEM and FL spectroscopies suggested that the  $\pi$ - $\pi$  interactions in response to solution conditions could be adjusted as a driving force or not. In DMSO/water or methanol/water systems, aromatic interactions are predominant and drive the assembly into lamellae, while in a THF/water system, hydrophobic effect drives the assembly into vesicles. When the driving force for



the FpC<sub>6</sub>Pyrene molecule was different, various nanostructures could be formed. This knowledge is fundamentally important in the context of protein and supramolecular chemistry.

Hydrophobic effect plays an important role for the self-assembly of proteins. However, few studies in supramolecular chemistry on this issue were reported, which was mainly due to lack of a suitable model system. In the sixth chapter, we synthesized hydrophobic FpC<sub>6</sub>, FpC<sub>6</sub>Azobenzene and FpC<sub>6</sub>Pyrene which could self-assemble into MCsomes in water. And these three different MCsomes were utilized as model systems to investigate the role of hydrophobic effect on their hierarchical self-assembly. CV, DLS, zeta potential characterization and fluorescence quenching experiments demonstrated that hydrophobic hydration could be adjusted by dilution which determined the stability of the MCsomes. Moreover, we also discussed how the hydrophobic interactions influence the hydrophobic hydration of MCsomes which solved a long-standing problem in protein chemistry.

In the seventh chapter, we summarized the self-assembly behavior of metal carbonyl complexes and provided new knowledge and theory for an improved understanding of biological events and rational design of waterborne materials.

## Bibliography

1. Whitesides, G. M.; Grzybowski, B., Self-assembly at all scales. *Science* **2002**, *295* (5564), 2418-2421.
2. Philp, D.; Stoddart, J. F., Self - assembly in natural and unnatural systems. *Angew. Chem., Int. Ed.* **1996**, *35* (11), 1154-1196.
3. Zhang, S., Fabrication of novel biomaterials through molecular self-assembly. *Nat. Biotechnol.* **2003**, *21* (10), 1171.
4. Wu, L.; Lal, J.; Simon, K. A.; Burton, E. A.; Luk, Y.-Y., Nonamphiphilic assembly in water: polymorphic nature, thread structure, and thermodynamic incompatibility. *J. Am. Chem. Soc.* **2009**, *131* (21), 7430-7443.
5. Akbarzadeh, A.; Rezaei-Sadabady, R.; Davaran, S.; Joo, S. W.; Zarghami, N.; Hanifehpour, Y.; Samiei, M.; Kouhi, M.; Nejati-Koshki, K., Liposome: classification, preparation, and applications. *Nanoscale Res. Lett* **2013**, *8* (1), 102.
6. Ong, L. L.; Hanikel, N.; Yaghi, O. K.; Grun, C.; Strauss, M. T.; Bron, P.; Lai-Kee-Him, J.; Schueder, F.; Wang, B.; Wang, P., Programmable self-assembly of three-dimensional nanostructures from 10,000 unique components. *Nature* **2017**, *552* (7683), 72.
7. Praetorius, F.; Dietz, H., Self-assembly of genetically encoded DNA-protein hybrid nanoscale shapes. *Science* **2017**, *355* (6331), eaam5488.

8. Zhang, C.; Su, M.; He, Y.; Zhao, X.; Fang, P.-a.; Ribbe, A. E.; Jiang, W.; Mao, C., Conformational flexibility facilitates self-assembly of complex DNA nanostructures. *Proc. Natl. Acad. Sci.* **2008**, *105* (31), 10665-10669.
9. Barnes, R.; Sun, S.; Fichou, Y.; Dahlquist, F. W.; Heyden, M.; Han, S., Spatially heterogeneous surface water diffusivity around structured protein surfaces at equilibrium. *J. Am. Chem. Soc.* **2017**, *139* (49), 17890-17901.
10. McManus, J. J.; Charbonneau, P.; Zaccarelli, E.; Asherie, N., The physics of protein self-assembly. *Curr. Opin. Colloid Interface Sci* **2016**, *22*, 73-79.
11. Cooper, G. M.; Hausman, R. E., *The cell: Molecular approach*. Medicinska naklada: 2004.
12. McMahon, H. T.; Gallop, J. L., Membrane curvature and mechanisms of dynamic cell membrane remodelling. *Nature* **2005**, *438* (7068), 590.
13. Torchilin, V. P., Recent advances with liposomes as pharmaceutical carriers. *Nat. Rev. Drug Discov.* **2005**, *4* (2), 145.
14. Lunn, D. J.; Finnegan, J. R.; Manners, I., Self-assembly of “patchy” nanoparticles: a versatile approach to functional hierarchical materials. *Chem Sci* **2015**, *6* (7), 3663-3673.
15. Goodman, R. P.; Schaap, I. A.; Tardin, C. F.; Erben, C. M.; Berry, R. M.; Schmidt, C. F.; Turberfield, A. J., Rapid chiral assembly of rigid DNA building blocks for molecular nanofabrication. *Science* **2005**, *310* (5754), 1661-1665.
16. Sun, X.; Hyeon Ko, S.; Zhang, C.; Ribbe, A. E.; Mao, C., Surface-mediated DNA self-assembly. *J. Am. Chem. Soc.* **2009**, *131* (37), 13248-13249.
17. Seeman, N. C., DNA engineering and its application to nanotechnology. *Trends Biotechnol.* **1999**, *17* (11), 437-443.

18. Yan, H.; Park, S. H.; Finkelstein, G.; Reif, J. H.; LaBean, T. H., DNA-templated self-assembly of protein arrays and highly conductive nanowires. *Science* **2003**, *301* (5641), 1882-1884.
19. Chandler, D., Interfaces and the driving force of hydrophobic assembly. *Nature* **2005**, *437* (7059), 640.
20. Tielrooij, K.-J.; Hunger, J.; Buchner, R.; Bonn, M.; Bakker, H. J., Influence of Concentration and Temperature on the Dynamics of Water in the Hydrophobic Hydration Shell of Tetramethylurea. *J. Am. Chem. Soc.* **2010**, *132* (44), 15671-15678.
21. Cheng, Y.-K.; Rossky, P. J., Surface topography dependence of biomolecular hydrophobic hydration. *Nature* **1998**, *392* (6677), 696.
22. Fratzl, P.; Weinkamer, R., Nature's hierarchical materials. *Prog. Mater Sci.* **2007**, *52* (8), 1263-1334.
23. Wang, Y.; He, J.; Liu, C.; Chong, W. H.; Chen, H., Thermodynamics versus kinetics in nanosynthesis. *Angew. Chem., Int. Ed.* **2015**, *54* (7), 2022-2051.
24. Buehler, M. J.; Yung, Y. C., Deformation and failure of protein materials in physiologically extreme conditions and disease. *Nat Mater* **2009**, *8* (3), 175.
25. Gillam, J.; MacPhee, C., Modelling amyloid fibril formation kinetics: mechanisms of nucleation and growth. *Journal of Physics: Condensed Matter* **2013**, *25* (37), 373101.
26. Palma, C.-A.; Cecchini, M.; Samorì, P., Predicting self-assembly: from empirism to determinism. *Chem. Soc. Rev.* **2012**, *41* (10), 3713-3730.
27. Knowles, T. P.; Oppenheim, T. W.; Buell, A. K.; Chirgadze, D. Y.; Welland, M. E., Nanostructured films from hierarchical self-assembly of amyloidogenic proteins. *Nat. Nanotechnol.* **2010**, *5* (3), 204.

28. Binder, W. H.; Barragan, V.; Menger, F. M., Domains and rafts in lipid membranes. *Angew. Chem., Int. Ed.* **2003**, *42* (47), 5802-5827.
29. Antonietti, M.; Förster, S., Vesicles and liposomes: a self - assembly principle beyond lipids. *Adv Mater* **2003**, *15* (16), 1323-1333.
30. Mai, Y.; Eisenberg, A., Self-assembly of block copolymers. *Chem. Soc. Rev.* **2012**, *41* (18), 5969-5985.
31. Kunitake, T., Synthetic Bilayer Membranes: Molecular Design, Self - Organization, and Application. *Angew. Chem., Int. Ed.* **1992**, *31* (6), 709-726.
32. Discher, D. E.; Eisenberg, A., Polymer Vesicles. *Science* **2002**, *297* (5583), 967-973.
33. Discher, B. M.; Won, Y.-Y.; Ege, D. S.; Lee, J. C.; Bates, F. S.; Discher, D. E.; Hammer, D. A., Polymersomes: tough vesicles made from diblock copolymers. *Science* **1999**, *284* (5417), 1143-1146.
34. Vriezema, D. M.; Comellas Aragonès, M.; Elemans, J. A.; Cornelissen, J. J.; Rowan, A. E.; Nolte, R. J., Self-assembled nanoreactors. *Chem Rev* **2005**, *105* (4), 1445-1490.
35. Rodríguez-Hernández, J.; Lecommandoux, S., Reversible inside– out micellization of pH-responsive and water-soluble vesicles based on polypeptide diblock copolymers. *J. Am. Chem. Soc.* **2005**, *127* (7), 2026-2027.
36. Nowak, A. P.; Breedveld, V.; Pakstis, L.; Ozbas, B.; Pine, D. J.; Pochan, D.; Deming, T. J., Rapidly recovering hydrogel scaffolds from self-assembling diblock copolypeptide amphiphiles. *Nature* **2002**, *417* (6887), 424.
37. Holowka, E. P.; Pochan, D. J.; Deming, T. J., Charged polypeptide vesicles with controllable diameter. *J. Am. Chem. Soc.* **2005**, *127* (35), 12423-12428.

38. Vandermeulen, G. W.; Klok, H. A., Peptide/protein hybrid materials: enhanced control of structure and improved performance through conjugation of biological and synthetic polymers. *Macromol Biosci* **2004**, *4* (4), 383-398.
39. Hartgerink, J. D.; Beniash, E.; Stupp, S. I., Self-assembly and mineralization of peptide-amphiphile nanofibers. *Science* **2001**, *294* (5547), 1684-1688.
40. Salim, M.; Minamikawa, H.; Sugimura, A.; Hashim, R., Amphiphilic designer nano-carriers for controlled release: from drug delivery to diagnostics. *Medchemcomm* **2014**, *5* (11), 1602-1618.
41. Karayianni, M.; Pispas, S., Self-assembly of amphiphilic block copolymers in selective solvents. In *Fluorescence Studies of Polymer Containing Systems*, Springer: 2016; pp 27-63.
42. Kelley, E. G.; Murphy, R. P.; Seppala, J. E.; Smart, T. P.; Hann, S. D.; Sullivan, M. O.; Epps, T. H., Size evolution of highly amphiphilic macromolecular solution assemblies via a distinct bimodal pathway. *Nat Commun* **2014**, *5*, 3599.
43. Gröschel, A. H.; Schacher, F. H.; Schmalz, H.; Borisov, O. V.; Zhulina, E. B.; Walther, A.; Müller, A. H., Precise hierarchical self-assembly of multicompart ment micelles. *Nat Commun* **2012**, *3*, 710.
44. Cui, H.; Chen, Z.; Zhong, S.; Wooley, K. L.; Pochan, D. J., Block copolymer assembly via kinetic control. *Science* **2007**, *317* (5838), 647-650.
45. Pochan, D. J.; Chen, Z.; Cui, H.; Hales, K.; Qi, K.; Wooley, K. L., Toroidal triblock copolymer assemblies. *Science* **2004**, *306* (5693), 94-97.
46. Hayward, R. C.; Pochan, D. J., Tailored assemblies of block copolymers in solution: it is all about the process. *Macromolecules* **2010**, *43* (8), 3577-3584.

47. Lavasanifar, A.; Samuel, J.; Kwon, G. S., Poly (ethylene oxide)-block-poly (L-amino acid) micelles for drug delivery. *Adv. Drug Delivery Rev.* **2002**, *54* (2), 169-190.
48. Bleul, R.; Thiermann, R.; Maskos, M., Techniques to control polymersome size. *Macromolecules* **2015**, *48* (20), 7396-7409.
49. Choi, K. Y.; Liu, G.; Lee, S.; Chen, X., Theranostic nanoplatfoms for simultaneous cancer imaging and therapy: current approaches and future perspectives. *Nanoscale* **2012**, *4* (2), 330-342.
50. Sanson, C.; Diou, O.; Thevenot, J.; Ibarboure, E.; Soum, A.; Brûlet, A.; Miraux, S.; Thiaudière, E.; Tan, S.; Brisson, A., Doxorubicin loaded magnetic polymersomes: theranostic nanocarriers for MR imaging and magneto-chemotherapy. *ACS Nano* **2011**, *5* (2), 1122-1140.
51. Meng, F.; Zhong, Z.; Feijen, J., Stimuli-responsive polymersomes for programmed drug delivery. *Biomacromolecules* **2009**, *10* (2), 197-209.
52. Walter, H., *Partitioning in aqueous two-phase system: theory, methods, uses, and applications to biotechnology*. Elsevier: 2012.
53. Blanazs, A.; Warren, N. J.; Lewis, A. L.; Armes, S. P.; Ryan, A. J., Self-assembly of double hydrophilic block copolymers in concentrated aqueous solution. *Soft Matter* **2011**, *7* (14), 6399-6403.
54. Valverde Serrano, C. Self-assembly behavior in hydrophilic block copolymers. Universität Potsdam Potsdam, 2011.
55. Taubert, A.; Furrer, E.; Meier, W., Water-in-water mesophases for templating inorganics. *Chem Commun* **2004**, (19), 2170-2171.
56. Casse, O.; Shkilnyy, A.; Linders, J. r.; Mayer, C.; Häussinger, D.; Völkel, A.; Thünemann, A. F.; Dimova, R.; Cölfen, H.; Meier, W., Solution behavior of double-hydrophilic block copolymers in dilute aqueous solution. *Macromolecules* **2012**, *45* (11), 4772-4777.

57. Nguyen, B. T.; Wang, W.; Saunders, B. R.; Benyahia, L.; Nicolai, T., pH-responsive water-in-water Pickering emulsions. *Langmuir* **2015**, *31* (12), 3605-3611.
58. Brosnan, S. M.; Schlaad, H.; Antonietti, M., Aqueous Self - Assembly of Purely Hydrophilic Block Copolymers into Giant Vesicles. *Angew. Chem., Int. Ed.* **2015**, *54* (33), 9715-9718.
59. Zhou, X.; Li, X.; Mao, T.; Zhang, J.; Li, X., Facile engineering of nano-and microparticles via self-assembly of homopolymers. *Soft Matter* **2011**, *7* (13), 6264-6272.
60. Savariar, E. N.; Aathimanikandan, S. V.; Thayumanavan, S., Supramolecular assemblies from amphiphilic homopolymers: testing the scope. *J. Am. Chem. Soc.* **2006**, *128* (50), 16224-16230.
61. Mane, S. R.; Rao, N. V.; Chatterjee, K.; Dinda, H.; Nag, S.; Kishore, A.; Das Sarma, J.; Shunmugam, R., Amphiphilic Homopolymer Vesicles as Unique Nano-Carriers for Cancer Therapy. *Macromolecules* **2012**, *45* (19), 8037-8042.
62. Basu, S.; Vutukuri, D. R.; Thayumanavan, S., Homopolymer micelles in heterogeneous solvent mixtures. *J. Am. Chem. Soc.* **2005**, *127* (48), 16794-16795.
63. Arumugam, S.; Vutukuri, D. R.; Thayumanavan, S.; Ramamurthy, V., Amphiphilic homopolymer as a reaction medium in water: Product selectivity within polymeric nanopockets. *J. Am. Chem. Soc.* **2005**, *127* (38), 13200-13206.
64. Zhu, Y.; Yang, B.; Chen, S.; Du, J., Polymer vesicles: Mechanism, preparation, application, and responsive behavior. *Prog. Polym. Sci.* **2017**, *64*, 1-22.
65. Fan, L.; Lu, H.; Zou, K.; Chen, J.; Du, J., Homopolymer vesicles with a gradient bilayer membrane as drug carriers. *Chem Commun* **2013**, *49* (98), 11521-11523.
66. Zhu, Y.; Liu, L.; Du, J., Probing into homopolymer self-assembly: how does hydrogen bonding influence morphology? *Macromolecules* **2012**, *46* (1), 194-203.



67. Duan, H.; Chen, D.; Jiang, M.; Gan, W.; Li, S.; Wang, M.; Gong, J., Self-assembly of unlike homopolymers into hollow spheres in nonselective solvent. *J. Am. Chem. Soc.* **2001**, *123* (48), 12097-12098.
68. Cha, J. N.; Birkedal, H.; Euliss, L. E.; Bartl, M. H.; Wong, M. S.; Deming, T. J.; Stucky, G. D., Spontaneous formation of nanoparticle vesicles from homopolymer polyelectrolytes. *J. Am. Chem. Soc.* **2003**, *125* (27), 8285-8289.
69. Changez, M.; Kang, N. G.; Lee, C. H.; Lee, J. S., Reversible and pH - Sensitive Vesicles from Amphiphilic Homopolymer Poly (2 - (4 - vinylphenyl) pyridine). *Small* **2010**, *6* (1), 63-68.
70. Zhou, C.; Wang, M.; Zou, K.; Chen, J.; Zhu, Y.; Du, J., Antibacterial polypeptide-grafted chitosan-based nanocapsules as an “armed” carrier of anticancer and antiepileptic drugs. *ACS Macro Lett* **2013**, *2* (11), 1021-1025.
71. Zhu, Y.; Fan, L.; Yang, B.; Du, J., Multifunctional homopolymer vesicles for facile immobilization of gold nanoparticles and effective water remediation. *ACS Nano* **2014**, *8* (5), 5022-5031.
72. Wang, X.; Cao, K.; Liu, Y.; Tsang, B.; Liew, S., Migration insertion polymerization (MIP) of cyclopentadienyldicarbonyldiphenylphosphinopropyliron (FpP): a new concept for main chain metal-containing polymers (MCPs). *J. Am. Chem. Soc.* **2013**, *135* (9), 3399-3402.
73. Murshid, N.; Wang, X., Iron–Carbonyl Aqueous Vesicles (MCsomes) by Hydration of [Fe(CO){CO(CH<sub>2</sub>)<sub>5</sub>CH<sub>3</sub>}(Cp)(PPh<sub>3</sub>)](FpC6): Highly Integrated Colloids with Aggregation - Induced Self - Enhanced IR Absorption (AI - SEIRA). *Chem. - Eur. J.* **2015**, *21* (52), 19223-19230.

74. Murshid, N.; Rahman, M. A.; Wang, X. S., Aggregation-enhanced IR absorption (AEIRA) of molybdenum-carbonyl organometallic aqueous colloids. *J Organomet Chem* **2016**, *819*, 109-114.
75. Murshid, N.; Yuyama, K.-i.; Wu, S.-L.; Wu, K.-Y.; Masuhara, H.; Wang, C.-L.; Wang, X., Highly-integrated, laser manipulable aqueous metal carbonyl vesicles (MCsomes) with aggregation-induced emission (AIE) and aggregation-enhanced IR absorption (AEIRA). *J. Mater. Chem. C* **2016**, *4* (23), 5231-5240.
76. Pannell, K. H.; Sharma, H. K., (Cyclopentadienyl) dicarbonylmethyliron (( $\eta^5$ -C<sub>5</sub>H<sub>5</sub>) Fe (CO)<sub>2</sub>CH<sub>3</sub>, FpMe), a seminal transition-metal alkyl complex: mobility of the methyl group. *Organometallics* **2010**, *29* (21), 4741-4745.
77. Theys, R. D.; Dudley, M. E.; Hossain, M. M., Recent chemistry of the  $\eta^5$ -cyclopentadienyl dicarbonyl iron anion. *Coord. Chem. Rev.* **2009**, *253* (1-2), 180-234.
78. Scharrer, E.; Brookhart, M., Insertion reactions of electrophilic iron carbene complexes with organosilanes: A synthetic and mechanistic study. *J Organomet Chem* **1995**, *497* (1-2), 61-71.
79. Cao, K.; Murshid, N.; Li, L.; Lopez, A.; Tam, K. C.; Wang, X., Hydration of hydrophobic iron-carbonyl homopolymers via water-carbonyl interaction (WCI): creation of uniform organometallic aqueous vesicles with exceptionally high encapsulation capacity. *Macromolecules* **2015**, *48* (21), 7968-7977.
80. Cao, K.; Ward, J.; Amos, R. C.; Jeong, M. G.; Kim, K. T.; Gauthier, M.; Foucher, D.; Wang, X., Organometallic macromolecules with piano stool coordination repeating units: chain configuration and stimulated solution behaviour. *Chem Commun* **2014**, *50* (70), 10062-10065.
81. Murshid, N.; Wang, X., Hydrophobic Effect of Alkyl Groups Stabilizing Self-Assembled Colloids in Water. *J. Phys. Chem. B* **2017**, *121* (25), 6280-6285.

82. Guan, Z.; Liu, D.; Lin, J.; Wang, X., Aqueous self-assembly of hydrophobic macromolecules with adjustable rigidity of the backbone. *Soft matter* **2017**, *13* (30), 5130-5136.
83. Liu, D.; Wang, X.-S., Hierarchical Self - Assembly Induced by Dilution - Enhanced Hydrophobic Hydration. *Chem. - Eur. J.* **2018**, *24* (26), 6737-6741.
84. Tantakitti, F.; Boekhoven, J.; Wang, X.; Kazantsev, R. V.; Yu, T.; Li, J.; Zhuang, E.; Zandi, R.; Ortony, J. H.; Newcomb, C. J., Energy landscapes and functions of supramolecular systems. *Nat Mater* **2016**, *15* (4), 469.
85. Görl, D.; Zhang, X.; Stepanenko, V.; Würthner, F., Supramolecular block copolymers by kinetically controlled co-self-assembly of planar and core-twisted perylene bisimides. *Nat. Commun.* **2015**, *6*, 7009.
86. Scherer, A.; Zhou, C.; Michaelis, J.; Brauchle, C.; Zumbusch, A., Intermolecular interactions of polymer molecules determined by single-molecule force spectroscopy. *Macromolecules* **2005**, *38* (23), 9821-9825.
87. Sedlák, M. n., Homopolymer self-assembly into stable nanoparticles: concerted action of hydrophobic association and hydrogen bonding in thermoresponsive poly (alkylacrylic acid) s. *J. Phys. Chem. B* **2012**, *116* (8), 2356-2364.
88. Sedlák, M. n.; Koňák, C. e. r., A new approach to polymer self-assembly into stable nanoparticles: poly (ethylacrylic acid) homopolymers. *Macromolecules* **2009**, *42* (19), 7430-7438.
89. Johnson, B. K.; Prud'homme, R. K., Flash nanoprecipitation of organic actives and block copolymers using a confined impinging jets mixer. *Aust J Chem* **2003**, *56* (10), 1021-1024.

90. Gindy, M. E.; Panagiotopoulos, A. Z.; Prud'homme, R. K., Composite block copolymer stabilized nanoparticles: simultaneous encapsulation of organic actives and inorganic nanostructures. *Langmuir* **2008**, *24* (1), 83-90.
91. Johnson, B. K.; Prud'homme, R. K., Mechanism for rapid self-assembly of block copolymer nanoparticles. *Phys Rev Lett* **2003**, *91* (11), 118302.
92. Alexandridis, P.; Lindman, B., *Amphiphilic block copolymers: self-assembly and applications*. Elsevier: 2000.
93. Li, Z.; Kesselman, E.; Talmon, Y.; Hillmyer, M. A.; Lodge, T. P., Multicompartment micelles from ABC miktoarm stars in water. *Science* **2004**, *306* (5693), 98-101.
94. Cui, H.; Chen, Z.; Zhong, S.; Wooley, K. L.; Pochan, D. J., Block copolymer assembly via kinetic control. *Science* **2007**, *317* (5838), 647-50.
95. He, X.; He, Y.; Hsiao, M.-S.; Harniman, R. L.; Pearce, S.; Winnik, M. A.; Manners, I., Complex and Hierarchical 2D Assemblies via Crystallization-Driven Self-Assembly of Poly (L-lactide) Homopolymers with Charged Termini. *J. Am. Chem. Soc.* **2017**, *139* (27), 9221-9228.
96. Wang, X. S.; Cao, K.; Liu, Y. B.; Tsang, B.; Liew, S., Migration Insertion Polymerization (MIP) of Cyclopentadienyldicarbonyldiphenylphosphinopropyliron (FpP): A New Concept for Main Chain Metal-Containing Polymers (MCPs). *J. Am. Chem. Soc.* **2013**, *135* (9), 3399-3402.
97. Cao, K.; Tsang, B.; Liu, Y.; Chelladural, D.; Power, W. P.; Wang, X., Synthesis, Cyclization, and Migration Insertion Oligomerization of CpFe (CO) <sub>2</sub> (CH<sub>2</sub>) <sub>3</sub>PPh<sub>2</sub> in Solution. *Organometallics* **2014**, *33* (2), 531-539.

98. Liu, J.; Cao, K.; Nayyar, B.; Tian, X.; Wang, X., Synthesis and migration insertion polymerization (MIP) of CpFe (CO) 2 (CH 2) 6 PPh 2 (FpC6P) for PFpC6P: macromolecule stability, degradability and redox activity. *Polym. Chem.* **2014**, *5* (23), 6702-6709.
99. Liu, J.; Guan, Z.; Tian, X.; Lin, J.; Wang, X., Solvent-dependent chain conformation for ring closure of metal carbonyl oligomers via migration insertion polymerization (MIP) of CpFe (CO) 2 (CH 2) 6 PPh 2. *Polym. Chem.* **2016**, *7* (26), 4419-4426.
100. Seuring, J.; Agarwal, S., Polymers with upper critical solution temperature in aqueous solution. *Macromol. Rapid Commun.* **2012**, *33* (22), 1898-1920.
101. Aseyev, V.; Tenhu, H.; Winnik, F. M., Non-ionic Thermoresponsive Polymers in Water. *Adv Polym Sci* **2011**, *242*, 29-89.
102. Higashi, N.; Sonoda, R.; Koga, T., Thermo-responsive amino acid-based vinyl polymers showing widely tunable LCST/UCST behavior in water. *Rsc Adv* **2015**, *5* (83), 67652-67657.
103. Winnik, F. M., Phase transition of aqueous poly-(N-isopropylacrylamide) solutions: a study by non-radiative energy transfer. *Polymer* **1990**, *31* (11), 2125-2134.
104. Badiger, M.; Lele, A.; Bhalerao, V.; Varghese, S.; Mashelkar, R., Molecular tailoring of thermoreversible copolymer gels: Some new mechanistic insights. *J. Chem. Phys.* **1998**, *109* (3), 1175-1184.
105. Stannard, A., Dewetting-mediated pattern formation in nanoparticle assemblies. *Journal of Physics: Condensed Matter* **2011**, *23* (8), 083001.
106. Förster, S.; Hermsdorf, N.; Leube, W.; Schnablegger, H.; Regenbrecht, M.; Akari, S.; Lindner, P.; Böttcher, C., Fusion of charged block copolymer micelles into toroid networks. *J. Phys. Chem. B* **1999**, *103* (32), 6657-6668.

107. Kim, T. H.; Huh, J.; Hwang, J.; Kim, H.-C.; Kim, S. H.; Sohn, B.-H.; Park, C., Ordered arrays of PS-b-P4VP micelles by fusion and fission process upon solvent annealing. *Macromolecules* **2009**, *42* (17), 6688-6697.
108. Esselink, F.; Dormidontova, E.; Hadziioannou, G., Evolution of block copolymer micellar size and structure evidenced with cryo electron microscopy. *Macromolecules* **1998**, *31* (9), 2925-2932.
109. Dormidontova, E. E., Micellization kinetics in block copolymer solutions: Scaling model. *Macromolecules* **1999**, *32* (22), 7630-7644.
110. Choueiri, R. M.; Klinkova, A.; Thérien-Aubin, H. I. s.; Rubinstein, M.; Kumacheva, E., Structural transitions in nanoparticle assemblies governed by competing nanoscale forces. *J. Am. Chem. Soc.* **2013**, *135* (28), 10262-10265.
111. Pradhan, N.; Reifsnnyder, D.; Xie, R.; Aldana, J.; Peng, X., Surface ligand dynamics in growth of nanocrystals. *J. Am. Chem. Soc.* **2007**, *129* (30), 9500-9509.
112. Schlenoff, J. B.; Li, M.; Ly, H., Stability and self-exchange in alkanethiol monolayers. *J. Am. Chem. Soc.* **1995**, *117* (50), 12528-12536.
113. Yin, Y.; Alivisatos, A. P., Colloidal nanocrystal synthesis and the organic–inorganic interface. *Nature* **2004**, *437* (7059), 664.
114. Lehn, J.-M., *Supramolecular chemistry*. Vch, Weinheim: 1995; Vol. 1.
115. Lehn, J. M., Supramolecular chemistry—scope and perspectives molecules, supermolecules, and molecular devices (Nobel Lecture). *Angew. Chem. Int. Ed.* **1988**, *27* (1), 89-112.
116. Kolesnichenko, I. V.; Anslyn, E. V., Practical applications of supramolecular chemistry. *Chem. Soc. Rev.* **2017**.
117. Mattia, E.; Otto, S., Supramolecular systems chemistry. *Nat. Nanotechnol.* **2015**, *10* (2), 111.

118. Schatz, C.; Louguet, S.; Le Meins, J. F.; Lecommandoux, S., Polysaccharide-block-polypeptide Copolymer Vesicles: Towards Synthetic Viral Capsids. *Angew Chem Int Edit* **2009**, *48* (14), 2572-2575.
119. Blanz, A.; Madsen, J.; Battaglia, G.; Ryan, A. J.; Armes, S. P., Mechanistic Insights for Block Copolymer Morphologies: How Do Worms Form Vesicles? *J. Am. Chem. Soc.* **2011**, *133* (41), 16581-16587.
120. Zhang, S.; Marini, D. M.; Hwang, W.; Santoso, S., Design of nanostructured biological materials through self-assembly of peptides and proteins. *Curr. Opin. Chem. Biol.* **2002**, *6* (6), 865-871.
121. Petka, W. A.; Harden, J. L.; McGrath, K. P.; Wirtz, D.; Tirrell, D. A., Reversible hydrogels from self-assembling artificial proteins. *Science* **1998**, *281* (5375), 389-392.
122. Marsh, E. N. G.; DeGrado, W. F., Noncovalent self-assembly of a heterotetrameric diiron protein. *Proc. Natl. Acad. Sci.* **2002**, *99* (8), 5150-5154.
123. Douglas, S. M.; Dietz, H.; Liedl, T.; Högberg, B.; Graf, F.; Shih, W. M., Self-assembly of DNA into nanoscale three-dimensional shapes. *Nature* **2009**, *459* (7245), 414-418.
124. Aggeli, A.; Nyrkova, I. A.; Bell, M.; Harding, R.; Carrick, L.; McLeish, T. C.; Semenov, A. N.; Boden, N., Hierarchical self-assembly of chiral rod-like molecules as a model for peptide  $\beta$ -sheet tapes, ribbons, fibrils, and fibers. *Proc. Natl. Acad. Sci.* **2001**, *98* (21), 11857-11862.
125. He, Y.; Mao, C., Balancing flexibility and stress in DNA nanostructures. *Chemical communications* **2006**, (9), 968-969.
126. Bellomo, E. G.; Wyrsta, M. D.; Pakstis, L.; Pochan, D. J.; Deming, T. J., Stimuli-responsive polypeptide vesicles by conformation-specific assembly. *Nat Mater* **2004**, *3* (4), 244-248.
127. Wooley, K. L.; Fréchet, J. M.; Hawker, C. J., Influence of shape on the reactivity and properties of dendritic, hyperbranched and linear aromatic polyesters. *Polymer* **1994**, *35* (21), 4489-4495.

128. Okamoto, K.; Luscombe, C. K., Controlled polymerizations for the synthesis of semiconducting conjugated polymers. *Polym. Chem.* **2011**, *2* (11), 2424-2434.
129. Wu, D.; Huang, Y.; Xu, F.; Mai, Y.; Yan, D., Recent advances in the solution self - assembly of amphiphilic “rod - coil” copolymers. *J. Polym. Sci., Part A: Polym. Chem.* **2017**.
130. Olsen, B. D.; Segalman, R. A., Self-assembly of rod-coil block copolymers. *Materials Science and Engineering: R: Reports* **2008**, *62* (2), 37-66.
131. Jenekhe, S. A.; Chen, X. L., Self-assembled aggregates of rod-coil block copolymers and their solubilization and encapsulation of fullerenes. *Science* **1998**, *279* (5358), 1903-1907.
132. Jenekhe, S. A.; Chen, X. L., Self-assembly of ordered microporous materials from rod-coil block copolymers. *Science* **1999**, *283* (5400), 372-375.
133. Jiang, T.; Wang, L.; Lin, S.; Lin, J.; Li, Y., Structural evolution of multicompart ment micelles self-assembled from linear ABC triblock copolymer in selective solvents. *Langmuir* **2011**, *27* (10), 6440-6448.
134. Zhu, X.; Guan, Z.; Lin, J.; Cai, C., Strip-Pattern-Spheres Self-Assembled from Polypeptide-Based Polymer Mixtures: Structure and Defect Features. *Scientific Reports* **2016**, *6*.
135. He, X.; Hsiao, M.-S.; Boott, C. E.; Harniman, R. L.; Nazemi, A.; Li, X.; Winnik, M. A.; Manners, I., Two-dimensional assemblies from crystallizable homopolymers with charged termini. *Nat Mater* **2017**.
136. Khalatur, P.; Khokhlov, A.; Mologin, D., Simulation of self-associating polymer systems. II. Rheological properties. *J. Chem. Phys.* **1998**, *109* (21), 9614-9622.



137. Fu, C.-L.; Sun, Z.-Y.; An, L.-J., Relationship between Structural Gel and Mechanical Gel for ABA Triblock Copolymer in Solutions: A Molecular Dynamics Simulation. *J. Phys. Chem. B* **2011**, *115* (39), 11345-11351.
138. Li, X.; Deng, M.; Liu, Y.; Liang, H., Dissipative particle dynamics simulations of toroidal structure formations of amphiphilic triblock copolymers. *J. Phys. Chem. B* **2008**, *112* (47), 14762-14765.
139. Guo, L.; Luijten, E., Reversible gel formation of triblock copolymers studied by molecular dynamics simulation. *J. Polym. Sci., Part B: Polym. Phys.* **2005**, *43* (8), 959-969.
140. Azzam, T.; Eisenberg, A., Fully collapsed (kippah) vesicles: preparation and characterization. *Langmuir* **2010**, *26* (13), 10513-10523.
141. Meeuwissen, S. A.; Kim, K. T.; Chen, Y.; Pochan, D. J.; van Hest, J., Controlled shape transformation of polymersome stomatocytes. *Angew. Chem., Int. Ed.* **2011**, *50* (31), 7070-7073.
142. Kim, K. T.; Zhu, J.; Meeuwissen, S. A.; Cornelissen, J. J.; Pochan, D. J.; Nolte, R. J.; van Hest, J. C., Polymersome stomatocytes: controlled shape transformation in polymer vesicles. *J. Am. Chem. Soc.* **2010**, *132* (36), 12522-12524.
143. Rikken, R.; Engelkamp, H.; Nolte, R.; Maan, J.; Van Hest, J.; Wilson, D.; Christianen, P., Shaping polymersomes into predictable morphologies via out-of-equilibrium self-assembly. *Nat Commun* **2016**, *7*.
144. Groot, R. D.; Warren, P. B., Dissipative particle dynamics: Bridging the gap between atomistic and mesoscopic simulation. *J. Chem. Phys* **1997**, *107* (11), 4423-4435.
145. Perlmutter, J. D.; Qiao, C.; Hagan, M. F., Viral genome structures are optimal for capsid assembly. *Elife* **2013**, *2*.

146. Brown, J. C.; Newcomb, W. W., Herpesvirus capsid assembly: insights from structural analysis. *Curr Opin Virol.* **2011**, *1* (2), 142-149.
147. Tanner, P.; Baumann, P.; Enea, R.; Onaca, O.; Palivan, C.; Meier, W., Polymeric vesicles: from drug carriers to nanoreactors and artificial organelles. *Accounts Chem Res* **2011**, *44* (10), 1039-1049.
148. Hickey, R. J.; Koski, J.; Meng, X.; Riggleman, R. A.; Zhang, P.; Park, S.-J., Size-controlled self-assembly of superparamagnetic polymersomes. *ACS Nano* **2014**, *8* (1), 495-502.
149. Geiger, W. E., Reflections on future directions in organometallic electrochemistry. *Organometallics* **2011**, *30* (1), 28-31.
150. Shi, S.; Liu, D.; Wang, X., The Effect of Solution Conditions on the Driving Forces for Self-Assembly of a Pyrene Molecule. *Chem. - Eur. J.* **2017**, *23* (41), 9736-9740.
151. Wurthner, F., Perylene bisimide dyes as versatile building blocks for functional supramolecular architectures. *Chem Commun* **2004**, (14), 1564-1579.
152. Yamamoto, Y.; Fukushima, T.; Suna, Y.; Ishii, N.; Saeki, A.; Seki, S.; Tagawa, S.; Taniguchi, M.; Kawai, T.; Aida, T., Photoconductive coaxial nanotubes of molecularly connected electron donor and acceptor layers. *Science* **2006**, *314* (5806), 1761-4.
153. Wurthner, F.; Saha-Moller, C. R.; Fimmel, B.; Ogi, S.; Leowanawat, P.; Schmidt, D., Perylene Bisimide Dye Assemblies as Archetype Functional Supramolecular Materials. *Chem Rev* **2016**, *116* (3), 962-1052.
154. Cho, J.; Cheon, K. H.; Ahn, H.; Park, K. H.; Kwon, S. K.; Kim, Y. H.; Chung, D. S., High Charge-Carrier Mobility of 2.5 cm<sup>2</sup> V<sup>-1</sup> s<sup>-1</sup> from a Water-Borne Colloid of a Polymeric Semiconductor via Smart Surfactant Engineering. *Adv Mater* **2015**, *27* (37), 5587-5592.

155. Hoeben, F. J. M.; Jonkheijm, P.; Meijer, E. W.; Schenning, A. P. H. J., About Supramolecular Assemblies of  $\pi$ -Conjugated Systems. *Chemical Reviews* **2005**, *105* (4), 1491-1546.
156. Zang, L.; Che, Y.; Moore, J. S., One-Dimensional Self-Assembly of Planar  $\pi$ -Conjugated Molecules: Adaptable Building Blocks for Organic Nanodevices. *Accounts Chem Res* **2008**, *41* (12), 1596-1608.
157. Li, C.; Liu, M.; Pschirer, N. G.; Baumgarten, M.; Müllen, K., Polyphenylene-Based Materials for Organic Photovoltaics. *Chem Rev* **2010**, *110* (11), 6817-6855.
158. Lei, Y.; Liao, Q.; Fu, H.; Yao, J., Orange–Blue–Orange Triblock One-Dimensional Heterostructures of Organic Microrods for White-Light Emission. *J. Am. Chem. Soc.* **2010**, *132* (6), 1742-1743.
159. Wang, S.; Zhang, Y.; Xia, Y.; Song, B., Polymorphic transformation towards formation of nanotubes by self-assembly of an achiral molecule. *Nanoscale* **2015**, *7* (42), 17848-17854.
160. Chen, S.; Slattum, P.; Wang, C.; Zang, L., Self-Assembly of Perylene Imide Molecules into 1D Nanostructures: Methods, Morphologies, and Applications. *Chem Rev* **2015**, *115* (21), 11967-11998.
161. Grimme, S., Do Special Noncovalent  $\pi$ – $\pi$  Stacking Interactions Really Exist? *Angew. Chem., Int. Ed.* **2008**, *47* (18), 3430-3434.
162. Martinez, C. R.; Iverson, B. L., Rethinking the term "pi-stacking". *Chem Sci* **2012**, *3* (7), 2191-2201.
163. Yang, L. X.; Brazier, J. B.; Hubbard, T. A.; Rogers, D. M.; Cockroft, S. L., Can Dispersion Forces Govern Aromatic Stacking in an Organic Solvent? *Angew Chem Int Edit* **2016**, *55* (3), 912-916.
164. Wheeler, S. E., Understanding Substituent Effects in Noncovalent Interactions Involving Aromatic Rings. *Accounts Chem Res* **2013**, *46* (4), 1029-1038.

165. Yang, L.; Brazier, J. B.; Hubbard, T. A.; Rogers, D. M.; Cockroft, S. L., Can Dispersion Forces Govern Aromatic Stacking in an Organic Solvent? *Angew. Chem., Int. Ed.* **2016**, *55* (3), 912-916.
166. Price, S. L.; Stone, A. J., The Electrostatic Interactions in Vanderwaals Complexes Involving Aromatic-Molecules. *J Chem Phys* **1987**, *86* (5), 2859-2868.
167. Tsuzuki, S.; Honda, K.; Uchimaru, T.; Mikami, M.; Tanabe, K., Origin of attraction and directionality of the  $\pi/\pi$  interaction: Model chemistry calculations of benzene dimer interaction. *J. Am. Chem. Soc.* **2002**, *124* (1), 104-112.
168. Hunter, C. A.; Sanders, J. K. M., The nature of  $\pi$ - $\pi$  interactions. *J. Am. Chem. Soc.* **1990**, *112* (14), 5525-5534.
169. Matthews, J. R.; Goldoni, F.; Schenning, A. P. H. J.; Meijer, E. W., Non-ionic polythiophenes: a non-aggregating folded structure in water. *Chem Commun* **2005**, (44), 5503-5505.
170. Guckian, K. M.; Schweitzer, B. A.; Ren, R. X. F.; Sheils, C. J.; Tahmassebi, D. C.; Kool, E. T., Factors contributing to aromatic stacking in water: Evaluation in the context of DNA. *J. Am. Chem. Soc.* **2000**, *122* (10), 2213-2222.
171. Murshid, N.; Wang, X., Iron-Carbonyl Aqueous Vesicles (MCsomes) by Hydration of [Fe(CO){CO(CH<sub>2</sub>)<sub>5</sub>CH<sub>3</sub>}(Cp)(PPh<sub>3</sub>)](FcC6): Highly Integrated Colloids with Aggregation - Induced Self - Enhanced IR Absorption (AI - SEIRA). *Chemistry - A European Journal* **2015**, *21* (52), 19223-19230.
172. Murshid, N.; Wang, X., Aqueous Self-Assembly of Multifunctional Metal-Carbonyl Nanovesicles.
173. Murshid, N.; Rahman, M. A.; Wang, X., Aggregation-enhanced IR absorption (AEIRA) of molybdenum-carbonyl organometallic aqueous colloids. *J Organomet Chem* **2016**, *819*, 109-114.

174. Tateishi, Y.; Kai, N.; Noguchi, H.; Uosaki, K.; Nagamura, T.; Tanaka, K., Local conformation of poly(methyl methacrylate) at nitrogen and water interfaces. *Polym. Chem.* **2010**, *1* (3), 303-311.
175. Kroning, A.; Furchner, A.; Adam, S.; Uhlmann, P.; Hinrichs, K., Probing carbonyl-water hydrogen-bond interactions in thin polyoxazoline brushes. *Biointerphases* **2016**, *11* (1).
176. Chandra, A. K.; Zeegers-Huyskens, T., A theoretical investigation of the interaction between substituted carbonyl derivatives and water: Open or cyclic complexes? *J. Comput. Chem.* **2012**, *33* (11), 1131-1141.
177. Murshid, N.; Yuyama, K.-i.; Wu, S.-L.; Wu, K.-Y.; Masuhara, H.; Wang, C.-L.; Wang, X., Highly-integrated, laser manipulable aqueous metal carbonyl vesicles (MCsomes) with aggregation-induced emission (AIE) and aggregation-enhanced IR absorption (AEIRA). *J Mater Chem C* **2016**.
178. Tidhar, Y.; Weissman, H.; Tworowski, D.; Rybtchinski, B., Mechanism of Crystalline Self-Assembly in Aqueous Medium: A Combined Cryo-TEM/Kinetic Study. *Chem. - Eur. J.* **2014**, *20* (33), 10332-10342.
179. Zheng, Y.; Zhou, H.; Liu, D.; Floudas, G.; Wagner, M.; Koynov, K.; Mezger, M.; Butt, H.-J.; Ikeda, T., Supramolecular Thiophene Nanosheets. *Angew. Chem., Int. Ed.* **2013**, *52* (18), 4845-4848.
180. Vybornyi, M.; Rudnev, A. V.; Langenegger, S. M.; Wandlowski, T.; Calzaferri, G.; Häner, R., Formation of Two-Dimensional Supramolecular Polymers by Amphiphilic Pyrene Oligomers. *Angew. Chem., Int. Ed.* **2013**, *52* (44), 11488-11493.
181. Vybornyi, M.; Rudnev, A.; Häner, R., Assembly of Extra-Large Nanosheets by Supramolecular Polymerization of Amphiphilic Pyrene Oligomers in Aqueous Solution. *Chemistry of Materials* **2015**, *27* (4), 1426-1431.

182. Acree Jr, W. E.; Abraham, M. H., Solubility predictions for crystalline polycyclic aromatic hydrocarbons (PAHs) dissolved in organic solvents based upon the Abraham general solvation model. *Fluid Phase Equilib.* **2002**, *201* (2), 245-258.
183. Qin, L.; Lu, B.; Xu, J.; Zhang, G.; Zhang, S., Novel functionalized conjugated polypyrene with polyacrylate: synthesis, electrochemistry, luminescence, and chemical sensing properties. *Rsc Adv* **2014**, *4* (54), 28368-28376.
184. Winnik, F. M., Photophysics of Preassociated Pyrenes in Aqueous Polymer-Solutions and in Other Organized Media. *Chem Rev* **1993**, *93* (2), 587-614.
185. Winnik, F. M., Photophysics of preassociated pyrenes in aqueous polymer solutions and in other organized media. *Chem Rev* **1993**, *93* (2), 587-614.
186. Hong, Y.; Lam, J. W.; Tang, B. Z., Aggregation-induced emission. *Chem. Soc. Rev.* **2011**, *40* (11), 5361-5388.
187. Datta, S.; Grant, D. J. W., Effect of supersaturation on the crystallization of phenylbutazone polymorphs. *Cryst. Res. Technol.* **2005**, *40* (3), 233-242.
188. Blokzijl, W.; Engberts, J. B. F. N., Hydrophobic Effects. Opinions and Facts. *Angew. Chem. Int. Ed.* **1993**, *32* (11), 1545-1579.
189. Israelachvili, J.; Wennerström, H., Role of hydration and water structure in biological and colloidal interactions. *Nature* **1996**, *379* (6562), 219-225.
190. Ball, P., Water as an active constituent in cell biology. *Chem Rev* **2008**, *108* (1), 74-108.
191. Ball, P., Water is an active matrix of life for cell and molecular biology. *Proc. Natl. Acad. Sci.* **2017**, 201703781.

192. Wielgus-Kutrowska, B.; Narczyk, M.; Buszko, A.; Bzowska, A.; Clark, P. L., Folding and unfolding of a non-fluorescent mutant of green fluorescent protein. *J. Phys. Condens. Matter* **2007**, *19* (28), 285223-285223.
193. Baskakov, I. V.; Legname, G.; Prusiner, S. B.; Cohen, F. E., Folding of prion protein to its native  $\alpha$ -helical conformation is under kinetic control. *J Biol Chem* **2001**, *276* (23), 19687-19690.
194. Pace, C. N.; Fu, H.; Fryar, K. L.; Landua, J.; Trevino, S. R.; Shirley, B. A.; Hendricks, M. M.; Imura, S.; Gajiwala, K.; Scholtz, J. M., Contribution of hydrophobic interactions to protein stability. *J Mol Biol* **2011**, *408* (3), 514-528.
195. Liu, J.; Chakraborty, S.; Hosseinzadeh, P.; Yu, Y.; Tian, S.; Petrik, I.; Bhagi, A.; Lu, Y., Metalloproteins containing cytochrome, iron–sulfur, or copper redox centers. *Chem. Rev* **2014**, *114* (8), 4366-4469.
196. Dey, A.; Jenney, F. E.; Adams, M. W. W.; Babini, E.; Takahashi, Y.; Fukuyama, K.; Hodgson, K. O.; Hedman, B.; Solomon, E. I., Solvent tuning of electrochemical potentials in the active sites of HiPIP versus ferredoxin. *Science* **2007**, *318* (5855), 1464-1468.
197. Ma, C. D.; Wang, C.; Acevedo-Vélez, C.; Gellman, S. H.; Abbott, N. L., Modulation of hydrophobic interactions by proximally immobilized ions. *Nature* **2015**, *517* (7534), 347-350.
198. Patel, A. J.; Varilly, P.; Jamadagni, S. N.; Hagan, M. F.; Chandler, D.; Garde, S., Sitting at the edge: How biomolecules use hydrophobicity to tune their interactions and function. *J. Phys. Chem. B* **2012**, *116* (8), 2498-2503.
199. Tielrooij, K. J.; Garcia-Araez, N.; Bonn, M.; Bakker, H. J., Cooperativity in Ion Hydration. *Science* **2010**, *328* (5981), 1006-1009.

200. Ortony, J. H.; Qiao, B.; Newcomb, C. J.; Keller, T. J.; Palmer, L. C.; Deiss-Yehiely, E.; Olvera de la Cruz, M.; Han, S.; Stupp, S. I., Water Dynamics from the Surface to the Interior of a Supramolecular Nanostructure. *J. Am. Chem. Soc.* **2017**, *139* (26), 8915-8921.
201. Davis, J. G.; Gierszal, K. P.; Wang, P.; Ben-Amotz, D., Water structural transformation at molecular hydrophobic interfaces. *Nature* **2012**, *491* (7425), 582-585.
202. Jiang, L.; Cao, S.; Cheung, P. P.; Zheng, X.; Leung, C. W. T.; Peng, Q.; Shuai, Z.; Tang, B. Z.; Yao, S.; Huang, X., Real-time monitoring of hydrophobic aggregation reveals a critical role of cooperativity in hydrophobic effect. *Nat Commun* **2017**, *8*, 15639.
203. Cornelissen, J. J. L. M.; Fischer, M.; Sommerdijk, N. A. J. M.; Nolte, R. J. M., Helical Superstructures from Charged Poly(styrene)-Poly(isocyanodipeptide) Block Copolymers. *Science* **1998**, *280* (5368), 1427-1430.
204. King, R. B., Reactions of Alkali Metal Derivatives of Metal Carbonyls. II. Reactions between Acid Chloride Derivatives and the Sodium Derivative of Cyclopentadienyliron Dicarbonyl. *J. Am. Chem. Soc.* **1963**, *85* (13), 1918-1922.
205. Frank, H. S.; Evans, M. W., Free volume and entropy in condensed systems III. Entropy in binary liquid mixtures; partial molal entropy in dilute solutions; structure and thermodynamics in aqueous electrolytes. *J. Chem. Phys.* **1945**, *13* (11), 507-532.
206. Raschke, T. M.; Tsai, J.; Levitt, M., Quantification of the hydrophobic interaction by simulations of the aggregation of small hydrophobic solutes in water. *Proc Natl Acad Sci U S A* **2001**, *98* (11), 5965-9.
207. Espósito, B. P.; Breuer, W.; Cabantchik, Z. I., Design and applications of methods for fluorescence detection of iron in biological systems. *Biochem. Soc. Trans.* **2002**, *30* (4), 729-732.



208. Scheu, R.; Rankin, B. M.; Chen, Y.; Jena, K. C.; Ben-Amotz, D.; Roke, S., Charge asymmetry at aqueous hydrophobic interfaces and hydration shells. *Angew. Chem. Int. Ed.* **2014**, *53* (36), 9560-9563.
209. Grzelczak, M.; Vermant, J.; Furst, E. M.; Liz-Marzán, L. M., Directed Self-Assembly of Nanoparticles. *ACS Nano* **2010**, *4* (7), 3591-3605.
210. Gröschel, A. H.; Walther, A.; Löbbling, T. I.; Schacher, F. H.; Schmalz, H.; Müller, A. H. E., Guided hierarchical co-assembly of soft patchy nanoparticles. *Nature* **2013**, *503* (7475), 247-251.
211. Lunn, D. J.; Gould, O. E. C.; Whittell, G. R.; Armstrong, D. P.; Mineart, K. P.; Winnik, M. A.; Spontak, R. J.; Pringle, P. G.; Manners, I., Microfibrils and macroscopic films from the coordination-driven hierarchical self-assembly of cylindrical micelles. *Nat Commun* **2016**, *7*, ncomms12371-ncomms12371.
212. Voskuhl, J.; Jan Ravoo, B., Molecular recognition of bilayer vesicles. *Chem. Soc. Rev.* **2009**, *38* (2), 495-505.
213. Zhao, J.; Zhang, Y. M.; Sun, H. L.; Chang, X. Y.; Liu, Y., Multistimuli-responsive supramolecular assembly of cucurbituril/cyclodextrin pairs with an azobenzene-containing bispyridinium guest. *Chem. - Eur. J.* **2014**, *20* (46), 15108-15.
214. Murshid, N.; Yuyama, K.-i.; Wu, S.-L.; Wu, K.-Y.; Masuhara, H.; Wang, C.-L.; Wang, X., Highly-integrated, laser manipulable aqueous metal carbonyl vesicles (MCsomes) with aggregation-induced emission (AIE) and aggregation-enhanced IR absorption (AEIRA). *J. Mater. Chem. C* **2016**, *4* (23), 5231-5240.

215. Hermans, T. M.; Broeren, M. A. C.; Gomopoulos, N.; Van Der Schoot, P.; Van Genderen, M. H. P.; Sommerdijk, N. A. J. M.; Fytas, G.; Meijer, E. W., Self-assembly of soft nanoparticles with tunable patchiness. *Nat. Nanotechnol.* **2009**, *4* (11), 721-726.
216. Rulkens, R.; Lough, A. J.; Manners, I.; Lovelace, S. R.; Grant, C.; Geiger, W. E., Linear Oligo(ferrocenyldimethylsilanes) with between Two and Nine Ferrocene Units: Electrochemical and Structural Models for Poly(ferrocenylsilane) High Polymers. *J. Am. Chem. Soc.* **1996**, *118* (50), 12683-12695.
217. Tang, Z.; Kotov, N. A.; Giersig, M., Spontaneous Organization of Single CdTe Nanoparticles into Luminescent Nanowires. *Science* **2002**, *297* (5579), 237-240.
218. Hill, J. P.; Jin, W.; Kosaka, A.; Fukushima, T.; Ichihara, H.; Shimomura, T.; Ito, K.; Hashizume, T.; Ishii, N.; Aida, T., Self-Assembled Hexa-peri-hexabenzocoronene Graphitic Nanotube. *Science* **2004**, *304* (5676), 1481-1483.
219. Bong, D. T.; Clark, T. D.; Granja, J. R.; Ghadiri, M. R., Self-Assembling Organic Nanotubes. *Angew. Chem., Int. Ed.* **2001**, *40* (6), 988-1011.
220. Hu, Q.; Wang, Y.; Jia, J.; Wang, C.; Feng, L.; Dong, R.; Sun, X.; Hao, J., Photoresponsive chiral nanotubes of achiral amphiphilic azobenzene. *Soft Matter* **2012**, *8* (45), 11492-11498.
221. Selinger, J. V.; MacKintosh, F. C.; Schnur, J. M., Theory of cylindrical tubules and helical ribbons of chiral lipid membranes. *Phys Rev E* **1996**, *53* (4), 3804-3818.
222. Riley, K. E.; Hobza, P., On the Importance and Origin of Aromatic Interactions in Chemistry and Biodisciplines. *Accounts Chem Res* **2013**, *46* (4), 927-936.

223. Hoshino, M.; Uchida, E.; Norikane, Y.; Azumi, R.; Nozawa, S.; Tomita, A.; Sato, T.; Adachi, S.-i.; Koshihara, S.-y., Crystal Melting by Light: X-ray Crystal Structure Analysis of an Azo Crystal Showing Photoinduced Crystal-Melt Transition. *J. Am. Chem. Soc.* **2014**, *136* (25), 9158-9164.
224. Liang, X.; Asanuma, H.; Komiyama, M., Photoregulation of DNA Triplex Formation by Azobenzene. *J. Am. Chem. Soc.* **2002**, *124* (9), 1877-1883.
225. Wolfenden, R., Interaction of the peptide bond with solvent water: a vapor phase analysis. *Biochemistry-Us* **1978**, *17* (1), 201-204.
226. Ulman, A., *An Introduction to Ultrathin Organic Films: From Langmuir--Blodgett to Self-Assembly*. Academic press: 2013.

## Chapter 8 Appendices

This chapter mainly includes supporting figures for each chapters and dissipative particle dynamic (DPD) simulation methods for chapter 3. In the end of the chapter, synthesis of Fp-based dendrimers was described. Moreover, the preliminary results to explore the function of CO groups in the P(FpP) were discussed. The experimental results included the fabrication of nanoparticles arrays using P(FpP) film as a template and coordination of  $Gd^{3+}$  to P(FpP) MCsomes in water.

### 8.1 Supporting information for Chapter 2

**Table 8.1. The viscosity and refractive index for DMSO at different temperatures.**

| Temperature / °C | Viscosity / cP | Refractive index | Dielectric Constant |
|------------------|----------------|------------------|---------------------|
| 25               | 1.990          | 1.479            | 47.24               |
| 30               | 1.808          | 1.479            | 47.24               |
| 35               | 1.654          | 1.479            | 47.24               |
| 40               | 1.511          | 1.479            | 47.24               |
| 45               | 1.396          | 1.479            | 47.24               |
| 50               | 1.286          | 1.479            | 47.24               |
| 75               | 0.916          | 1.479            | 47.24               |

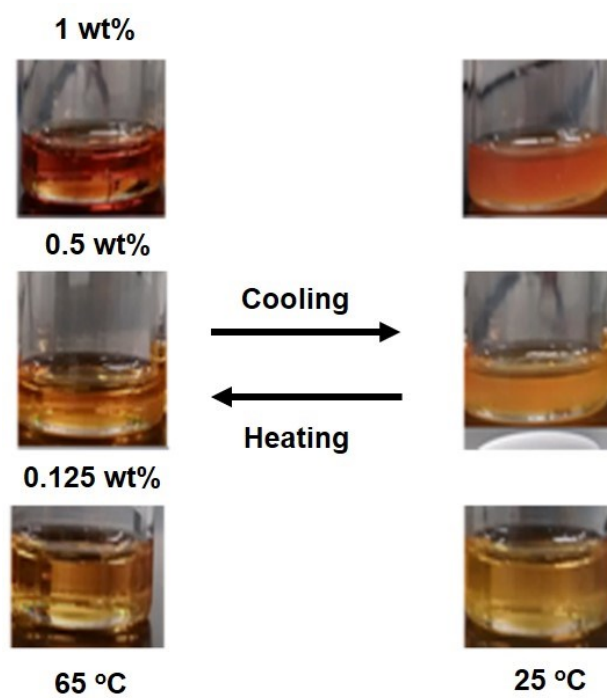


**Figure 8.1. Concentration-dependent thermoresponsive behaviors for the solution of P(FpP) in DMSO.**

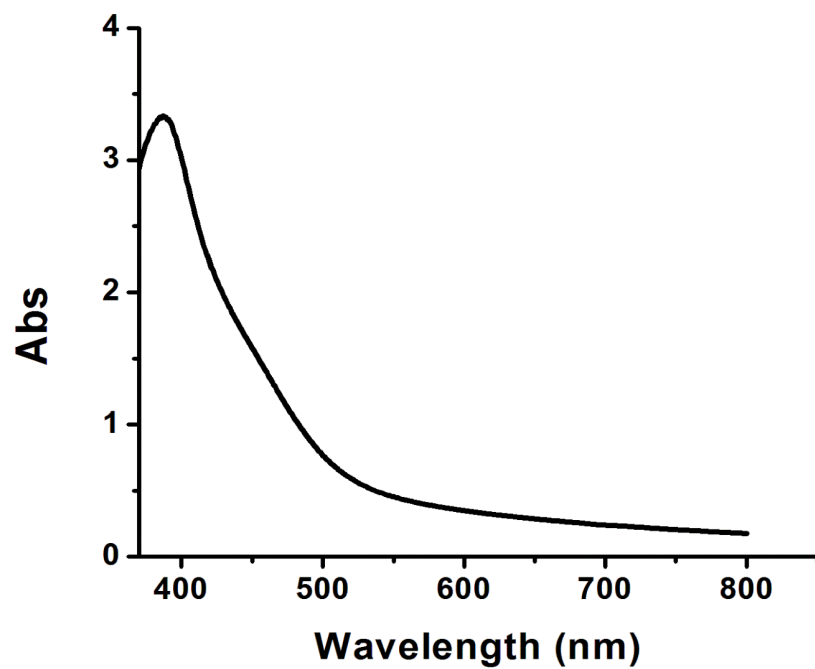


**Figure 8.2.** UV-vis absorption spectrum for the solution of P(FpP) in DMSO at 65 °C.

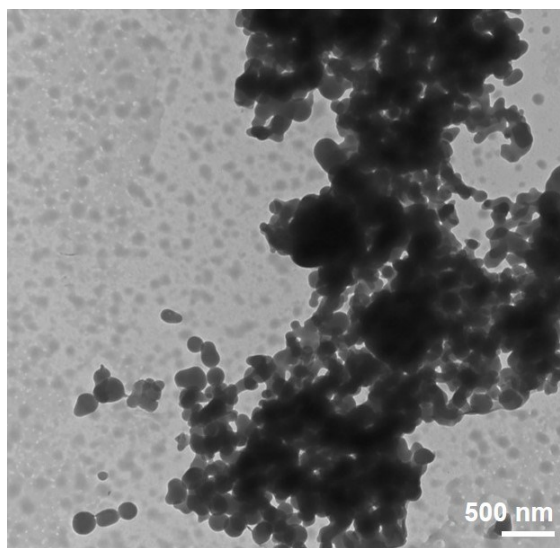


**Figure 8.3.** TEM images for the precipitates of P(FpP) suspension in DMSO at room temperature.

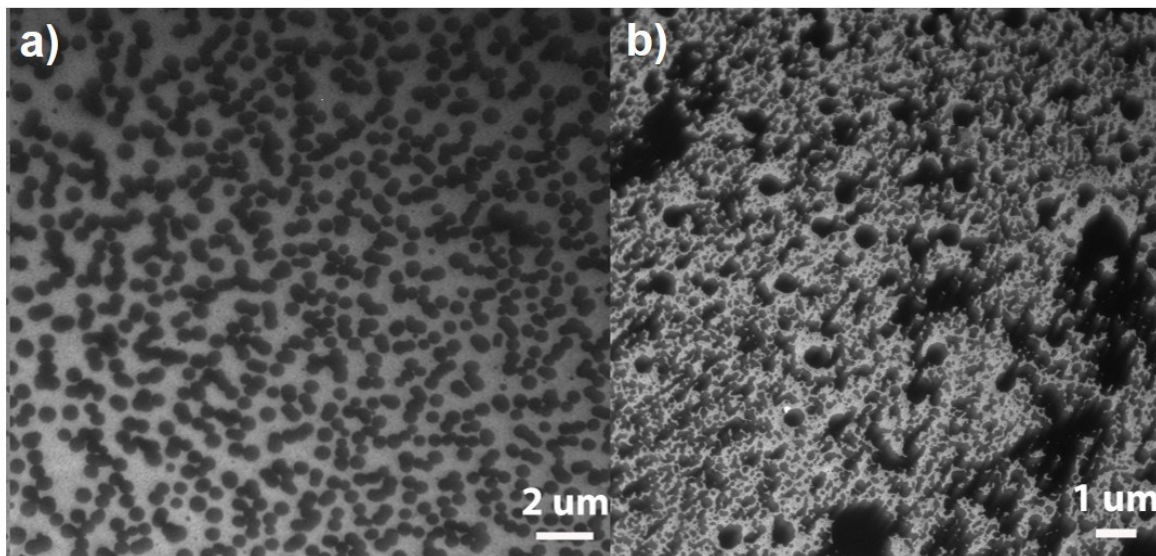


**Figure 8.4.** TEM images of the particles prepared from DMSO solution of P(FpP) a) 0.5 wt% and b) 1 wt%) after cooling to room temperature.

## **8.2 Supporting information for Chapter 3**

**Table 8.2** The repulsive parameter ( $a_{ij}$ ) and the chain stiffness potential ( $\kappa_c$ ) of P(FpP) as a function of temperature.

| Temperature                         | 25°C                                     | 40 °C                                    | 60 °C                                    | 70 °C                              |
|-------------------------------------|--|--|--|------------------------------------|
| The repulsive parameters $a_{ij}$   | $a_{RO} = a_{RP} = 60,$<br>$a_{RS} = 70$ | $a_{RO} = a_{RP} = 50,$<br>$a_{RS} = 60$ | $a_{RO} = a_{RP} = 40,$<br>$a_{RS} = 50$ | $a_{RO} = a_{RP} = a_{RS} =$<br>30 |
| The chain stiffness potential $k_c$ | $k_c = 5k_B T$                           | $k_c = 2k_B T$                           | $k_c = 0k_B T$                           | $k_c = 0k_B T$                     |
| Simulated morphologies              | Nanosheet                                | Nanovesicle                              | Irregular nanoparticle                   | Worm-like nanostructure            |

(Note: 1. R, O, P and S denotes benzyl/Cp, COFeCO,  $(CH_2)_3P$  groups and solvents; 2.  $k_B$  is the Boltzmann constant and T is temperature)

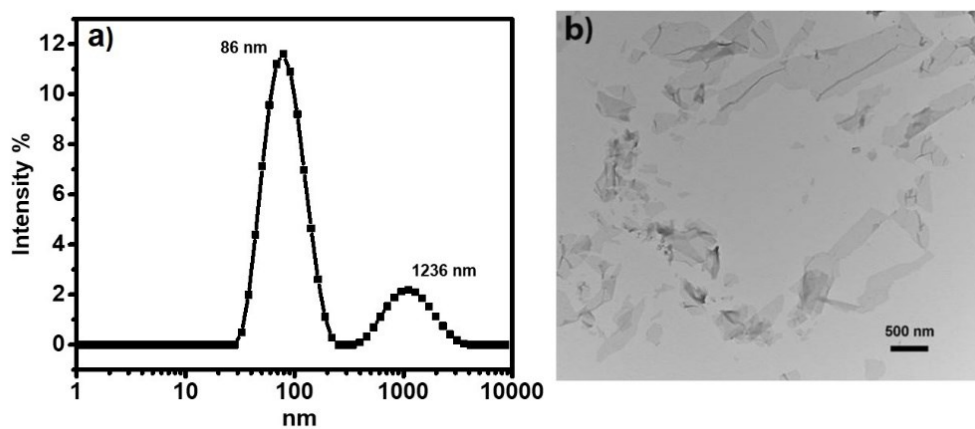


**Figure 8.5 a) The DLS profile of the prepared P(FpP) aggregates at 25 °C. b) nanosheets observed in the TEM images for the prepared P(FpP) aggregates at 25 °C.**



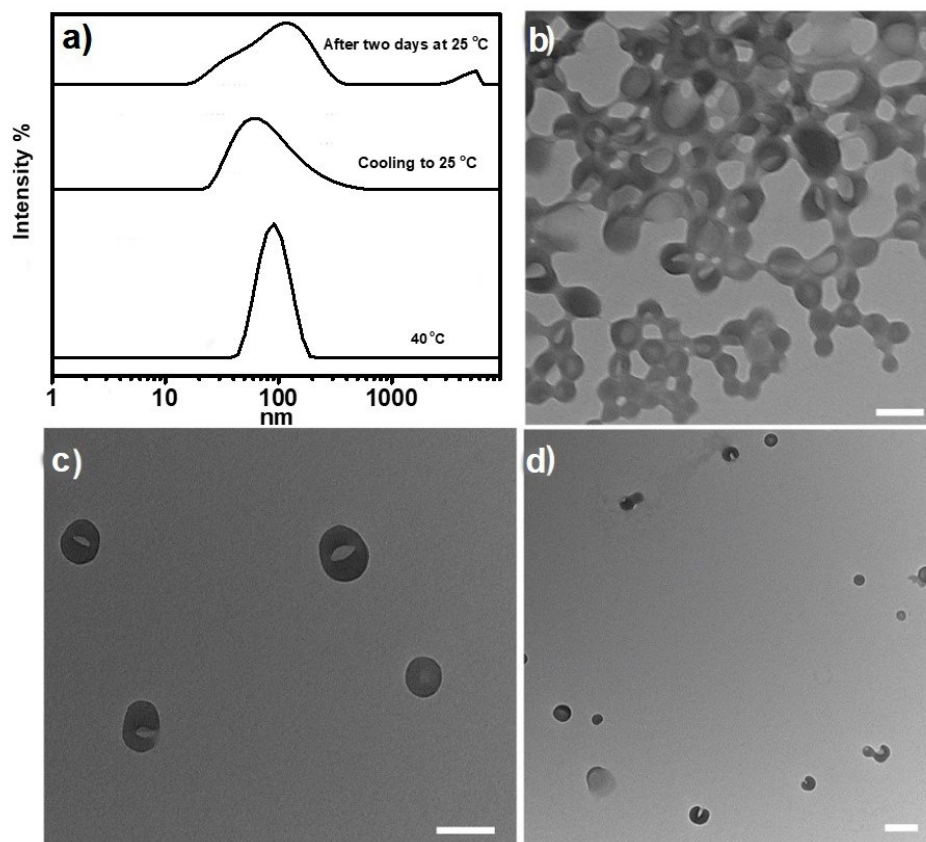


**Figure 8.6 DLS profile of P(FpP) nanovesicles at 40 °C cooling to 25 °C and 25 °C for 2 days TEM images of P(FpP) nanovesicles formed at 40 °C. b) The aggregation of nanovesicles. c) and d) Independent nanovesicles found in the same TEM grid. Scale bar: 100 nm**

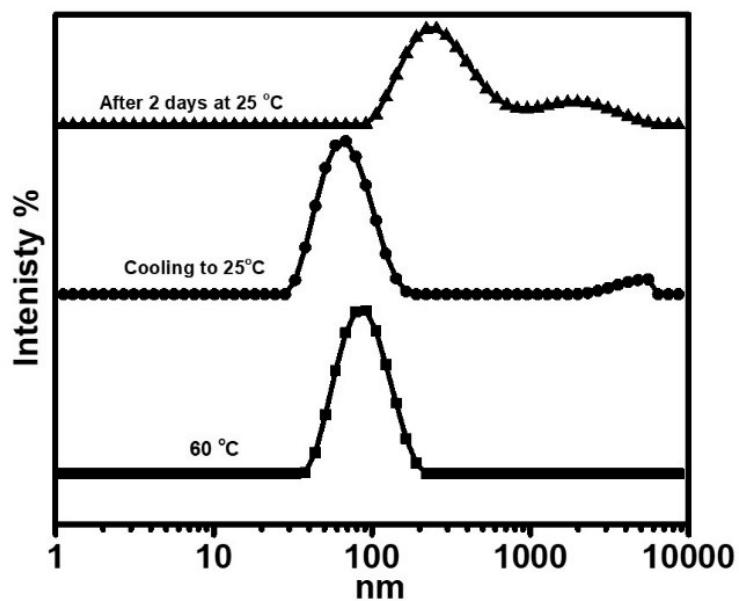


**Figure 8.7 DLS profile of the formed P(FpP) irregular aggregates at 60 °C, cooling to 25 °C and 2 days later at 25 °C.**

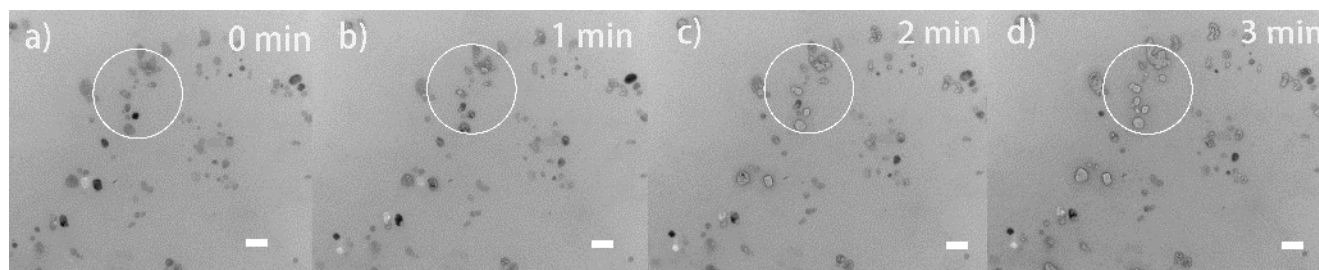


**Figure 8.8 TEM images of the irregular P(FpP) aggregates breaking up with time aging under electron beam of TEM. Scale bar: 100 nm**

### 8.2.1 Dissipative Particle Dynamic (DPD) simulation method

Dissipative particle dynamics (DPD) is a mesoscopic simulation method originated by Hoogerbrugge and Koelman<sup>S1, S2</sup> and developed by Robert and Patrick.<sup>S3</sup> In this method, several neighboring molecules are coarse-grained into a single particle. Newton's equations of motion are applied to calculate the trajectories of beads in the system. A modified velocity-Verlet algorithm is used for the propagation of the positions and velocities of the beads.

According to the DPD method the force  $F_i$  acting on a coarse-grained DPD bead,  $i$  is the sum of the conservative force, dissipative force, and random force, represented by the following equation:

$$\mathbf{F}_i = \sum_{i \neq j} (\mathbf{F}_{ij}^C + \mathbf{F}_{ij}^D + \mathbf{F}_{ij}^R) \quad (\text{S1})$$

The three kinds of forces on the right side of the above equation take the following forms:

$$\mathbf{F}_{ij}^C = \begin{cases} a_{ij} (1 - r_{ij} / r_c) \hat{\mathbf{r}}_{ij} & r_{ij} < r_c \\ 0 & r_{ij} \geq r_c \end{cases} \quad (\text{S2})$$

$$\mathbf{F}_{ij}^D = \begin{cases} -\gamma (1 - r_{ij} / r_c)^2 (\hat{\mathbf{r}}_{ij} \cdot \mathbf{v}_{ij}) \hat{\mathbf{r}}_{ij} & r_{ij} < r_c \\ 0 & r_{ij} \geq r_c \end{cases} \quad (\text{S3})$$

$$\mathbf{F}_{ij}^R = \begin{cases} (2\gamma k_B T)^{1/2} (1 - r_{ij} / r_c) \theta_{ij} (dt)^{-1/2} \hat{\mathbf{r}}_{ij} & r_{ij} < r_c \\ 0 & r_{ij} \geq r_c \end{cases} \quad (\text{S4})$$

$a_{ij}$  is the repulsive parameter between two arbitrary beads  $i$  and  $j$ ,  $r_{ij}$  is the distance between these two beads  $r_{ij} = |\mathbf{r}_i - \mathbf{r}_j|$ , and  $\hat{\mathbf{r}}_{ij}$  is the unit vector  $\hat{\mathbf{r}}_{ij} = (\mathbf{r}_i - \mathbf{r}_j) / r_{ij}$ .  $r_c$  is the cutoff distance.  $\gamma$  is the strength of the dissipation between bead  $i, j$ . According to our previous work, the friction factor  $\gamma$  was set to 4.5<sup>S4, S5</sup>.

$v_{ij} = v_i - v_j$ .  $\theta_{ij}$  is a random fluctuating variable with Gaussian statistics and has zero mean and unit deviation.

For diblock copolymers, an additional harmonic spring potential  $U_{ij}^s = \frac{1}{2} k_s (r_{ij} - r_0)^2$  is applied on each pair of two bonded beads  $i$  and  $j$ , and the chain stiffness potential  $U_{ijk}^c = \frac{1}{2} k_c (\cos(\theta) - \cos(\theta_0))^2$  is performed on three neighboring beads  $i$ ,  $j$  and  $k$  in rod blocks.

### 8.2.2 $\pi$ - $\pi$ stack conjugate potential

In DPD method, the conservative potential (Equation S2) provides a repulsive force between the interacted particles. However, there are high densities of benzyl and Cp (denoted by R) groups along the polymer chains. The interactions among these groups are p-p stack conjugation. Accordingly, the traditional repulsive force in DPD method is insufficient to simulate the conjugation among R groups. In addition to the potentials in DPD method, an attractive potential should be applied for providing this conjugation. In present work, we adopted the attractive potential as follows<sup>S6</sup>:

$$U_{ij}^{\pi} = -k_{\pi} \cos^2 \left[ \pi (r - r_c) / 2 / (r_{\text{ext}} - r_c) \right] \quad r_c \leq r \leq r_{\text{ext}}$$

(S5)

where  $k_{\pi}$  is the strength of the potential,  $r_c$  is the lower cutoff distance, which equals to the  $r_c$  in DPD method and  $r_{\text{ext}}$  is the upper cutoff distance. This potential is firstly proposed by Cooke et al., which has been adopted to simulate the layer structure formed by phospholipids.

### 8.2.3 Parameter setting

Repulsive parameter. In the DPD method, there is a linear relationship between the Flory-Huggins parameter  $\chi_{ij}$  and interaction parameters  $a_{ij}$ .<sup>S3</sup> Larger  $\chi_{ij}$  means larger  $a_{ij}$ . For beads of the same species,

the repulsive parameters  $a_{ij}$  were set to 25. Since the COFeCO and  $(\text{CH}_2)_3\text{P}$  groups are hydrophilic (hydrogen bonding can be formed among these groups and water), while the benzyl and Cp groups are hydrophobic, we set  $a_{\text{OP}} = a_{\text{OS}} = a_{\text{PS}} = 25$ ,  $a_{\text{RO}} = a_{\text{RP}} = 60$ ,  $a_{\text{RS}} = 75$  at 25 °C, where R, O, P and S denotes to benzyl/Cp, COFeCO,  $(\text{CH}_2)_3\text{P}$  groups and solvents, respectively. The values of repulsive parameters  $a_{\text{RO}}$ ,  $a_{\text{RP}}$  and  $a_{\text{RS}}$  were varied with temperature. In present work, we used Materials Studio (Blend Module) to calculate the values of  $\chi_{ij}$  between those groups at different temperatures. The results are shown in Figure 8.9. It can be seen that the values of  $\chi_{ij}$  for O-P, O-S and P-S pairs almost remain unchanged with varying temperature. However, for the case of R-O, R-P and R-S pairs, the values of  $\chi_{ij}$  are linearly decreased with increasing temperature. Accordingly, we set the  $a_{\text{RO}} = a_{\text{RP}} = 50$ ,  $a_{\text{RS}} = 60$  at 40 °C,  $a_{\text{RO}} = a_{\text{RP}} = 40$ ,  $a_{\text{RS}} = 50$  at 60 °C and  $a_{\text{RO}} = a_{\text{RP}} = a_{\text{RS}} = 35$  at 70 °C.

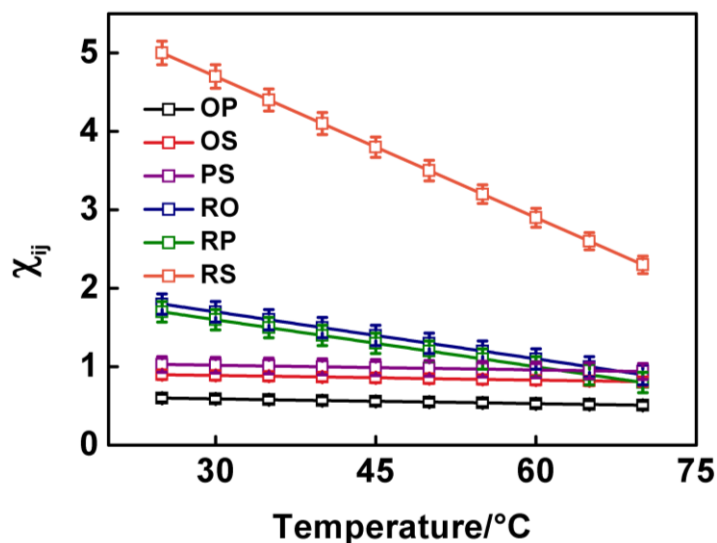


**Figure 8.9.** Values of  $\chi_{ij}$  for the pairs of different species as a function of temperature.

**Harmonic spring potential.** In this work, the equilibrium bond distance  $r_0$  and were set to be  $0.7r_c$ . The values of  $k_s$  were set as  $100k_B T/r_c^2$  ( $k_B$  is the Boltzmann constant and  $T$  is temperature).<sup>S7</sup> These values are constant at different temperatures.

**Chain stiffness potential.** In some cases, the chain conformations may be transformed with temperatures. In the present work, we used Materials Studio to investigate these transformations. The simulation system with one polymer and a certain amount of solvents was constructed using the Amorphous Cell module. Then, using the Discover module, all-atom molecular dynamic simulations were performed under different temperatures. The simulation protocols and the parameters were all chosen according to those in our previous work. With varying the temperature from 25 to 75 °C, the structures of polymers at equilibrium state were obtained after the simulations. Herein, we analyzed the persistence lengths ( $l_p$ ) of the backbones of these polymers under different temperatures. The formula of  $l_p$  is as follows:<sup>S8</sup>

$$\langle \cos(\theta_i) \rangle = \exp(-l_b / l_p)$$

(S6)

$\theta_i$  is the angle between two neighboring bonds along the chain.  $l_b$  is the average length of all the  $i$  bonds. The profile of  $l_p$  as a function of  $k_a$  is shown as the red profile in Figure 8.10. The value of  $l_p$  is largest at 25 °C, which is approximately 70 nm. When the temperature is lower than 60 °C, with increasing temperature, the value of  $l_p$  is decreased almost linearly. For the case of temperature is higher than 60 °C, the value of  $l_p$  nearly keeps unchanged at 15 nm. The morphologies of polymers at 25, 50 and 75 °C are provided in the inset of Figure 8.10. The profile of  $l_p$  and morphologies of polymers both represent the evolutionary chain stiffness of polymers with varying temperature.

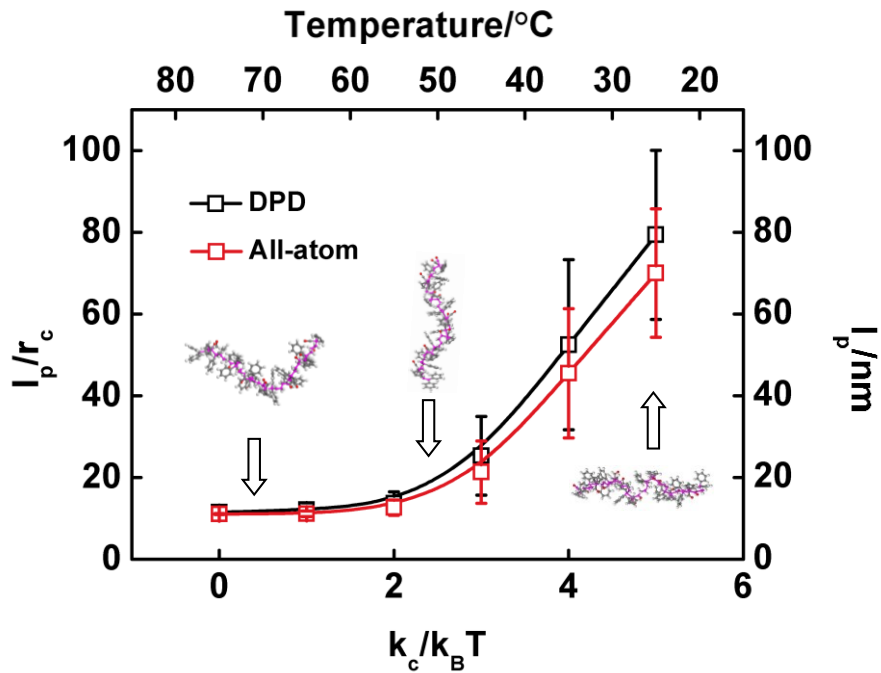


**Figure 8.10. Persistence length as a function of  $k_c$  in DPD simulation and temperature in the all-atom simulation. The all-atom morphologies under different temperatures are shown in the figure.**

In order to denote the transformation of chain stiffness of polymer backbone with changing temperature in our DPD simulations, we reduced the chain stiffness potential  $k_c$  from 5 to 0  $k_B T$  as the temperature was increased from 25 to 70 °C. The equilibrium value of the angle  $\theta_0$  was set to be  $\pi$ . A larger value of  $k_c$  corresponds to a stronger rigidity of polymer chain. Similar to the case of all-atom simulations, the values of  $l_p$  at different temperatures in the DPD simulations were also examined. The statistical result is shown as the black profile in Figure 8.10. It can be seen that this profile is extremely close to that obtained from the all-atom simulations. The value of  $l_p$  almost keeps 10  $r_c$  when  $k_c$  is smaller than 2  $k_B T$ , while it is linearly increased with  $k_c$  for the case of  $k_c > 2 k_B T$ . Accordingly, we can

find a quantitative consistent result between the results from all-atom and DPD simulations, indicating the setting values of  $k_c$  in the DPD simulations can effectively capture the conformations of polymer backbones under various temperatures. Specifically, the value of  $k_c$  was set to 5, 2, 0 and 0  $k_B T$  at 25, 40, 60 and 70 °C, respectively. The  $k_c$  for 60 and 70 °C were both set to 0  $k_B T$  because the  $l_p$  reaches to the smallest under these two temperatures. For clarity, we provide the  $a_{ij}$  and  $k_c$  at 25, 40, 60 and 70 °C adopted in the present work in Table 8.2.

### 8.3 Supporting information for Chapter 4

**Table 8.3 The viscosity and refractive index for THF/water mixed solvents with varied THF contents.**

| <b>THF contents (vol%)</b> | <b>Viscosity/cP</b> | <b>Refractive index</b> | <b>Dielectric Constant</b> |
|----------------------------|---------------------|-------------------------|----------------------------|
| <b>10</b>                  | 0.880               | 1.330                   | 74.20                      |
| <b>20</b>                  | 0.860               | 1.320                   | 67                         |
| <b>30</b>                  | 0.840               | 1.280                   | 60.96                      |
| <b>40</b>                  | 0.820               | 1.220                   | 53.44                      |
| <b>50</b>                  | 0.796               | 1.12                    | 45.30                      |

### 8.4 Supporting information for Chapter 5



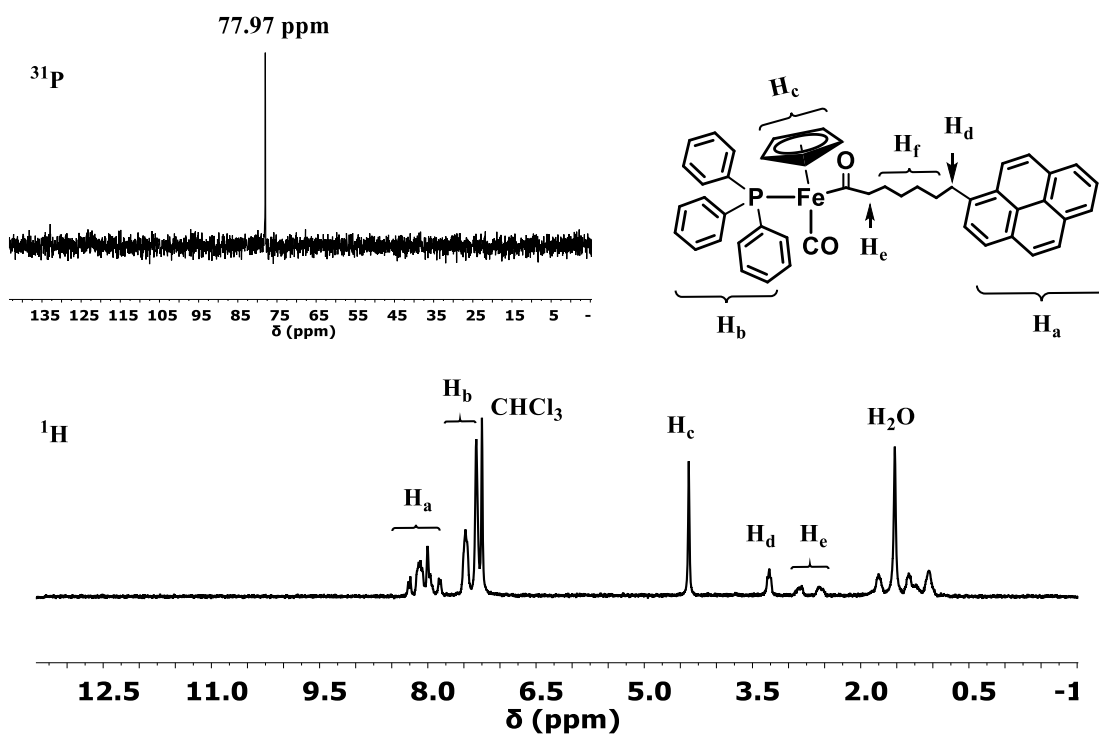


Figure 8.11.  $^1\text{H}$ -NMR and  $^{31}\text{P}$ -NMR spectra of  $\text{FpC}_6\text{Pyrene}$  in  $\text{CDCl}_3$

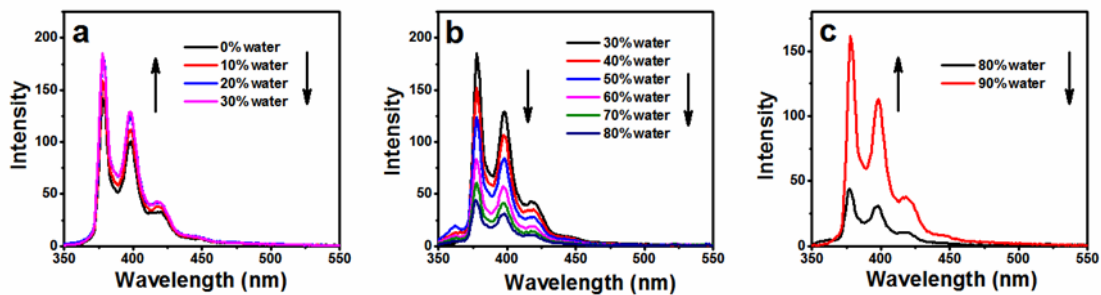


Figure 8.12. The intensity of fluorescent emission as a function of water content in  $\text{DMSO}/\text{water}$  system ( $1.4 \times 10^{-4} \text{ M}$ ).

Figure 8.12 indicates that the intensity of the fluorescent emission increase in the solution of DMSO/water with water content increasing from 0 to 30 vol%. If this enhancement were caused by the variation in the polarity of the mixed solvents, a red shift in the emission should be observed (M. Haidekker, et al. Bioorganic chemistry 2005, 33, 415-425). This is not the case. Viscosity is another possible reason affecting the intensity, but causing no shift in the absorption wavelength (M. Haidekker, et al. Bioorganic Chemistry 2005, 33, 415-425; M. Homocianu et.al Journal of Advanced Research in Physics 2011, 2 (1)). The viscosity of DMSO (*ca.*1.99 centipoises) increases to *ca.*3.73 centipoises when the DMSO/water mixed solvents containing 30% of water (Table 8.4), so the enhancement can be ascribed to the increase in viscosity. The fluorescent intensity for the solution in THF/water also increases with water content increasing from 0 to 60 vol% (Figure 5.3b), which is also attributed to the increase in the viscosity (Table 8.5).

**Table 8.4. The viscosity of DMSO/water\***

| <b>Water content (vol % H<sub>2</sub>O/DMSO)</b> | <b>Viscosity (centipoise)</b> |
|--|-------------------------------|
| 0  | 1.99                          |
| 10   | 2.70                          |
| 20   | 3.45                          |
| 30   | 3.73                          |

\*Journal of Chemical and Engineering Data 7.1 (1962): 100-101.

**Table 8.5. The viscosity of THF/water\***

| Water content (vol % H <sub>2</sub> O/THF) | Viscosity (centipoise) |
|--|------------------------|
| 0  | 0.46                   |
| 10   | 0.66                   |
| 20   | 1.02                   |
| 30   | 1.22                   |
| 40   | 1.49                   |
| 50   | 1.68                   |
| 60   | 1.73                   |

\* Indian Journal of Chemical Technology 1994, 1, 93-97.

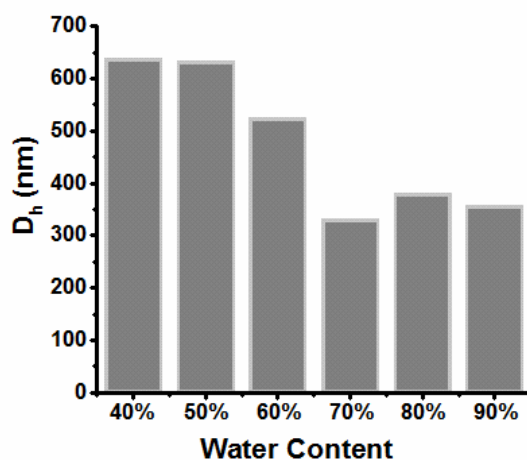


**Figure 8.13. Hydrodynamic diameters ( $D_h$ ) of the colloids assembled from FpC<sub>6</sub>Pyrene in DMSO/water (40-90 vol% water content, concentration:  $1.4 \times 10^{-4}$  M). The experiments were performed right after the preparation of the solution.**

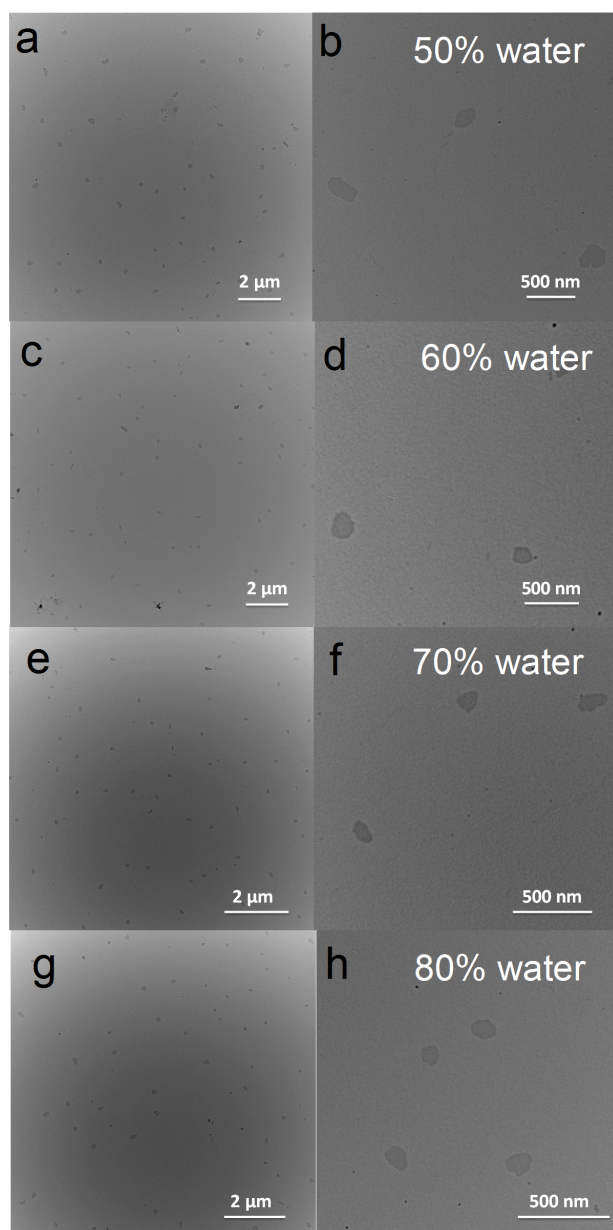


**Figure 8.14. TEM images of FpC<sub>6</sub>Pyrene assemblies formed in DMSO/water solutions (50-80 vol% water content, concentration:  $1.4 \times 10^{-4}$  M). The experiments were performed right after the preparation of the solutions.**

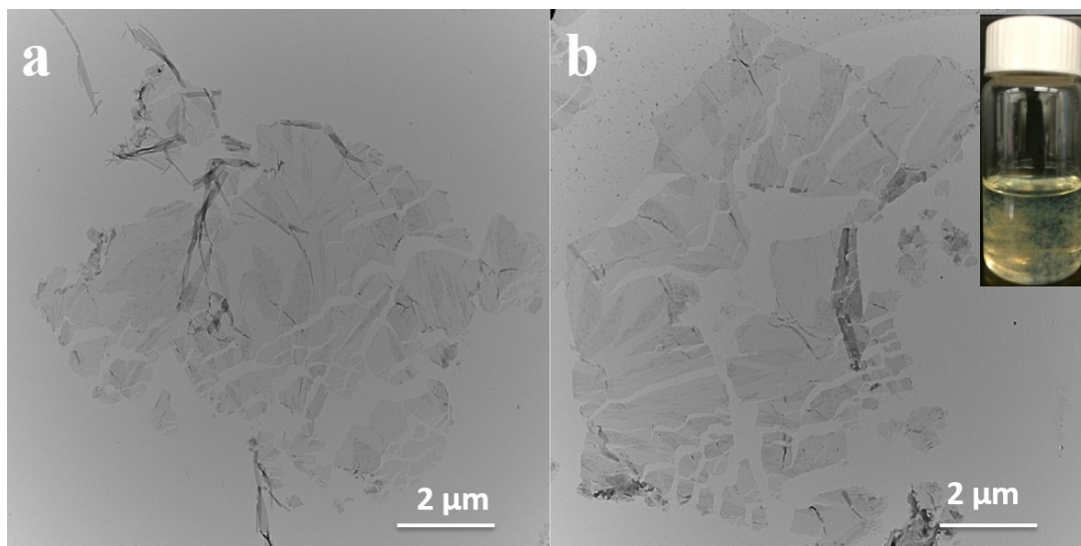


**Figure 8.15. Representative TEM images of the cotton-like suspension formed in DMSO/water solution of FpC<sub>6</sub>Pyrene (40-80 vol% water content, concentration:  $1.4 \times 10^{-4}$  M).**

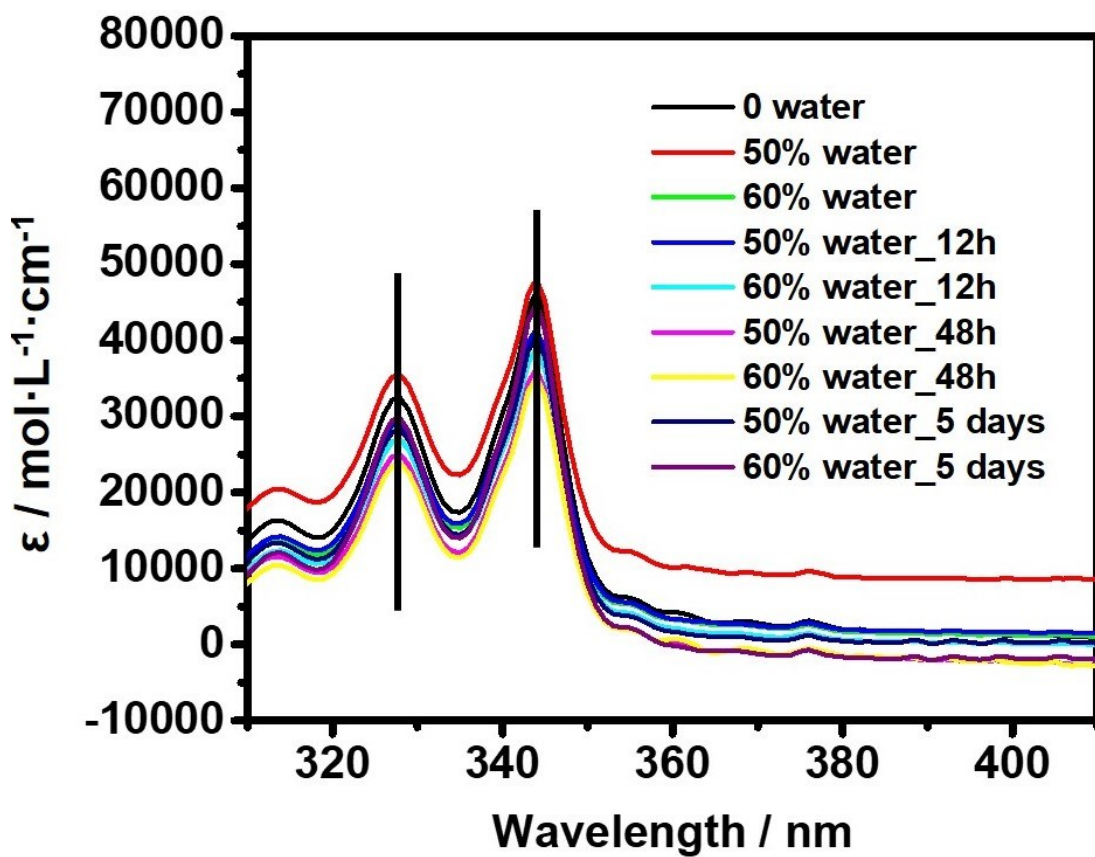
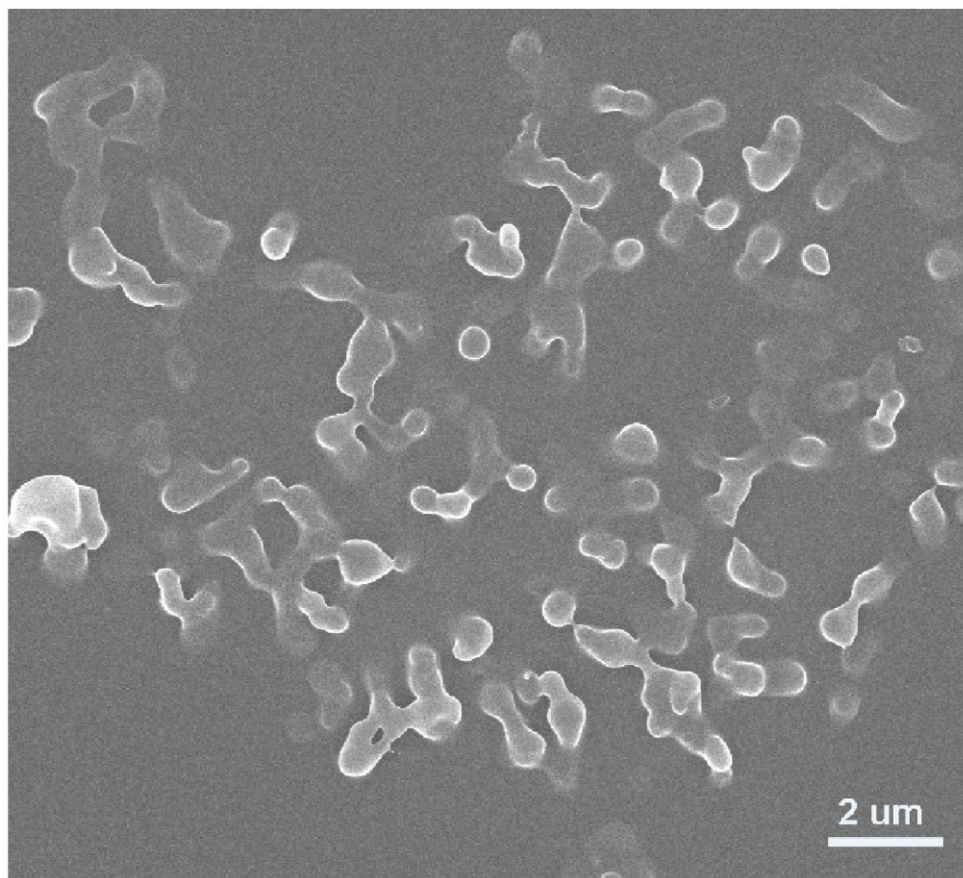
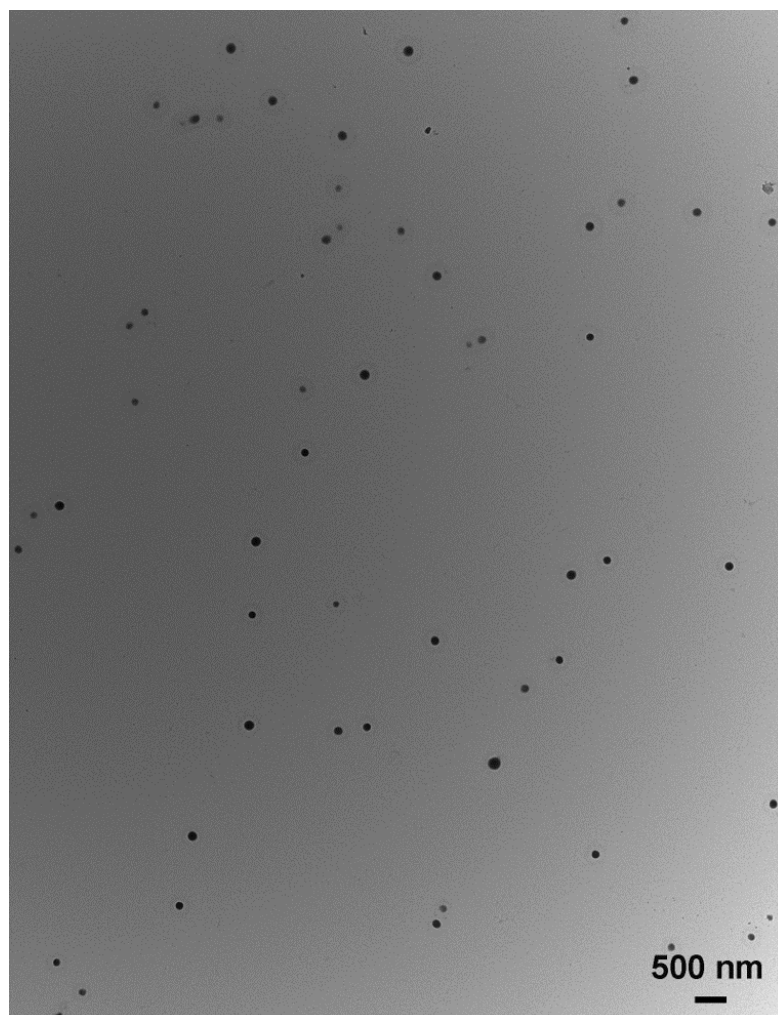


Figure 8.16 UV spectra of FpC<sub>6</sub>Pyrene (50 vol% and 60 vol% water content) aqueous solution at the different time.



**Figure 8.17. SEM image of FpC<sub>6</sub>Pyrene aggregates dried from the solution of THF/water (90 vol% water).**



**Figure 8.18. TEM image of FpC<sub>6</sub>Pyrene precipitates formed in methanol ( $2.5 \times 10^{-4}$  M). The sample was prepared after aging the solution for a few days. The solution was prepared via a cycle of heating at 60 °C and cooling to 23 °C**



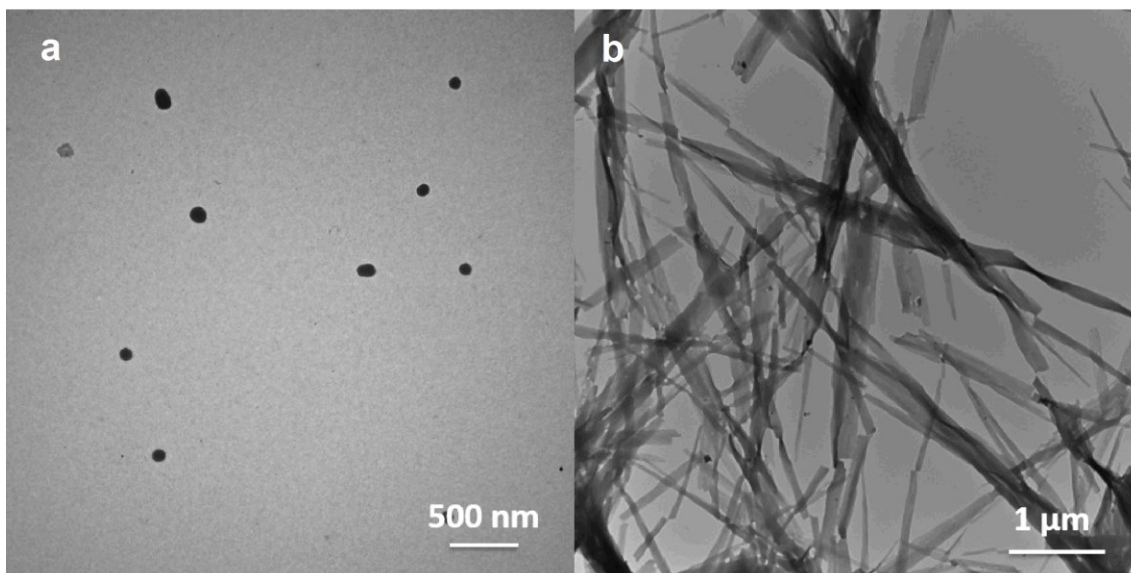


**Figure 8.19. TEM images of FpC<sub>6</sub>Pyrene aggregates formed in ethanol solution with a various degree of supersaturation. The solution was prepared via a cycle of heating at 60 °C and cooling to 23 °C. (a) The solution with a lower degree of supersaturation ( $2.5 \times 10^{-4}$  M) is aged for a week, (b) the solution with a higher degree of supersaturation ( $1.1 \times 10^{-3}$  M) results in a cotton-like suspension in a few hours.**

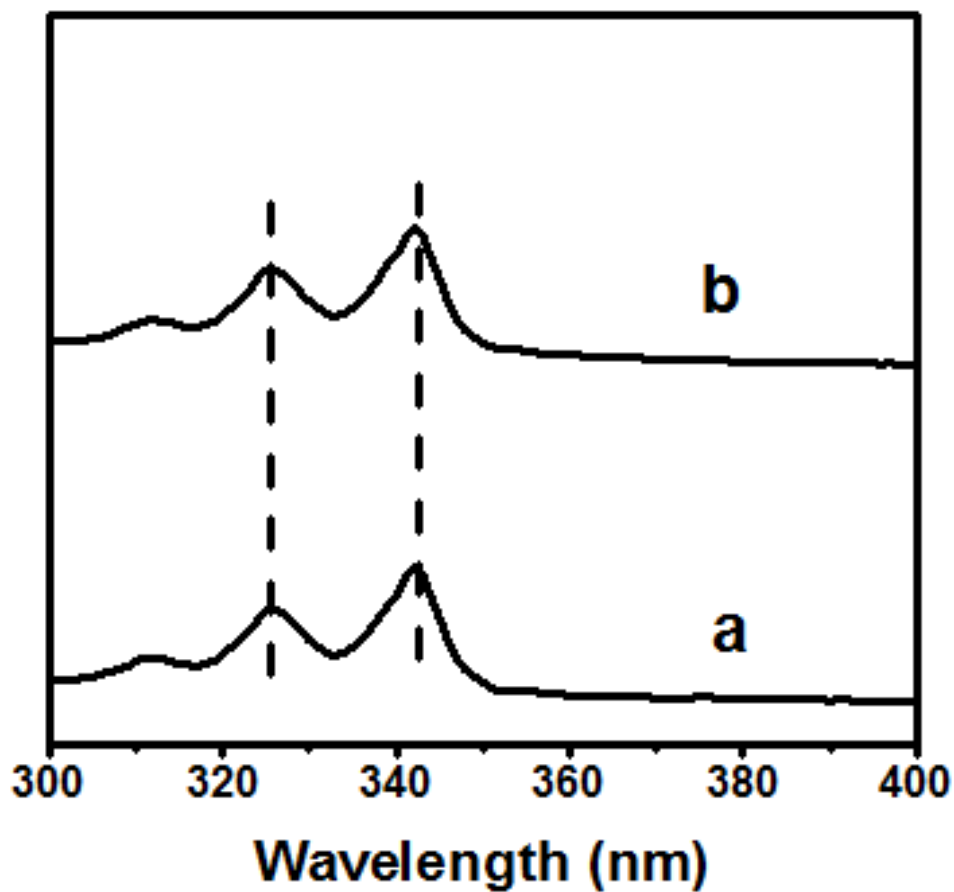
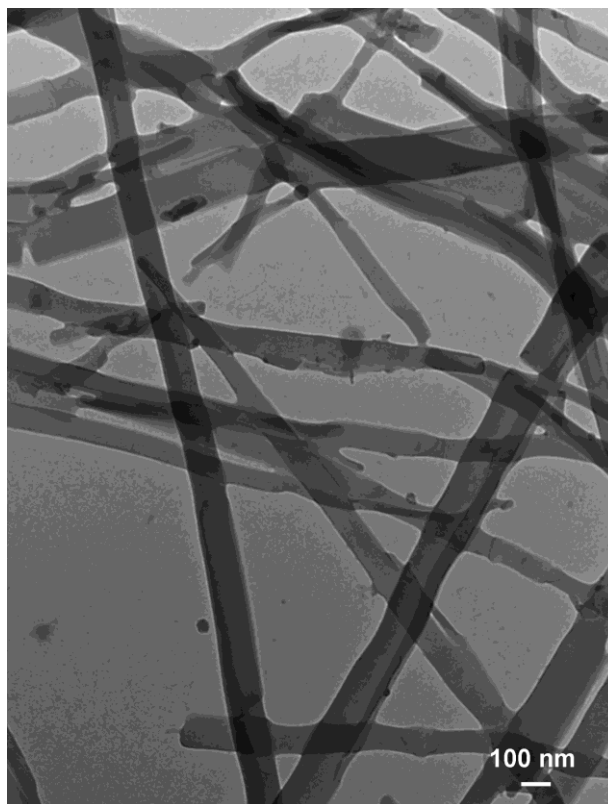


Figure 8.20. UV-Vis spectra of the ethanol solution of FpC<sub>6</sub>Pyrene with a lower degree of supersaturation ( $2.5 \times 10^{-5}$ M). (a) the freshly prepared solution (b) the colloid formed after aging for a week.



**Figure 8.21** TEM image with a relatively large magnification for the aggregates assembled from FpC<sub>6</sub>Pyrene in methanol with a higher  $\sigma$  ( $5.5 \times 10^{-4}$  M).

### **8.5 Supporting information for Chapter 6**

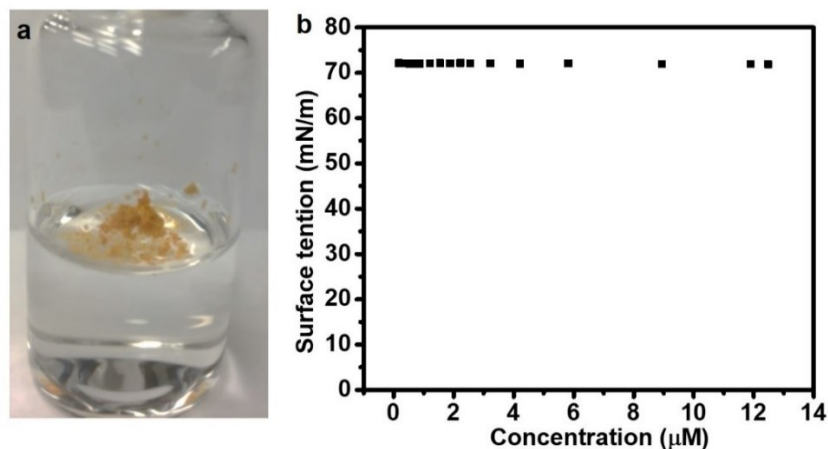


Figure 8.22. a,  $\text{FpC}_6\text{Azobenzene}^{\text{trans}}$  directly mixed with water. b, Concentration-dependent surface tension of  $\text{FpC}_6\text{Azobenzene}^{\text{trans}}$  MCsomes in water. Figure 8.22 indicate that  $\text{FpC}_6\text{Azobenzene}^{\text{trans}}$  is hydrophobic and non-surface active.

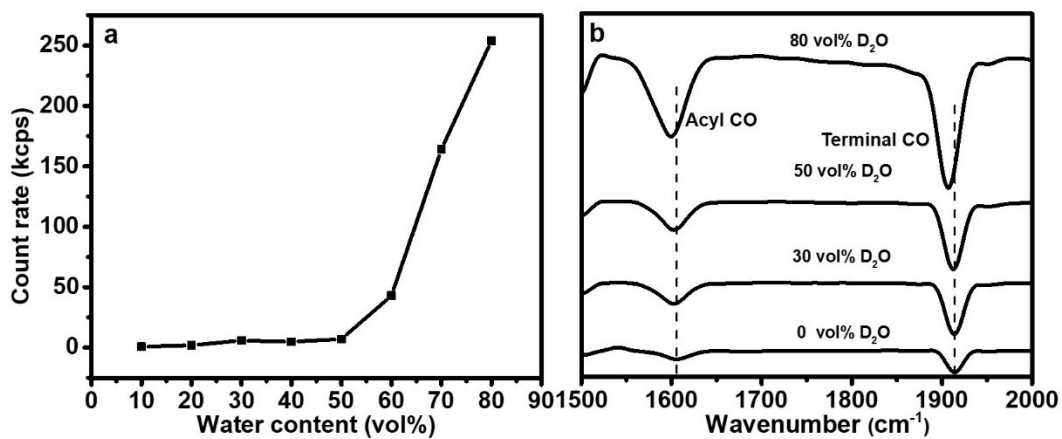


Figure 8.23. a, DLS count rates of  $\text{FpC}_6\text{Azobenzene}^{\text{trans}}$  in THF/water solutions with varied water contents. b, IR absorption of the terminal and acyl CO groups for the solutions of  $\text{FpC}_6\text{Azobenzene}^{\text{trans}}$  in THF/ $\text{D}_2\text{O}$  with varied  $\text{D}_2\text{O}$  contents. As shown in

Figure 8.23a,  $\text{FpC}_6\text{Azobenzene}^{\text{trans}}$  starts to aggregate when the water content is larger than 50 vol%. After the aggregation (80 vol%), the IR signals for the acyl CO and terminal CO groups shift to lower wavenumbers (Figure 8.23b), suggesting the presence of water carbonyl interactions (WCIs).

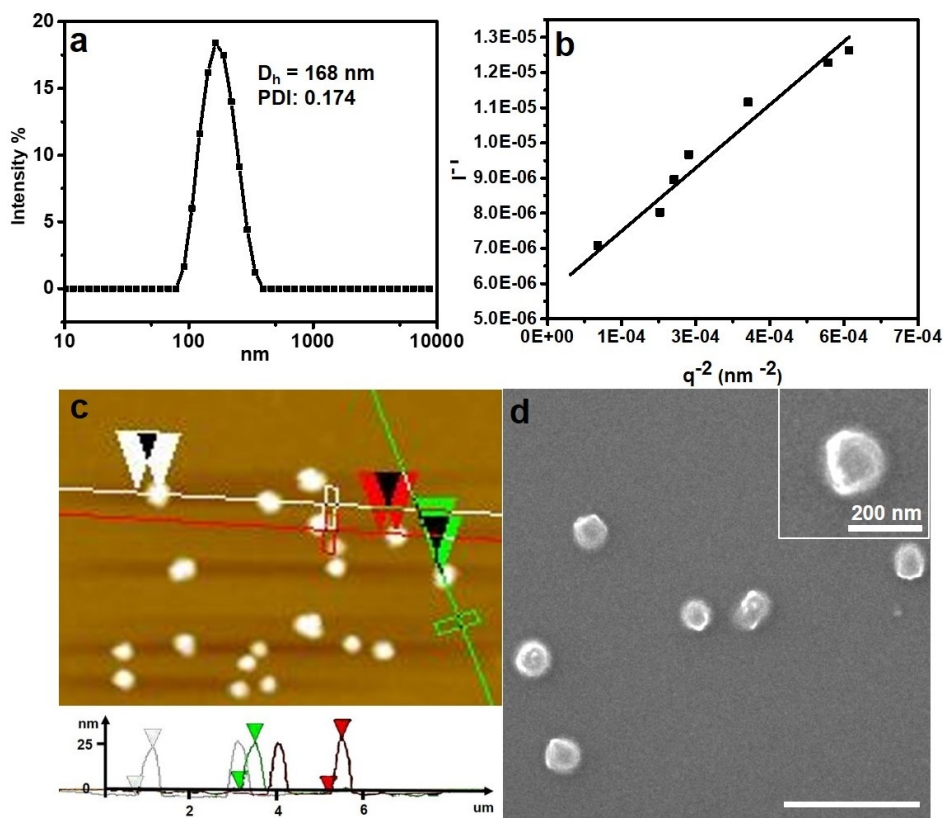


Figure 8.24 a, DLS curve and b Berry plot for  $\text{FpC}_6\text{Azobenzene}^{\text{trans}}$  MCsome in water (1.4  $\mu\text{M}$ ). Figures 8.24a and 8.24b reveal that the hydrophobic radius ( $R_h$ ) and gyration radius ( $R_g$ ) are *ca.* 84 nm and 83 nm, respectively. The  $R_g/R_h$  of *ca.* 1.0 indicates that  $\text{FpC}_6\text{-azobenzene}^{\text{trans}}$  assembles into nanovesicles. c, AFM height mode image with

height profiles for FpC<sub>6</sub>Azobenzene<sup>trans</sup> nanovesicles. The AFM analysis of the aggregates shows that the ratio of diameter-to-height is *ca.*5.0 due to the deformation of hollow structure upon dry. d, SEM image for FpC<sub>6</sub>Azobenzene<sup>trans</sup> nanovesicles. The inset image is the large magnification of a bowl-shaped vesicle due to the deformation of hollow structure. Scale bar = 500 nm, unless otherwise indicated.

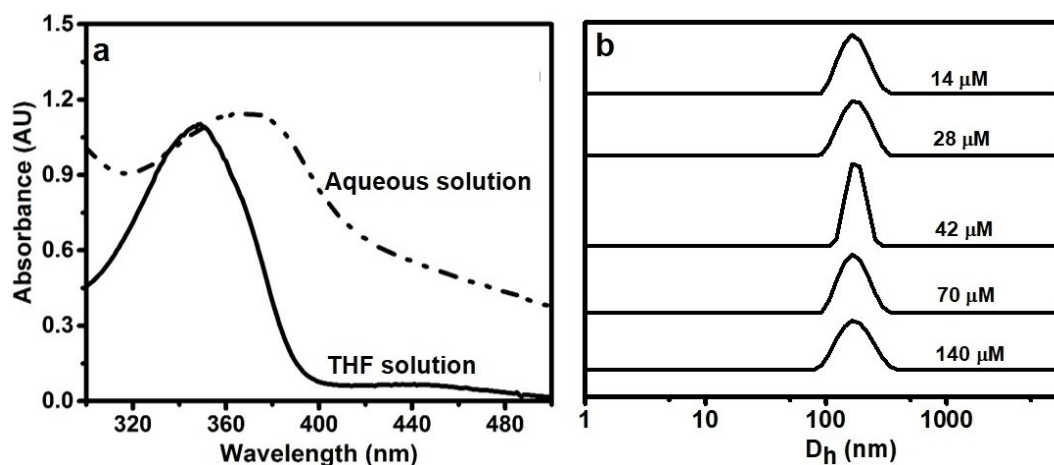
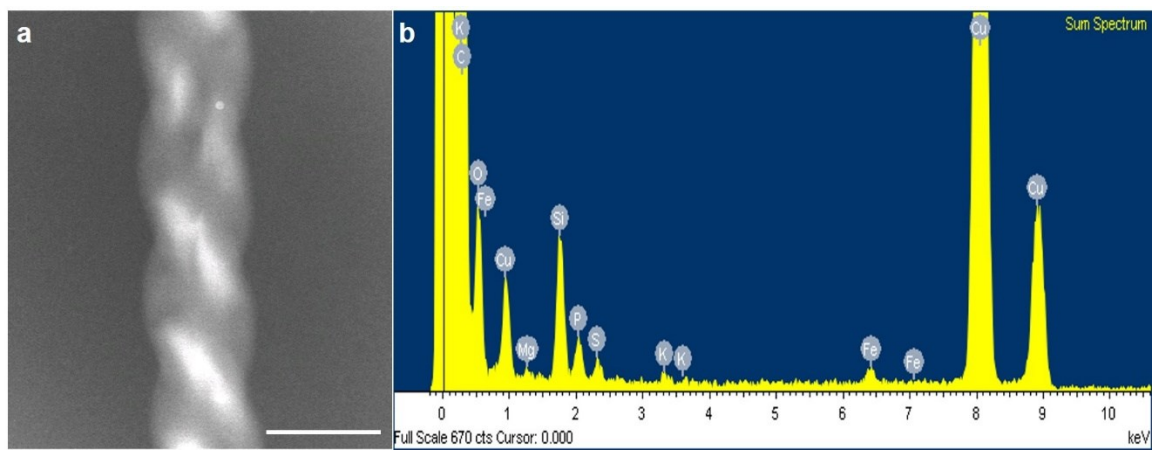
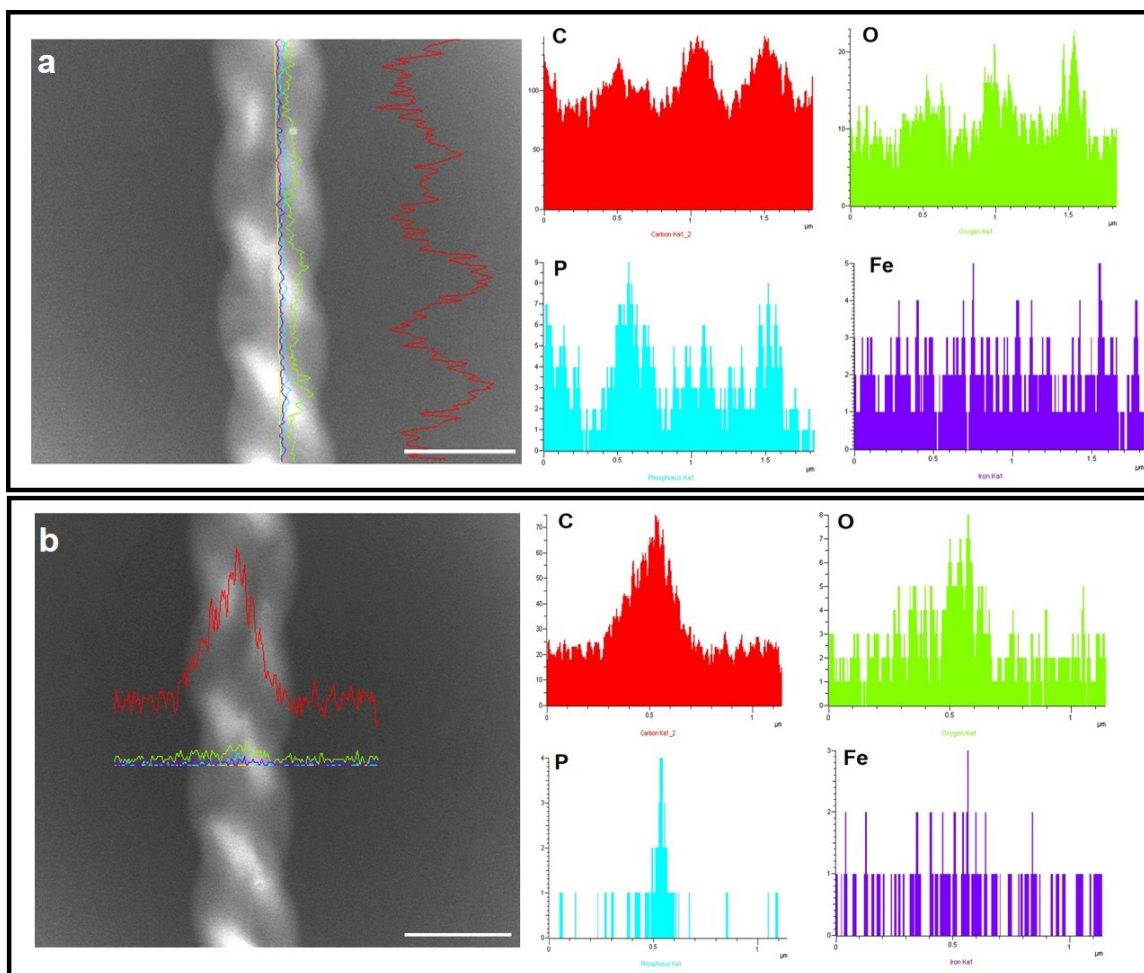


Figure 8.25. a, UV/Vis absorption spectra for FpC<sub>6</sub>Azobenzene<sup>trans</sup> molecules in THF (50 μM) and FpC<sub>6</sub>Azobenzene<sup>trans</sup> MCsomes (60 μM) in water. The shift of the absorption peak to a larger wavelength suggests that the azobenzene groups in the MCsomes are intermolecular  $\pi$ - $\pi$  interacted. b, Concentration-dependent DLS profiles for FpC<sub>6</sub>Azobenzene<sup>trans</sup> MCsomes in water. The solutions were diluted from a prepared MCsome (140 μM) and measured right after the dilution. It indicates that the dilution process does not change the size of the MCsomes.



**Figure 8.26. Dark-field TEM images of the helix assembled from FpC<sub>6</sub>Azobenzene<sup>trans</sup> MCsomes and its EDX analysis profile. Scale bar: 500 nm.**



**Figure 8.27. (a and b) EDX line scanning for the elements of C, O, P and Fe (a) along the helix and (b) normal to the helix. Scale bar: 500 nm. The same element distributions for all the elements confirm that the helix is assembled from FpC<sub>6</sub>Azobenzene<sup>trans</sup>.**



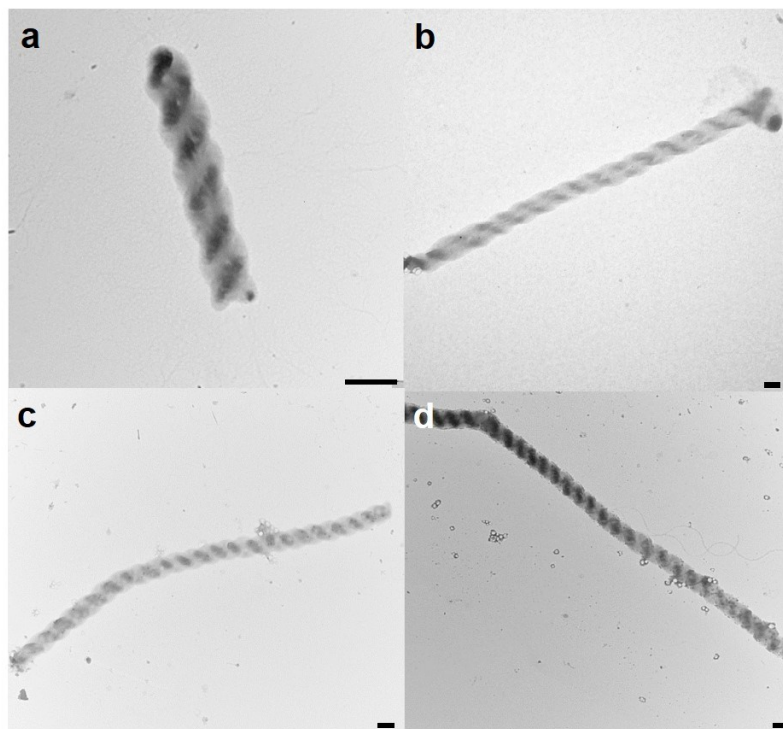


**Figure 8.28.** TEM images recorded after aging the diluted FpC<sub>6</sub>Azobenzene<sup>trans</sup> MCsomes in water (14  $\mu$ M) for 30 days. The long helices have a low concentration, so each image only captures one helix. Scale bar: 500 nm.

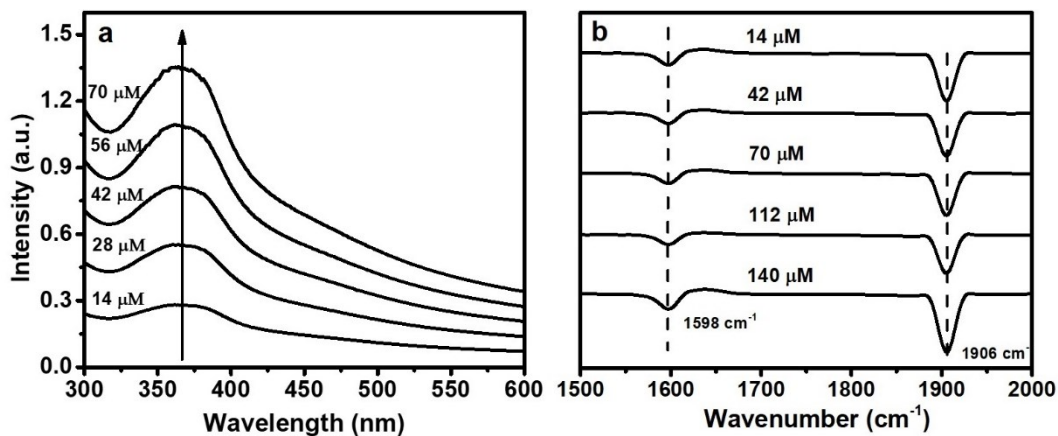


Figure 8.29 a, Concentration-dependent UV absorption at 360 nm for  $\text{FpC}_6\text{Azobenzene}^{\text{trans}}$  MCsomes in water. No shift in the wavelength of the absorption peak suggests that the dilution does not alter the  $\pi$ - $\pi$  interactions. b, Concentration-dependent IR absorption for the acyl and terminal CO groups. No shifts in the wavenumbers for the absorption peaks suggest that the dilution results in no detectable variation in WCIs.

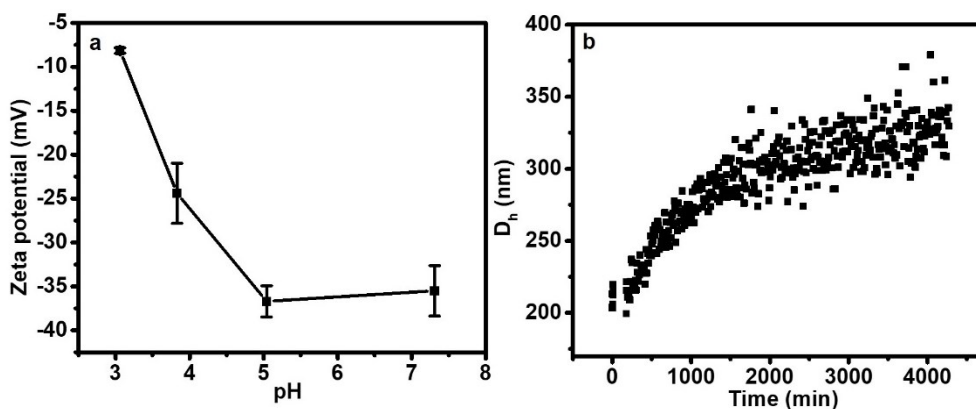


Figure 8.30. a, pH-dependent zeta potential of the diluted FpC<sub>6</sub>Azobenzene<sup>trans</sup> MCsomes (14 μM). b, Time-dependent D<sub>h</sub> of diluted FpC<sub>6</sub>Azobenzene<sup>trans</sup> MCsomes (14 μM) at pH 3.

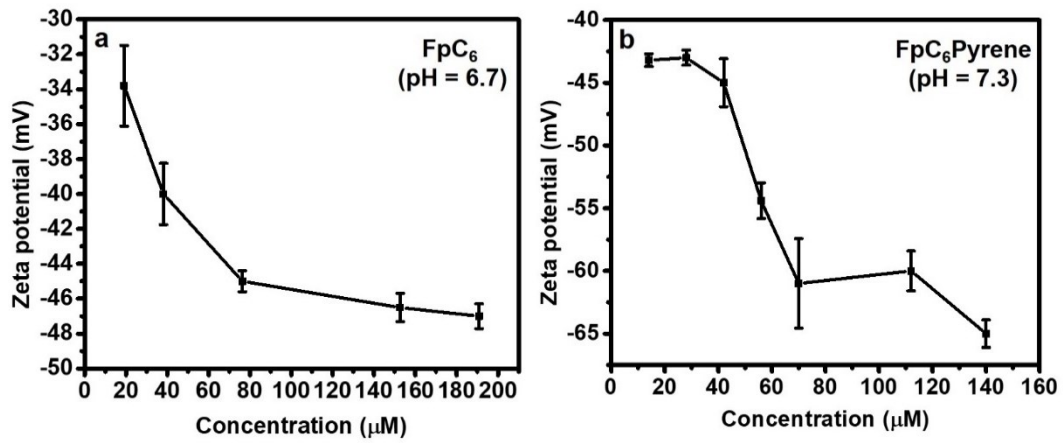


Figure 8.31. Concentration-dependent zeta potential recorded in a process of dilution of a, FpC<sub>6</sub> MCsomes and b, FpC<sub>6</sub>Pyrene MCsomes.

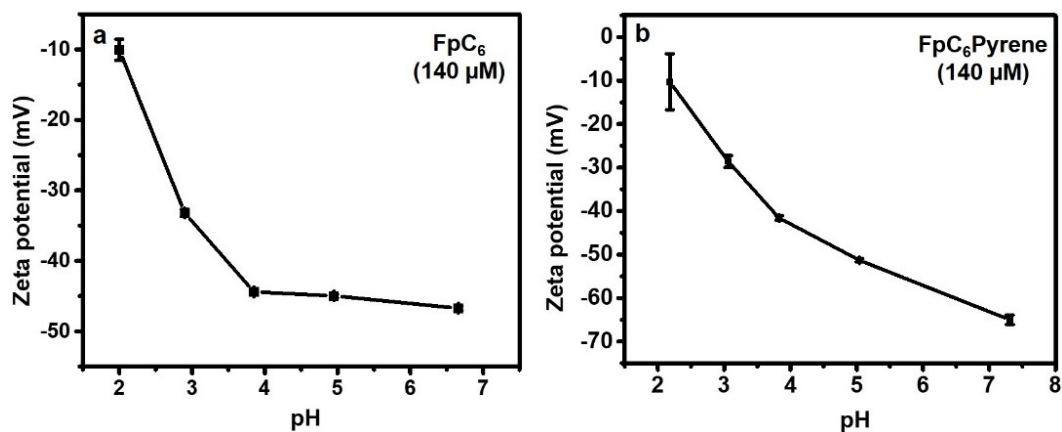


Figure 8.32. pH-dependent zeta potential of a FpC<sub>6</sub> MCsomes and b FpC<sub>6</sub>Pyrene MCsomes. The concentrations for both MCsomes are 140 μM.

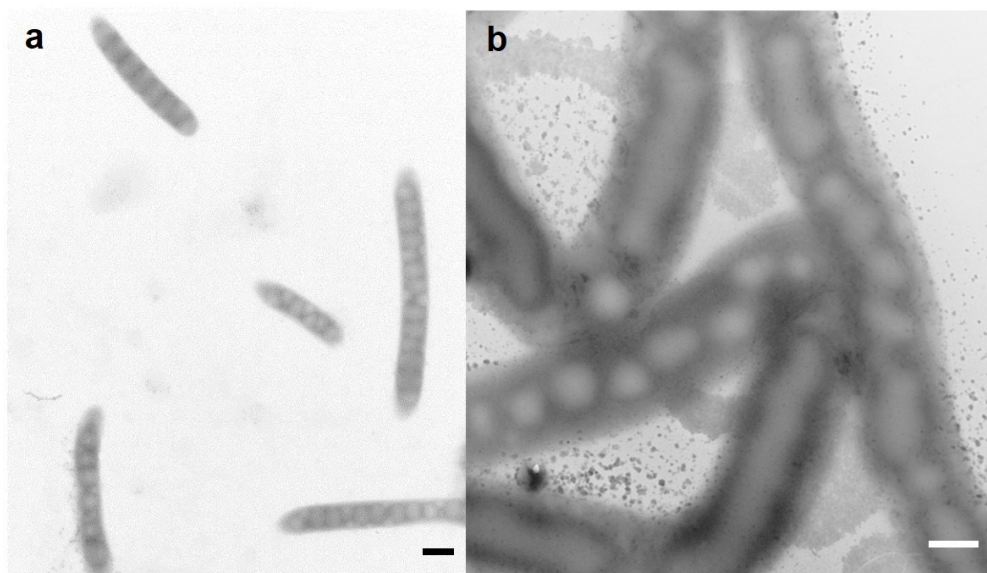
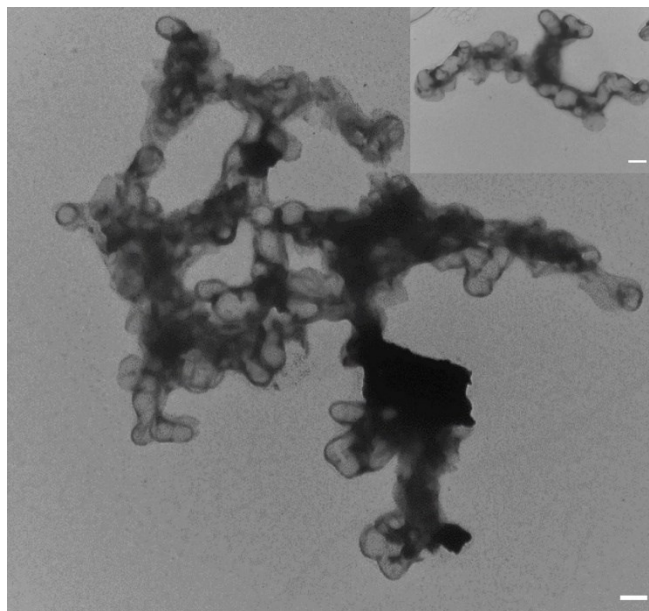
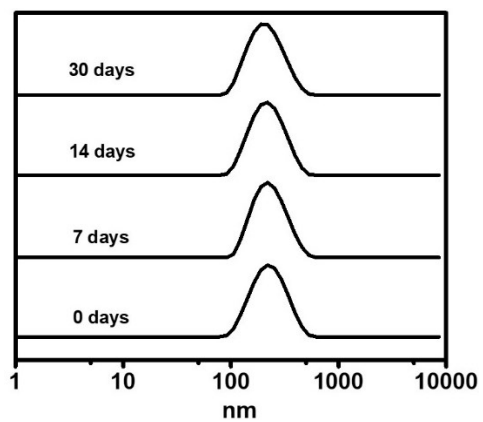


Figure 8.33. TEM images recorded for the diluted FpC<sub>6</sub>Azobenzene<sup>trans</sup> MCsomes (14 μM) after aging for 14 and 17 days. a, one-dimensional arrays of vesicles and b, the arrays with partial coalescence of vesicles. Scale bar: 500 nm.



**Figure 8.34.** TEM images of the precipitates resulting from FpC<sub>6</sub>Azobenzene<sup>trans</sup> MCsomes (140  $\mu$ M) at pH = 3 after aging for *ca.*2 weeks. Scale Bar: 500 nm



**Figure 8.35.** Time-dependent DLS profiles for FpC<sub>6</sub>Pyrene MCsomes in water (140  $\mu$ M).

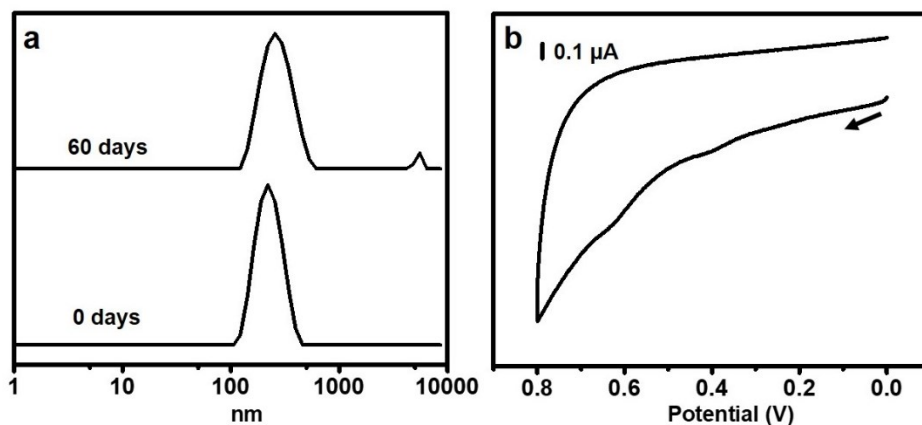


Figure 8.36. a, DLS profiles for the diluted FpC<sub>6</sub>Pyrene MCSomes (14 μM) in water before and after aging. b, The cyclic voltammogram (CV) for FpC<sub>6</sub>Pyrene MCSome in water (140 μM).

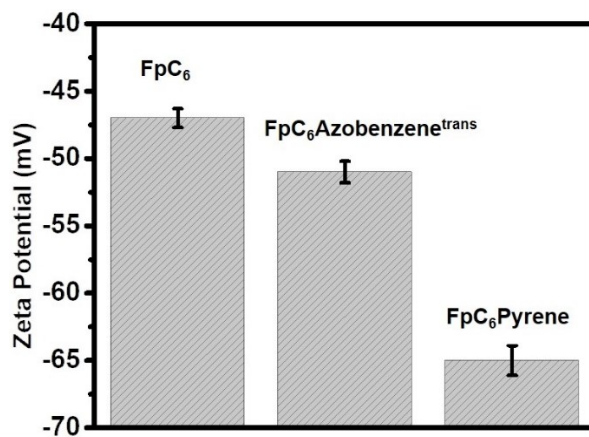
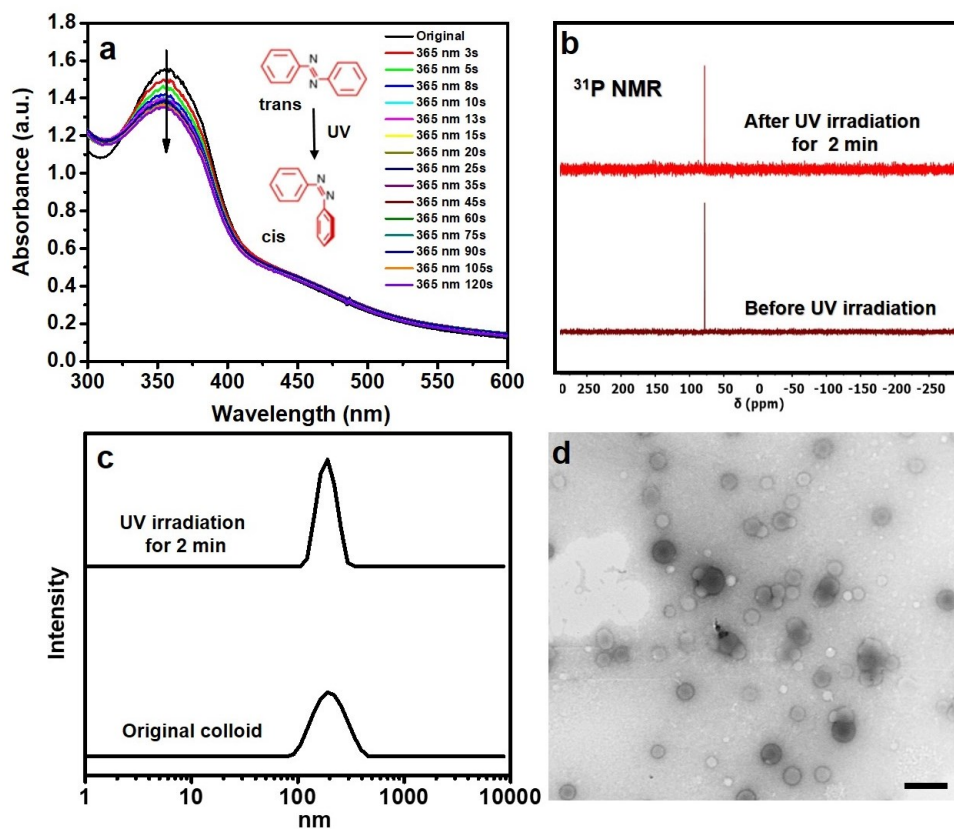


Figure 8.37. Zeta potential of the three different MCSomes in water at 140 μM.



**Figure 8.38. a, UV/Vis spectra of FpC<sub>6</sub>Azobenzene<sup>trans</sup> MCsomes (70 μM) in water after UV light (wavelength = 365 nm) irradiation for different times. b, <sup>31</sup>P NMR spectra of FpC<sub>6</sub>Azobenzene<sup>trans</sup> molecules in CDCl<sub>3</sub>. These molecules were recovered from their aqueous solutions via freeze-drying before and after UV irradiation (365 nm). There is no change in the spectra after the irradiation suggesting no degradation of the molecules. c, DLS profile of FpC<sub>6</sub>Azobenzene<sup>trans</sup> MCsomes (140 μM) before and after UV irradiation. d, TEM image of the FpC<sub>6</sub>Azobenzene<sup>trans</sup> MCsomes after UV**

**irradiation for 2 min (Scale bar: 500 nm). Figures 8.38c and 8.38d indicate that the irradiation does not change the vesicular morphology.**



## 8.6 Synthesis and solution behavior of Fp-dendrimer complex

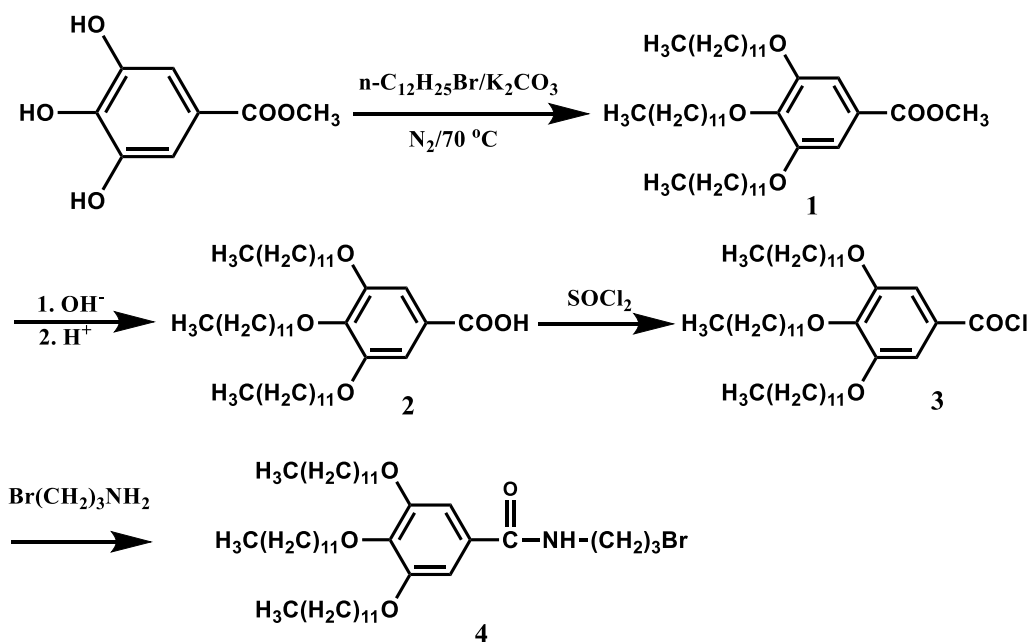
### 8.6.1 Materials and instruments

Methyl 3,4,5-trihydroxybenzoate, 1-bromododecane, triethylamine, xx are purchased from Sigma-Aldrich. Anhydrous potassium carbonate, thionyl chloride and sodium hydroxide are commercial. The solvents mentioned in the paper are used without further purification.

$^1\text{H-NMR}$  were measured on a Bruker-300 (300 MHz) spectrometer at ambient temperature using either  $\text{CDCl}_3$  as a solvent. Dynamic light scattering (DLS experiments) were performed on a Malvern Zetasizer (Nano S90).

### 8.6.2 Synthesis of Fp-dendrimer complex 6

#### 8.6.2.1 Synthesis of the ligand N-(3-bromopropyl)-3,4,5-tris(dodecyloxy)benzamide (4)



Scheme 8.1 Synthetic route for the ligand-complex 4

### Synthesis of methyl 3,4,5-tris(dodecyloxy)benzoate (1)

Methyl 3,4,5-trihydroxybenzoate (3.0 g, 16.3 mmol) and  $K_2CO_3$  (13.5 g, 98 mmol) were first dissolved in 60 mL dry DMF under nitrogen atmosphere. The mixture was stirred at room temperature for 1 h and then 1-bromododecane (13.0 g, 52.0 mmol) was added dropwise into the mixture. The reaction mixture was stirred at 80°C for 24 h. After cooling to room temperature, the reaction mixture was poured into a large amount of water and extracted three times with  $CHCl_3$ . The combined organic layer was washed with water and brine. Then the organic solvent was removed under reduced pressure. The residue was subjected to column chromatography (5% ethylacetate/hexane) over silica gel to afford the pure product. Yield: 80%.  $^1H$  NMR spectroscopy (300MHz,  $CDCl_3$ , Figure 8.39) :  $\delta$  = 7.25 (s, 2H), 4.03-3.99 (m, 6H), 3.89 (s, 3H), 1.84-1.81(m, 6H), 1.50-1.45 (m, 6H), 1.35-1.27 (m, 48H), 0.89-0.88 (t, 9H)

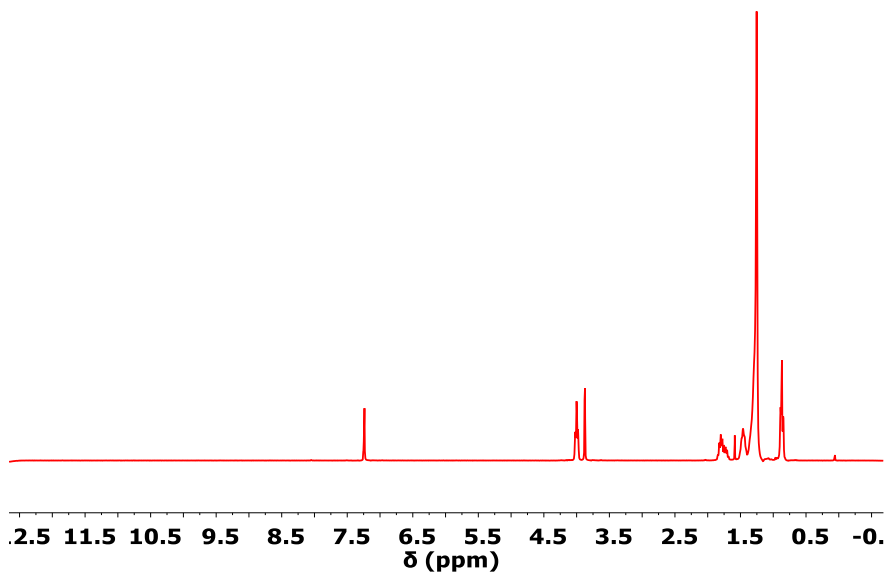


**Figure 8.39  $^1\text{H}$  NMR spectrum of 3,4,5-tris(dodecyloxy)benzoate in chloroform- $\text{d}_1$  at 298 K**

Synthesis of 3,4,5-tridodecyloxybenzoic acid (**2**)

Potassium hydroxide (1.63g, 30 mmol) was added to a solution of compound **1** (10g, 15 mmol) in ethanol (200 mL). The mixture was heated at reflux for 8 h and then cooled to room temperature. The solution was diluted with deionized water and acidified by addition of 1M hydrochloric acid to pH 1. The precipitate was then filtered, washed with deionized water and dried under vacuum. Recrystallize from hot ethanol gave white solid (6.34g, 63%).  $^1\text{H}$  NMR ( $\text{CDCl}_3$ , 300 MHz, Figure 8.40):  $\delta=7.29$  (s, 2H, Ar-H), 4.00 (m, 6H,  $\text{OCH}_2$ ), 1.81-1.72 (m, 6H,  $\text{CH}_2$ ), 1.45-1.24 (m, 54H,  $\text{CH}_2$ ), 0.87 (t, 9H,  $\text{CH}_3$ )

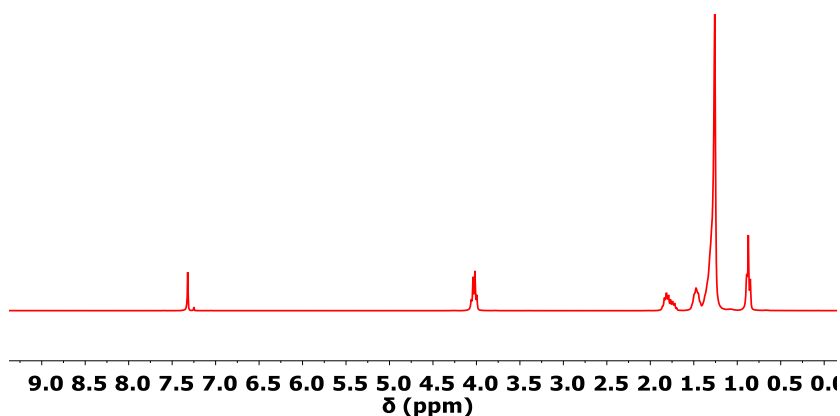


**Figure 8.40  $^1\text{H}$  NMR spectrum of 3,4,5-tris(dodecyloxy)benzoic acid in chloroform- $\text{d}_1$  at 298 K**

Synthesis of 3,4,5-tris(dodecyloxy)benzoyl chloride (**3**)

Compound **2** (5.0 g, 7.41 mmol) first dissolved in thionyl chloride and refluxed for overnight. After cooling to room temperature, the Thionyl chloride (13.22 g, 11.10 mmol) was evaporated under reduced pressure, and the resulting precipitate was dried under vacuum to give the compound **3**. The compound **3** was directly used for the next step without further purification.

#### Synthesis of N-(3-bromopropyl)-3,4,5-tris(dodecyloxy)benzamide (**4**)

Compound **3** (5.0 g, 7.23 mmol) was added to a 40 mL mixed solution of DCM/H<sub>2</sub>O (1:1). Then 5.0 g K<sub>2</sub>CO<sub>3</sub> was directly added into the mixed solution. The solution was stirred for 30 minutes at room temperature. Then NH<sub>2</sub>(CH<sub>2</sub>)<sub>3</sub>BrHBr (2.5 g, 11.52 mmol) was quickly added and the mixture was stirred for overnight at room temperature. After the reaction, the mixture was extracted three times with CHCl<sub>2</sub>. The combined organic layer was washed with water and brine. Then the organic solvent was removed under reduced pressure. The residue was subjected to column chromatography (15% ethylacetate/hexane) over silica gel to afford the pure product. Yield: 90%. <sup>1</sup>H NMR spectroscopy (300MHz, CDCl<sub>3</sub>, Figure 8.41): δ = 7.0 (s, 2H), 6.22-6.33 (t, 3H), 4.03-3.90 (m, 6H), 3.46-3.62 (m, 4H), 2.16-2.25(m, 2H), 1.62-1.86 (m, 6H), 1.20-1.52 (m, 48H), 0.83-0.93 (t, 9H)

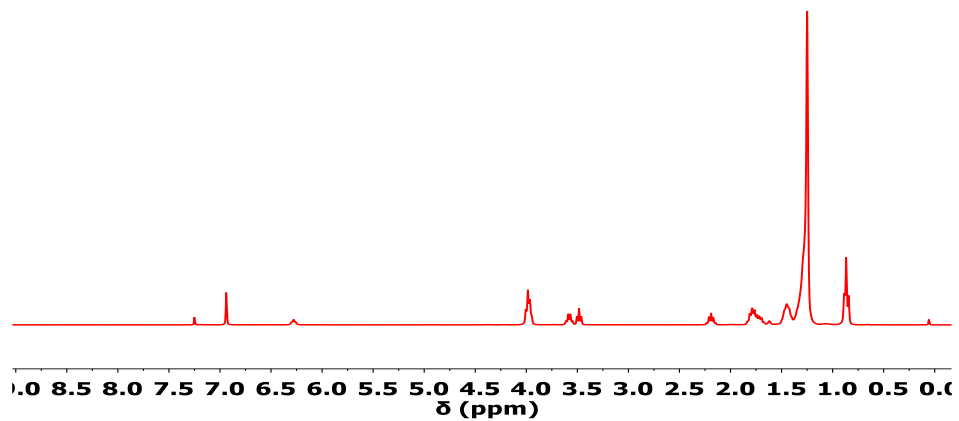
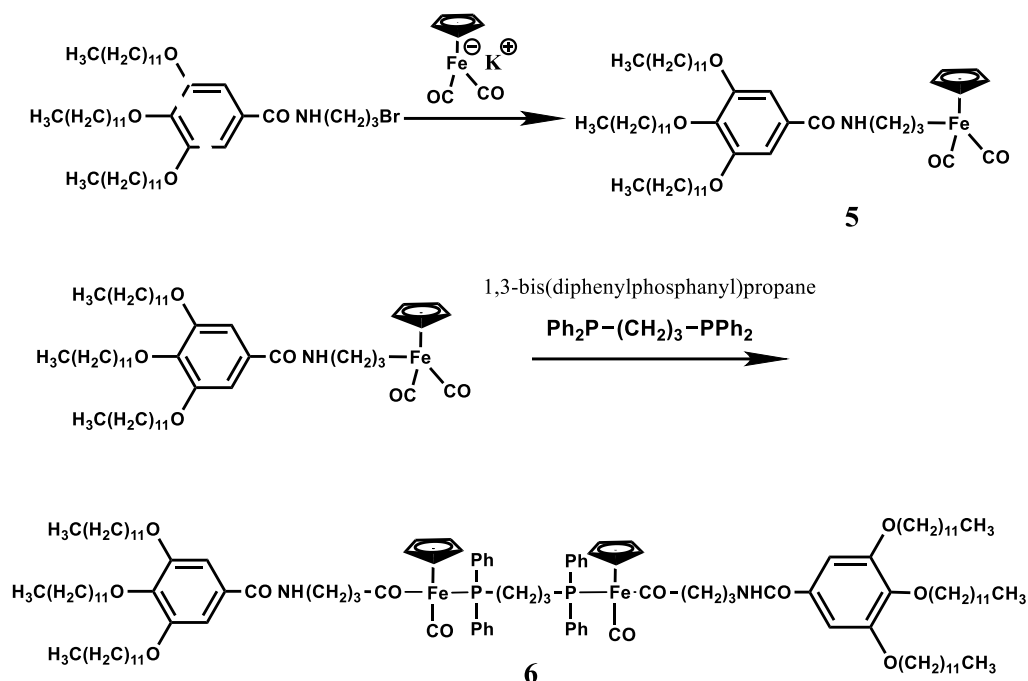


**Figure 8.41**  $^1\text{H}$  NMR spectrum of N-(3-bromopropyl)-3,4,5-tris(dodecyloxy)benzamide in chloroform- $\text{d}_1$  at 298 K

### 8.6.2.2 Synthesis of target compound 6



### Scheme 8.2 Synthetic route for target complex 6

#### Synthesis of complex 5

FpK was synthesized based on previous literature. (Polym. Chem., 2016,7, 4419-4426) Complex 4 (1.50 g, 1.89 mmol) in dry THF was added dropwise into FpK (1.0 g, 4.63 mmol) in THF solution at 0 °C. Then the mixture was stirred at room temperature for 3 h. After the reaction was over, the organic solvent was removed under reduced pressure. Then the crude product was dissolved in DCM followed by filtration to remove the salts to obtain a dark brown solution. DCM was removed under reduced pressure followed by purification with column chromatography (DCM) over silica gel to afford the pure product. Yield: 94 %.  $^1\text{H}$  NMR spectroscopy (300MHz,  $\text{CDCl}_3$ , Figure 8.42):  $\delta = 6.9$  (s, 2H), 6.00-

6.08 (t, 3H), 4.69-4.79 (s, 5H), 3.92-3.05 (m, 6H), 3.31-3.43 (m, 2H), 1.53-1.83 (m, 12H), 1.15-1.52 (m, 48H), 0.78-0.96 (t, 9H).

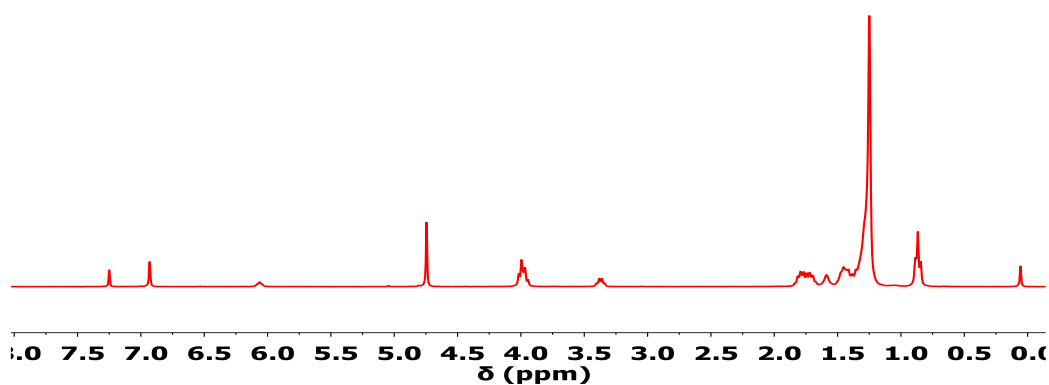


**Figure 8.42**  $^1\text{H}$  NMR spectrum of complex **5** in chloroform- $\text{d}_1$  at 298 K

#### Synthesis of complex **6**

Complex **5** (1.90 g, 2.1 mmol) was mixed with 1,3-bis(diphenylphosphanyl)propane (0.44 g, 1.0 mmol) in THF at room temperature. Then the mixture was refluxed for 24 h. After the reaction is over, THF was first removed under reduced pressure. Then the crude product was purified with column chromatography (25% ethyl acetate/hexane) over silica gel to afford the pure product. Yield 26%.  $^1\text{H}$  NMR spectroscopy (300MHz,  $\text{CDCl}_3$ , Figure 8.43):  $\delta$  = 6.63-6.80 (d, 2H), 6.95-7.08 (d, 4H), 7.19-7.35 (m, 20H), 4.14 - 4.27 (d, 10H), 3.84-4.05 (m, 12H), 2.13-3.27 (m, 12H), 1.65-1.87 (m, 12H), 1.15-1.52 (m, 96H), 0.78-0.96 (t, 18H).  $^{31}\text{P}$  NMR spectroscopy (300 MHz,  $\text{CDCl}_3$ , Figure 8.44):  $\delta$  = 71.6 ( $\text{PPh}_3$ ).

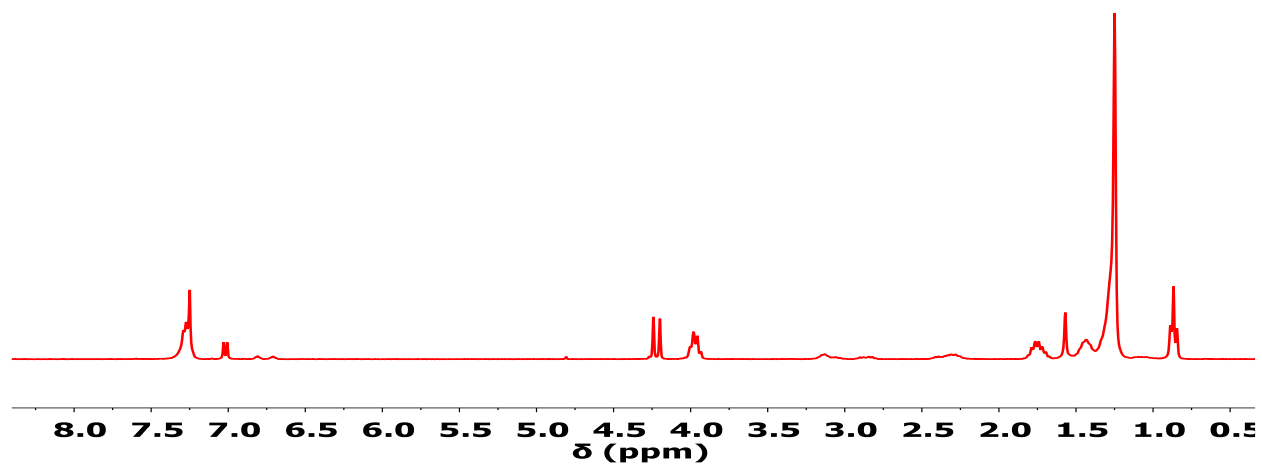


Figure 8.43  $^1\text{H}$  NMR spectrum of target complex 6 in chloroform- $\text{d}_1$  at 298 K

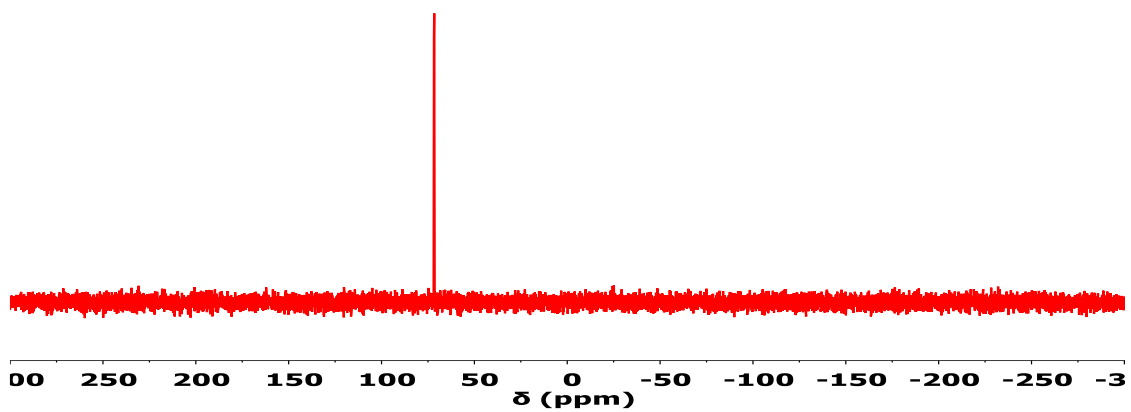


Figure 8.44  $^{31}\text{P}$  NMR spectrum of target complex 6 in chloroform- $\text{d}_1$  at 298 K



### 8.6.3 Solution behavior of complex 6 in organic solvents

The solution behavior of complex 6 in organic solvents was first investigated. We first check the solubility of complex 6 in different organic solvents. As shown in Table 8.6, the complex 6 has a good solubility in the organic solvents such as hexane, MCH and THF when the concentration was 1 mg/mL. For the sample of complex 6 in MCH, when the concentration increased to 10 mg/mL, the complex is still soluble. And there was no signal was detected by DLS measurements.

**Table 8.6 The solubility of complex 6 in different organic solvents**

| Solvent     | Concentration | Solution behavior |
|-------------|---------------|-------------------|
| Hexane      | 1 mg/mL       | Dissolved         |
| Toluene     | 1 mg/mL       | Dissolved         |
| MCH*        | 1 mg/mL       | Dissolved         |
| Heptane     | 1 mg/mL       | Dissolved         |
| Isopropanol | 1 mg/mL       | Dissolved         |
| Cyclohexane | 1 mg/mL       | Dissolved         |
| THF         | 1 mg/mL       | Dissolved         |

\* Increasing the concentration from 1 mg/mL to 37 mg/mL, complex 6 was still soluble.

## 8.7 Fabrication of gold nanoparticle arrays using P(FpP) film as a template

### 8.7.1 Proposal

P(FpP) polymer is hydrophobic and can self-assemble into a P(FpP) film on the water surface by the Langmuir–Blodgett method.<sup>226</sup> The carbonyl CO groups in the P(FpP) can interact with water which could make CO groups distribute on the interface between film and water. Meanwhile, the water-carbonyl interactions could make the film possess negative charge.<sup>79</sup> Here we hypothesis that CO groups on the surface of P(FpP) films may attract and coordinate Au ions onto the P(FpP) film. Then reducing Au nanoparticles could form nanoparticles arrays on the surface.

### 8.7.2 Preparation method

4.04 mg P(FpP) polymer (FpP = CpFe(CO)<sub>2</sub>(CH<sub>2</sub>)<sub>3</sub>PPh<sub>2</sub>, DP = 20) was dissolved in 5 mL toluene to obtain 57 μM P(FpP)/toluene yellow solution. 50 μL of the P(FpP)/toluene solution was gently dropped into 10 mL HAuCl<sub>4</sub> aqueous solution (10<sup>-5</sup> M) which loaded in the 20 mL vial with a 2.5 cm diameter. The obtained solution was colorless and transparent. Then the vial was immediately capped and the samples were left to make toluene evaporated slowly without disturbances. After a few days, the solution became pink from colorless. and there was a thin film formed on the surface of the pink solution.

### 8.7.3 TEM characterization and preliminary results

The formed thin films were transferred into the TEM carbon grid by a pipette which inhaled a small piece. As shown in Figure 8.45a, the large-area continuous film was observed. Interestingly, in the TEM image with a large magnification (Figure 8.45b), some branched fibers could be observed. The preliminary results suggested that the P(FpP) film could be fabricated. Future experiments could be

done to check if Au nanoparticle arrays are formed on the P(FpP) film. According to previous knowledge,<sup>71</sup> to immobilize the Au nanoparticles, -NH, -SH, -COOH moieties are needed. which suggest that the formed Au nanoparticles could be hard to attach on the P(FpP) film.

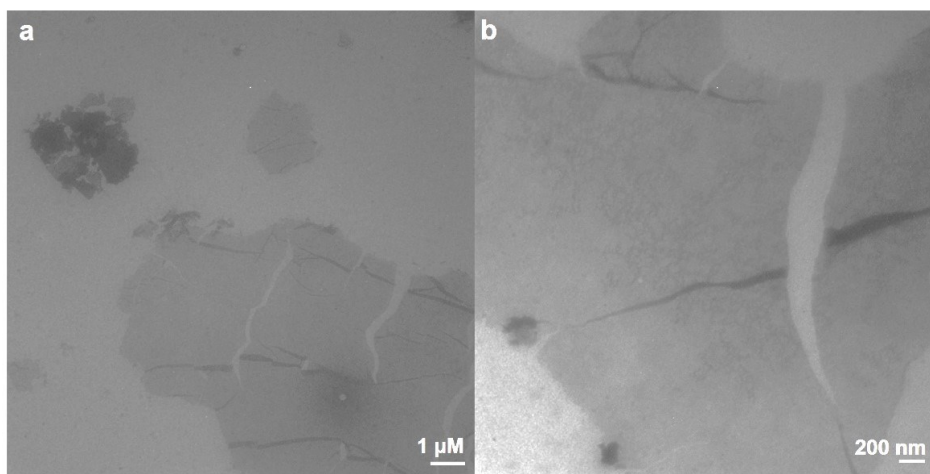


**Figure 8.45** TEM images of the film formed on the surface of the solution a) low magnification, b) large magnification.

## **8.8 To coordinate $Gd^{3+}$ on the P(FpP) MCsomes**

### **8.8.1 Proposal**

From previous report<sup>79</sup> we know that hydrophobic P(FpP) could self-assemble into nanovesicles in water. The CO groups from P(FpP) interacts with water to form water carbonyl interactions to stabilize the formed nanovesicles. Here we hypothesis CO groups on the surface of the P(FpP) MCsomes may attract and coordinate heavy metal ion such as  $Gd^{3+}$  onto the P(FpP) MCsomes.

### 8.8.2 Preparation of P(FpP) aqueous colloid

0.025 mg/mL P(FpP) (FpP = CpFe(CO)<sub>2</sub>(CH<sub>2</sub>)<sub>3</sub>PPh<sub>2</sub>, DP = 20) aqueous colloid was prepared followed previous reported method.<sup>79</sup> First P(FpP) was dissolved in THF to obtain P(FpP)/THF solution (0.25 mg/mL). Then large amount of water (10 mL) was quickly added into the P(FpP)/THF solution (1 mL, 0.25 mg/mL). The obtained colloid was N<sub>2</sub> bubbled for *ca.* 30 minutes to remove THF.

### 8.8.3 Adding GdCl<sub>3</sub> aqueous solution into P(FpP) colloid

Various amounts (0 mL, 1 mL, 2 mL, 3 mL and 4 mL) of GdCl<sub>3</sub> aqueous solution (25 μM) were added into the prepared P(FpP) colloid (0.025 mg/mL, 5 mL). DLS was used to measure the size change of P(FpP) aggregates. As shown in Figure 8.46a, by addition of GdCl<sub>3</sub> solution, the size of P(FpP) aggregates exhibited increasing trend. TEM was employed to characterize the freshly prepared P(FpP) colloids with various amounts of GdCl<sub>3</sub> solutions. As shown in Figure 8.46b, by addition of 1 mL GdCl<sub>3</sub> solution, uniform and black spherical nanoparticles were observed. When 2 mL GdCl<sub>3</sub> solution was added, some large P(FpP) aggregates were witnessed (Figure 8.46c). DLS and TEM characterization suggested that addition of GdCl<sub>3</sub> solution could cause the aggregation of P(FpP) aggregates. But more experiments are needed in the future to prove the Gd<sup>3+</sup> has attached on the surface of P(FpP) aggregates and check the loading efficiency of metal ion Gd<sup>3+</sup>.

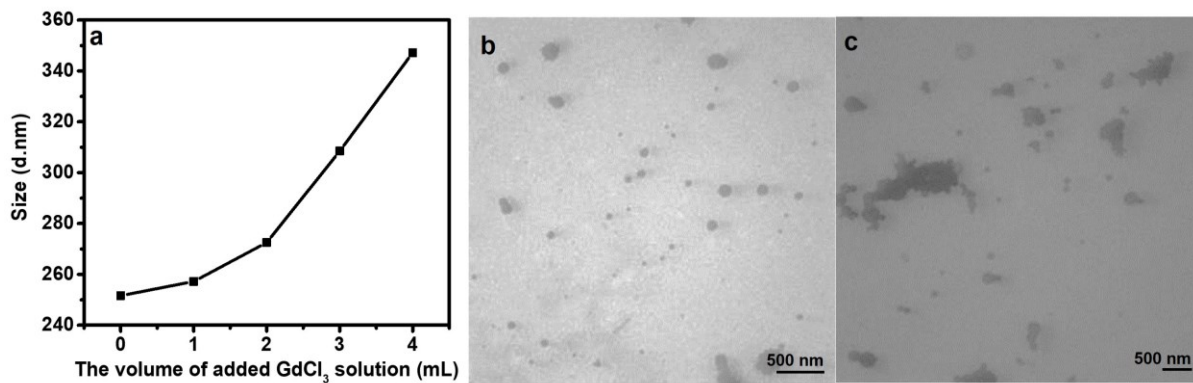


**Figure 8.46** The size change ( $D_h$ ) of P(FpP) aggregates by addition of various amounts of GdCl<sub>3</sub> solution. And TEM images of P(FpP) colloids with various amounts of GdCl<sub>3</sub> aqueous solution (25 μM), b) 1 mL, c) 2 mL GdCl<sub>3</sub> aqueous solution.